Volume II:
Technical Documentation

for

UTCHEM-9.0

A Three-Dimensional
Chemical Flood Simulator

Prepared by

Reservoir Engineering Research Program
Center for Petroleum and Geosystems Engineering
The University of Texas at Austin
Austin, Texas 78712

July, 2000

Table of Contents

Section 5: Dual Porosity Model

Section 6: UTCHEM Model of Gel Treatment

Section 7: Multiple Organic Components

Section 8: Mathematical Formulation of Reaction Equilibrium

Section 9: UTCHEM Biodegradation Model Formulation and Implementation

Section 10: Well Models

Section 11: Effect of Alcohol on Phase Behavior

Section 1
Introduction

Pioneering research being conducted at The University of Texas at Austin is providing a scientific and engineering basis for modeling the enhanced recovery of oil and the enhanced remediation of aquifers through the development and application of compositional simulators. This research has resulted in the development and application of UTCHEM, a 3-D, multicomponent, multiphase, compositional model of chemical flooding processes which accounts for complex phase behavior, chemical and physical transformations and heterogeneous porous media properties, and uses advanced concepts in high-order numerical accuracy and dispersion control and vector and parallel processing. The simulator was originally developed by Pope and Nelson in 1978 to simulate the enhanced recovery of oil using surfactant and polymer processes. Thus, the complex phase behavior of micellar fluids as a function of surfactant, alcohol, oil, and aqueous components was developed early and has been extensively verified against enhanced oil recovery experiments. Generalizations by Bhuyan *et al.* in 1990 have extended the model to include other chemical processes and a variety of geochemical reactions between the aqueous and solid phases. The nonequilibrium dissolution of organic components from a nonaqueous phase liquid into a flowing aqueous or microemulsion phase is modeled using a linear mass-transfer model. In this simulator, the flow and mass-transport equations are solved for any number of user-specified chemical components (water, organic contaminants, surfactant, alcohols, polymer, chloride, calcium, other electrolytes, microbiological species, electron acceptors, etc.). These components can form up to four fluid phases (air, water, oil, and microemulsion) and any number of solid minerals depending on the overall composition. The microemulsion forms only above the critical micelle concentration of the surfactant and is a thermodynamically stable mixture of water, surfactant and one or more organic components. All of these features taken together, but especially the transport and flow of multiple phases with multiple species and multiple chemical and biological reactions make UTCHEM unique.

UTCHEM groundwater applications:

- NAPL spill and migration in both saturated and unsaturated zones
- Partitioning interwell test in both saturated and unsaturated zones of aquifers
- Remediation using surfactant/cosolvent/polymer
- Remediation using surfactant/foam
- Remediation using cosolvents
- Bioremediation
- Geochemical reactions (e.g., heavy metals and radionuclides)

UTCHEM oil reservoir applications:

- Waterflooding
- Single well, partitioning interwell, and single well wettability tracer tests
- Polymer flooding
- Profile control using gel
- Surfactant flooding
- High pH alkaline flooding
- Microbial EOR
- Surfactant/foam and ASP/foam EOR

UTCHEM features:

- 3-dimensional, variable temperature
- IMPES-type formulation
- Third-order finite difference with a flux limiter
- Four phase (water, oil, microemulsion, and gas)
- Vertical and horizontal wells
- Constant pressure boundaries
- Cartesian, radial, and curvilinear grid options
- Heterogeneous permeability and porosity
- Full tensor dispersion coefficient and molecular diffusion
- Adsorption of surfactant, polymer, and organic species
- Solubilization and mobilization of oil
- Clay/surfactant cation exchange
- Water/surfactant (cosolvent)/oil phase behavior
- Polymer with non-Newtonian rheology
- Tracers (partitioning, reaction, adsorption, and radioactive decay)
- Compositional density and viscosity functions
- Surfactant/foam model
- Multiple organic properties
- Trapping number including both viscous and buoyancy forces
- Dual porosity model for tracer
- Geochemical reactions
- Biological reactions
- Several polymer/gel kinetics
- Equilibrium and rate-limited organic dissolution
- Rock dependent capillary pressure and relative permeability
- Brooks-Corey capillary pressure and relative permeability functions
- Water-wet hysteretic capillary pressure and relative permeability model of Parker and Lenhard
- Mixed-wet hysteretic two-phase oil/water capillary pressure and relative permeability model of Lenhard

Section 2
UTCHEM Model Formulation

This section is an expanded version of a paper by Delshad *et al.* [1996] which describes a three-dimensional, multicomponent, multiphase compositional finite difference simulator for application to the analysis of contaminant transport and surfactant enhanced aquifer remediation (SEAR) of nonaqueous phase liquid (NAPL) pollutants. The simulator can model capillary pressures, three-phase relative permeabilities (water/gas/organic phases or water/organic/microemulsion phases), dispersion, diffusion, adsorption, chemical reactions, non equilibrium mass transfer between phases and other related phenomena. The finite-difference method uses second- and third-order approximations for all of the time and space derivatives and a flux limiter that makes the method total variation diminishing (TVD). Mixtures of surfactant, alcohol, water and NAPL can form many types of micellar and microemulsion phases with a complex and important dependence on many variables of which the dilute aqueous solution typically assumed in SEAR models is just one example. The phase behavior model is central to our approach and allows for the full range of the commonly observed micellar and microemulsion behavior pertinent to SEAR. The other surfactant related properties such as adsorption, interfacial tension, capillary pressure, capillary number and microemulsion viscosity are all dependent on an accurate phase behavior model. This has proven to be a highly successful approach for surfactant enhanced oil recovery modeling, so it was adapted to SEAR modeling. However, there are many significant differences between petroleum and environmental applications of surfactants, so many new features have been added to model contaminant transport and remediation and these are described and illustrated for the first time here.

2.1 Introduction

Many nonaqueous phase liquids (NAPLs) are used in large quantities by many industries throughout the world. Due to their wide usage, organic liquids are among the most common type of soil and groundwater pollutants. Of the organic chemical contaminants which have been detected in groundwaters, dense nonaqueous phase liquids (DNAPLs) such as chlorinated solvents are among the most frequently and serious types encountered. DNAPLs are heavier than water, typically volatile, and only slightly soluble in water. Many conventional remediation techniques such as pump-and-treat, vapor extraction, and in-situ biorestoration have proven to be unsuccessful or of limited success in remediating soil and groundwater contaminated by DNAPL due to low solubility, high interfacial tension, and the sinking tendency below the water table of most DNAPLs. Surfactant enhanced aquifer remediation is actively under research and development as a promising technology that avoids at least some of the problems and limitations of many other remediation methods.

Surfactants have been studied and evaluated for many years in the petroleum industry for enhanced oil recovery from petroleum reservoirs (Nelson and Pope, 1978). Surfactants are injected to create low interfacial tension to reduce capillary forces and thus mobilize trapped oil. Solubilization and mobilization are the two mechanisms by which surfactants can enhance the removal of NAPLs from saturated zones. Surfactants can also be used to increase the solubility without generating ultra-low interfacial tension or mobilizing the trapped oil. Enhanced solubility is the main mechanism for recovery of entrapped organic residuals in surfactant enhanced aquifer remediation (Fountain, 1992; Fountain and Hodge, 1992; Powers *et al.*, 1991; West and Harwell, 1992; Wunderlich *et al.*, 1992; Brown *et al.*, 1994; Pennell *et al.*, 1994). For example, the solubility of perchloroethylene (PCE) is increased 300 fold by the addition of a 4% blend of sodium diamyl and dioctyl sulfosuccinates (Abriola *et al.*, 1993). SEAR can also be based on mobilization of the residual DNAPL, which has a greater potential to increase the remediation but is riskier because of the movement of free-phase DNAPL.

The objective of SEAR modeling is to aid in the scaleup and optimization of the design of SEAR, to assess the performance of the method at both the laboratory and field scales with respect to both risk and effectiveness, to improve our understanding of process mechanisms, and to explore alternative strategies and approaches to remediation. To the extent that these modeling objectives are met, risk will be reduced and fewer mistakes will be made, the performance and cost effectiveness of the method will be improved, and the number of field trials will be minimized. The model should have the capability of modeling

advection, dispersion, and the mass transfer of species (surfactant, water, organic contaminants, air) in the aquifer under various pumping and injection strategies. Most multiphase compositional models reported in the environmental engineering literature (Abriola and Pinder, 1985a,b; Baehr and Corapcioglu, 1987; Faust *et al.*, 1989; Letniowski and Forsyth, 1990; Sleep and Sykes, 1990; Mayer and Miller; 1990; Kalurachchi and Parker, 1990; Sleep and Sykes, 1993) are limited in their applicability in one way or another (1-or 2-dimensional modeling, single species, equilibrium mass transfer, inadequate numerical accuracy, and lack of modeling miscibility which occurs during surfactant flooding). The only SEAR models reported in the literature are for single phase flow and are those of Wilson [1989], Wilson and Clarke [1991] and Abriola *et al.* [1993] with simplified surfactant phase behavior and properties. None of these models account for the effects of surfactant on interfacial tension (IFT), surfactant phase behavior, capillary number, or surfactant adsorption. This paper describes the formulation and application of a general purpose chemical compositional simulator, The University of Texas Chemical Flooding simulator (UTCHEM), for use in SEAR studies, that does not have these common limitations.

Enhanced oil recovery processes such as polymer flooding or surfactant/polymer flooding have utilized polymer to reduce fluid mobility to improve the sweep efficiency of the reservoir, i.e., to increase the volume of the permeable medium contacted at any given time (Lake, 1989; Sorbie, 1991). Sweep efficiency is reduced by streamline pattern effects, gravity effects, viscous fingering, channeling (caused by contrasts in the permeability) and flow barriers. Polymers could be used in the SEAR process to improve the sweep efficiency just as they have been in enhanced oil recovery and this may reduce the cost, risk and time required to remediate the aquifer. Under some conditions, polymers can also reduce the dispersion and adsorption of the surfactant and this is another potential benefit of using them. Polymer concentrations on the order of 500 mg/L are likely to be adequate for SEAR applications, so the additional cost of the polymer is small compared to the potential reduction in surfactant costs assuming that fewer pore volumes of surfactant will be needed as a result of the polymer.

UTCHEM can be used to simulate a wide range of displacement processes at both the field and laboratory scales. The model is a multiphase, multicomponent, three-dimensional finite-difference simulator. The model was originally developed to model surfactant enhanced oil recovery but modified for applications involving the use of surfactant for enhanced remediation of aquifers contaminated by NAPLs. The balance equations are the mass conservation equations, an overall balance that determines the pressure for up to four fluid phases, and an energy balance equation to determine the temperature. The number of components is variable depending on the application, but would include at least surfactant, oil and water for SEAR modeling. When electrolytes, tracers, co-solvents, polymer, and other commonly needed components are included, the number of components may be on the order of twenty or more. When the geochemical option is used, a large number of additional aqueous components and solid phases may be used.

A significant portion of the research effort on chemical flooding simulation at The University of Texas at Austin has been directed toward the development and implementation of accurate physical and chemical property models in UTCHEM. Heterogeneity and variation in relative permeability and capillary pressure are allowed throughout the porous medium, since for example each gridblock can have a different permeability and porosity.

Surfactant phase behavior modeling is based in part on the Hand representation of the ternary phase diagram (Hand, 1939). A pseudophase theory (Prouvost *et al*., 1984b; Prouvost *et al.*, 1985) reduces the water, oil, surfactant, and co-surfactant fluid mixtures to a pseudoternary composition space. The major physical phenomena modeled are density, viscosity, velocity-dependent dispersion, molecular diffusion, adsorption, interfacial tension, relative permeability, capillary pressure, capillary trapping, cation exchange, and polymer and gel properties such as permeability reduction, inaccessible pore volume, and non-Newtonian rheology. The phase mobilization is modeled through entrapped phase saturation and relative permeability dependence on trapping number.

The reaction chemistry includes aqueous electrolyte chemistry, precipitation/dissolution of minerals, ion exchange reactions with the matrix (the geochemical option), reactions of acidic components of oil with

the bases in the aqueous solution (Bhuyan, 1989; Bhuyan *et al.*, 1990 and 1991) and polymer reactions with crosslinking agents to form gel (Garver *et al.*, 1989; Kim, 1995).

Nonequilibrium mass transfer of an organic component from the oleic phase to the surfactant-rich microemulsion phase is modeled using a linear mass transfer model similar to that given by Powers *et al.* [1991]. Even in the absence of surfactant, the model allows for a small dissolution of oil in the aqueous phase. Nonequilibrium mass transfer of tracer components is modeled by a generalized Coats-Smith model (Smith *et al.*, 1988).

The model includes options for multiple wells completed either horizontally or vertically. Aquifer boundaries are modeled as constant-potential surfaces or as closed surfaces.

A dual-porosity formulation to model transport in fractured media has recently been added to the simulator (Liang, 1997). We have recently incorporated a biodegradation model in UTCHEM. Multiple organic compounds can be degraded by multiple microbial species using multiple electron acceptors (de Blanc, 1998; Delshad *et al.*, 1994).

The resulting flow equations are solved using a block-centered finite-difference scheme. The solution method is implicit in pressure and explicit in concentration (IMPES type). One- and two-point upstream and third-order spatial discretization are available as options in the code. To increase the stability and robustness of the second-and third-order methods, a flux limiter that is total-variation-diminishing (TVD) has been added (Liu, 1993; Liu *et al.*, 1994). The third-order method gives the most accurate solution.

2.2 Model Formulation

2.2.1 General Description

In this section, a brief description of the model formulation is given. Additional features needed only for enhanced oil recovery can be found in Datta Gupta *et al.*, [1986], Bhuyan *et al.*, [1990], and Saad [1989]. The balance equations are as follows:

1. The mass balance equation for each species.
2. The aqueous phase pressure is obtained by an overall mass balance on volume-occupying components (water, oil, surfactant, co-solvent, and air). The other phase pressures are computed by adding the capillary pressure between phases.
3. The energy balance equation.

Four phases are modeled. The phases are a single component gas phase (ℓ=4) and up to three liquid phases: aqueous (ℓ=1), oleic (ℓ=2), and microemulsion (ℓ=3), depending on the relative amounts and effective electrolyte concentration (salinity) of the phase environment. Any number of water, oil, or gas tracers can be modeled. The tracers can partition, adsorb, and decay if they are radioactive. UTCHEM can model partitioning interwell tracer tests (PITT) for the detection and estimation of contaminants and for the remediation performance assessment in both saturated and vadose zones (Jin *et al.*, 1995).

The flow equations allow for compressibility of soil and fluids, dispersion and molecular diffusion, chemical reactions, and phase behavior and are complemented by constitutive relations.

2.2.2 Mass Conservation Equations

The assumptions imposed when developing the flow equations are local thermodynamic equilibrium except for tracers and dissolution of organic component, immobile solid phases, slightly compressible soil and fluids, Fickian dispersion, ideal mixing, and Darcy's law. The boundary conditions are no flow and no dispersive flux across the impermeable boundaries.

The continuity of mass for component κ in association with Darcy's law is expressed in terms of overall volume of component κ per unit pore volume ($\tilde{C}_\kappa$) as

$$\frac{\partial}{\partial t}\left(\phi \tilde{C}_\kappa \rho_\kappa\right) + \vec{\nabla}\cdot\left[\sum_{\ell=1}^{n_p}\rho_\kappa\left(C_{\kappa\ell}\vec{u}_\ell - \vec{\tilde{D}}_{\kappa\ell}\right)\right] = R_\kappa \tag{2.1}$$

where the overall volume of component κ per unit pore volume is the sum over all phases including the adsorbed phases:

$$\tilde{C}_\kappa = \left(1 - \sum_{\kappa=1}^{n_{cv}}\hat{C}_\kappa\right)\sum_{\ell=1}^{n_p} S_\ell C_{\kappa\ell} + \hat{C}_\kappa \qquad \text{for } \kappa = 1,..., n_c \tag{2.2}$$

n_{cv} is the total number of volume-occupying components. These components are water, oil, surfactant, and air. n_p is the number of phases; $\hat{C}_\kappa$ is the adsorbed concentration of species κ; and ρ_κ is the density of pure component κ at a reference phase pressure P_R relative to its density at reference pressure P_{R0}, usually taken at the surface condition of 1 atm. We assume ideal mixing and small and constant compressibilities C^o_κ.

$$\rho_\kappa = 1 + C^o_\kappa\left(P_R - P_{R0}\right) \tag{2.3}$$

The dispersive flux is assumed to have a Fickian form:

$$\vec{\tilde{D}}_{\kappa\ell,x} = \phi S_\ell \vec{\vec{K}}_{\kappa\ell}\cdot\vec{\nabla}C_{\kappa\ell} \tag{2.4}$$

The dispersion tensor $\vec{\vec{K}}_{\kappa\ell}$ including molecular diffusion ($D_{k\ell}$) are calculated as follows (Bear, 1979):

$$\vec{\vec{K}}_{\kappa\ell ij} \equiv \frac{D_{\kappa\ell}}{\tau}\delta_{ij} + \frac{\alpha_{T\ell}}{\phi S_\ell}\left|\vec{u}_\ell\right|\delta_{ij} + \frac{\left(\alpha_{L\ell} - \alpha_{T\ell}\right)}{\phi S_\ell}\frac{u_{\ell i}\, u_{\ell j}}{\left|\vec{u}_\ell\right|} \tag{2.5}$$

where $\alpha_{L\ell}$ and $\alpha_{T\ell}$ are phase ℓ longitudinal and transverse dispersivities; τ is the tortuosity factor with the definition of being a value greater than one; $u_{\ell i}$ and $u_{\ell j}$ are the components of Darcy flux of phase ℓ in directions i and j; and δ_{ij} is the Kronecker delta function. The magnitude of vector flux for each phase is computed as

$$\left|\vec{u}_\ell\right| = \sqrt{\left(u_{x\ell}\right)^2 + \left(u_{y\ell}\right)^2 + \left(u_{z\ell}\right)^2} \tag{2.6}$$

The phase flux from Darcy's law is

$$\vec{u}_\ell = -\frac{k_{r\ell}\vec{\vec{k}}}{\mu_\ell}\cdot\left(\vec{\nabla}P_\ell - \gamma_\ell\vec{\nabla}h\right) \tag{2.7}$$

where $\vec{\vec{k}}$ is the intrinsic permeability tensor and h is the vertical depth. Relative permeability ($k_{r\ell}$), viscosity (μ_ℓ), and specific weight (γ_ℓ) for phase ℓ are defined in the following sections.

The source terms R_κ are a combination of all rate terms for a particular component and may be expressed as

$$R_\kappa = \phi \sum_{\ell=1}^{n_p} S_\ell \, r_{\kappa\ell} + (1-\phi)\, r_{\kappa s} + Q_\kappa \tag{2.8}$$

where Q_κ is the injection/production rate for component κ per bulk volume. $r_{\kappa\ell}$ and $r_{\kappa s}$ are the reaction rates for component κ in phase ℓ and solid phase s respectively.

Analogous equations apply for the fluxes in the y- and z-directions.

2.2.3 Energy Conservation Equation

The energy balance equation is derived by assuming that energy is a function of temperature only and energy flux in the aquifer or reservoir occurs by advection and heat conduction only.

$$\frac{\partial}{\partial t}\left[(1-\phi)\rho_s C_{vs} + \phi \sum_{\ell=1}^{n_p} \rho_\ell S_\ell C_{v\ell}\right] T + \vec{\nabla}\cdot\left(\sum_{\ell=1}^{n_p} \rho_\ell C_{p\ell} u_\ell T - \lambda_T \vec{\nabla} T\right) = q_H - Q_L \tag{2.9}$$

where T is the reservoir temperature; C_{vs} and $C_{v\ell}$ are the soil and phase ℓ heat capacities at constant volume; $C_{p\ell}$ is the phase ℓ heat capacity at constant pressure; and λ_T is the thermal conductivity (all assumed constant). q_H is the enthalpy source term per bulk volume. Q_L is the heat loss to overburden and underburden formations or soil computed using the Vinsome and Westerveld [1980] heat loss method.

2.2.4 Pressure Equation

The pressure equation is developed by summing the mass balance equations over all volume-occupying components, substituting Darcy's law for the phase flux terms, using the definition of capillary pressure, and noting that $\sum_{\kappa=1}^{n_{cv}} C_{\kappa\ell} = 1$. The pressure equation in terms of the reference phase pressure (phase 1) is

$$\phi C_t \frac{\partial P_1}{\partial t} + \vec{\nabla}\cdot\vec{\vec{k}}\cdot\lambda_{rTc}\vec{\nabla}P_1 = -\vec{\nabla}\cdot\sum_{\ell=1}^{n_p}\vec{\vec{k}}\cdot\lambda_{r\ell c}\vec{\nabla}h + \vec{\nabla}\sum_{\ell=1}^{n_p}\vec{\vec{k}}\cdot\lambda_{r\ell c}\vec{\nabla}P_{c\ell 1} + \sum_{\kappa=1}^{n_{cv}} Q_\kappa \tag{2.10}$$

where $\lambda_{r\ell c} = \dfrac{k_{r\ell}}{\mu_\ell}\sum_{\kappa=1}^{n_{cv}} \rho_\kappa C_{\kappa\ell}$ and total relative mobility with the correction for fluid compressibility is $\lambda_{rTc} = \sum_{\ell=1}^{n_p} \lambda_{r\ell c}$.

The total compressibility, C_t, is the volume-weighted sum of the rock or soil matrix (C_r) and component compressibilities (C_κ^o):

$$C_t = C_r + \sum_{\kappa=1}^{n_{cv}} C_\kappa^o \tilde{C}_\kappa \tag{2.11}$$

where $\phi = \phi_R\left[1 + C_r\left(P_R - P_{R0}\right)\right]$.

2.2.5 Nonequilibrium Dissolution of Nonaqueous Phase Liquids

Mathematical models of multiphase flow in subsurface environments generally employ a local equilibrium assumption; that is, it is assumed that the concentration of water leaving a region of residual NAPL has dissolved concentrations of the organic phase at the solubility level. However, field data frequently indicate that contaminant concentrations in groundwater are lower than their corresponding equilibrium values (Mackay *et al*, 1985; Mercer and Cohen, 1990). Experimental investigations indicate that the dissolution process is mass-transfer limited when (1) NAPL is distributed nonuniformly due to aquifer heterogeneity, (2) water velocity is high and (3) NAPL saturation is low (Powers *et al.*, 1991; Guarnaccia *et al.*, 1992; Powers *et al.*, 1992). UTCHEM has the capability of modeling a non equilibrium mass transfer relationship between NAPL and water or microemulsion phases. The NAPL dissolution rate is assumed to be represented by a linear driving force model similar to the one proposed by Abriola *et al.*, [1992], Powers *et al.*, [1991], Mayer and Miller, [1990], and Powers *et al.*, [1992]. The species mass transfer rate at the interface between the two phases ($R^I_{\kappa\ell}$) is modeled as

$$R^I_{\kappa\ell} = -M_\kappa\left(C_{\kappa\ell} - C^{eq}_{\kappa\ell}\right) \quad \text{for } \ell = 1 \text{ or } 3 \tag{2.12}$$

where M_κ is the mass transfer coefficient for species κ across the boundary layer and $C_{\kappa\ell}$ and $C^{eq}_{\kappa\ell}$ are the mass concentrations of κ in the bulk aqueous solution and at equilibrium, respectively. Equation 2.12 can be written in terms of volumetric concentration of organic species (κ=2) as

$$\frac{\partial\left(S_\ell C_{2\ell}\phi\right)}{\partial t} = \vec{\nabla}\cdot\left(C_{2\ell}\vec{u}_\ell - \vec{\vec{D}}_{2\ell}\right) + M_2\left(C^{eq}_{2\ell} - C_{2\ell}\right) \quad \text{for } \ell = 1 \text{ or } 3 \tag{2.13}$$

where $C_{2\ell}$ is the volumetric concentration of organic species in the aqueous phase and $C^{eq}_{2\ell}$ is the equilibrium concentration. The time derivative was discretized using a backward finite difference approximation.

The equilibrium concentration for pure NAPL in water or aqueous phase with surfactant concentration below the critical micelle concentration (CMC) is an input solubility limit which is small for many of the NAPLs of interest to contaminant hydrogeologists. In the presence of surfactant, however, the equilibrium concentrations are calculated for surfactant/NAPL/water phase behavior using Hand's equation. The nonequilibrium concentration of NAPL in water and phase saturations are then computed using the previous time step saturations and concentrations and the new time step equilibrium concentrations. The mass transfer coefficient is assumed to be a constant although it may be a function of groundwater velocity, composition, saturation, and porous medium properties (Pennell *et al.*, 1993).

2.2.6 Well Models

Injection and production wells are considered source and sink terms in the flow equations. Wells can be completed vertically in several layers of the aquifer or horizontally with any length and can be controlled according to pressure or rate constraints. The well models used are based on formulations by Peaceman [1983] and Babu and Odeh [1989].

2.2.7 Boundary Conditions

The basic boundary condition assumed in UTCHEM is no convective, no dispersive, and no thermal flux through all boundaries. Conductive thermal fluxes through the upper and lower boundaries of the aquifer may be modeled using the method of Vinsome and Westerveld [1980].

Alternatively, the no flow/no heat flux conditions may be replaced on part by specified pressure on the boundaries. A flag (IZONE) is added to define whether the saturated zone, vadose zone or both saturated and vadose zones are modeled. If the vadose zone is modeled, the top and lateral boundary pressures are set at the atmospheric pressure and all the other sides are closed/no flow boundaries. Air is the only phase

entering these boundaries whereas any fluid can exit the boundaries according to its saturation and relative mobility in the boundary gridblocks. The only exception is that NAPL can not exit the top boundary to allow modeling of contamination event in the vadose zone.

If the saturated zone is modeled, the lateral boundaries are the only sides open with a specified pressure gradient. Water is the only phase entering the lateral boundaries of the saturated zone. The water concentration and its salinity and hardness are also input to the simulator. The aqueous concentrations of biodegradation species entering the boundaries are set to their initial values.

If both vadose and saturated zones are modeled, the user needs to specify the depth to the water table at two lateral boundaries of the aquifer model and the potential gradient across the saturated zone. The top and lateral boundary pressures in the vadose zone are at atmospheric pressure with air as the only phase entering these boundaries.

If temperature variation is modeled, the boundary temperature is set to the initial temperature.

2.2.8 Fluid and Soil Properties

Geologic heterogeneities are probably the key factor which reduce the effectiveness of chemical enhanced recovery processes because their success depends on the delivery of injected chemical and water into the subsurface to contact the organic liquids. Heterogeneities result in a complex distribution of DNAPL in residual zones and pools. To capture some of the geologic features, reservoir properties such as formation permeability, porosity, residual phase saturation, phase relative permeability, and phase capillary pressure are allowed to vary spatially in UTCHEM. Phase trapping functions and adsorption of both surfactant and polymer are modeled as a function of permeability.

Many of the properties of anionic surfactants and polymers depend on the electrolyte concentrations in the water. Divalent cations such as calcium and magnesium ions are particularly important and can make significant differences in adsorption and other properties even at the low concentrations typically found in ground water. Furthermore, it cannot be assumed that these concentrations do not change since processes such as cation exchange and mineral dissolution occur during surfactant remediation. In this paper, we describe these electrolyte effects in terms of salinity or effective salinity (defined below) and these terms as used in this context refer to any electrolyte concentrations of interest, but especially to those of interest to surfactant remediation of aquifers containing ground water at low electrolyte concentrations. The same term and the same models are used to describe high salinities typical of oil reservoirs, but it should not be inferred that these electrolyte effects are only significant at high salinities. In fact, cation exchange between the water and clays and between the water and micelles (when anionic surfactant above its critical micellar concentration is present) is more important at low salinities typical of potable water than it is at high salinities such as sea water or high salinity oil reservoirs.

The description of properties in this paper assumes that alcohols, polymer/cross-linker, and components for high-pH flooding are absent. These property models are described in Saad [1989], Bhuyan *et al.* [1990], and Kim [1995].

2.2.9 Adsorption

2.2.9.1 Surfactant

Surfactant adsorption can be an important mechanism for a SEAR process since it causes retardation and consumption of surfactant. The remaining adsorbed surfactant after flushing with water at the end of the remediation process may also be important even for food grade surfactants and even though the mass concentration in the porous media at this time is likely to be very low on the order of the CMC. Some additional time will be required for this remaining surfactant to biodegrade and this will depend on the surfactant concentration among other variables. Surfactant adsorption has been the subject of extensive study for many decades and is now very well understood, especially for the types of surfactants and porous media of interest to SEAR. Rouse *et al.* [1993] and Adeel and Luthy [1994] are examples of recent studies done to compare the adsorption of different types of surfactant on soils. Somasundaran and Hanna [1977] and Scamehorn *et al.* [1982] are examples among the hundreds of studies done to evaluate the adsorption of surfactants on porous media in the context of surfactant enhanced oil recovery. These

studies show that surfactant adsorption isotherms are very complex in general. This is especially true when the surfactant is not isomerically pure and the substrate is not a pure mineral. However, we and others have found that for many if not most conditions of interest to us the general tendency is for the surfactant isotherm to reach a plateau at some sufficiently large surfactant concentration. For pure surfactants, this concentration is in fact the CMC, which is often 100 times or more below the injected surfactant concentration. Thus, the complex detailed shape of the isotherm below the CMC has little practical impact on the transport and effectiveness of the surfactant and for this reason it has been found that a Langmuir-type isotherm can be used to capture the essential features of the adsorption isotherm for this purpose. Camilleri *et al.* [1987a] illustrate this by simulating an oil recovery experiment and Saad *et al.* [1989] by successfully simulating a surfactant field project using this approach. We also used a Langmuir-type adsorption isotherm for the simulation of the surfactant remediation of the Borden cell test illustrated below.

UTCHEM uses a Langmuir-type isotherm to describe the adsorption level of surfactant which takes into account the salinity, surfactant concentration, and soil permeability (Hirasaki and Pope, 1974). The adsorption is irreversible with concentration and reversible with salinity. The adsorbed concentration of surfactant ($\kappa = 3$) is given by

$$\hat{C}_\kappa = \min\left(\tilde{C}_\kappa, \frac{a_\kappa\left(\tilde{C}_\kappa - \hat{C}_\kappa\right)}{1 + b_\kappa\left(\tilde{C}_\kappa - \hat{C}_\kappa\right)}\right) \qquad \kappa = 3 \text{ or } 4 \tag{2.14}$$

The concentrations are normalized by the water concentration in the adsorption calculations. The minimum is taken to guarantee that the adsorption is no greater than the total surfactant concentration. Adsorption increases linearly with effective salinity and decreases as the permeability increases as follows:

$$a_3 = \left(a_{31} + a_{32} C_{SE}\right)\left(\frac{k_{ref}}{k}\right)^{0.5} \tag{2.15}$$

where C_{SE} is the effective salinity described later. The value of a_3/b_3 represents the maximum level of adsorbed surfactant and b_3 controls the curvature of the isotherm. The adsorption model parameters a_{31}, a_{32}, and b_3 are found by matching laboratory surfactant adsorption data. The reference permeability (k_{ref}) is the permeability at which the input adsorption parameters are specified.

2.2.9.2 Polymer

The retention of polymer molecules in permeable media is due to both adsorption onto solid surfaces and trapping within small pores. The polymer retention similar to that of surfactant slows down the polymer velocity and depletes the polymer slug. Polymer adsorption is modeled as a function of permeability, salinity, and polymer concentration (Eq. 2.14 for $\kappa = 4$). The parameter a_4 is defined as

$$a_4 = \left(a_{41} + a_{42} C_{SEP}\right)\left(\frac{k_{ref}}{k}\right)^{0.5} \tag{2.16}$$

The effective salinity for polymer (C_{SEP}) is

$$C_{SEP} = \frac{C_{51} + \left(\beta_P - 1\right) C_{61}}{C_{11}} \tag{2.17}$$

where C_{51}, C_{61}, and C_{11} are the anion, calcium, and water concentrations in the aqueous phase and β_P is measured in the laboratory and is an input parameter to the model. The reference permeability (k_{ref}) is the permeability at which the input adsorption parameters are specified.

2.2.9.3 Organic

Organic sorption can be an important parameter in assessments of the fate and transport of DNAPLs in soils. The magnitude of sorbed organics is described in terms of a partition coefficient with respect to the organic fraction, K_{oc} (Karickhoff, 1984). The higher K_{oc}, the greater is its tendency to sorb into organic carbon in the subsurface. A linear sorption isotherm is used to model the organic sorption:

$$\hat{C}_2 = f_{oc} K_{oc} C_{21} \tag{2.18}$$

where $\hat{C}_2$ is the adsorbed organic, f_{oc} is the fraction of organic carbon in the soil, and C_{21} is the organic concentration in the water phase. K_{oc} is defined as the ratio of the amount of organic adsorbed per unit weight of organic carbon in the soil to the concentration of the organic in solution at equilibrium.

2.2.10 Cation Exchange

Cation exchange occurs when there is an incompatibility in the electrolyte composition of injected fluids and the initial fluids saturating the soil. Cation exchange affects the transport of ions in solution and therefore may have a significant effect on the optimum salinity and the surfactant phase behavior (Pope *et al.*, 1978; Fountain, 1992) and surfactant adsorption. The type and concentration of cations involved in the exchange process can also affect the hydraulic conductivity (Fetter, 1993). We use a cation exchange model based on Hirasaki's model [1982]. Cations exist in the form of free ions, adsorbed on clay surfaces, and associated with either surfactant micelles or adsorbed surfactant. The mass action equations for the exchange of calcium (κ=6) and sodium (κ=12) on clay and surfactant describe the cation exchange model as

$$\frac{\left(C_{12}^{s}\right)^2}{C_6^{s}} = \beta^{s} C_3^{m} \frac{\left(C_{12}^{f}\right)^2}{C_6^{f}} \tag{2.19}$$

$$\frac{\left(C_{12}^{c}\right)^2}{C_6^{c}} = \beta^{c} Q_v \frac{\left(C_{12}^{f}\right)^2}{C_6^{f}} \tag{2.20}$$

where the superscripts f, c, and s denote free cation, adsorbed cation on clay, and adsorbed cation on micelles, respectively. The simulator input parameters are Q_v, the cation exchange capacity of the mineral, β^c and β^s, the ion exchange constants for clay and surfactant, and C_3^m, the concentration of surfactant in meq/ml. The electrical neutrality and mass balances needed to close the system of ion exchange equations are

$$C_5 = C_{12}^{f} + C_6^{f} \tag{2.21}$$

$$C_6 = C_6^{f} + C_6^{s} + C_6^{c} \tag{2.22}$$

$$C_3 = C_6^{s} + C_{12}^{s} \tag{2.23}$$

$$Q_v = C_6^{c} + C_{12}^{c} \tag{2.24}$$

$$C_5 - C_6 = C_{12}^{f} + C_{12}^{s} + C_{12}^{c} \tag{2.25}$$

where C_κ^f is the fluid concentration for species κ normalized by water concentration All concentrations in ion exchange equations are expressed in meq/ml of water. The molar volume concentration of surfactant is computed as

$$C_3^m = \frac{1000\, C_3}{C_1\, M_3} \tag{2.26}$$

where M_3 is the equivalent weight of the surfactant.

The cation exchange equations are solved for the six unknowns $C_6^c, C_{12}^c, C_6^f, C_{12}^f, C_6^s,$ and C_{12}^s using Newton-Raphson method.

2.2.11 Phase Behavior

The surfactant/oil/water phase behavior is based on Winsor [1954], Reed and Healy [1977], Nelson and Pope [1978], Prouvost *et al.* [1985], and others. Surfactant phase behavior considers up to five volumetric components (oil, water, surfactant, and two alcohols) which form three pseudocomponents in a solution. In the absence of alcohols (the formulation described in this paper), only three components are modeled. The volumetric concentrations of these three components are used as the coordinates on a ternary diagram. Salinity and divalent cation concentrations have a strong influence on phase behavior. At low salinity, an excess oil phase that is essentially pure oil and a microemulsion phase that contains water plus electrolytes, surfactant, and some solubilized oil exist. The tie lines (distribution curves) at low salinity have negative slope (Fig. 2.1). This type of phase environment is called Winsor Type I, or alternatively Type II(–) in some of the literature. If the surfactant concentration is below CMC, the two phases are an aqueous phase containing all the surfactant, electrolytes, and dissolved oil at the water solubility limit and a pure excess oil phase. For high salinity, an excess water phase and a microemulsion phase containing most of the surfactant and oil, and some solubilized water exist. This type of phase environment is called Winsor Type II, or alternatively Type II(+) (Fig. 2.2). An overall composition at intermediate salinity separates into three phases. These phases are excess oil and water phases and a microemulsion phase whose composition is represented by an invariant point. This phase environment is called Winsor Type III, or just Type III (Fig. 2.3).

Other variables besides electrolyte concentrations, e.g. alcohol type and concentration, the equivalent alkane carbon number of the oil or solvent and changes in temperature or pressure also cause a phase environment shift from one type of phase behavior to another type. Three papers by Baran *et al.* [1994a,b,c] show that the phase behavior of surfactants with both pure chlorocarbons such as trichloroethylene (TCE) and mixtures of chlorocarbons such as TCE and carbon tetrachloride is essentially identical in form to the classical behavior with hydrocarbons, so we are justified in using the same approach for these contaminants as we have used for hydrocarbons.

The surfactant/oil/water phase behavior can be represented as a function of effective salinity once the binodal curve and tie lines are described. The phase behavior model in UTCHEM uses Hand's rule (Hand, 1939) and is based on the work by Pope and Nelson [1978], Prouvost *et al.* [1984b; 1985; 1986], Satoh [1984], and Camilleri *et al.* [1987a,b,c].

2.2.11.1 Effective Salinity

The effective salinity increases with the divalent cations bound to micelles (Glover *et al.*, 1979; Hirasaki, 1982; Camilleri *et al.*, 1987a,b,c) and decreases as the temperature increases for anionic surfactants and increases as the temperature increases for nonionic surfactants.

$$C_{SE} = C_{51}\left(1-\beta_6\, f_6^s\right)^{-1}\left[1+\beta_T\left(T-T_{ref}\right)\right]^{-1} \tag{2.27}$$

where C_{51} is the aqueous phase anion concentration; β_6 is a positive constant; f_6^s is the fraction of the total divalent cations bound to surfactant micelles as $f_6^s = \frac{C_6^s}{C_3^m}$; and β_T is the temperature coefficient.

The effective salinities at which the three equilibrium phases form or disappear are called lower and upper limits of effective salinity (C_{SEL} and C_{SEU}).

2.2.11.2 Binodal Curve

The formulation of the binodal curve using Hand's rule (Hand, 1939) is assumed to be the same in all phase environments. Hand's rule is based on the empirical observation that equilibrium phase concentration ratios are straight lines on a log-log scale. Figures 2.4a and 2.4b show the ternary diagram for a Type II(−) environment with equilibrium phases numbered 2 and 3 and the corresponding Hand plot. The binodal curve is computed from

$$\frac{C_{3\ell}}{C_{2\ell}} = A\left(\frac{C_{3\ell}}{C_{1\ell}}\right)^B \qquad \ell = 1, 2, \text{or } 3 \tag{2.28}$$

where A and B are empirical parameters. For a symmetric binodal curve where B = −1, which is the current formulation used in UTCHEM, all phase concentrations are calculated explicitly in terms of oil concentration $C_{2\ell}$ (recalling $\sum_{\kappa=1}^{3} C_{\kappa\ell} = 1$).

$$C_{3\ell} = \frac{1}{2}\left[-AC_{2\ell} + \sqrt{\left(AC_{2\ell}\right)^2 + 4AC_{2\ell}\left(1 - C_{2\ell}\right)}\right] \quad \text{for } \ell = 1, 2, \text{ or } 3 \tag{2.29}$$

Parameter A is related to the height of the binodal curve as follows

$$A_m = \left(\frac{2C_{3\,max,m}}{1 - C_{3\,max,m}}\right)^2 \qquad m = 0,\ 1,\ \text{and } 2 \tag{2.30a}$$

where m = 0, 1, and 2 are corresponding to low, optimal, and high salinities. The height of binodal curve is specified as a linear function of temperature:

$$C_{3\,max,m} = H_{BNC,m} + H_{BNT,m}\left(T - T_{ref}\right) \qquad m = 0,\ 1,\ \text{and } 2 \tag{2.30b}$$

where $H_{BNC,m}$ and $H_{BNT,m}$ are input parameters. A_m is linearly interpolated as

$$\begin{aligned} A &= \left(A_0 - A_1\right)\left(1 - \frac{C_{SE}}{C_{SEOP}}\right) + A_1 \quad \text{for } C_{SE} \le C_{SEOP} \\ A &= \left(A_2 - A_1\right)\left(\frac{C_{SE}}{C_{SEOP}} - 1\right) + A_1 \quad \text{for } C_{SE} > C_{SEOP} \end{aligned} \tag{2.31}$$

where C_{SEOP} is the optimum effective salinity and the arithmetic average of C_{SEL} and C_{SEU}. The heights of the binodal curve at three reference salinities are input to the simulator and are estimated based on phase behavior laboratory experiments.

2.2.11.3 Tie Lines for Two Phases

For both Type II(–) and Type II(+) phase behavior, there are only two phases below the binodal curve. Tie lines are the lines joining the composition of the equilibrium phases and are given by

$$\frac{C_{3\ell}}{C_{2\ell}} = E\left(\frac{C_{33}}{C_{13}}\right)^F \tag{2.32}$$

where ℓ=1 for Type II(+) and ℓ=2 for Type II(–). In the absence of available data for tie lines, F is calculated from F = –1/B. For a symmetric binodal curve (B=–1), F is equal to 1. Since the plait point is on both the binodal curve and tie line, we have

$$E = \frac{C_{1P}}{C_{2P}} = \frac{1 - C_{2P} - C_{3P}}{C_{2P}} \tag{2.33}$$

Applying the binodal curve equation to the plait point and substituting C_{3P} (Eq. 2.29) in Eq. 2.33, we have

$$E = \frac{1 - C_{2P} - \frac{1}{2}\left[-AC_{2P} + \sqrt{(AC_{2P})^2 + 4AC_{2P}(1 - C_{2P})}\right]}{C_{2P}} \tag{2.34}$$

where C_{2P} is the oil concentration at the plait point and is an input parameter for Type II(–) and Type II(+) phase environments.

2.2.11.4 Tie Lines for Type III

The phase composition calculation for the three-phase region of Type III is simple due to the assumption that the excess oleic and aqueous phases are pure. The microemulsion phase composition is defined by the coordinates of the invariant point. The coordinates of the invariant point (M) are calculated as a function of effective salinity:

$$C_{2M} = \frac{C_{SE} - C_{CSEL}}{C_{SEU} - C_{CSEL}} \tag{2.35}$$

C_{3M} is computed by substituting C_{2M} in Eq. 2.29 and noting that $C_{1M} = 1 - C_{2M} - C_{3M}$.

The phase composition calculations for lobes II(–) and II(+) are analogous. The plait point must vary from zero to the II(+) value, C^*_{2PL} or zero to II(–) value, C^*_{2PR}. Here, we only consider the II(–) lobe. The plait point is calculated by interpolation on effective salinity:

$$C_{2PR} = C^*_{2PR} + \frac{C_{SE} - C_{SEL}}{C_{SEU} - C_{SEL}}\left(1 - C^*_{2PR}\right) \tag{2.36}$$

In order to apply Hand's equation, we transform the concentrations as shown in Fig. 2.5. The transformed concentrations are

$$\begin{aligned} C'_{1\ell} &= C_{1\ell}\sec\theta \\ C'_{3\ell} &= C_{3\ell} - C_{2\ell}\tan\theta \quad \text{for } \ell = 2 \text{ or } 3 \\ C'_{2\ell} &= 1 - C'_{1\ell} - C'_{3\ell} \end{aligned} \tag{2.37}$$

The angle θ is

$$\tan\theta = \frac{C_{3M}}{C_{1M}}$$
$$\sec\theta = \frac{\sqrt{C_{1M}^2 + C_{3M}^2}}{C_{1M}} \tag{2.38}$$

Parameter E of the tie line equation is now calculated in terms of untransformed coordinates of the plait point as

$$E = \frac{C'_{1P}}{C'_{2P}} = \frac{1-(\sec\theta - \tan\theta)C_{2PR} - C_{3PR}}{C_{2PR}\sec\theta} \tag{2.39}$$

where C_{3PR} is given by Eq. 2.29 and $C_{1PR} = 1 - C_{2PR} - C_{3PR}$.

2.2.12 Phase Saturations

The phase saturations in the saturated zone in the presence of surfactant are calculated from the phase concentrations, overall component concentration, and saturation constraints once the phase environment and phase compositions are known. The overall component concentration and saturation constraints are

$$C_\kappa = \sum_{\kappa=1}^{3} S_\ell C_{\kappa\ell} \qquad \ell = 1, 2, \text{or } 3 \tag{2.40}$$

$$\sum_{\ell=1}^{3} S_\ell = 1 \tag{2.41}$$

The phase saturations in the vadose zone (phase 3 is absent) are computed from the overall component concentration and the saturation constraint by

$$S_2 = \frac{C_2 - C_{21}}{1 - C_{21}}, S_1 = \frac{C_1}{1 - C_{11}}, S_4 = 1 - S_1 - S_2 \tag{2.42}$$

where C_{21} is the concentration of dissolved organic species in the water phase.

2.2.13 Interfacial Tension

The two models for calculating microemulsion/oil (σ_{23}) and microemulsion/water (σ_{13}) interfacial tension (IFT) are based on Healy and Reed [1974] and Huh [1979]. The IFTs for water and oil (σ_{ow}) and water and air (σ_{aw}) are assumed to be known constants.

2.2.13.1 Healy *et al.*

The first IFT model is based on Hirasaki's modification (Hirasaki, 1981) of the model of Healy and Reed [1974]. Once the phase compositions have been determined, the interfacial tensions between microemulsion and the excess phases (σ_{13}, σ_{23}) are calculated as functions of solubilization parameters:

$$\begin{cases} \log_{10}\sigma_{\ell 3} = \log_{10} F_\ell + G_{\ell 2} + \dfrac{G_{\ell 1}}{1+G_{\ell 3}R_{\ell 3}} & \text{for } R_{\ell 3} \geq 1 \\ \log_{10}\sigma_{\ell 3} = \log_{10} F_\ell + (1-R_{\ell 3})\log_{10}\sigma_{ow} + R_{\ell 3}\left(G_{\ell 2} + \dfrac{G_{\ell 1}}{1+G_{\ell 3}}\right) & \text{for } R_{\ell 3} < 1 \end{cases} \quad \text{for } \ell=1,2 \quad (2.43)$$

where $G_{\ell 1}$, $G_{\ell 2}$, and $G_{\ell 3}$ are input parameters. $R_{\ell 3}$ is the solubilization ratio ($\frac{C_{\ell 3}}{C_{33}}$). The correction factor introduced by Hirasaki, F_ℓ, ensures that the IFT at the plait point is zero and is

$$F_\ell = \frac{1-e^{-\sqrt{con_\ell}}}{1-e^{-\sqrt{2}}} \quad \text{for } \ell = 1, 2 \quad (2.44)$$

where

$$con_\ell = \sum_{\kappa=1}^{3}(C_{\kappa\ell} - C_{\kappa 3})^2 \quad (2.45)$$

and in the absence of surfactant or the surfactant concentration below CMC, the IFTs equal σ_{ow}.

Chun-Huh

The interfacial tension is related to solubilization ratio in Chun-Huh's equation as

$$\sigma_{\ell 3} = \frac{c}{R_{\ell 3}^2} \quad \text{for } \ell = 1 \text{ or } 2 \quad (2.46)$$

where c is typically equal to about 0.3. We introduced Hirasaki's correction factor F_ℓ (Eq. 2.44) and modified Huh's equation so that it reduces to the water-oil IFT (σ_{ow}) as the surfactant concentration approaches zero.

$$\sigma_{\ell 3} = \sigma_{ow}\, e^{-a R_{\ell 3}} + \frac{c F_\ell}{R_{\ell 3}^2}\left(1 - e^{-a R_{\ell 3}^3}\right) \quad \text{for } \ell = 1 \text{ or } 2 \quad (2.47)$$

where a is a constant equal to about 10.

2.2.14 Density

Phase specific weights ($\gamma_\ell = g\rho_\ell$) are modeled as a function of pressure and composition as follows:

$$\gamma_\ell = C_{1\ell}\gamma_{1\ell} + C_{2\ell}\gamma_{2\ell} + C_{3\ell}\gamma_{3\ell} + 0.02533C_{5\ell} - 0.001299C_{6\ell} + C_{8\ell}\gamma_{8\ell} \quad \text{for } \ell = 1,..., n_p \quad (2.48)$$

where $\gamma_{k\ell} = \gamma_{kR}\left[1 + C_k^o(P_\ell - P_{R0})\right]$. γ_{kR} is the component κ specific weight at a reference pressure and is an input parameter. The numerical constants account for the weight of dissolved ions and have units of psi/ft per meq/ml of ions.

We have recently modified the density calculation for the microemulsion phase (ℓ = 3) to use an apparent oil component specific weight in the microemulsion phase (γ_{23R}) instead of the oil component specific weight (γ_{2R}).

2.2.15 Capillary Pressure

Both the Parker *et al.* [1987] generalization of the van Genuchten [1980] model and the Brooks and Corey [1966] model are options used to calculate the capillary pressure. Hysteresis in capillary pressure is taken into account in a very simplistic fashion discussed below, but a full hysteretic and trapping number dependent model that is more complete is also available (Delshad *et al.*, 1994).

2.2.15.1 Brooks-Corey

Capillary pressure in Brooks and Corey capillary pressure-saturation relationship (Brooks and Corey, 1966) is scaled for interfacial tension, permeability, and porosity (Leverett, 1941). The organic spill event in the unsaturated (vadose) zone is assumed to be in the imbibition direction (total liquid saturation increasing). The organic spill event in the saturated zone is taken to be in the first drainage direction (wetting phase, water, saturation decreasing) for the entire spill process. The water flushing or surfactant injection process is assumed to be in the imbibition direction for the entire injection period.

Vadose zone

Implicit assumptions in the capillary pressure formulation in the vadose zone where up to three phases exist are that the direction of descending wettability is water, organic, and air and that the water phase is always present. The capillary pressure between water and gas (no oil is present) or between water and oil phase is calculated based on the normalized water saturation as

$$\left(\frac{P_b}{P_{c1\ell}}\right)^{\lambda_i} = 1 - S_{n1} \quad \text{for } \ell = 2 \text{ or } 4 \tag{2.49}$$

where the maximum capillary pressure P_b is scaled by soil permeability and porosity and is equal to $C_{pci}\frac{\sigma_{1\ell}}{\sigma_{12}}\sqrt{\frac{\phi}{k}}$, which then gives

$$P_{c12} = C_{pci}\sqrt{\frac{\phi}{k}}\frac{\sigma_{12}}{\sigma_{12}}\left(1 - S_{n1}\right)^{-1/\lambda_i} \tag{2.50a}$$

where $P_2 = P_1 + P_{c12}$.

The capillary pressure between water and gas in the absence of the oil phases is calculated as:

$$P_{c14} = C_{pci}\sqrt{\frac{\phi}{k}}\frac{\sigma_{14}}{\sigma_{12}}\left(1 - S_{n1}\right)^{-1/\lambda_i} \tag{2.50b}$$

However, in the presence of the oil phase, the capillary pressure between gas and oil phases is calculated as:

$$P_{c24} = C_{pci}\sqrt{\frac{\phi}{k}}\frac{\sigma_{24}}{\sigma_{12}}\left(\frac{S_{n4}}{1 - S_{n1}}\right)^{-1/\lambda_i} \tag{2.50c}$$

and then the capillary pressure between gas and water is calculated from

$$P_4 = P_{c24} + P_2 \tag{2.50d}$$

$$P_{c14} = P_4 + P_1 \tag{2.50e}$$

C_{pci} and $EPC_i = -1/\lambda_i$ are positive input parameters. The normalized saturations are defined as

$$S_{n\ell} = \frac{S_\ell - S_{\ell r}}{1 - S_{1r} - S_{2r} - S_{4r}} \tag{2.51}$$

The entrapped organic saturation for three-phase (air/organic/water) flow (S_{2r}) is based on a function by Fayers and Matthews [1982] which uses the two-phase entrapped saturation values:

$$S_{2r} = S_{2r1}\left(1 - \frac{S_4}{1 - S_{1r} - S_{2r4}}\right) + S_{2r4}\left(\frac{S_4}{1 - S_{1r} - S_{2r4}}\right) \tag{2.52}$$

where S_{2r1} and S_{2r4} are the entrapped organic saturations to flowing water and air phases, respectively.

Saturated zone

The capillary pressure in the saturated zone where up to three phases (water, organic, microemulsion) exist according to the surfactant phase behavior is calculated as follows.

Two-phase organic-water

The drainage capillary pressure is modeled using the Brooks-Corey function:

$$\left(\frac{P_b}{P_{c12}}\right)^{\lambda_d} = S_{n1} \tag{2.53}$$

where λ_d is a measure of pore size distribution of the medium, the entry pressure P_b equals $C_{pcd}\sqrt{\frac{\phi}{k}}$ and the normalized water saturation is defined as

$$S_{n1} = \frac{S_1 - S_{1r}}{1 - S_{1r}} \tag{2.54}$$

where C_{pcd} and $EPC_d = -1/\lambda_d$ are input parameters. The UTCHEM input parameter EPC_d must be a negative value.

Two-phase water/microemulsion or organic/microemulsion

The imbibition capillary pressure using a Corey-type function is

$$\left(\frac{P_{b\ell}}{P_{c\ell 3}}\right)^{\lambda_i} = 1 - S_{n\ell'} \tag{2.55}$$

For $\ell = 1$, $\ell' = 1$ while for $\ell = 2$, $\ell' = 3$. $P_{b\ell}$ equals $C_{pci}\frac{\sigma_{\ell 3}}{\sigma_{12}}\sqrt{\frac{\phi}{k}}$. The normalized saturations are defined as

$$S_{n1} = \frac{S_1 - S_{1r}}{1 - S_{1r} - S_{3r}} \tag{2.56}$$

$$S_{n3} = \frac{S_3 - S_{3r}}{1 - S_{2r} - S_{3r}} \tag{2.57}$$

Three-phase water/organic/microemulsion

$$\left(\frac{P_{b1}}{P_{c13}}\right)^{\lambda_i} = 1 - S_{n1} \tag{2.58}$$

$$\left(\frac{P_{b2}}{P_{c23}}\right)^{\lambda_i} = 1 - \frac{S_2 - S_{2r}}{(S_1 - S_{1r}) + (S_3 - S_{3r})} \tag{2.59}$$

where $S_{n1} = \dfrac{S_1 - S_{1r}}{1 - S_{1r} - S_{2r} - S_{3r}}$ and $P_{b\ell}$ equals $C_{pci} \dfrac{\sigma_{\ell 3}}{\sigma_{12}} \sqrt{\dfrac{\phi}{k}}$.

The residual saturations ($S_{\ell r}$) in Brooks and Corey's model are either a constant and input to the simulator or computed as a function of trapping number discussed later.

2.2.15.2 van Genuchten

The three-phase capillary pressure-saturation function determined using the generalization of Parker *et al.* [1987] to the two-phase flow model of van Genuchten [1980] is represented by

$$\begin{aligned} \bar{S}_\ell &= \left[1 + \left(\alpha h^*\right)^n\right]^{-m} \qquad h^* > 0 \\ \bar{S}_\ell &= 1 \qquad\qquad\qquad\qquad h^* \le 0 \end{aligned} \tag{2.60}$$

where $\bar{S}_\ell = \dfrac{S_\ell - S_{1r}}{1 - S_{1r}}$ is the effective saturation, $h^* = \beta_{\ell\ell'} P_{C\ell\ell'}$ is the scaled capillary pressure; $\beta_{\ell\ell'}$ is the scaling coefficient for fluid pair of ℓ and ℓ'; α (UTCHEM parameter of CPC) and n (UTCHEM parameter of EPC) are the model parameters, and m = 1−1/n. A significant difference between the van Genuchten and Brooks Corey models is the discontinuity in the slope of the capillary pressure curve at the entry pressure in the latter model whereas Eq. 2.60 is both continuous and has a continuous slope. The implementation of this model in the simulator includes scaling α with soil permeability and porosity similar to that described in Brooks-Corey model.

2.2.16 Relative Permeability

Multiphase relative permeabilities are modeled based on either Corey-type functions (Brooks and Corey, 1966; Delshad and Pope, 1989) or Parker *et al.* [1987] extension of van Genuchten two-phase flow equation to three-phase flow. Hysteresis in the Corey-type relative permeability model discussed below is accounted for by assuming the flow in the saturated zone is on the drainage curve for the spill event and the remediation of the saturated zone is an imbibition process. However, a full hysteretic relative permeability model that is trapping number dependent is also available (Delshad *et al.*, 1994).

2.2.16.1 Corey-Type

Multiphase imbibition and drainage relative permeabilities in both the vadose and saturated zones are modeled using Corey-type functions that are a function of trapping number.

Vadose zone

The organic phase movement in a three-phase porous medium consisting of water/organic/air is assumed to be in the imbibition direction during the organic spill in the vadose zone. We also assume that water and air relative permeabilities are unique functions of their respective saturations only. Organic phase relative permeability, however, is assumed to be a function of two saturations (Delshad and Pope, 1989). These assumptions are consistent with relative permeability measurements (Corey *et al.*, 1956; Saraf and Fatt, 1967; Schneider and Owens, 1970; Saraf *et al.*, 1982; Fayers and Matthews, 1982; Oak, 1990; Oak, *et al.*, 1990).

$$k_{r\ell} = k^o_{r\ell} \left(S_{n\ell}\right)^{n_\ell} \qquad \text{for } \ell = 1, 2, \text{ or } 4 \tag{2.61}$$

where the normalized saturations are defined as

$$S_{n\ell} = \frac{S_\ell - S_{\ell r}}{1 - S_{1r} - S_{2r\ell} - S_{4r}} \qquad \text{for } \ell = 1, \text{ or } 4 \tag{2.62}$$

$$S_{n2} = \frac{S_2 - S_{2r}}{1 - S_{1r} - S_{2r} - S_{4r}} \tag{2.63}$$

where $k^o_{r\ell}$, n_ℓ, and $S_{\ell r}$ are the relative permeability endpoint, exponent, and entrapped saturation for phase ℓ. The trapped organic saturation for three-phase flow (S_{2r}) is calculated from Eq. 2.52. These equations reduce to two-phase flow relative permeabilities in the absence of the third phase.

Saturated zone

The organic phase movement during the spill event in the saturated zone where up to two fluid phases (water and organic) exist is assumed to be in the drainage direction. The organic movement during the remediation process, e.g., water flushing or surfactant injection, however, is assumed to be in the imbibition direction for the entire injection period.

Organic spill process

The relative permeabilities for water and organic fluid phases are

$$k_{r1} = k^o_{r1}\left(S_{n1}\right)^{n_1} \tag{2.64}$$

$$k_{r2} = k^o_{r2}\left(1 - S_{n1}\right)^{n_2} \tag{2.65}$$

where the normalized water saturation is $S_{n1} = \dfrac{S_1 - S_{1r}}{1 - S_{1r}}$.

Remediation process

There are up to three liquid phases present according to the surfactant/water/ organic phase behavior during a SEAR process in the saturated zone. The relative permeabilities are assumed to be unique functions of their respective saturations only. The latter assumption is supported by experimental data measured at The University of Texas at Austin for a mixture of petroleum sulfonate, n-decane, isobutyl alcohol, and water (Delshad *et al.*, 1987; Delshad, 1990). The relative permeability is defined by

$$k_{r\ell} = k^o_{r\ell}\left(S_{n\ell}\right)^{n_\ell} \quad \text{for } \ell = 1, 2, \text{ or } 3 \tag{2.66}$$

where the normalized saturations are defined as

$$S_{n\ell} = \frac{S_\ell - S_{\ell r}}{1 - \sum_{\ell=1}^{3} S_{\ell r}} \quad \text{for } \ell = 1, 2, \text{ or } 3 \tag{2.67}$$

The relative permeabilities reduce to water/organic, water/microemulsion, or organic/microemulsion two phase flow functions. The residual saturations, relative permeability endpoints, and exponents are either constants and input parameters or functions of trapping number as discussed in the next section.

2.2.16.2 Parker *et al.*

Parker *et al*. [1987] extended the two-phase relative permeability-saturation expression derived by van Genuchten to three-phase water/oil/air flow using scaled variables as follows:

$$k_{r1} = \bar{S}_1^{1/2}\left[1 - \left(1 - \bar{S}_1^{1/m}\right)^m\right]^2 \tag{2.68}$$

$$k_{r2} = \left(\bar{S}_t - \bar{S}_1\right)^{1/2}\left[\left(1 - \bar{S}_1^{1/m}\right)^m - \left(1 - \bar{S}_t^{1/m}\right)^m\right]^2 \tag{2.69}$$

$$k_{r4} = \left(\bar{S}_4\right)^{1/2}\left(1 - \bar{S}_t^{1/m}\right)^{2m} \tag{2.70}$$

where S_t is the total liquid saturation. The assumptions in deriving the above relative permeability functions are that water or gas relative permeability is a function of its own saturation only whereas oil relative permeability is a function of both water and oil saturations.

2.2.17 Trapping Number

One of the possible mechanisms for SEAR is the mobilization of trapped organic phase due to reduced interfacial tension resulting from the injection of surfactants into the aquifer (Tuck *et al.*, 1988; Cherry *et al.*, 1990; Pennell *et al.*, 1994; Brown *et al.*, 1994). Buoyancy forces can also affect the mobilization of a trapped organic phase and can be expressed by the Bond number (Morrow and Songkran, 1982). The Bond and capillary numbers for the trapping and mobilization of a nonwetting phase are usually treated as two separate dimensionless groups, one to represent gravity/capillary forces (Bond number) and the other to represent viscous/capillary forces (capillary number). One of several classical definitions of capillary number (Brownell and Katz, 1949; Stegemeier, 1977; Chatzis and Morrow, 1981; Lake, 1989) is as follows

$$N_{c\ell} = \frac{\left|\vec{\vec{k}} \cdot \vec{\nabla}\Phi_{\ell'}\right|}{\sigma_{\ell\ell'}} \qquad \text{for } \ell = 1,..., n_p \tag{2.71}$$

where ℓ and ℓ' are the displaced and displacing fluids and the gradient of the flow potential is given by $\nabla\Phi_{\ell'} = \nabla P_{\ell'} - g\rho_{\ell'}\nabla h$.

Bond number can be defined as

$$N_{B\ell} = \frac{k\, g\left(\rho_\ell - \rho_{\ell'}\right)}{\sigma_{\ell\ell'}} \qquad \text{for } \ell = 1,..., n_p \tag{2.72}$$

where k is the permeability and g is the gravitational force constant.

We have recently developed a new dimensionless number called the trapping number which includes both gravity and viscous forces. The dependence of residual saturations on interfacial tension is modeled in UTCHEM as a function of the trapping number. This is a new formulation that we found necessary to adequately model the combined effect of viscous and buoyancy forces in three dimensions. Buoyancy forces are much less important under enhanced oil recovery conditions than under typical SEAR conditions and so had not until now been carefully considered under three-dimensional surfactant flooding field conditions as a result.

The trapping number is derived by applying a force balance on the trapped NAPL globule. The forces controlling the movement of the blob are the viscous force due to the hydraulic gradient, the trapping force due to capillary pressure and the gravity force, which can act as either a driving or trapping force depending on the direction of the flow. The condition for mobilizing a trapped blob of length L is as follows

Hydraulic force + Buoyancy force ≥ Capillary force (2.72a)

Substituting the definition for each of these forces we have

$$\Delta L \left|\nabla\Phi_w - g\Delta\rho\right| \geq \Delta P_c \tag{2.72b}$$

The trapping number is defined by the left-hand side of Eq. 2.72b as

$$N_{T\ell} = \frac{\left|-\vec{k}\cdot\vec{\nabla}\Phi_{\ell'} - \vec{k}\cdot\left[g(\rho_{\ell'} - \rho_\ell)\vec{\nabla}h\right]\right|}{\sigma_{\ell\ell'}} \tag{2.72c}$$

For one-dimensional vertical flow, the viscous and buoyancy forces add directly and a trapping number can be defined as $N_{T_\ell} = \left|N_{c_\ell} + N_{B_\ell}\right|$. For two-dimensional flow a trapping number is defined as

$$N_{T_\ell} = \sqrt{N_{c\ell}^2 + 2\,N_{c\ell}\,N_{B\ell}\sin\theta + N_{B\ell}^2} \qquad \text{for } \ell = 1,..., n_p \tag{2.73}$$

where θ is the angle between the local flow vector and the horizontal (counter clockwise). The derivation of trapping number for three-dimensional heterogeneous, anisotropic porous media is given by Jin [1995]. Residual saturations are then computed as a function of trapping number as

$$S_{\ell r} = \min\left(S_\ell\ ,\ S_{\ell r}^{high} + \frac{S_{\ell r}^{low} - S_{\ell r}^{high}}{1 + T_\ell\,N_{T_\ell}}\right) \qquad \text{for } \ell = 1,..., n_p \tag{2.74}$$

where T_ℓ is a positive input parameter based on the experimental observation of the relation between residual saturations and trapping number. $S_{\ell r}^{low}$ and $S_{\ell r}^{high}$ are the input residual saturations for phase ℓ at low and high trapping numbers. This correlation was derived based on the experimental data for n-decane (Delshad, 1990) and have recently been successfully applied to residual PCE as a function of trapping number measured by Abriola *et al.* [1994; 1995].

The endpoints and exponents of both the relative permeability curves and capillary pressure curves change as the residual saturations change at high trapping numbers because of detrapping (Morrow and Chatzis, 1981; Morrow *et al.*, 1985; Fulcher *et al.*, 1985; Delshad *et al.*, 1986). The endpoints and exponents in relative permeability functions are computed as a linear interpolation (Delshad *et al.*, 1986) between the given input values at low and high trapping numbers $\left(k_{r\ell}^{o\,low}, k_{r\ell}^{o\,high}, n_\ell^{low}, n_\ell^{high}\right)$:

$$k_{r\ell}^o = k_{r\ell}^{o\,low} + \frac{S_{\ell' r}^{low} - S_{\ell' r}}{S_{\ell' r}^{low} - S_{\ell' r}^{high}}\left(k_{r\ell}^{o\,high} - k_{r\ell}^{o\,low}\right) \qquad \text{for } \ell = 1,..., n_p \tag{2.75}$$

$$n_\ell = n_\ell^{low} + \frac{S_{\ell' r}^{low} - S_{\ell' r}}{S_{\ell' r}^{low} - S_{\ell' r}^{high}}\left(n_\ell^{high} - n_\ell^{low}\right) \text{for } \ell = 1,..., n_p \tag{2.76}$$

The above correlations have successfully been tested against experimental data (Delshad *et al.*, 1986).

2.2.18 Viscosity

Liquid phase viscosities are modeled in terms of pure component viscosities and the phase concentrations of the organic, water and surfactant:

$$\mu_\ell = C_{1\ell}\mu_w e^{\alpha_1(C_{2\ell}+C_{3\ell})} + C_{2\ell}\mu_o e^{\alpha_2(C_{1\ell}+C_{3\ell})} + C_{3\ell}\alpha_3 e^{(\alpha_4 C_{1\ell}+\alpha_5 C_{2\ell})} \qquad \text{for } \ell = 1, 2, \text{ or } 3 \tag{2.77}$$

where the α parameters are determined by matching laboratory microemulsion viscosities at several compositions. In the absence of surfactant and polymer, water and oil phase viscosities reduce to pure water and oil viscosities (μ_w, μ_o). When polymer is present, μ_w is replaced by μ_p defined below.

The following exponential relationship is used to compute viscosities as a function of temperature (T).

$$\mu_\kappa = \mu_{\kappa,ref} \exp\left[b_\kappa \left(\frac{1}{T} - \frac{1}{T_{ref}} \right) \right] \quad \text{for } \kappa = \text{ water, oil, or air} \tag{2.78}$$

where $\mu_{\kappa,ref}$ is the viscosity at a reference temperature of T_{ref} and b_κ is an input parameter.

Air viscosity is computed as a linear function of pressure by

$$\mu_4 = \mu_{a0} + \mu_{aS} \left(P_R - P_{R0} \right) \tag{2.79}$$

where μ_{a0}, the air viscosity at a reference pressure of P_{R0} and μ_{aS}, the slope of air viscosity vs. pressure, are input parameters.

The viscosity of a polymer solution depends on the concentration of polymer and on salinity. The Flory-Huggins equation (Flory, 1953) was modified to account for variation in salinity as

$$\mu_p^0 = \mu_w \left(1 + \left(A_{p1} C_{4\ell} + A_{p2} C_{4\ell}^2 + A_{p3} C_{4\ell}^3 \right) C_{SEP}^{S_p} \right) \quad \text{for } \ell = 1 \text{ or } 3 \tag{2.80}$$

where $C_{4\ell}$ is the polymer concentration in the water or microemulsion phase, μ_w is the water viscosity, A_{P1}, A_{P2}, and A_{P3} are constants. The factor $C_{SEP}^{S_p}$ allows for dependence of polymer viscosity on salinity and hardness. The effective salinity for polymer is given by Eq. 2.17 and S_p is the slope of $\left(\frac{\mu_p^0 - \mu_w}{\mu_w} \right)$ vs. C_{SEP} on a log-log plot.

The reduction in polymer solution viscosity as a function of shear rate ($\dot{\gamma}$) is modeled by Meter's equation (Meter and Bird, 1964):

$$\mu_p = \mu_w + \frac{\mu_p^0 - \mu_w}{1 + \left(\frac{\dot{\gamma}}{\dot{\gamma}_{1/2}} \right)^{P_\alpha - 1}} \tag{2.81}$$

where $\dot{\gamma}_{1/2}$ is the shear rate at which viscosity is the average of μ_p^0 and μ_w and P_α is an empirical coefficient. When the above equation is applied to flow in permeable media, μ_p is usually called apparent viscosity and the shear rate is an equivalent shear rate $\dot{\gamma}_{eq}$. The in-situ shear rate for phase ℓ is modeled by the modified Blake-Kozeny capillary bundle equation for multiphase flow (Lin, 1981; Sorbie, 1991) as

$$\dot{\gamma}_{eq} = \frac{\dot{\gamma}_c |u_\ell|}{\sqrt{\bar{k} k_{r\ell} \phi S_\ell}} \tag{2.82}$$

where $\dot{\gamma}_c$ is equal to 3.97C sec^{-1} and C is the shear rate coefficient used to account for non-ideal effects such as slip at the pore walls (Wreath *et al*., 1990; Sorbie, 1991). The appropriate average permeability $\bar{k}$ is given by

$$\bar{k} = \left[\frac{1}{k_x} \left(\frac{u_{x\ell}}{u_\ell} \right)^2 + \frac{1}{k_y} \left(\frac{u_{y\ell}}{u_\ell} \right)^2 + \frac{1}{k_z} \left(\frac{u_{z\ell}}{u_\ell} \right)^2 \right]^{-1} \tag{2.83}$$

2.2.19 Polymer Permeability Reduction

Polymer solutions reduce both the mobility of the displacing fluid and the effective permeability of the porous medium. The permeability reduction is measured by a permeability reduction factor, R_k, defined as

$$R_k = \frac{\text{effective permeability of water}}{\text{effective permeability of polymer}} \tag{2.84}$$

The change in mobility due to the combined effect of increased viscosity and reduced permeability is called resistance factor, R_F, calculated by

$$R_F = R_k \frac{\mu_p}{\mu_w} \tag{2.85}$$

The effect of permeability reduction lasts even after the polymer solution has passed through the porous medium and is called the residual resistance factor, R_{RF}, defined as

$$R_{RF} = \frac{\text{mobility before polymer solution}}{\text{mobility after polymer solutio}} \tag{2.86}$$

The permeability reduction factor in UTCHEM is modeled as

$$R_k = 1 + \frac{(R_{k\,max} - 1)\, b_{rk}\, C_{4\ell}}{1 + b_{rk}\, C_{4\ell}}$$

where

$$R_{k\,max} = \max \left\{ \left[1 - \frac{c_{rk} \left(A_{p1} C_{SEP}^{S_p} \right)^{1/3}}{\left(\frac{\sqrt{k_x k_y}}{\phi} \right)^{1/2}} \right]^{-4}, \; 10 \right\} \tag{2.87}$$

and ℓ refers to the phase with the highest polymer concentration, b_{rk} and C_{rk} are the input parameters.

The effect of permeability reduction is assumed to be irreversible i.e., it does not decrease as polymer concentration decreases and thus $R_{RF} = R_k$. The viscosity of the phase that contains the polymer is multiplied by the value of the R_k to account for the mobility reduction in the simulator.

2.2.20 Polymer Inaccessible Pore Volume

The reduction in porosity due to inaccessible or excluded pores to the large size polymer molecules is called inaccessible pore volume. The resulting effect is a faster polymer velocity than the velocity of water. This effect is modeled by multiplying the porosity in the conservation equation for polymer by the input parameter of effective pore volume.

2.3 Numerical Methods

The pressure equation and species conservation equations are discretized spatially and temporally as described below. The discretized equations are given in Appendix A of the UTCHEM Technical Documentation.

2.3.1 Temporal Discretization

The temporal discretization in UTCHEM is implicit in pressure, explicit in concentration (IMPES-like). The solution of the pressure equation using the Jacobi conjugate gradient method is then followed by a back substitution into the explicit mass conservation equation for each component. The temporal accuracy for the conservation equation is increased by using a time-correction technique that is second-order in time (Liu, 1993; Liu *et al.*, 1994).

2.3.2 Spatial Discretization

Either one-point upstream, two-point upstream, or a third-order spatial discretization of the advective terms is used (see Appendix A of the UTCHEM Technical Documentation). It is well-known that lower-order upwind schemes cause smearing of the saturation and concentration profiles by increasing numerical dispersion. There have been a number of discretization methods developed to minimize these effects associated with multiphase flow and transport simulation (Todd *et al.*, 1972; Leonard, 1979; Taggart and Pinczewski, 1987; Bell *et al.*, 1989; Le Veque, 1990; Datta Gupta *et al.*, 1991; Blunt and Rubin, 1992; Dawson, 1993; Arbogast and Wheeler, 1995). We use a scheme that is approximately third-order in space to minimize numerical dispersion and grid-orientation effects. In order to obtain oscillation-free, high-resolution, high-order results, Harten [1983] developed the total-variation-diminishing scheme (TVD) that includes a limiting procedure. The limiter is a flux limiter with constraints on the gradient of the flux function (Sweby, 1984; Datta Gupta *et al*., 1991; Liu *et al*., 1994). The limiter function developed by Liu [1993], which varies as a function of timestep and gridblock size, was implemented in the simulator.

2.4 Model Verification and Validation

UTCHEM has extensively been verified by comparing problems such as one-dimensional two-phase flow with the Buckley-Leverett solution (Buckley and Leverett, 1942), one-dimensional miscible water/tracer flow against the analytical solution of the convection-diffusion equation, two-dimensional ideal tracer flow with the analytical solution given by Abbaszadeh-Dehghani and Brigham [1984], and two-dimensional nonlinear Burgers equation (Schiesser, 1991) by Liu [1993]. Excellent agreement between the numerical and analytical solutions were obtained when the TVD third-order scheme was used. The model has also been validated by comparisons with laboratory surfactant floods (Camilleri *et al.*, 1987a), field data from the Big Muddy surfactant pilot (Saad *et al.*, 1989), and a multiwell waterflood tracer field project (Allison *et al.*, 1991). Pickens *et al.* [1993] have compared UTCHEM results with a tetrachloroethylene (PCE) infiltration experiment in a sandpack with four types of sands performed by Kueper [1989] and Kueper and Frind [1991]. They concluded that the simulator can accurately predict the vertical and lateral distribution of DNAPL in a heterogeneous medium.

The model has recently been used to model the surfactant-enhanced remediation of PCE in a test cell at Canadian Forces Base Borden in Allison, Ontario (Freeze *et al.*, 1994). The model was 3 m by 3 m by 4 m deep test cell described as layered with soil properties estimated from the field data. The detailed description of the test cell is given by Kueper *et al.* [1993]. PCE in the amount of 231 L was first injected to the center of the test cell. The remediation process involved the following steps:

1. Direct pumping of free-phase for about two weeks where 47 L of PCE was recovered,

2. Pump and treat for about two months where additional 12 L of free-phase and dissolved PCE was removed, and

3. Surfactant flushing to solubilize additional PCE for about seven months. The surfactant solution was 1 wt% nonyl phenol ethoxylate (NP 100) and 1 wt% phosphate ester of the nonyl phenol ethoxylate (Rexophos 25-97). A total of 130,000 L of surfactant solution was recirculated through the test cell. Additional 62 L of PCE was recovered as a result of enhanced solubility by the surfactant solution. The surfactant-enhanced solubility of PCE was measured to be about 11,700 mg/L as compared to an aqueous solubility of about 200 mg/L.

The measured and simulated vertical distributions of PCE before and after the surfactant injection are shown in Figs. 2.6 and 2.7 and show good agreement. Here we discuss the features of UTCHEM model that were used in this application and the input parameters for the physical property models since Freeze *et al*. did not discuss these in their paper. The assumptions made based on the test cell conditions were 1) isothermal simulations, 2) insignificant electrolyte concentration, incompressible fluids and soil, equilibrium PCE dissolution, and no mobilization of PCE. The species considered in the simulation were water, PCE, and surfactant and the resulting phases were water, PCE, and microemulsion. The phase behavior parameters were chosen such that either residual PCE/microemulsion, residual PCE/water, or single phase microemulsion are present. Due to lack of any phase behavior measurements for this surfactant mixture, the phase behavior parameters (C_{2P}, H_{bnc70} in Eq. 2.30b) were adjusted such that the simulated solubility is similar to the measured value of 11700 mg/L. Table 2.1 gives the input parameters for the physical properties. The test cell was simulated using 12 and 9 gridblocks in the x and y directions and 14 vertical layers. The porosity was constant equal to 0.39 and the hydraulic conductivity in the range of 0.003 to 0.01 cm/s. The ratio of vertical to horizontal permeability was 1. Longitudinal and transverse dispersivities for all three phases were assumed to be 0.03 and 0.01 m, respectively. The 201-day simulation of surfactant flooding took 22 minutes on a DEC 3000/500 alpha workstation.

UTCHEM was able to closely reproduce both the PCE recovery and the vertical distribution of PCE over the period of 201 days. The favorable comparison of UTCHEM results with the field test results demonstrates the utility of the model in predicting SEAR processes at the field scale.

2.5 Summary and Conclusions

We have presented the description of a three-dimensional, multicomponent, multiphase compositional model, UTCHEM, for simulating the contamination of aquifers by organic species and the remediation of aquifers by surfactant injection. UTCHEM has the capability of simulating both enhanced dissolution and separate phase removal of NAPLs from both saturated and vadose zones. The simulator has been verified with several analytical solutions and validated by comparisons with both laboratory and field experiments.

The model uses a block-centered finite-difference discretization. The solution method is analogous to the implicit in pressure and explicit in concentration method. Either one-, two-point upstream, or third-order spatial weighting schemes is used. A flux limiter that is total-variation-diminishing has also been added to the third-order scheme to increase stability and robustness.

UTCHEM accounts for effects of surfactants on interfacial tension, surfactant phase behavior, capillary trapping, and surfactant adsorption. Multiphase capillary pressures, relative permeabilities, physical dispersion, molecular diffusion, cation exchange, and partitioning of NAPLs to the aqueous phase which accounts for nonequilibrium effects are some of the important physical properties features in the simulator.

UTCHEM can be used to design the most efficient surfactant remediation strategies taking into account realistic soil and fluid properties. Due to its capability, several important variables that can significantly affect the outcome of any SEAR program such as mobilization vs. solubilization, mobility control by adding polymer, nonequilibrium interphase mass transfer, temperature gradient, and electrolyte concentrations where the soil/water interactions are important; e.g., fresh water in the presence of clay can be studied before implementing a field project.

2.6 Nomenclature

a_3 Surfactant adsorption parameter

a_{31} Surfactant adsorption parameter, $(L^2)^{0.5}$

a_{32} Surfactant adsorption parameter, $(L^2)^{0.5}$ $(Eq/L^3)^{-1}$

b_3 Surfactant adsorption parameter

a_4 Polymer adsorption parameter

a_{41} Polymer adsorption parameter, $(L^2)^{0.5}$

a_{42} Polymer adsorption parameter, $(L^2)^{0.5}$ $(Eq/L^3)^{-1}$

b_4 Polymer adsorption parameter, L^3/wt% polymer

b_{rk} Permeability reduction factor parameter, L^3/wt% polymer

$C_{i,\kappa}$ Total concentration of species κ in gridblock i, L^3/L^3 PV

C_{SE} Effective salinity for phase behavior and surfactant adsorption, Eq/L^3

C_{SEL} Salinity for Type II(–)/III phase boundary or lower effective salinity limit, Eq/L^3

C_{SEP} Effective salinity for polymer, Eq/L^3

C_{SEU} Salinity for Type III/II(+) phase boundary or upper effective salinity limit, Eq/L^3

C_6^o Concentration of free calcium cations, L^3/L^3

C_9^o Concentration of free sodium cations, L^3/L^3

C_κ Overall concentration of species κ in the mobile phases, L^3/L^3

C_κ^{eq} Equilibrium concentration of species κ, L^3/L^3

C_κ^o Compressibility of species κ, $(mL^{-1}t^{-2})^{-1}$

$\hat{C}_\kappa$ Adsorbed concentration of species κ, L^3/L^3 PV

$\tilde{C}_\kappa$ Overall concentration of species κ in the mobile and stationary phases, L^3/L^3 PV

$C_{\kappa\ell}$ Concentration of species κ in phase ℓ, L^3/L^3

$C_{p\ell}$ Constant pressure heat capacity of phase ℓ, $QT^{-1}m^{-1}$

C_r Rock compressibility, $(mL^{-1}t^{-2})^{-1}$

C_T Total compressibility, $(mL^{-1}t^{-2})^{-1}$

$C_{v\ell}$ Volumetric heat capacity of phase ℓ, $QT^{-1}m^{-1}$

C_{vs} Volumetric heat capacity of soil, $QT^{-1}m^{-1}$

c_{rk} Permeability reduction factor parameter, $L(wt\%)^{1/3}$

D_a Damkohler number

$D_{\kappa\ell}$ Diffusion coefficient of species κ in phase ℓ, L^2t^{-1}

f_{oc} Organic carbon fraction in soil

f_κ^s Amount of species κ associated with surfactant, L^3/L^3

g Gravitational constant, Lt^{-2}

h Depth, L

K Dispersion coefficient, L^2t^{-1}

$\bar{k}$ Average permeability, L^2

$\vec{K}$	Permeability tensor, L^2
k	Soil permeability, L^2
k_a	Apparent permeability used in capillary pressure calculations, L^2
K_{oc}	Amount of organic adsorbed per unit weight of organic carbon in soil, $(mL^{-3})^{-1}$
$k_{r\ell}$	Relative permeability of phase ℓ
$k^o_{r\ell}$	Endpoint relative permeability of phase ℓ
$k^{o\,high}_{r\ell}$, $k^{o\,low}_{r\ell}$	Endpoint relative permeability of phase ℓ at high and low capillary numbers
k_x, k_y, k_z	Absolute permeability in the x, y and z directions, L^2
L	Length of the core, or reservoir length, L
M_κ	Mass transfer coefficient for species κ, t^{-1}
n_{pc}	Capillary pressure exponent
n_ℓ	Relative permeability exponent for phase ℓ (dimensionless)
n^{high}_ℓ, n^{low}_ℓ	Relative permeability exponent for phase ℓ at high and low capillary numbers
$N_{B\ell}$	Bond number of phase ℓ
$N_{c\ell}$	Capillary number of phase ℓ
$N_{T\ell}$	Trapping number of phase ℓ
$P_{C\ell\ell'}$	Capillary pressure between phases ℓ and ℓ', $mL^{-1}t^{-2}$
P_ℓ	Pressure of phase ℓ, $mL^{-1}t^{-2}$
P_R	Reference pressure, $mL^{-1}t^{-2}$
Q_κ	Source/sink for species κ, L^3/T
Q_L	Heat loss, $Qt^{-1}L^{-2}$
Q_v	Cation exchange capacity of clay, $Eq./L^3$
q_H	Enthalpy source per bulk volume, $Qt^{-1}L^{-3}$
R_F	Polymer resistance factor
R_k	Polymer permeability reduction factor
R_{RF}	Polymer residual resistance factor
$R_{\ell 3}$	Solubilization ratio for phase ℓ, L^3/L^3
R_κ	Total source/sink for species κ, $mL^{-3}t^{-1}$
$R^I_{\kappa\ell}$	Mass exchange rate at interface for species κ in phase ℓ, $mL^{-3}t^{-1}$
$r_{\kappa\,\ell}$	Reaction rate for species κ in phase ℓ, $mL^{-3}t^{-1}$
$r_{\kappa\,s}$	Reaction rate for species κ in solid phase, $mL^{-3}t^{-1}$
$S_{n\ell}$	Normalized mobile saturation of phase ℓ used in relative permeability and capillary pressure calculations
S_ℓ	Saturation of phase ℓ, L^3/L^3 PV
$S_{\ell r}$	Residual saturation of phase ℓ, L^3/L^3 PV
$S^{high}_{\ell r}$, $S^{low}_{\ell r}$	Residual saturation of phase ℓ at high and low capillary numbers L^3/L^3 PV
t	Time, t

Δt^n, Δt^{n+1}	Time-step size at n^{th} and $n+1^{th}$ time level, t
T	Temperature, T
T_ℓ	Trapping parameter for phase ℓ
$\vec{u}_\ell$	Darcy flux, Lt^{-1}
Δx_i, Δy_i, Δz_i	Size of gridblock i in the x, y, and z directions, L

Greek Symbols

α_1-α_5	Microemulsion phase viscosity parameters
α_L, α_T	Longitudinal and Transverse dispersivity, L
β^C	Cation exchange constant for clay
β^S	Cation exchange constant for surfactant
β_6	Effective salinity parameter for calcium
γ_κ	Specific weight of species κ, $mL^{-2}t^{-2}$
$\dot{\gamma}$	Shear rate, t^{-1}
$\gamma_{\kappa R}$	Specific weight of species κ at reference pressure, $mL^{-2}t^{-2}$
μ_o	Oil viscosity, $ML^{-1}T^{-1}$
μ_P	Polymer viscosity, $ML^{-1}T^{-1}$
μ_p^0	Polymer viscosity at zero shear rate, $mL^{-1}t^{-1}$
μ_w	Water viscosity, $mL^{-1}t^{-1}$
μ_ℓ	Viscosity of phase ℓ, $mL^{-1}t^{-1}$
$\mu_{a,ref}$	Viscosity of air at reference pressure, $mL^{-1}t^{-1}$
$\mu_{a,s}$	Slope of air viscosity function
λ_d	Drainage Capillary pressure exponent
λ_i	Imbibition Capillary pressure exponent
λ_ℓ	Relative mobility of phase ℓ, $(mL^{-1}t^{-1})^{-1}$
λ_{rT}	Total relative mobility, $(mL^{-1}t^{-1})^{-1}$
λ_T	Thermal conductivity, $Qt^{-1}T^{-1}L$
ρ_g	Rock density, m/L^3
ρ_s	Soil density, m/L^3
ρ_ℓ	Density of phase ℓ, m/L^3
σ_{aw}	Interfacial tension between air and water, mt^2
σ_{wo}	Interfacial tension between oil and water, mt^2
$\sigma_{\ell\ell'}$	Interfacial tension between phases ℓ and ℓ', mt^2
ϕ	Porosity, fraction
ϕ_i	Porosity of gridblock i, fraction
Φ	Potential, $mL^{-1}t^{-2}$
τ	Tortuosity factor

Subscripts

κ species number
1 - Water
2 - Oil
3 - Surfactant
4 - Polymer
5 - Chloride
6 - Calcium
7 - Alcohol
8 - air
9-κ - Tracer components

ℓ Phase number
1 - Aqueous
2 - Oleic
3 - Microemulsion
4 - Air

r Residual

s Solid

Superscripts

C Cation

f Free

S Surfactant

2.7 Tables and Figures

Table 2.1. Physical Property Input Parameters for the Test Cell Simulation

Property	Value	References and Comments
Density		
Pure water, g/cc	1	
Pure PCE, g/cc	1.6249	
Surfactant, g/cc	1.15	
Viscosity		Eq. 2.77; Parameters were estimated based on the measured data for a different surfactant mixture (Pennell *et al.*, 1994)
Pure water (μ_w), cp	1	
Pure PCE (μ_o), cp	0.89	
Microemulsion (max. value)	4	
α_1 - α_5 parameter values	3.4, 1.0, 3.0, 1.0, 1.0	
Interfacial tension		Eq. 2.43; parameters are based on the measured data for a different surfactant mixture (Pennell *et al.*, 1994)
PCE/water (σ_{ow}), dyne/cm	45	
PCE/microemulsion (minimum value), dyne/cm	0.02	
G_{21}, G_{22}, G_{23} (Healy and Reed, 1974)	13, -14.5, 0.01	
PCE solubility		
Max. in water, mg/L	200	West and Harwell [1992]
Max. in surfactant, mg/L	11,700	Fountain [1992]
Surfactant adsorption		Eq. 2.15; but assuming surfactant adsorption is independent of permeability
Max. value, mg/g soil	0.311	
Parameter values: a_{31}, a_{32}, b_3	1.1, 0.0, 1000	
Capillary pressure (Corey function)		Eq. 2.55; based on Kueper [1989]
Imbibition: C_{pci}, λ_i	2.7, -0.454	
Relative permeability (Corey function)		Eq. 2.66; based on Kueper [1989]
Water (Imbibition):S_{1r}, n_1, k^o_{r1}	0.306, 2.2, 0.556	
PCE: S_{2r}, n_2, k^o_{r2}	0.0, 2.2, 0.309	
Microemulsion: S_{3r}, n_3, k^o_{r3}	0.306, 2.2, 0.556	

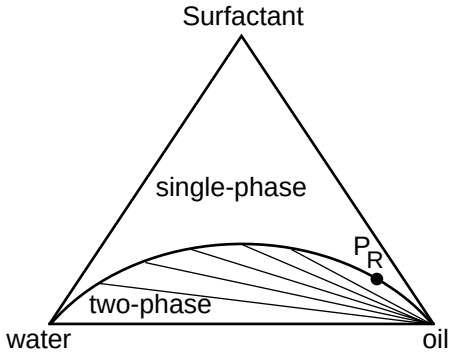

Figure 2.1. Schematic representation of Type II (-).

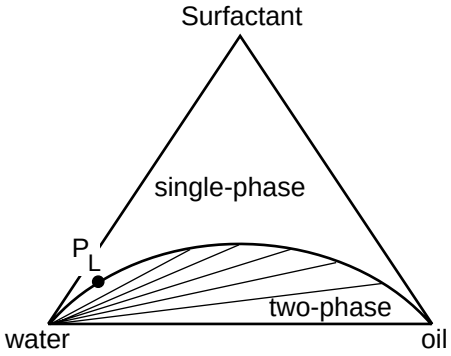

Figure 2.2. Schematic representation of high-salinity Type II (+).

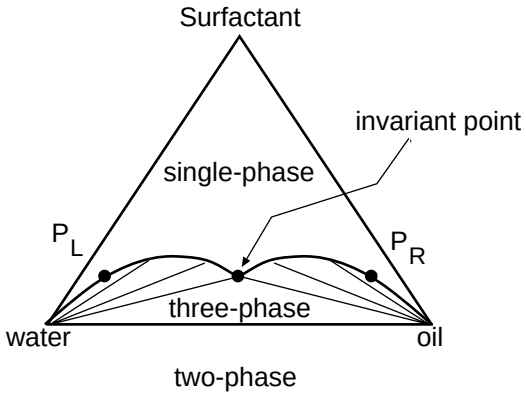

Figure 2.3. Schematic representation of Type III.

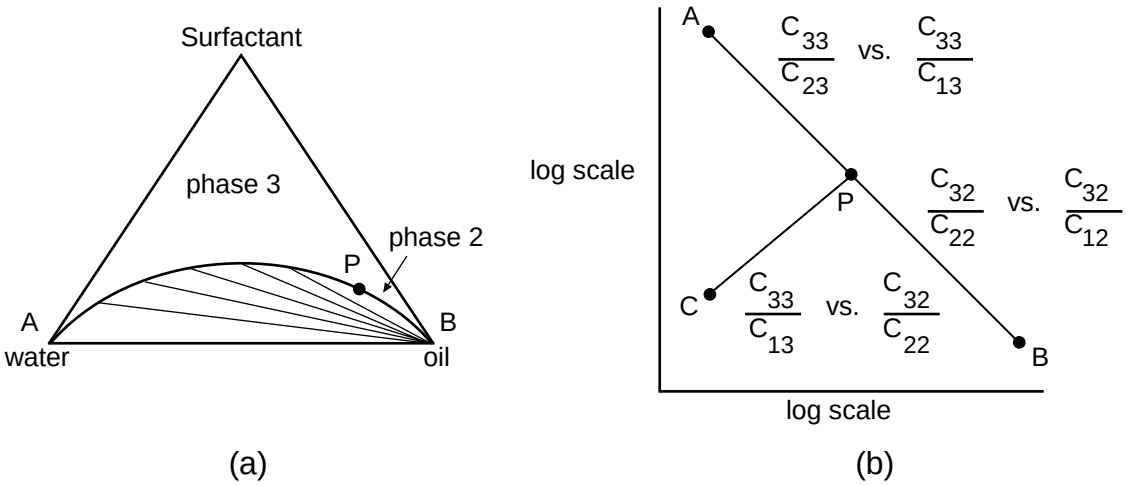

Figure 2.4. Correspondence between (a) ternary diagram and (b) Hand plot.

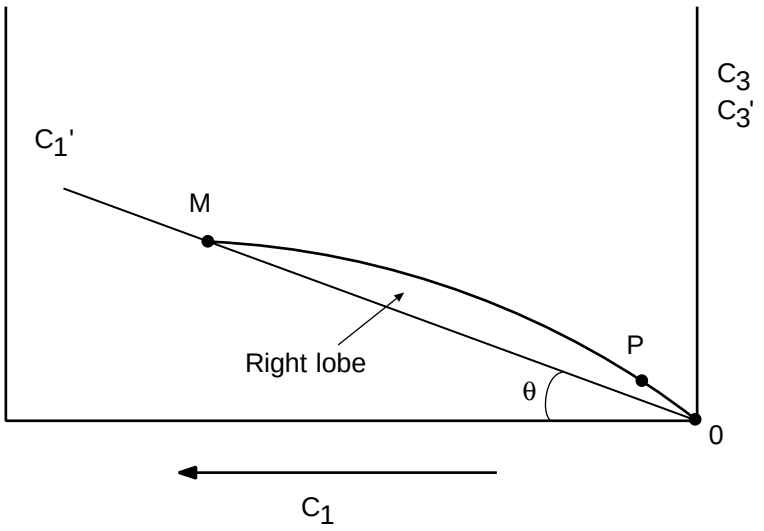

Figure 2.5. Coordinate transformation for the two-phase calculations in Type III.

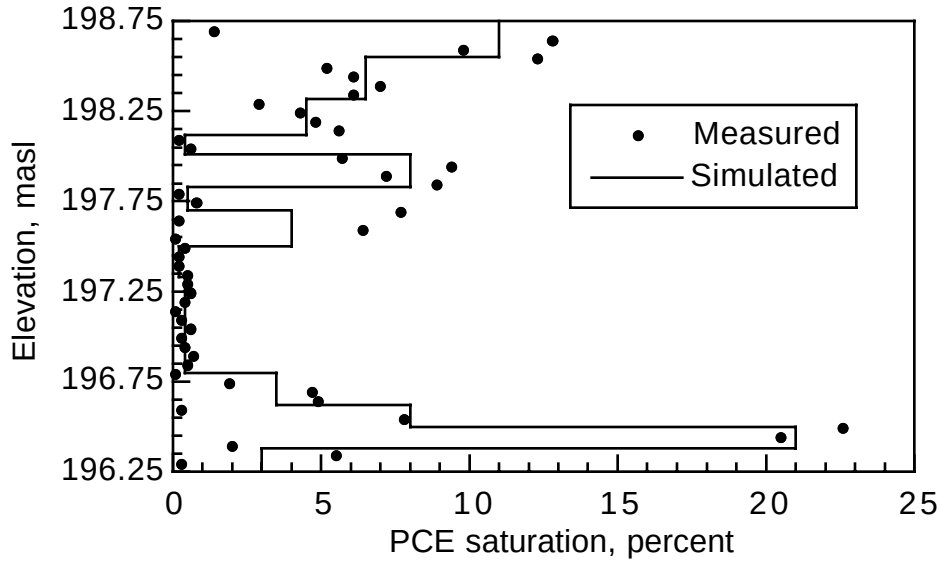

Figure 2.6. Measured and simulated PCE saturation at the location of Core 3 prior to surfactant flooding (after Freeze *et al.*, 1994).

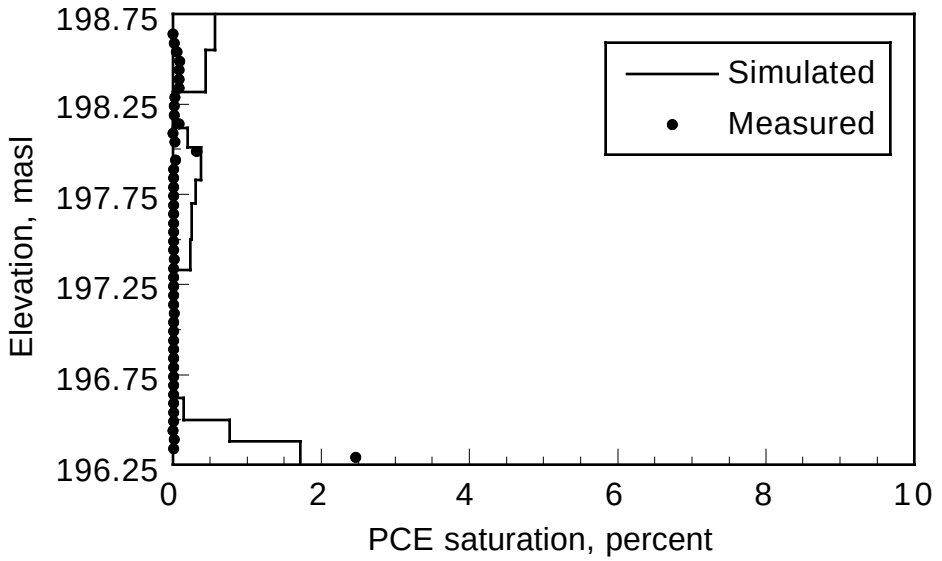

Figure 2.7. Measured and simulated PCE saturation at the location of Core 6 at the end of surfactant flooding (after Freeze *et al.*, 1994).

Section 3
Water-Wet Hysteretic Relative Permeability and Capillary Pressure Models

3.1 Introduction

The hysteresis modeling in UTCHEM is based on the work by Kalurachchi and Parker [1992]. Both capillary pressure and relative permeability functions account for hysteresis due to arbitrary changes in saturation path by incorporating an oil phase entrapment model. The assumptions made in developing and applying this model are

- The model applies only to strongly water-wet media where the wettability in descending order is for water (or microemulsion), oil, and gas phases. Oil will be used in this report to mean any non-aqueous phase liquid (NAPL).
- The model applies to three-phase air-water-oil flow in the vadose zone and two-phase oil-water or oil-microemulsion flow in the saturated zone
- To avoid numerical oscillations with changes from two phases (air-water) to three phases (air-water-oil), once a location is classified as a three-phase node, it will not revert back to two phases (air-water).
- Gas entrapment is neglected for the three-phase case. Therefore, oil entrapment in a three-phase air-water-oil can be inferred directly from that in a two-phase oil-water system.
- Water relative permeability is unaffected by oil entrapment, e.g. $k_{rw} = f(S_w)$.
- There is no oil entrapment on the main drainage curve.
- There is no oil entrapment when water saturation is at its residual value in the vadose zone.

We use the notation adapted from Parker *et al*. [1987] shown in Table 3.1.

3.2 Oil Phase Entrapment

On any scanning curve (e.g., point A on Fig. 3.1), effective residual oil saturation is estimated from Land's equation (Land, 1968), where the residual nonwetting phase saturation after imbibition is related empirically to the initial nonwetting saturation $(1 - \bar{S}_w^{min})$ as

$$\bar{S}_{or}^{A} = \frac{1 - \bar{S}_w^{min}}{1 + R\left(1 - \bar{S}_w^{min}\right)} \qquad (3.1)$$

$$\text{where } R = \frac{1}{\bar{S}_{or}^{max}} - 1$$

The trapped oil saturation at nonzero capillary pressure is calculated from the following relationships.

3.2.1 Kalurachchi and Parker

To estimate trapped oil saturation at nonzero capillary pressure, Kalurachchi and Parker estimated the trapped oil saturation as the difference between residual oil saturation for the actual scanning curve and that for a curve with a reversal point equal to the free (continuous) oil saturation on the actual path. This is exactly the same idea as proposed by Stegemeier in 1977 and described in Lake [1989]. For example,

consider point B on the scanning curve on Fig. 3.1 with apparent water saturation of $\bar{\bar{S}}_w = \bar{S}_w + \bar{S}_{ot}$. Points B and C have the same capillary pressure, therefore the difference between the x coordinates of points B and C is the disconnected nonwetting phase saturation ($\bar{S}_{ot}$). Using Land's relation for the residual oil saturation for the scanning path starting from point A ($\bar{S}_{or}^{A}$) and that starting from point C ($\bar{S}_{or}^{C}$) we have

$$\bar{S}_{or}^{A} = \frac{1 - \bar{S}_w^{min}}{1 + R\left(1 - \bar{S}_w^{min}\right)} \tag{3.2}$$

$$\bar{S}_{or}^{C} = \frac{1 - \bar{\bar{S}}_w}{1 + R\left(1 - \bar{\bar{S}}_w\right)} \tag{3.3}$$

and

$$\bar{S}_{ot} = \bar{S}_{or}^{A} - \bar{S}_{or}^{C}$$

$$\bar{S}_{ot} = \begin{cases} \left[\min\left(\dfrac{1 - \bar{S}_w^{min}}{1 + R\left(1 - \bar{S}_w^{min}\right)} - \dfrac{1 - \bar{\bar{S}}_w}{1 + R\left(1 - \bar{\bar{S}}_w\right)}, \bar{S}_o \right) \right] & \text{when } \bar{S}_w > \bar{S}_w^{min} \\ 0.0 & \text{otherwise} \end{cases} \tag{3.4}$$

Equation 3.4 is a conditional quadratic equation that can be solved for $\bar{S}_{ot}$ since $\bar{\bar{S}}_w = \bar{S}_w + \bar{S}_{ot}$. Once $\bar{S}_{ot}$ is computed, capillary pressures and relative permeabilities are computed from the equations discussed below.

3.2.2 Parker and Lenhard

The trapped oil saturation is calculated by linear interpolation since the effective trapped oil saturation along any scanning curve (e.g., the curve with reversal point of A in Fig. 3.1) varies from zero at the reversal point of $\bar{S}_w^{min}$ to $\bar{S}_{or}^{A}$ at $\bar{\bar{S}}_w = 1$ as

$$\bar{S}_{ot} = \min\left(\bar{S}_{or}^{A}\left(\frac{\bar{\bar{S}}_w - \bar{S}_w^{min}}{1 - \bar{S}_w^{min}} \right), \bar{S}_o \right) \tag{3.5}$$

where $\bar{S}_{or}^{A}$ is calculated from Eq. 3.2.

3.3 Capillary Pressure

The two-phase air-water, water-oil or microemulsion-oil and three-phase oil-water-air capillary pressure-saturation function determined using the generalization of Parker *et al.* [1987] to the two-phase flow model of van Genuchten [1980] is represented as follows.

3.3.1 Two-Phase Flow

$$\bar{\bar{S}}_w = \left[1 + \left(\alpha \beta_{\ell\ell'} P_{c\ell\ell'} \right)^n \right]^{-m} \tag{3.6}$$

where $\beta_{\ell\ell'}$ is the scaling coefficient for fluid pair ℓ and ℓ'; α and n are the adjustable parameters, and m = 1–1/n. The implementation of this model in the simulator includes scaling with intrinsic permeability (k) and porosity (ϕ) where α is replaced by $\alpha\sqrt{\frac{k}{\phi}}$. β is approximated by the ratio of water-air interfacial tension (σ_{aw}) to the interfacial tension of the fluid pair. Here and elsewhere the subscript w applies to either water or microemulsion for the case of two-phase flow with oil.

$$\beta_{\ell\ell'} = \sigma_{aw} / \sigma_{\ell\ell'}$$

3.3.2 Three-Phase Oil/Water/Air Flow

$$\bar{\bar{S}}_w = \left[1 + \left(\alpha\beta_{ow} P_{cow}\right)^n\right]^{-m} \tag{3.7}$$

$$\bar{S}_t = \left[1 + \left(\alpha\beta_{ao} P_{cao}\right)^n\right]^{-m} \tag{3.8}$$

3.4 Relative Permeability

The two- and three-phase relative permeabilities are based on the generalization of Parker and Lenhard to the two-phase flow model of van Genuchten.

$$k_{rw} = \bar{S}_w^{1/2}\left[1 - \left(1 - \bar{S}_w^{1/m}\right)^m\right]^2 \tag{3.9}$$

$$k_{ro} = \left(\bar{S}_t - \bar{\bar{S}}_w\right)^{1/2}\left[\left(1 - \bar{\bar{S}}_w^{1/m}\right)^m - \left(1 - \bar{S}_t^{1/m}\right)^m\right]^2 \tag{3.10}$$

$$k_{ra} = \left(1 - \bar{S}_t\right)^{1/2}\left(1 - \bar{S}_t^{1/m}\right)^{2m} \tag{3.11}$$

3.5 Capillary Number Dependent Hysteretic Model

An important new extension of these models is the inclusion of their dependence on interfacial tension via the trapping number. The capillary number traditionally used by both the groundwater and oil reservoir literatures has been generalized by Jin [1995] and is now called the trapping number. We assume that 1) the capillary pressure parameters n and m are independent of trapping number and 2) the residual oil saturation (S_{or}^{max}) and residual water (or microemulsion) saturation (S_{wr}) are functions of trapping number. We compute the residual water and residual oil saturations as a function of trapping number as follows:

$$S_{\ell r} = \min\left(S_\ell\ ,\ S_{\ell r}^{high} + \frac{S_{\ell r}^{low} - S_{\ell r}^{high}}{1 + T_\ell N_{T\ell}}\right) \quad \text{where } \ell = \text{w (or microemulsion), oil} \tag{3.12}$$

where the $S_{\ell r}^{high}$ and $S_{\ell r}^{low}$ are the phase ℓ residual saturations at high and low trapping numbers, T_ℓ is the adjustable parameter. This correlation was derived based on the experimental data for n-decane (Delshad, 1990) and have recently been successfully applied to residual PCE as a function of trapping number measured by Pennell *et al.* [1996]. The trapping number $N_{T\ell}$ is computed as

$$N_{T\ell} = \frac{\left| -\vec{k} \cdot \vec{\nabla}\Phi_{\ell'} - \vec{k} \cdot \left[g(\rho_{\ell'} - \rho_{\ell})\vec{\nabla}h \right] \right|}{\sigma_{\ell\ell'}} \tag{3.13}$$

where h is the vertical depth (positive downward), ρ_{ℓ} and $\rho_{\ell'}$ are the displaced and displacing fluid densities, and the gradient of the flow potential is given by $\vec{\nabla}\Phi_{\ell'} = \vec{\nabla}P_{\ell'} - g\rho_{\ell'}\vec{\nabla}h$.

We then substitute the water (or microemulsion) and oil residual saturations calculated from Eq. 3.13 for S_{wr} and S_{or}^{max} in the calculations of entrapped oil phase saturations (S_{ot}), capillary pressure, and relative permeabilities described above. This extension makes the hysteretic model suitable for remediation processes that involve changes in interfacial tension; e.g., co-solvent, surfactant, etc. (Delshad *et al.*, 1996). The reduction in interfacial tension due to the presence of surfactant or co-solvent in the above equations is calculated from a modified Huh's equation (Huh, 1979) where the interfacial tension is related to the solubilization ratio (Delshad *et al.*, 1996). The interfacial tension for oil-water in the absence of surfactant or co-solvent or water-air fluid pairs is assumed to be a constant.

3.6 Tables and Figures

Table 3.1. Notation Used in Section 3

Water and oil saturations:	S_w, S_o
Residual water saturation:	S_{wr}
Effective water saturation :	$\bar{S}_w = \frac{S_w - S_{wr}}{1 - S_{wr}}$
Effective total liquid saturation:	$\bar{S}_t = \frac{S_w + S_o - S_{wr}}{1 - S_{wr}}$
Effective oil saturation:	$\bar{S}_o = \frac{S_o}{1 - S_{wr}}$
Apparent water saturation:	$\bar{\bar{S}}_w = \bar{S}_w + \bar{S}_{ot}$
Residual and trapped oil saturation:	Residual oil saturation corresponds to the trapped oil saturation at zero capillary pressure, $\bar{S}_{or} = \bar{S}_{ot}(@P_c = 0.0)$
Minimum effective water saturation (corresponds to the reversal from drainage to imbibition):	$\bar{S}_w^{min}$
Maximum effective residual oil saturation (corresponds to main imbibition curve):	$\bar{S}_{or}^{max} = \frac{S_{or}^{max}}{1 - S_{wr}}$

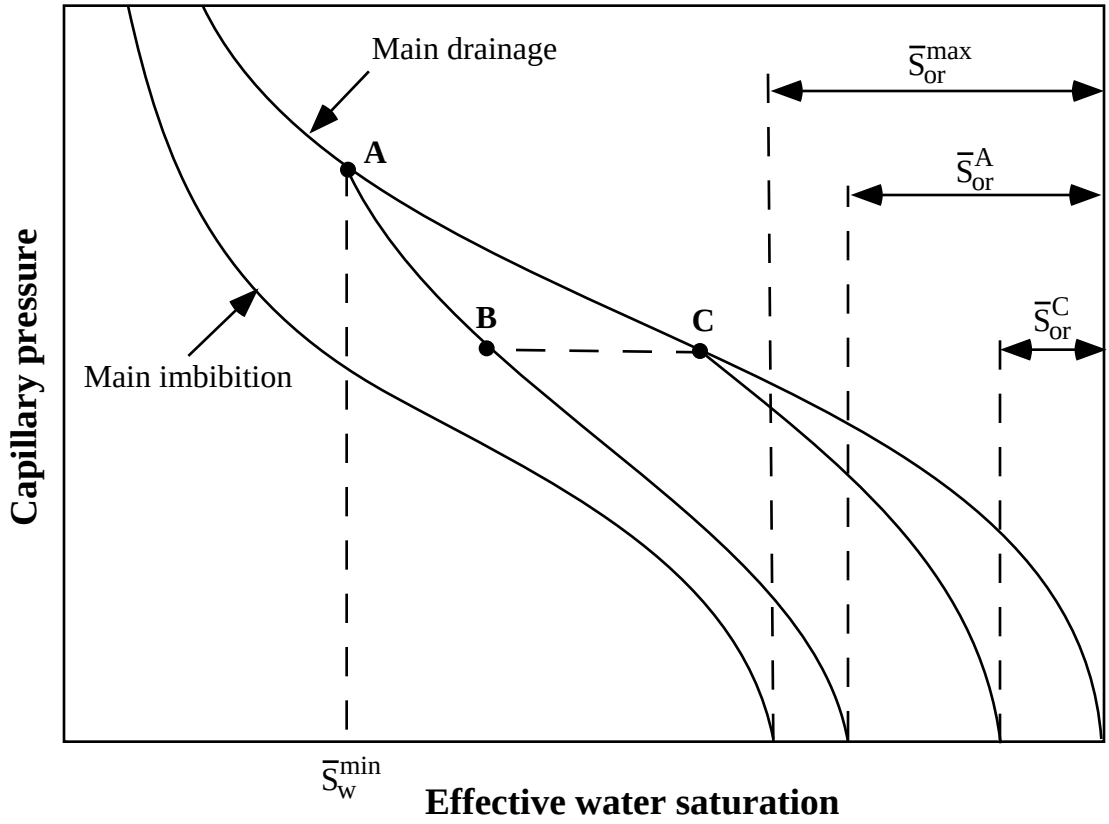

Figure 3.1. Capillary pressure curves as a function of effective water saturation.

Section 4
UTCHEM Tracer Options

4.1 Introduction

Any number of tracers can be modeled in UTCHEM. These tracers can be water tracer, oil tracer, partitioning oil/water tracer, gas tracer, and partitioning gas/oil tracer. There are up to two reacting tracers allowed. Reacting tracers are considered only for water/oil tracers and tracer components 2 and 3 are reacting and product tracers for the first reacting tracer. Tracer components 4 and 5 are reacting and product tracers for the second reacting tracer. The assumptions made in the modeling of tracers are:

1. Tracers do not occupy volume
2. Tracers have no effect on the physical properties

The overall tracer concentrations are computed from the species conservation equations which include a reaction term for the reacting tracer. The tracer phase concentrations are calculated according to the tracer type: water, oil, gas, or partitioning.

UTCHEM can model single-well tracer test (Descant, 1989), partitioning interwell tracer tests (Allison *et al.*, 1991; Jin *et al*., 1995), and single-well wettability tracer test (Ferreira *et al.*, 1992).

4.2 Non-Partitioning Tracer

The tracer phase composition for a non-partitioning tracer is proportional to the ratio of the total tracer concentration to the total concentration of water, oil, or gas depending on the tracer type as

$$C_{T_\ell} = C_{\kappa\ell}\frac{C_T}{C_\kappa} \qquad \text{T = water, oil, or gas tracer} \tag{4.1}$$

4.3 Partitioning Tracer

4.3.1 Water/Oil

The tracer partitioning coefficient for a water/oil tracer is defined on the basis of water or oil pseudocomponent concentration as

$$K_T = \frac{C_{T_2}}{C_{T_1}} \tag{4.2}$$

where C_{T_1} and C_{T_2} are the tracer concentrations in the water and oil pseudocomponents. The tracer phase compositions are then computed from the tracer material balance equation as

$$C_{T_\ell} = C_{1\ell}C_{T_1} + C_{2\ell}C_{T_2}$$

where

$$C_{T_1} = \frac{C_T}{C_1 + C_2K_T} \tag{4.3}$$

$$C_{T_2} = K_T\frac{C_T}{C_1 + C_2K_T}$$

where C_1, C_2 are the overall concentrations for water and oil species.

The partitioning coefficient of tracer i as a function of reservoir salinity is modeled using a linear relationship as

$$K_{T_i} = K_{T_{i,Sref}}\left(1 + TKS_i\left(C_{51} - C_{51,ref}\right)\right) \tag{4.4}$$

where C_{51} is the concentration of anions in aqueous phase and $C_{51,ref}$ is the electrolytes concentration in chloride equivalent (eq/l) at a reference condition (initial electrolyte concentrations). TKS_i is a constant input parameter in $(eq/l)^{-1}$ and $K_{Ti,Sref}$ is the partitioning coefficient at the reference salinity of $C_{51,ref}$ in eq/l.

UTCHEM also has the capability of modeling tracer partitioning coefficients as a function of reservoir temperature. Partitioning coefficient for tracer i as a function of temperature is given by a linear function as:

$$K_{T_i} = K_{T_{i,Tref}}\left(1 + TK_i\left(T - T_{ref}\right)\right) \quad \text{for tracer i} \tag{4.5}$$

where the temperatures are in $^\circ F$ and $K_{Ti,Tref}$ is the partitioning coefficient of tracer i at reference temperature, T_{ref}. TK_i is a constant input parameter in $(^\circ F)^{-1}$.

4.3.2 Gas/Oil

The partitioning coefficient for a gas/oil tracer is defined as

$$K_T = \frac{C_{T_2}}{C_{T_8}} \tag{4.6}$$

and the phase concentration for the tracer is computed using the tracer material balance equation as

$$C_{T_\ell} = C_{8\ell}C_{T_8} + C_{2\ell}C_{T_2}$$

where

$$C_{T_8} = \frac{C_T}{C_8 + C_2K_T} \qquad \ell = 2 \text{ and } 4 \tag{4.7}$$

$$C_{T_2} = K_T\frac{C_T}{C_8 + C_2K_T}$$

where C_8, C_2 are the overall concentrations for gas and oil species.

UTCHEM has the capability of modeling gas/oil tracer partitioning coefficients as a function of reservoir temperature. Partitioning coefficient for tracers as a function of temperature is given by a linear function as:

$$K_{T_i} = K_{T_{i,ref}}\left[1 + TK_i\left(T - T_{ref}\right)\right] \quad \text{for tracer i} \tag{4.8}$$

where the temperatures are in $^\circ F$ and $K_{T_{i,ref}}$ is the partitioning coefficient of tracer i at reference temperature (T_{ref}) and TK_i is a constant input parameter in $(^\circ F)^{-1}$.

4.4 Radioactive Decay

Radioactive decay can be used for any type of tracer (oil, water, gas) as

$$\frac{dC_T}{dt} = -\lambda C_T \tag{4.9}$$

$$\lambda = -\frac{\ln(0.5)}{t_{1/2}} \tag{4.10}$$

where λ is a constant input radioactive decay coefficient in $(days)^{-1}$ and $t_{1/2}$ is the half life of the tracer. The above equation is solved for decayed tracer concentration once the overall tracer concentration (C_T) is solved for as

$$(C_T)_{decay} = C_T(1 - \lambda\Delta t) \tag{4.11}$$

where Δt is the time step size in days.

4.5 Adsorption

The tracer adsorption for any type of tracer is assumed to be linear and can be modeled using an input retardation factor parameter (D_s) as

$$D_s = \frac{\bar{C}_T}{C_{T\ell}} = \frac{(1-\phi)\rho_r a_T}{\phi\rho_\ell C_{T\ell}} \qquad \ell = 1 \text{ or } 4 \tag{4.12}$$

where a_T is the mass of adsorbed tracer divided by the mass of rock. ρ_r and ρ_ℓ are the rock and water (ℓ = 1) or gas phase (ℓ = 4) densities. $\bar{C}_T$ is the adsorbed tracer concentration. The adsorption is applied to total tracer flux (convective and dispersive) and modeled as

$$(V_t)_{ret.} = \frac{u}{\phi S_\ell}\left(\frac{1}{1+D_s}\right) \tag{4.13}$$

where u is the Darcy flux in ft/d and ϕ is the porosity.

4.6 Reaction

Hydrolysis of an ester to form an alcohol is assumed to be irreversible and of first order. The reaction of an acetate as an example is:

1 $CH_3COO[C_nH_{2n+1}]$ + **1** H_2O --------> **1** $C_nH_{2n+1}[OH]$ + **1** $C_2H_4O_2$

Acetate Water Alcohol Acetic Acid

where 1 mole of acetate (e.g., component 10) generates one mole of product alcohol (e.g., component 11). The reaction is modeled as

$$\frac{\partial C_{10}}{\partial t} = -K_h C_{10}$$

and (4.14)

$$\frac{\partial C_{11}}{\partial t} = K_h C_{10}$$

where K_h is an input reaction rate in day^{-1}. UTCHEM has the capability of modeling the tracer reaction rate as a function of reservoir temperature. The rate of hydrolysis of tracer as a function of reservoir temperature is given by:

$$K_{h_i} = K_{h_i,ref} \exp\left[HK_i \left(\frac{1}{T} - \frac{1}{T_{ref}} \right) \right] \quad \text{for tracer i} \tag{4.15}$$

where the temperature is in $^\circ$K and $K_{h_i,ref}$ is the rate of tracer hydrolysis at reference temperature (T_{ref}) and HK_i is a constant input parameter in ($^\circ$K)$^{-1}$.

4.7 Capacitance

The capacitance model is based on a generalized Coats-Smith model (Smith *et al.*, 1988) and is applied to water/oil tracer components and gas tracer components (κ). The model is unsteady state, therefore the flowing and dendritic saturations can change in each time step. The phase saturations and phase composition from the overall species concentration and phase flash are the flowing saturation (S_ℓ^f) and phase concentrations ($C_{\kappa\ell}^f$) in the capacitance model in UTCHEM. The mass transfer between the flowing and dendritic fraction is given by

$$\frac{\partial}{\partial t}\left(S_\ell^d C_{\kappa\ell}^d \right) = M_{\kappa\ell}\left(C_{\kappa\ell}^f - C_{\kappa\ell}^d \right) \tag{4.16}$$

The dendritic saturation is calculated from:

$$S_\ell^d = \left(1 - F_\ell\right) S_\ell \tag{4.17}$$

where F_ℓ is the flowing fraction for phase ℓ defined as

$$F_\ell = \frac{S_\ell^f}{S_\ell} = F_{\ell 0} + \left(F_{\ell 1} - F_{\ell 0}\right) f_\ell \tag{4.18}$$

where the flowing fraction (F_ℓ) is assumed to be a linear function of fractional flow (f_ℓ). The intercepts of the flowing fraction line versus fractional flow at the residual saturation of nonwetting phase ($f_1 = 0.0$) and wetting phase ($f_1 = 1.0$) are $F_{\ell 0}$ and $F_{\ell 1}$ and are input parameters. The product of dendritic saturation (S_ℓ^d) and dendritic phase composition ($C_{\kappa\ell}^d$) is

$$\left(C_{\kappa\ell}^d S_\ell^d \right)^{n+1} = \left(C_{\kappa\ell}^d S_\ell \right)^n + \Delta t M_\kappa \left(C_{\kappa\ell}^f - C_{\kappa\ell}^d \right)^n \tag{4.19}$$

where M_κ is the input mass transfer coefficient in (day)$^{-1}$ and the dendritic phase composition ($C_{\kappa\ell}^d$) is calculated from

$$C_{\kappa\ell}^d = \frac{C_{\kappa\ell}^d S_\ell^d}{S_\ell^d} \tag{4.20}$$

The flowing phase saturations are then determined from

$$S_\ell^f = F_\ell S_\ell \tag{4.21}$$

and the total flowing tracer concentrations are computed as

$$C_\kappa^f = \sum_{\ell=1}^{n_p} \left(C_{\kappa\ell}^f \, S_\ell^f \right) = C_\kappa - \sum_{\ell=1}^{n_p} \left(C_{\kappa\ell}^d \, S_\ell^d \right) \tag{4.22}$$

Section 5
Dual Porosity Model

5.1 Introduction

In most naturally fractured reservoirs, fractures tend to be developed in a way that makes the fractures interconnected and the bulk reservoir rock isolated into blocks. Fractured reservoirs can thus be considered as blocks of porous rock matrix surrounded by a network of communicating channels (fractures). The rock matrix generally has high bulk volume and high porosity, but very low permeability. In contrast, the fractures occupy very small volume, but have high permeability. The dual porosity model assumes that there are two flow systems coexisting in a fractured reservoir – an interconnected fracture system and a disjoint matrix system. In the dual porosity model, continuity equations are solved for the two systems using conventional methods, while the mass transfer between the two systems is calculated by so-called transfer functions that characterize flow between matrix blocks and fractures. By dividing the matrix system into subgrids at each fracture node, transient flow of fluid in the matrix and between matrix and fractures can be studied. For simplicity, matrix blocks are often assumed to be regularly shaped. In this implementation, we use parallelepiped matrix blocks to handle vertical fractures and slabs for horizontal fractures.

This section presents results of a project to implement dual porosity behavior for tracer studies in UTCHEM, a chemical flood simulator developed at the University of Texas at Austin. Two approaches were implemented. In the first, a capacitance model already existing in UTCHEM was made to mimic dual porosity behavior by setting capacitance parameters to equivalent dual porosity parameters. This approach is equivalent to a dual porosity model with no subgridding. The second approach involved adapting a subgridding approach developed by J. Chen [1993] for counter current imbibition in fractured reservoirs. Test runs and comparisons with the SWIFT II simulator (Reeves *et al.*, 1986) are also made.

5.2 Capacitance Model

Dispersion into matrix blocks from surrounding fractures is typically calculated by assuming that the tracer concentration in the fractures is uniform within a given volume of reservoir rock. This assumption results in the following equation for diffusion of a single tracer in a single fluid phase:

$$\frac{\partial\left(\phi^m \bar{C}^m\right)}{\partial t} = \phi^m K^m S_A \left[\frac{\partial C^m}{\partial n}\right]_f \tag{5.1}$$

where

ϕ^m = matrix porosity, fraction

$\bar{C}^m$ = average tracer concentration in matrix block, m/L^3

K^m = tracer diffusion coefficient in matrix, L^2/t

S_A = matrix block surface area per unit bulk volume of reservoir, L^{-1}

$\left[\frac{\partial C^m}{\partial n}\right]_f$ = tracer concentration gradient normal to matrix block surface, m/L^4

If transient behavior is ignored, Eq. 5.1 may be approximated by

$$\frac{\partial\left(\bar{C}^m\right)}{\partial t} = \sigma K^m \left(C^f - \bar{C}^m\right) \tag{5.2}$$

where σ is a shape factor to account for matrix block geometry and number of matrix blocks per unit reservoir volume, and C^f is the tracer concentration in the fracture. Note that the shape factor has units of L^{-2}. Kazemi *et al.* [1976] recommended a shape factor for cubic matrix blocks of

$$\sigma = \frac{4nN}{L^2} \tag{5.3}$$

where n is the number of matrix blocks per unit bulk volume of reservoir and N is the "dimensionality" of the fracture set. A good discussion of shape factors can be found in M. M. Chen [1993].

UTCHEM includes a "capacitance" model that treats diffusive transfer in a similar manner. In the capacitance model a fluid phase is divided into two fractions: a flowing fraction (which is analogous to the fracture system in a dual porosity model) and a dendritic fraction (which is analogous to the matrix system). Since matrix and fracture porosities are both based on total reservoir bulk volume, the flowing fraction, F, and the dendritic fraction, 1–F, are equivalent to:

$$F = \frac{\phi^f}{\phi^m + \phi^f} = \frac{S^f}{S} \tag{5.4}$$

$$1 - F = \frac{\phi^m}{\phi^m + \phi^f} = \frac{S^d}{S} \tag{5.5}$$

For single phase flow, of course, S = 1. Total porosity is simply

$$\phi = \phi^m + \phi^f \tag{5.6}$$

In the capacitance model, mass transfer from the flowing to dendritic fractions is calculated by

$$\frac{\partial\left[(1-F)C^d\right]}{\partial t} = M\left(C^f - C^d\right) \tag{5.7}$$

or for a fixed dendritic fraction:

$$\frac{\partial\left(C^d\right)}{\partial t} = \frac{M}{1-F}\left(C^f - C^d\right) \tag{5.8}$$

where C^d is the tracer concentration in the dendritic fraction, C^f is the tracer concentration in the flowing fraction, and M is the capacitance mass transfer coefficient. The capacitance model can thus be made to calculate dual porosity behavior using the equivalents given in Table 5.1.

Figure 5.1 shows comparisons of capacitance runs in UTCHEM compared to UTDUAL, a dual porosity simulator developed at the University of Texas at Austin. Although UTDUAL has the capability of subgridding matrix blocks (which would yield more accurate results), these comparisons were made with no subgridding. For these comparisons, UTDUAL was modified slightly to account for tracer diffusion in a manner similar to counter current water imbibition. Data used to generate Fig. 5.1 are given in Table 5.2. Note the high degree of agreement. In fact, for a mass transfer coefficient of 10^{-5} sec^{-1}, the two curves are indistinguishable on the graph.

5.3 Subgridding

Due to the relatively low permeability in matrix blocks, viscous convection of phases is very slow and is ignored in this formulation. Molecular diffusion of tracer becomes the dominant process flow within the matrix. The equation for tracer diffusion into the matrix can be simplified into the following equation:

$$\frac{\partial}{\partial t}\left(\phi^m C^m\right) = \nabla \cdot \left(\phi^m \bar{\bar{K}}^m \cdot \nabla C^m\right) - \lambda \phi^m C^m \tag{5.9}$$

where λ is the radioactive decay constant of the tracer.

Parallelepiped matrix blocks are assumed for the subgridding. In the horizontal direction (j-index) the matrix is subdivided into N_{sub} concentric grids. In the vertical direction (k-index), the matrix is sliced into M_{sub} slabs. Figure 5.2 shows the discretization of a single matrix block. The advantage of subgridding the matrix this way is that many types of fracture systems can be described. By setting M_{sub}=1 and the vertical diffusion coefficient to zero, a vertical fracture network can be simulated. If N_{sub}=1 and the horizontal diffusion coefficient is equal to zero, then horizontal fractures can be simulated. A combination of subgridding in these two directions can be used to simulate a 3D fracture system. When M_{sub}=1 and N_{sub}=1, the system reduces to the capacitance (no subgridding) model.

The volume fraction of each subgrid is an input value with the property:

$$\sum_{j=1}^{N_{sub}} f_{jk} = 1 \qquad k = 1,...,M_{sub} \tag{5.10}$$

The volume fraction of the j^{th} ring and k^{th} layer subgrid is:

$$f_{jk} = \frac{\left(L_{xjk}L_{yjk} - L_{xj-1k}L_{yj-1k}\right)h_k}{V_{bk}^m} \tag{5.11}$$

where V_{bk}^m is the bulk volume of the k^{th} layer of the matrix, L_{xjk} and L_{yjk} are the outer dimensions of the subgrid, h_k is the thickness of the k^{th} layer, and N_{sub} is the number of the subgrids in the horizontal direction (Fig. 5.2).

From Eqs. 5.10 and 5.11, the outer dimensions for each subgrid are calculated by:

$$L_{xjk} = L_x\left[\sum_{i=1}^{j} f_{ik}\right]^{\frac{1}{2}} \qquad j = 1,...,N_{sub};\ \ k = 1,...,M_{sub} \tag{5.12}$$

$$L_{yjk} = L_y\left[\sum_{i=1}^{j} f_{ik}\right]^{\frac{1}{2}} \qquad j = 1,...,N_{sub};\ \ k = 1,...,M_{sub} \tag{5.13}$$

where L_x and L_y are the dimensions of the matrix block.

The dimensions of a matrix block can be different than the dimensions of a grid block. The mass transfer rate is simply calculated by multiplying the mass transfer rate of one representative matrix block by the number of matrix blocks per grid block.

Using one-point upstream weighting, the finite-difference form of Eq. 5.9 becomes

$$\phi^m\left[\left(C^m\right)^{n+1}-\left(C^m\right)^n\right] = \frac{\Delta t}{\Delta V^m_{jk}}\left[TV_{jk-\frac{1}{2}}\left(C^m\right)^n_{jk-1}+TH_{j-\frac{1}{2}k}\left(C^m\right)^n_{j-1k}+TC_{jk}\left(C^m\right)^n_{jk}\right.$$
$$\left.+TH_{j+\frac{1}{2}k}\left(C^m\right)^n_{j+1k}+TV_{jk+\frac{1}{2}}\left(C^m\right)^n_{jk+1}-\Delta V^m_{jk}\lambda\phi^m\left(C^m\right)^n_{jk}\right] \tag{5.14}$$

where ΔV^m_{jk} is the volume of the j^{th} ring and the k^{th} layer, and TV and TH are the transmissibilities in the vertical and horizontal directions, respectively:

$$TH_{j+\frac{1}{2}k}=\frac{L_{yjk}h_kK^m_{xy}}{L_{xj+1k}-L_{xjk}}+\frac{L_{xjk}h_kK^m_{xy}}{L_{yj+1k}-L_{yjk}} \tag{5.15}$$

$$TV_{jk+\frac{1}{2}}=\frac{f_{jk}L_xL_yK^m_z}{h_{jk+1}+h_{jk}} \tag{5.16}$$

and TC is calculated by:

$$TC_{jk}=-(TV_{jk-\frac{1}{2}}+TH_{j-\frac{1}{2}k}+TH_{j+\frac{1}{2}k}+TV_{jk+\frac{1}{2}}) \tag{5.17}$$

The boundary condition is

$$C^m_{jk}=C^f \qquad \begin{array}{l} j=N_{sub};\ k=1,...,M_{sub}\ \text{(sides)} \\ j=1,...,N_{sub};\ k=1 \text{ and } k=M_{sub}\ \text{(top and bottom)}\end{array} \tag{5.18}$$

5.4 Implementation

In this implementation the original 3D compositional code, UTCHEM, solves the pressure distributions and tracer concentrations in the fracture system. After solving the fracture system equations, the tracer concentration at each node is used as the boundary condition for the matrix at the same node. Only a single tracer in single phase flow is handled.

An additional subroutine, TDIFFU, is added to UTCHEM to do the matrix calculations. The methodology used for this implementation is described by J. Chen [1993] and Chen *et al*. [1994]. In this routine, the equations developed above are used to solve the tracer concentration distribution in the subgridded matrix system. Concentrations in the fracture are modified to account for mass transfer between the matrix and fracture.

Several other subroutines are also modified. Subroutine INOUT is extended to read in the parameters used to describe the subgridding system. The initial values of the matrix tracer concentration are also read in this routine. Subroutine TIME0 is modified to set the initial tracer concentrations in the matrix system. Calculations of the horizontal and vertical transmissibilities of the subgrids are added to the TRAN1 routine. Some output commands are added to subroutine OUTDT1. And, of course, the MAIN program is also modified to handle the new calculations. The distribution of tracer concentrations within the matrix are written to output file CAPP.

In order to minimize the code changes to the whole system, the control flag for the dual porosity option is the variable ICAP, which is also used to flag use of the capacitance model. A value of 2 is used to represent that the dual porosity model with subgridding is used.

5.5 Results

Several test runs were made with this implementation. The first test is a comparison of the capacitance model with the case of only one subgrid. A 1D linear reservoir 1000 ft long with 10 ft width and depth is simulated. Grid block size is 10x10x10 ft^3. Matrix blocks are also 10x10x10 ft^3. There are thus 100 gridblocks in the x–direction. Fracture and matrix porosities are 0.01 and 0.19, respectively. Permeability in the fractures is 1000 md and longitudinal dispersivity is 1.0 ft. Fluid injection rate is 0.5 ft^3/day. Figure 5.3 shows results for mass transfer coefficients of 10^{-5}, 10^{-8} and 10^{-9} sec^{-1}. Results show that the dual porosity model reduces to the capacitance model when there is no subgridding.

The second comparison is between UTCHEM and UTDUAL (J. Chen, 1993). The reservoir and fluid conditions are the same as the first set of runs, except that a diffusion coefficient (K^m) of $4.32x10^{-3}$ ft^2/day was used. The subgrid numbers compared are 1, 2, 4, and 8. One more run with 16 subgrids was run on UTDUAL which showed that the curve converges with only 8 subgrids. Figure 5.4 shows the results. Figure 5.5 shows agreement between UTCHEM and UTDUAL. The pore volumes reported in these figures refer to the total (fracture + matrix) pore volumes. The UTCHEM output files, however, give the fracture pore volumes only.

The third case run was a 2D case. The reservoir is 100x100x10 ft^3 and with grid number of 10x10x1. Each grid size is 10x10x10 ft^3. Fluid is injected in one corner and produced from an opposite corner, simulating a quarter of a five-spot pattern. All other properties are the same as the second set of runs. The number of matrix subgrids ranges from 1 to 8. Figure 5.6 shows the result. Note that the solid line is the overlap of the two curves of the capacitance model and the dual porosity model with one subgrid.

It is expected that increasing the number of subgrids will increase computing time. However, the amount of additional time required for additional subgridding is very small in this implementation. Figures 5.7 and 5.8 show CPU times for the runs made above. Note that only slightly more time was needed, even with 8 subgrids.

The last comparison is with SWIFT II (Reeves *et al*., 1986), a code developed for contaminant transport studies. The case simulated is the transport of a decaying radionuclide in a fractured porous medium. A thin fracture is situated within a saturated porous rock matrix. Both the fracture and matrix are semi-infinite in extent. The radionuclide is convected and dispersed through the fracture with constant velocity and is diffused into the rock matrix. The fracture aperture is 10^{-4} m, matrix porosity is 0.01, matrix tortuosity is 0.1, fracture dispersivity is 0.5 m, molecular diffusion coefficient in water is $1.6x10^{-5}$ cm^2/sec, radionuclide decay constant is 0.0561 yr^{-1}, and fracture velocity is 0.01 m/day. Note that the value of the dispersivity in UTCHEM (K^m) is equivalent to the product of tortuosity times the molecular diffusion coefficient in water used by SWIFT II. A constant tracer concentration boundary condition on the source side of the system is required to match an analytical solution to this problem (Tang *et al.,* 1981). UTCHEM was modified slightly to handle this boundary condition. Variable grid blocks are used in both fracture and matrix. A 10,000-day period was simulated. Figure 5.9 shows the radionuclide concentration in the fracture. Note that the simulated results and the analytical solution by Tang *et al*. match very well. Figure 5.10 shows the radionuclide concentration in the matrix 1.5 m from the injection point at 10,000 days. The result also matches the analytical solution. This problem is described in detail in the SWIFT II manual (Reeves *et al.*, 1986).

5.6 Conclusions

From the above test runs and comparisons with other simulators, the following conclusions are made:

1. A dual porosity formulation to model tracer flow in fractured reservoirs has been implemented in the UTCHEM chemical flooding simulator. Good matches are obtained compared with other simulators.

2. Different fracture systems can be modeled by the simulator. These include vertical fractures, horizontal fractures, and combinations of the two.

3. Computer time required to refine the matrix system does not appreciably increase for reasonable numbers of subgrids.

4. The dual porosity model reduces to the capacitance model when the number of subgrids is equal to one.

5.7 Nomenclature

C^d = tracer concentration in dendritic fraction, m/L^3

C^f = tracer concentration in flowing fraction or fracture system, m/L^3

C^m = matrix block tracer concentration, m/L^3

$\bar{C}^m$ = average tracer concentration in matrix block, m/L^3

f_{jk} = volume fraction of subgrid j, k, dimensionless

F = flowing fraction $\left(\frac{S^f}{S}\right)$, dimensionless

$1-F$ = dendritic fraction $\left(\frac{S^d}{S}\right)$, dimensionless

h_k = thickness of k^{th} layer, L

K^m = tracer diffusion coefficient in matrix, L^2/t

K^m_{xy} = tracer diffusion coefficient in matrix in horizontal direction, L^2/t

K^m_z = tracer diffusion coefficient in matrix in vertical direction, L^2/t

L_x, L_y = matrix dimensions, L

L_{xjk}, L_{yjk} = subgrid dimensions in x and y directions, L

M = capacitance mass transfer coefficient, t^{-1}

M_{sub} = number of subgrids in vertical direction (layers)

n = number of matrix blocks per unit bulk volume of reservoir

N = dimensionality of fracture set

N_{sub} = number of subgrids in horizontal direction (rings)

S_A = matrix block surface area per unit bulk volume of reservoir, L^{-1}

S^d = dendritic saturation, dimensionless

S^f = flowing saturation, dimensionless

TC = sum of transmissibilities in the vertical and horizontal directions, L^3/t

TH = transmissibility in the horizontal direction, L^3/t

TV = transmissibility in the vertical direction, L^3/t

t = time, t

V_{bk}^m = bulk volume of layer k of the matrix, L^{-3}

ΔV_{jk}^m = volume of the j^{th} ring and the k^{th} layer of matrix subgrids, L^{-3}

ϕ = total porosity, fraction

ϕ^f = fracture porosity, fraction

ϕ^m = matrix porosity, fraction

λ = radioactive decay constant, t^{-1}

σ = shape factor, L^{-2}

$\left[\frac{\partial C^m}{\partial n}\right]_f$ = tracer concentration gradient normal to matrix block surface, m/L^4

5.8 Tables and Figures

Table 5.1. Equivalence Between Capacitance and Dual Porosity Models

Capacitance Model	Dual Porosity Model
Porosity (ϕ)	$\phi^m + \phi^f$
Flowing fraction (F)	$\frac{\phi^f}{\phi^m + \phi^f}$
Dendritic fraction (1– F)	$\frac{\phi^m}{\phi^m + \phi^f}$
Flowing fraction tracer concentration (C^f)	C^f
Dendritic fraction tracer concentration (C^d)	$\overline{C}^m$
Mass transfer coefficient (M)	$\sigma K^m \frac{\phi^m}{\phi^m + \phi^f}$

Table 5.2. Input Data for the Comparisons of Capacitance Model in UTCHEM to Dual Porosity Model in UTDUAL

System size	100x10x10	ft
Fluid injection rate	0.5	ft^3/day
Capacitance Model		
Total porosity	0.20	
Flowing fraction	0.05	
Dendritic fraction	0.95	
Mass transfer coef.	10^{-5}	sec^{-1}
	10^{-8}	sec^{-1}
	10^{-9}	sec^{-1}
Dual Porosity Model		
Fracture porosity	0.01	
Matrix porosity	0.19	
Shape factor	0.08	ft^{-2}
Matrix block size	10x10x10	ft
Diffusion coef.	10.8	ft^2/day
	$1.08x10^{-2}$	ft^2/day
	$1.08x10^{-3}$	ft^2/day

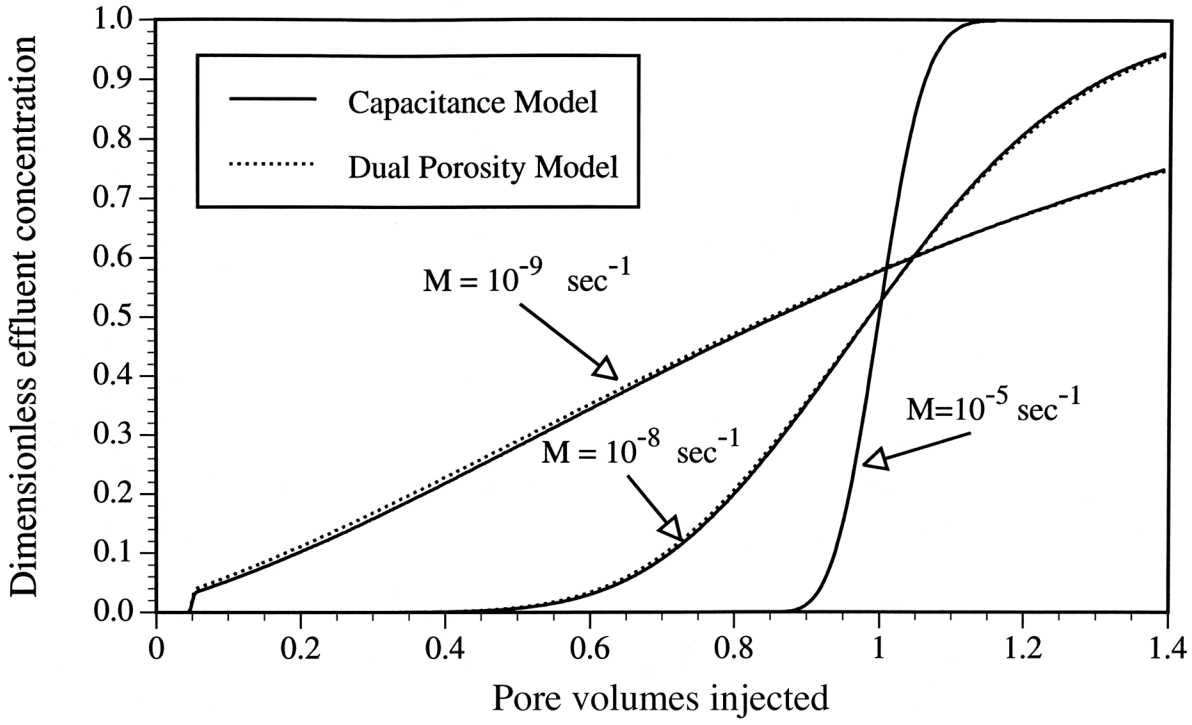

Figure 5.1. Comparison of capacitance model (UTCHEM) to equivalent dual porosity model (UTDUAL) results.

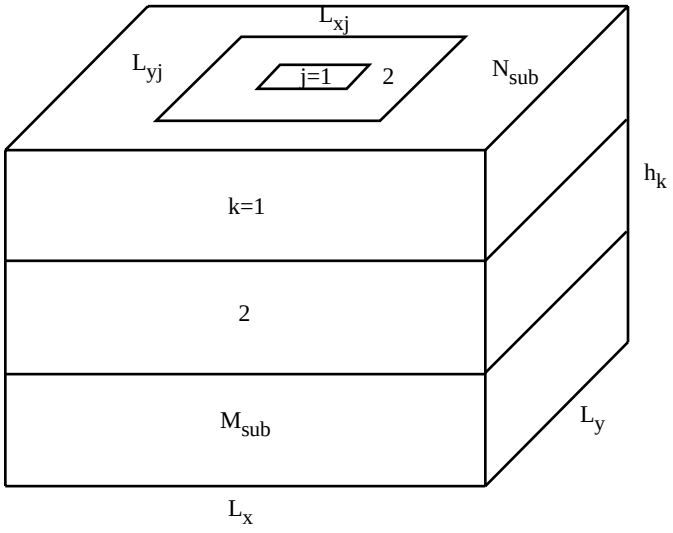

Figure 5.2. Schematic of matrix block subgrids.

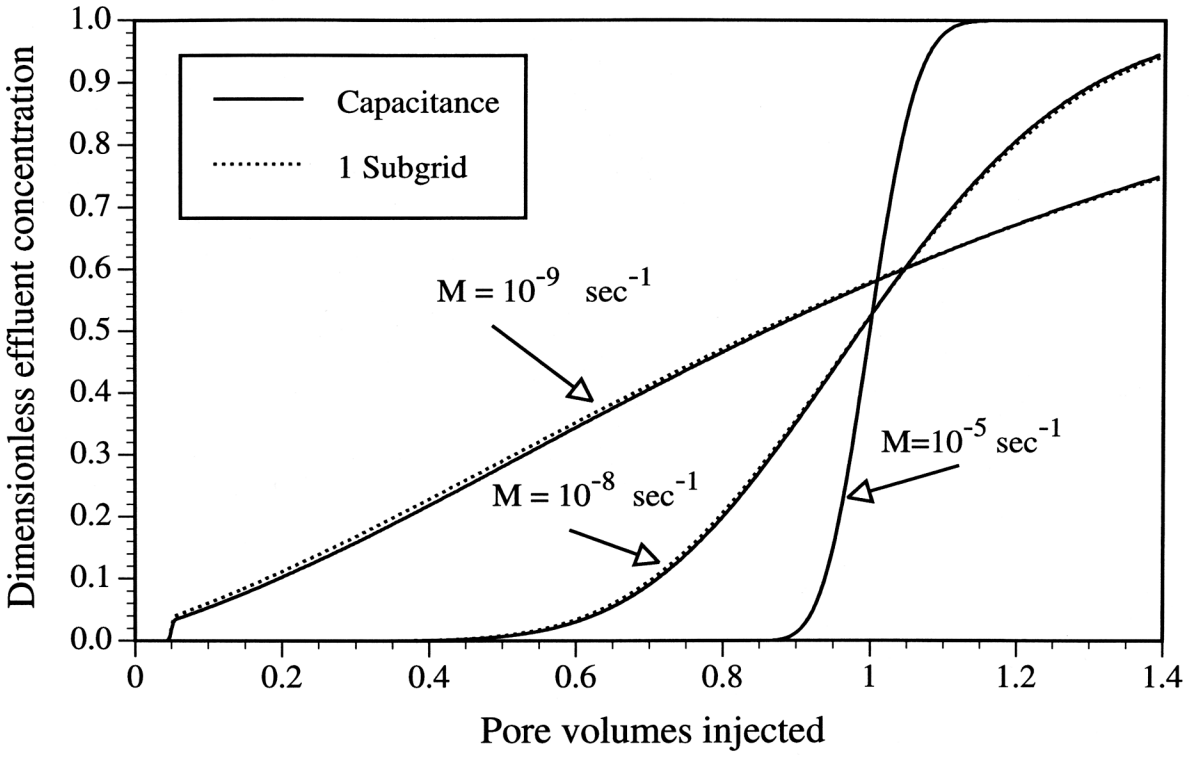

Figure 5.3. Comparison of capacitance model vs. subgrid model in UTCHEM.

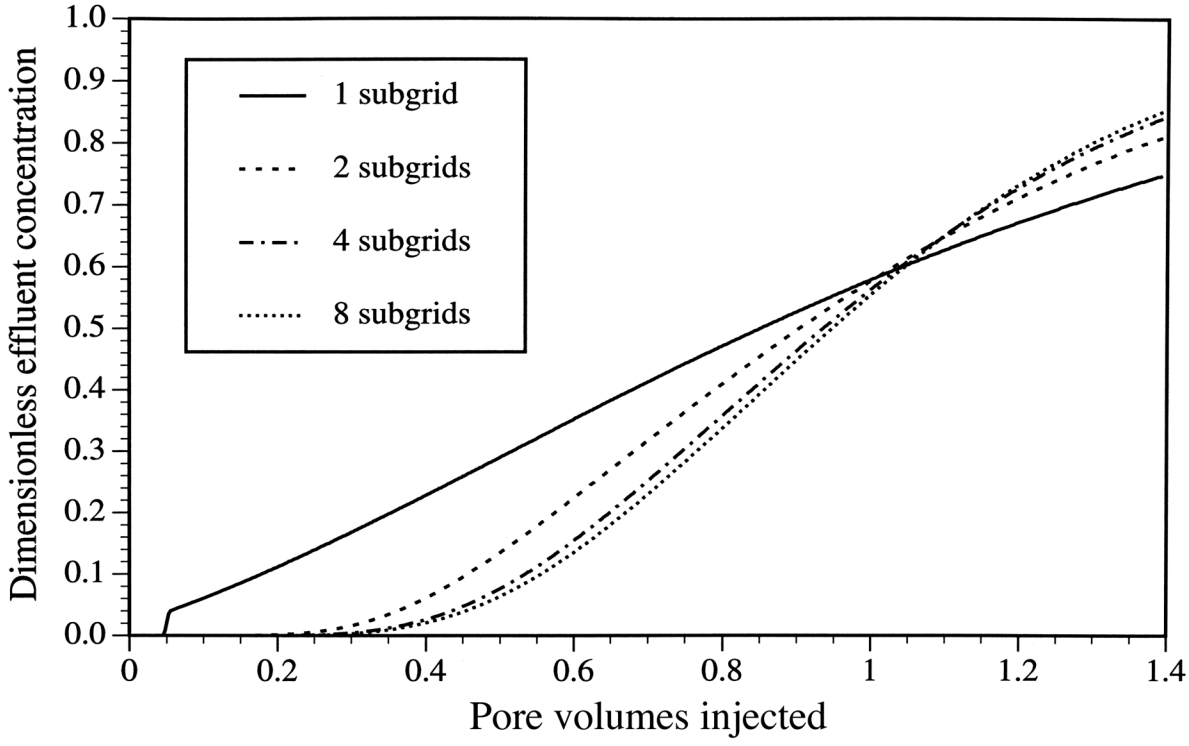

Figure 5.4. Subgrid refinement studies with UTCHEM, $K^m = 3.243 \times 10^{-2}$ ft^2/day.

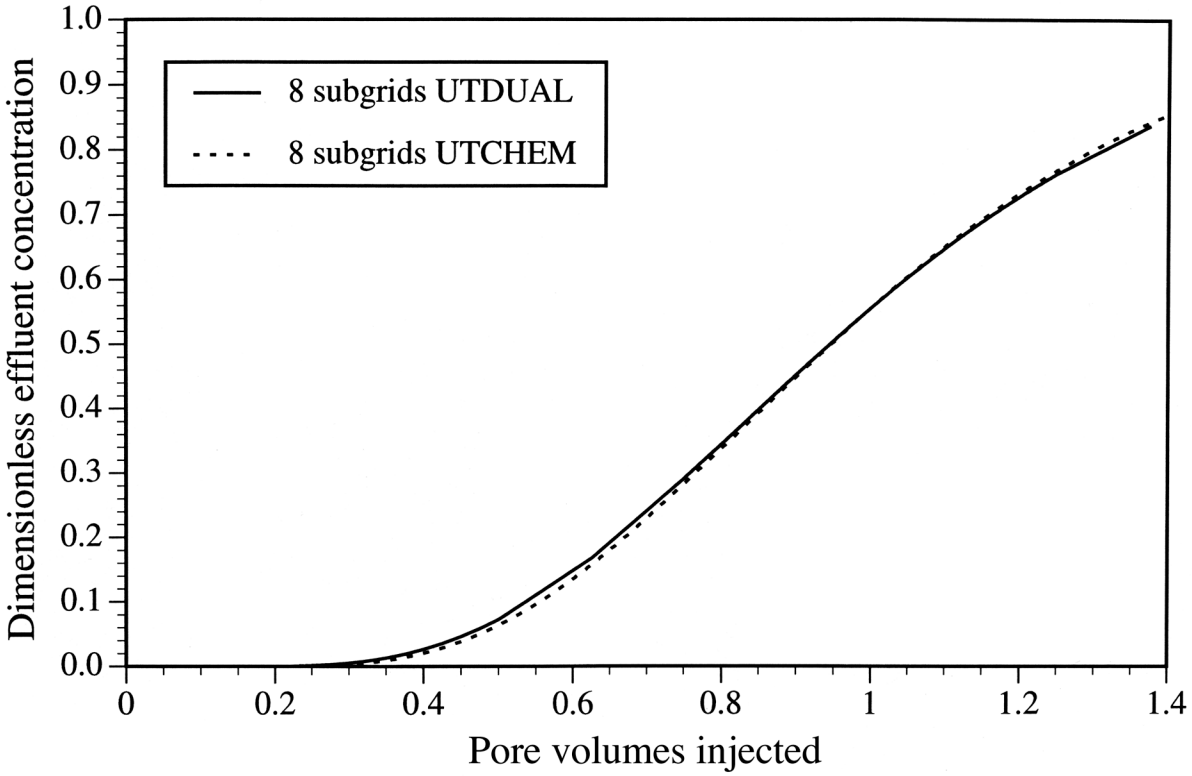

Figure 5.5. Comparison of UTCHEM and UTDUAL subgridding.

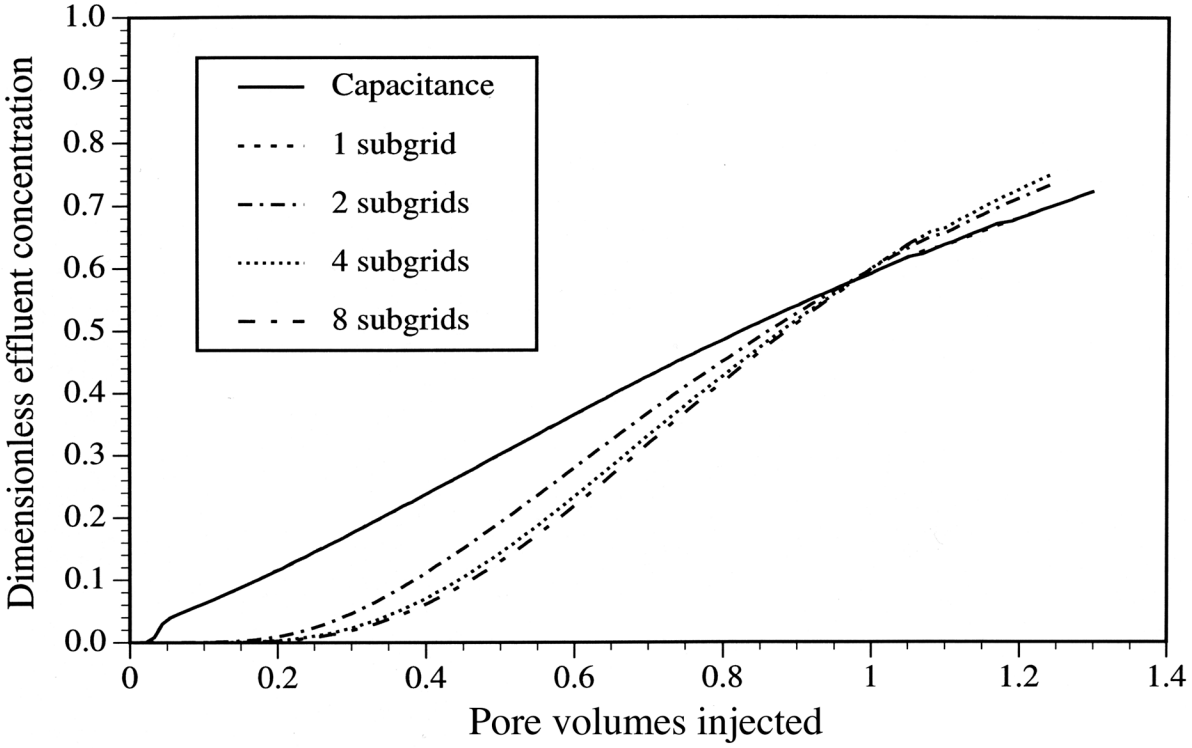

Figure 5.6. 2D subgrid refinement studies with UTCHEM.

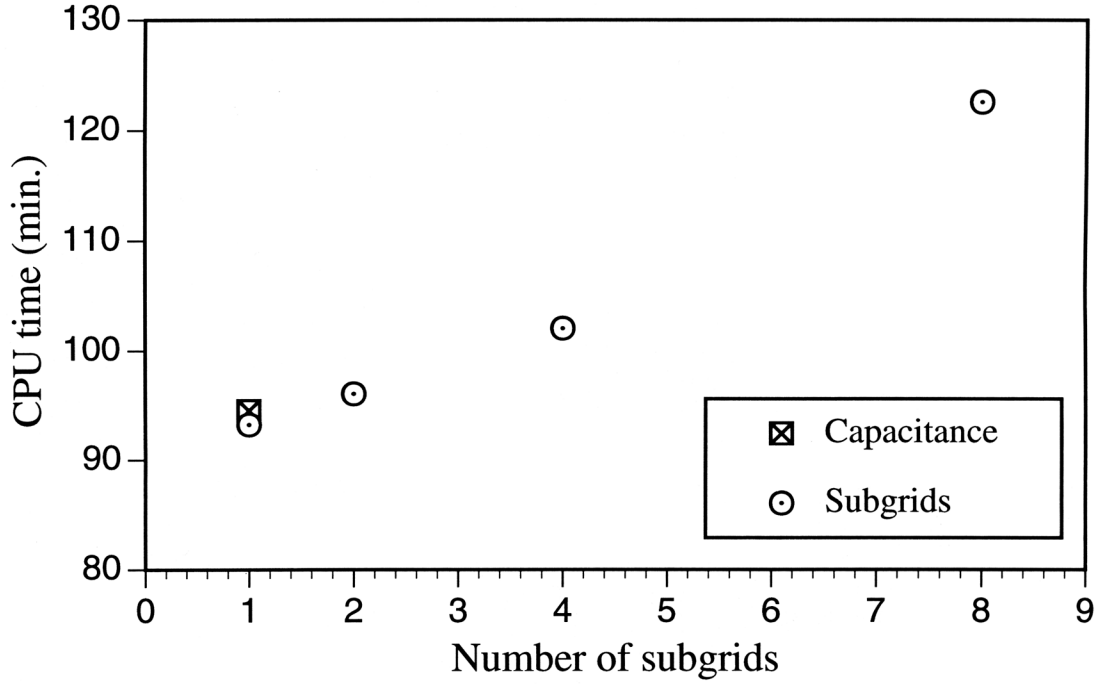

Figure 5.7. Comparison of execution time with different numbers of subgrids, 1D case.

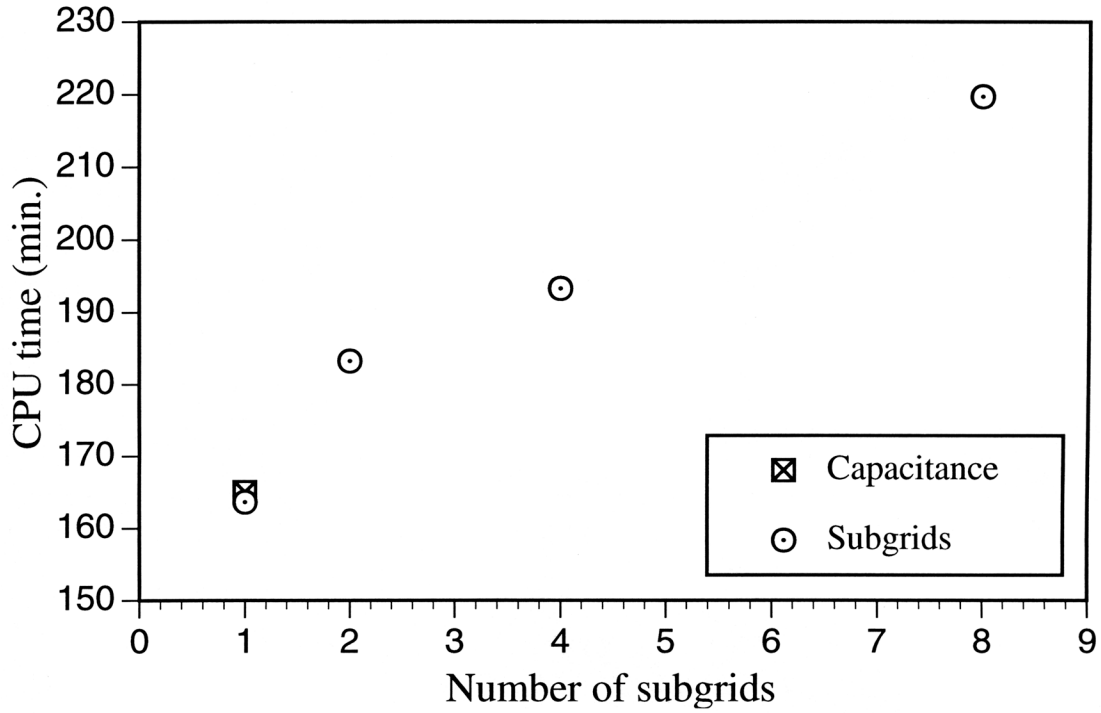

Figure 5.8. Comparison of execution time with different numbers of subgrids, 2D case.

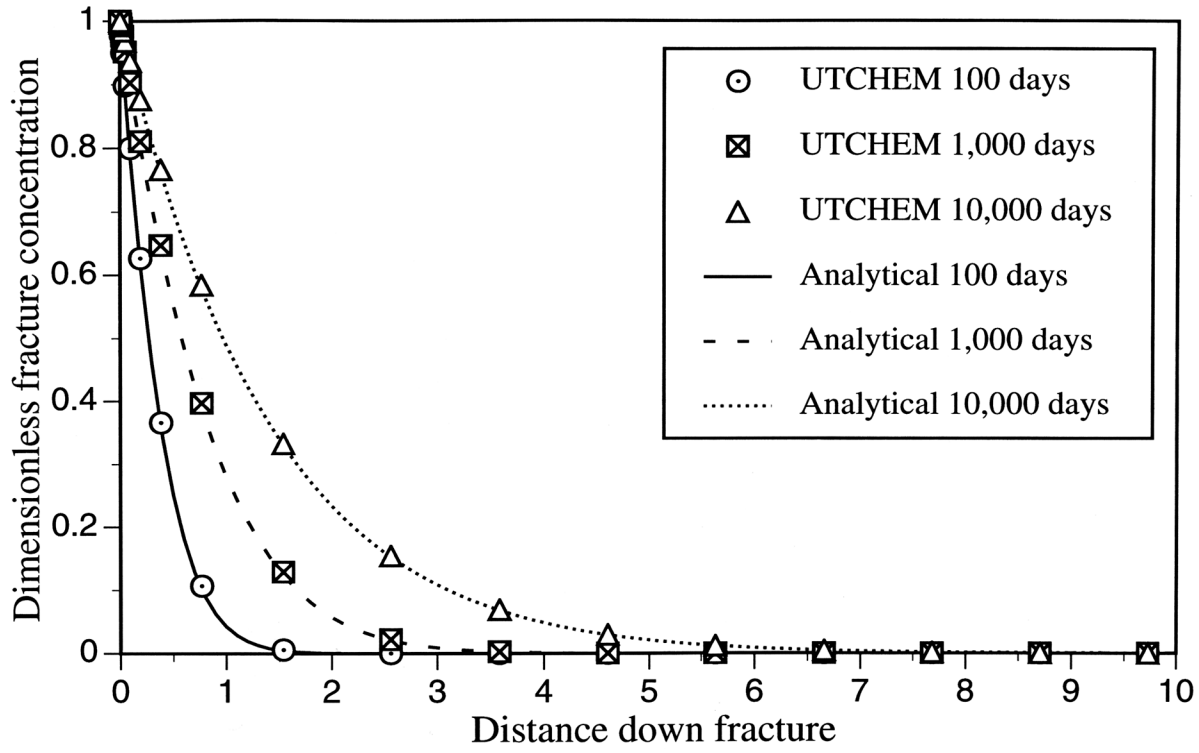

Figure 5.9. Comparison of simulated results vs. analytical solution (Tang *et al.*, 1981) for radionuclide concentration in the fracture.

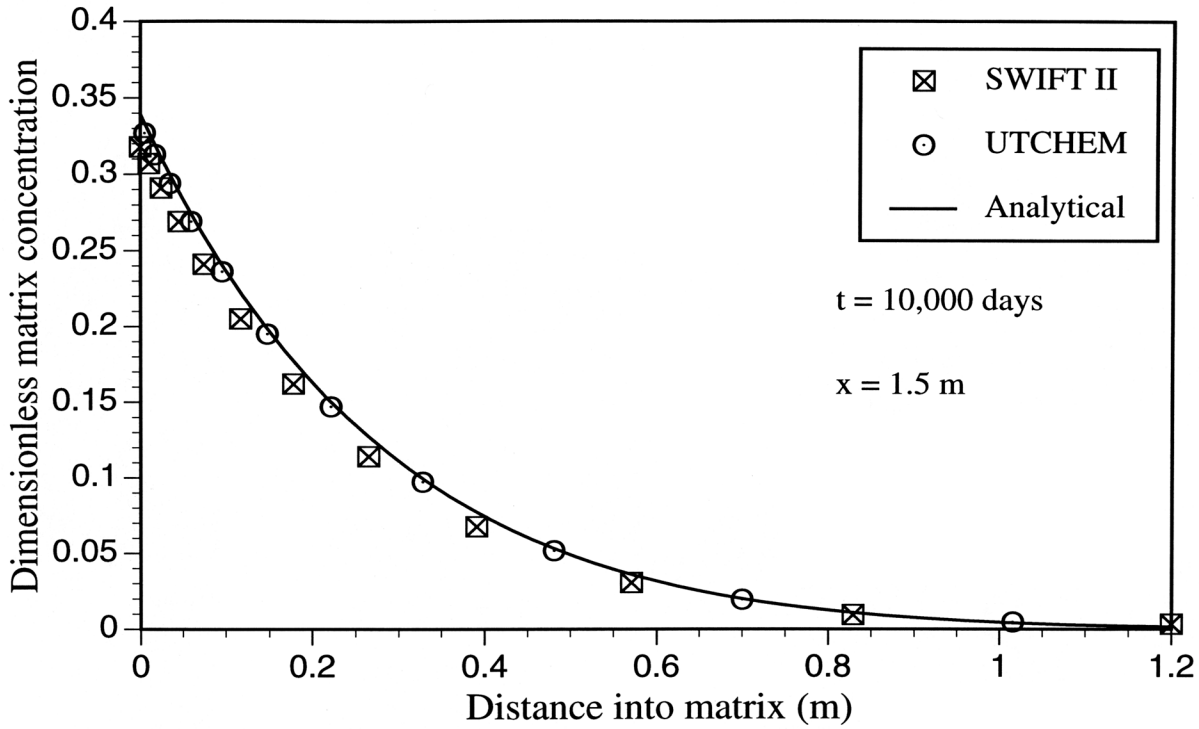

Figure 5.10. Comparison of simulated results vs. analytical solution (Tang *et al.*, 1981) and SWIFT II (Reeves *et al.*, 1986) for radionuclide concentration in the matrix.

Section 6
UTCHEM Model of Gel Treatment

6.1 Introduction

This section is based on the work done by Kim [1995].

6.2 Gel Conformance Treatments

The operational aspect of a gel treatment includes the following :

- Zonal isolation
- Types of gel treatments
- Shut-in time
- Gel injection rate
- Amount of gelant

The types of gel treatments are 1) simultaneous injection of polymer and crosslinker into the reservoir, 2) alternate injection of polymer and crosslinker slugs, and 3) injection of pre-gelled fluid into the reservoir. The type of gel treatment selected influences the placement of the gel in the reservoir. In this study, the simultaneous mode of injection of polymer and crosslinker was modeled.

The shut-in time allowed after injection, before the well is put back on production, is critical to the success of a gel job. If the gel does not reach most of its strength, its efficacy in plugging the high-permeability layer will suffer.

The injection rate determines the rate of shearing of the polymer and gel as well as the injection pressure. The injection rate should be such that the wellbore pressure does not exceed the fracture pressure of the rock matrix.

The amount of gelants injected determines the depth of penetration of the gel into the formation. The amount injected must ensure adequate plugging of the high-permeability, watered-out zone.

Zonal isolation is used to selectively treat the problem zone. In some wells, improper well completion or casing damage may lead to mechanical difficulties in achieving zonal isolation. In this work, gel treatments were simulated with and without zonal isolation to demonstrate the effectiveness of zonal isolation.

The polymer-gel system chosen for a particular treatment will depend on its compatibility with the reservoir and operational conditions. The properties considered when choosing a particular system are

- Viscosity
- Gelation time
- Permeability reduction
- Thermal and mechanical stability
- Mechanical strength
- Safety

Viscosity of the gel and polymer determines the wellbore pressure during injection. Very high viscosities may cause the wellbore pressure to exceed the fracture pressure of the reservoir.

Gelation time depends on the kinetics of gel formation and influences the injection rate and shut-in time used during the treatment. Ideally, the gelation time should allow proper placement of the gel before full gel strength develops.

The permeability reduction caused by the gel in the porous medium is an indicator of its ability to modify the flow patterns in the reservoir. In near-wellbore treatments, the gel should be able to plug the high water-cut zones.

The ultimate mechanical strength developed by a gel is a measure of the pressure it can withstand before breaking down. The gel should have enough mechanical strength to remain in place when subjected to normal drawdown during production.

Safety of the gel, polymer and crosslinker may ultimately determine its usage. Gel components need to be safe for handling and storage and should pose no risk to the environment. The application of some toxic gels may be limited or restricted by the environmental concerns in certain locations. Studies of environmentally benign gels that do not use any toxic materials as a gel component are active.

It is important to characterize the reservoir in which the gel is ultimately going to be placed. Some reservoir characteristics that have a significant impact on gel treatment success are

- Permeability contrast
- Vertical communication
- Rock properties such as clay content
- Salinity
- Temperature

The permeability contrast between the layers influences the relative depth of penetration in the layers. A high permeability contrast mitigates the damage done to the oil-producing low-permeability zone.

Crossflow between the layers leads to mixing of fluids between the layers. This can cause some penetration of low-permeability layers even during selective treatments. During post-gel treatment production, crossflow may cause the water to bypass the plugged zone and be produced.

The clay content and the cation exchange capacity of the clays can have a significant impact on crosslinker propagation. Experiments indicate that a significant portion of injected cations like chromium may be retained on the clays and hence are not available for gelation. Salinity influences polymer and gel viscosities, while the temperature of the reservoir affects the rate of gelation and the stability of the gel for an extended period of time.

The gel properties modeled in UTCHEM include

- effect of gel on aqueous-phase viscosity,
- gel retention on matrix, and
- aqueous phase permeability reduction.

6.3 Gel Viscosity

The viscosity of an aqueous solution containing gel is modeled using the Flory-Huggins equation with additional terms for gel (Thurston *et al.*, 1987).

$$\mu_1 = \mu_w\left[1+\left(A_{p1}\,C_{4,1}+A_{p2}\,C_{4,1}^{\,2}+A_{p3}\,C_{4,1}^{\,3}\right)C_{SEP}^{S_p}+A_{g1}\,C_{15,1}+A_{g2}\,C_{15,1}^{\,2}\right] \tag{6.1}$$

6.4 Gel Adsorption

Gel retention modeling is done using a "Langmuir-type" isotherm to correlate adsorbed concentration with the aqueous-phase concentrations.

$$\hat{C}_{15} = \frac{a_{15}\,C_{15,1}}{1 + b_{15}\,C_{15,1}} \tag{6.2}$$

6.5 Gel Permeability Reduction

The effect of gel on aqueous-phase permeability reduction is taken into account through a residual resistance factor commonly used for polymer flooding.

$$R_{RF} = 1 + \frac{\left(R_{RF\,max} - 1\right) A_{gk}\,C_{15,1}}{1 + B_{gk}\,C_{15,1}} \tag{6.3a}$$

where the maximum residual resistance factor is calculated by

$$R_{RF\,max} = \left[1-\frac{c_{rg}\left(A_{p1}\,C_{SEP}^{S_p}\right)^{1/3}}{\left(\frac{\sqrt{k_x\,k_y}}{\phi}\right)^{1/2}}\right]^{-4} \tag{6.3b}$$

The parameter c_{rg} is an input parameter which depends on the gel type. The permeability reduction for silicate gel (KGOPT=3) is independent of the silicate viscosity and the maximum residual resistance factor (R_{RFmax}) is equal to 10.

6.5.1 Chromium Retention

The following equilibria have been implemented in UTCHEM to simulate the exchange between chromium, sodium and hydrogen on the clays.

6.5.2 Cation Exchange

6.5.2.1 Chromium-Sodium Exchange

$$3\,\widehat{Na^+} + Cr^{3+} = 3\,Na^+ + \widehat{Cr^{3+}}$$

$$K_{14,9} = \frac{\hat{C}_{14}\,C_{9,1}^{\,3}}{\hat{C}_9^{\,3}\,C_{14,1}} \tag{6.4}$$

6.5.2.2 Hydrogen-Sodium Exchange

$$\widehat{Na^+} + H^+ = Na^+ + \widehat{H^+}$$

$$K_{16,9} = \frac{\hat{C}_{16}\,C_{9,1}}{\hat{C}_9\,C_{16,1}} \tag{6.5}$$

6.5.3 Adsorption

As an alternative to cation exchange, the retention of chromium has also been modeled as a "Langmuir-type" isotherm in UTCHEM.

$$\hat{C}_{14} = \frac{a_{14} C_{14,1}}{1 + b_{14} C_{14,1}} \tag{6.6}$$

6.5.4 Precipitation

Chromium precipitation is modeled using geochemical reaction equilibria in UTCHEM. Cr(III) precipitates in the form of chromium hydroxide complex.

$$Cr^{3+} + H_2O = Cr(OH)^{2+} + H^+ \tag{6.7}$$

$$Cr^{3+} + 2\,H_2O = Cr(OH)_2^+ + 2\,H^+ \tag{6.8}$$

$$Cr(OH)_3 \downarrow = Cr^{3+} + 3\,OH^- \tag{6.9}$$

Gel reactions are implemented in the source term as gel kinetic equations and the mass-conservation equation is solved with reacted amount of each gel component.

Polymer molecules are crosslinked by Cr(III), which is known to be one of the most widely used crosslinkers. Three types of gel reactions and kinetics are implemented in UTCHEM. The kinetics of polymer/chromium chloride gel were modified, and gel reactions of polymer/chromium malonate gel and silicate were modeled.

6.5.5 Polymer/Chromium Chloride Gel

Two sets of reactions and kinetics for polymer/chromium chloride gel are implemented in UTCHEM. The first is in-situ gelation of polymer with sodium dichromate with reducing agent thiourea, and the second is the gelation of Cr(III) with polymer to form gel.

The kinetics for the reaction between polymer and chromium have been generalized to allow for any exponent (Hunt, 1987). The gel is formed by fast reaction of trivalent chromium (Cr(III)) and polymer. There is an option for the slow delaying reaction between Cr(VI) and thiourea. The sodium dichromate ($Na_2Cr_2O_7$) and thiourea ($(CS(NH_2))_2$ are treated like tracers in the sense that they do not occupy any volume. The Cr(III) for the gelation process can be generated in situ by redox reaction between Cr(VI) and thiourea.

$$Cr_2O_7^{2-} + 6CS(NH_2)_2 + 8H^+ \xrightarrow{k_1} 2Cr^{3+} + 3\left[CS(NH_2)_2\right]_2 + 7H_2O$$

The gel reaction is highly dependent on pH (Lockhart, 1992; Seright and Martin, 1991). For more realistic simulations of gel reactions, pH was implemented in the gel kinetic equation as hydrogen ion concentration.

6.5.6 Polymer/Chromium Malonate Gel

The components of polymer/chromium chloride gel are as follows:

1. Polymer – Hydrolyzed polyacrylamide (HPAM) and HE-100 (acrylamido-3-propane sulfonic acid co-polymer) were used. HE-100/chromium malonate is reported to have a longer gelation time than HPAM/chromium malonate (Lockhart, 1992).
2. Crosslinker – Chromium malonate, $Cr\,(\,HOOC - CH_2 - COOH\,)_3$. Among various complexes of chromium, chromium malonate has the longest gelation time and stability at high temperature (Lockhart, 1992).

3. Ligand (delaying) – Malonate ion (uncomplexed), $(HOOC - CH - COOH)^-$. The uncomplexed malonate ion as a delaying ligand is an optional component that gives a longer gelation time.

6.5.6.1 Kinetics

Case I (polymer and crosslinker only)

The kinetics for this gel are the same as the kinetics of chromium chloride gel except with different exponents:

$$[\text{polymer}] + n [\text{Cr(III)}] = [\text{gel}] ,$$

$$\frac{d [\text{Cr (III)}]}{dt} = - k \frac{[\text{Cr (III)}]^{X14} [\text{polymer}]^{X4}}{[H^+]^{X16}} ,$$

$$\frac{d [\text{gel}]}{dt} = - \frac{1}{n} \frac{d [\text{Cr (III)}]}{dt} ,$$

where the possible values for exponents from Lockhart [1992] are

X4	2.6
X14	0.6
X16	1.0

Case II (polymer, crosslinker, and malonate ion)

When the malonate ion is used as a delaying ligand, the gelation kinetics are different, with zero-order reaction for chromium :

$$\frac{d [\text{Cr (III)}]}{dt} = - k \frac{[\text{polymer}]^{X4}}{[\text{malonate}]^{X13} [H^+]^{X16}} ,$$

$$\frac{d [\text{gel}]}{dt} = - \frac{1}{n} \frac{d [\text{Cr (III)}]}{dt}$$

where some possible values for exponents from Lockhart [19912] are

X4	2.6
X13	0.3
X16	1.0

The uncomplexed malonate ion slowly decomposes to acetate and carbon dioxide, and this is a first-order reaction:

$$(HOOC - CH - COOH)^- \quad \text{-----> } \quad CH_3COO^- + CO_2$$

First-order reaction :

$$\frac{d [\text{malonate}]}{dt} = - 0.037347 [\text{malonate}]$$

6.5.7 Silicate Gel

UTCHEM was modified to simulate the gel reaction of the silicate gel. Polymer and chromium were replaced with silicate (SiO_2) and hydroxyl ion (OH^-), respectively. The gelation was limited to occur only for pH > 7 (Bennett *et al.*, 1988; Iler, 1979) to eliminate complex behavior of gel reaction rate at pH < 7, and the aqueous-phase permeability-reduction factor was independent of silicate viscosity.

Silicate gel is formed by polymerization when appropriate conditions are established. The exact mechanism of gelation is not clear yet; several authors (Iler, 1979; Jurinak *et al*., 1989) explain the general mechanism of gelations of various types of gels.

The general process of gelation is as follows (Jurinak *et al*., 1989):

- condensation of monomer and dimer silicate species to form higher-order oligomers,
- intramolecular condensation of silanol groups within polymers leading to ring closure and eventual particle formation, and
- aggregation of individual particles to form chains and microgel.

The rate of gelation (Kristensen *et al.*, 1993) is a function of

- silicate concentration
- pH
- ionic strength
- temperature

The basic equations that govern polymerization of silicate (Iler, 1979) are as follows:

$$SiO_2 + 2\,H_2O = Si(OH)_4 \qquad (6.10)$$

$$\text{- SiOH} + \text{HOSi -} = \text{- SiOSi -} + H_2O \qquad (6.11)$$

In general form,

$$n\,SiO_2 + z\,OH^- = Si_nO_y(OH)^{z-}_{(nx-z)} + (y-2)\,H_2O \quad , \qquad (6.12)$$

where

n = degree of polymerization

x = ratio of OH:Si

$$x = 4.85\,n^{-1/3} - 7.8\,n^{-2/3} + 4.2\,n^{-1}$$

$$y = \frac{4n - nx}{2} + z$$

z = number of charges on polymer

Equation 6.12 can be written in simplified form as

$$[SiO_2] + m\,[OH^-] = [\text{silicate gel}] \quad , \qquad (6.13)$$

where m is the stoichiometric ratio.

From Eq. 6.13, the gelation kinetics equation can be derived.

$$\frac{d[SiO_2]}{dt} = -k[SiO_2]^{X4}[OH^-]^{X14} \tag{6.14}$$

where

X4 = gelation kinetics exponent for silicate

X14 = gelation kinetics exponent for hydroxyl ion

$$\frac{d[\text{ gel }]}{dt} = - \frac{d[\ SiO_2\ ]}{dt}$$

where some possible values for exponents (Kristensen *et al.*, 1993) are

X4 3.8

X14 -2.5

6.6 Temperature Effects

The reaction constants for gel (k) and the delaying reaction of sodium dichromate and thiourea (k_1) are calculated as a function of temperature if the temperature variation is modeled in the simulations as below.

$$k_1 = k_{1ref} \exp\left[k_{T1}\left(\frac{1}{T} - \frac{1}{T_{ref}}\right)\right]$$

where the temperature T and T_{ref} are in ^{0}R. The input parameters are T_{ref} , K_{T1}, and k_{1ref} for the dichromate reaction.

$$k = k_{ref} \exp\left[k_{T2}\left(\frac{1}{T} - \frac{1}{T_{ref}}\right)\right]$$

where the input parameters are T_{ref} , K_{T2}, and k_{ref} for the gel reaction.

Section 7
Multiple Organic Components

We have added multiple organic components so that we can model NAPL mixtures. Adding this capability to UTCHEM required developing a phase behavior model for NAPL mixtures and the physical property models such as density and viscosity for each phase.

7.1 Introduction

Nonaqueous phase liquids (NAPLs) usually consist of more than one organic species that mix and form a single liquid. Common examples of such miscible species include TCE, TCA and PCE among many others. When NAPLs leak to the subsurface, they can dissolve and migrate into groundwater. To model the fate and transport of these soluble organics during remediation processes such as pump-and-treat, bioremediation and surfactant remediation, it is important to determine the migration of the individual soluble organics. The dissolution can be either a local equilibrium or a rate-limited (non-equilibrium) mass transfer process. We have added the capability of multiple organic components to UTCHEM to model these NAPL mixtures. The multiple organic dissolution can be either at local equilibrium partitioning or a rate-limited mass transfer. We also present the phase behavior model developed for a mixture of NAPL mixtures, surfactant, and water. The physical property models to calculate the density, viscosity, and adsorption of the organic species and NAPL mixtures are also included.

7.2 Mass Transfer for Nonaqueous Phase Liquid

When a NAPL component dissolves in water, its concentration in ground water can reach its solubility (equilibrium mass transfer) but often is much lower than the solubility due to a rate-limited mass transfer. UTCHEM allows for both equilibrium and nonequilibrium mass transfer for a multiple organic NAPL. The mass transfer is modeled for the cases with or without surfactant.

7.2.1 No Surfactant or Surfactant Concentration Below CMC

7.2.1.1 Equilibrium Mass Transfer

For the equilibrium case, a constant partition coefficient between water and NAPL is assumed for each organic species:

$$K_k^o = \frac{C_{k1}^o}{C_{k2}^o} \qquad k=1,2,3,...,n_o \tag{7.1}$$

The overall fluid concentrations for water (C_1), surfactant (C_3), and each organic components (C_k^o) are solved from the species mass conservation equation. The overall fluid phase concentration is the summation of phase concentrations over all the phases:

$$C_k = C_{k1} S_1 \quad k=1,3 \tag{7.2}$$

and

$$C_k^o = C_{k1}^o S_1 + C_{k2}^o S_2 \qquad k=1,2,3,..., n_o \tag{7.3}$$

The definitions of overall phase concentrations (Eqs. 7.2 and 7.3), the constraints that phase concentrations sum up to one ($C_{31} + \sum_{k=1}^{n_o} C_{k1}^o + C_{11} = 1$ and $\sum_{k=1}^{n_o} C_{k2}^o = 1$), and the known partition coefficients for organic components (Eq. 7.1) are used to solve the phase concentrations and saturations. These equations are solved by reformulating C_{31} and C_k^o in terms of C_{11} and using Newton's method to

solve $f(C_{11}) = C_{31} + \sum_{k=1}^{n_o} C_{k1}^0 + C_{11} - 1 = 0$. A phase stability rule is used to determine the number of phases. If $\sum_{k=1}^{n_o} \frac{C_k^o}{K_k^o} > 1$, the fluid is two phases. Otherwise, it is a single phase.

7.2.1.2 Nonequilibrium Mass Transfer

For nonequilibrium mass transfer, a linear driving force rate, as proposed by Powers *et al.* [1992] is used. The mass transfer rate between NAPL and water interface for each NAPL component is a mass transfer coefficient times the driving force that is the difference between the equilibrium and phase concentrations. The mass transfer coefficient is currently modeled as a constant. The computational procedure for non-equilibrium mass transfer requires the calculation of the equilibrium organic concentrations, C_{k1}^{oeq}, first. Then we solve for the phase concentrations and saturations for the nonequilibrium case. It is similar to the equilibrium case, except that the mass balance equation for the organic in the water phase is used instead of constant partition coefficient of the equilibrium case. The organic species mass balance equations in the water phase are given by:

$$\frac{\partial\phi\left[1-\sum_{n=1}^{n_c}\hat{C}_n\right]\left[1+c_k^a\left(P_1-P_{Ra}\right)\right]S_1C_{k1}^o}{\partial t} + \bar{\nabla}\cdot\left[1+c_k^a\left(P_1-P_{Ra}\right)\right]\left(C_{k1}^o\bar{u}_1\bar{\bar{D}}_{k1}^o\right) \tag{7.4}$$

$$= R_{k1}^o + Q_{k1}^o + M_k^o\left(C_{k1}^{oeq} - C_{k1}^o\right) \qquad k = 1,2,3,...,n_o$$

7.2.2 Surfactant Concentration Above CMC

7.2.2.1 Equilibrium Mass Transfer

When the surfactant concentration is greater than the CMC, micelles form. When organic species are solubilized into these micelles under certain conditions, a microemulsion forms. Organic species dissolve by two mechanisms: (1) organic components dissolve into water according to their equilibrium solubilities in water and (2) the organic mixture solubilized by the micelles has the same composition as the NAPL. To model both mechanisms, each organic component is divided into two parts, one associated with water, C_k^{ow}, and the other associated with the micelles, C_k^{oo}.

The organic dispersed into water follows the constant partition coefficient as described above. The remainder of the organic is assumed to follow the same microemulsion as used for a single component (as given in Appendix C and based upon Hand's equation). The calculations of phase compositions are divided into two parts. First, assume the surfactant is not present and calculate phase equilibrium concentrations as before. This calculation gives the overall concentration of each organic components associated with water, $C_k^{ow} = C_1 \frac{C_{k1}^{ow}}{1-\sum_{k=1}^{n_o} C_{k1}^{ow}}$.

Hand's equation is then used to calculate the phase concentrations and saturations using the normalized total concentrations as

$$C_{1N} = \frac{C_1}{1 - \sum_{k=1}^{n_o} C_k^{ow} - CMC} \tag{7.5}$$

$$C_{2N} = \frac{\sum_{k=1}^{n_o} C_k^{o} - \sum_{k=1}^{n_o} C_k^{ow}}{1 - \sum_{k=1}^{n_o} C_k^{ow} - CMC} \tag{7.6}$$

$$C_{3N} = \frac{C_3 - CMC}{1 - \sum_{k=1}^{n_o} C_k^{ow} - CMC} \tag{7.7}$$

The phase concentrations and saturations for the normalized concentrations are calculated from Hand's equations.

$$C_{kN} = \sum_{\ell=1}^{3} C_{k\ell N} S_{\ell N} \qquad k=1,2,3 \tag{7.8}$$

For the Type II(-) phase environment with corner plait point, C_{12N}=0, C_{22N}=1, C_{32N}=0, and S_{1N}=0. The phase concentrations in terms of the original concentrations are calculated from the following equations:

$$C_{1\ell} = C_{1\ell N}\left(1 - \sum_{k=1}^{n_o} C_k^{ow} - CMC\right) \tag{7.9}$$

$$C_{k\ell}^{o} = C_{k2}^{oo} C_{2\ell N}\left(1 - \sum_{k=1}^{n_o} C_k^{ow} - CMC\right) + C_k^{ow} \qquad k = 1,2,...,n_o \tag{7.10}$$

$$C_{3\ell} = C_{3\ell N}\left(1 - \sum_{k=1}^{n_o} C_k^{ow} - CMC\right) + CMC \tag{7.11}$$

and the saturation is unaffected by the normalization.

7.2.2.2 Nonequilibrium Mass Transfer

Once the equilibrium saturations and concentrations are known, the organic species mass balance equations in the aqueous phase (Eq. 7.12) are used to calculate the nonequilibrium saturations and concentrations. A single mass transfer coefficient is assumed for all organic components.

$$\frac{\partial\phi\left[1-\sum_{n=1}^{n_c}\hat{C}_n\right]\left[1+c_k^a\left(P_1-P_{Ra}\right)\right]S_1C_{k1}^o}{\partial t}+\vec{\nabla}\cdot\left[1+c_k^a\left(P_1-P_{Ra}\right)\right]\left(C_{k1}^o\vec{u}_1\bar{\bar{D}}_{k1}^o\right) \tag{7.12}$$

$$=R_{k1}^o+Q_{k1}^o+M_2\left(C_{k1}^{oeq}-C_{k1}^o\right)\qquad k=1,2,3,...,n_o$$

where the equilibrium concentrations and saturations are already known from the phase behavior calculations.

7.3 Physical Properties for NAPL Mixture

Phase behavior, adsorption, viscosity, and density are the physical property relations modeled for the NAPL mixtures.

7.3.1 Phase Behavior

Three recent papers by Baran *et al.* [1994a,b,c] show that the phase behavior of surfactants with both pure chlorocarbons and mixtures of chlorocarbons is similar to classical phase behavior with hydrocarbons. The phase behavior changes from microemulsion in equilibrium with excess oil (Winsor Type I or Type II(-)) to microemulsion in equilibrium with excess aqueous and organic phase (Winsor Type III), and to microemulsion in equilibrium with excess water (Winsor Type II or Type II(+)) as salinity increases. The lower (C_{SEL}) and upper (C_{SEU}) limits of effective salinity are the effective salinity which three phases form or disappear. The optimal salinity (C_{SEOP}) is defined as the midpoint of these two salinity limits (Salager *et al*. 1979).

Hand's equation (Pope and Nelson, 1978) is used in UTCHEM to describe the phase envelope, binodal curve. The concentrations at binodal curve are described by the following equation:

$$\frac{C_{3\ell}}{C_{2\ell}}=A\left(\frac{C_{3\ell}}{C_{1\ell}}\right)^B\qquad \ell=1,\,2,\,3 \tag{7.13}$$

where parameter A and B are empirical parameters. Parameter A is related to the height of the binodal curve and B is assumed to be -1 in UTCHEM for a symmetric binodal curve. Parameter A is a function of salinity and is linearly interpolated with the values of A at low (m=0), optimal (m=1) and high (m=2) salinities as following:

$$A=\left(A_0-A_1\right)\left(1-\frac{C_{SE}}{C_{SEOP}}\right)+A_1\quad C_{SE}\le C_{SEOP} \tag{7.14}$$

and

$$A=\left(A_2-A_1\right)\left(\frac{C_{SE}}{C_{SEOP}}-1\right)+A_1\quad C_{SE}>C_{SEOP} \tag{7.15}$$

Parameter A in terms of the height of binodal curve is described as

$$A_m=\left(\frac{2C_{3\max,m}}{1-C_{3\max,m}}\right)^2\qquad m=0,1,2 \tag{7.16}$$

For organic mixtures, the upper and lower limits of effective salinity for Type III region, the height of binodal curve at lower, optimal, and upper salinities are functions of organic species concentrations.

These parameters are modeled as functions of the equivalent alkane carbon number (E_{ACN}) of the mixture, which is a function of organic species concentrations.

$$E_{ACN} = \sum_{k=1}^{n_o} E^o_{ACN,k} x^o_k \tag{7.17}$$

where x^o_k is the molar fraction for organic components only, $\sum_{k=1}^{n_o} x^o_k = 1$. E_{ACN} for an alkane is the number of carbons in the alkane chain of the hydrocarbon, for example it is equal to 6 for hexane. E_{ACN} for a nonalkane is obtained by measuring the optimal salinity for a binary mixture of an alkane and a nonalkane with known molar fractions. The measured optimal salinity is used to determine E_{ACN} for the binary mixture from Salager's equation. Then E_{ACN} for the nonalkane is calculated from Equation (7.17). The E_{ACN} data listed in the Baran *et al.* papers are built into the UTCHEM database: C_2Cl_4 (PCE, E_{ACN} = 2.90), CCl_4 (E_{ACN} = -0.06), C_2HCl_3 (TCE, E_{ACN} = -3.81), p-xylene (E_{ACN} = 2), toluene (E_{ACN} = 1), 1,2-$C_6H_4Cl_2$ (DCB, E_{ACN} = -4.89), 1,2-$C_2H_4Cl_2$ (E_{ACN} = -12.10), $CHCl_3$ (E_{ACN} = -13.67), CH_2Cl_2 (DCE, E_{ACN} = -13.79), and 1,1,2,2-$C_2H_2Cl_4$ (E_{ACN} = -22.15).

The natural log of the optimal salinity is a linear function of E_{ACN} (Salager *et al.*, 1979; Baran *et al.*, 1994a,b.c)

$$\ln C_{SEOP} = s_{se}(E_{ACN} - E_{min}) \tag{7.18}$$

The slope s_{se} is about 0.16 for the optimal salinity with the unit of wt.% per liter. The difference of the upper and lower effective salinities for the three-phase region is assumed as a linear function of E_{ACN}

$$\frac{C_{SEU} - C_{SEL}}{C_{SEOP}} = s_{ds} E_{ACN} + b_{ds} \tag{7.19}$$

where

$$C_{SEOP} = \frac{C_{SEU} + C_{SEL}}{2} \tag{7.20}$$

C_{SEOP}, C_{SEL}, and C_{SEU} can be solved using Eqs. 7.18-7.20.

The solubilization parameter is usually reported by experimentalists doing surfactant phase behavior measurements rather than the height of the binodal curve. The solubilization parameter is defined as the oil concentration divided by the surfactant concentration in the microemulsion phase as $\sigma = \frac{C_{2,max}}{C_{3,max}}$. Thus, parameter A can be expressed in terms of the solubilization parameter:

$$A_m = (\sigma_m)^{-2} \quad m = 0,1,2 \tag{7.21}$$

The solubilization parameter is a linear function of E_{ACN} as

$$\sigma_m = s_{\sigma,m} E_{ACN} + b_{\sigma,m} \quad m = 0,1,2 \tag{7.22}$$

In UTCHEM, coefficients s_{se}, E_{min}, s_{ds}, b_{ds}, $s_{\sigma,m}$, and $b_{\sigma,m}$ are not input data. Instead, data for two measured samples including concentrations and component names, the optimal salinity, the difference of the lower and upper salinity limits, and the solubilization parameters at three salinities are specified since these are what are typically measured and reported (see Baran *et al.*, 1994a,b.c for examples). UTCHEM

calculates the coefficients based on the input values for the two specified compositions and $E^o_{ACN,k}$ values in the UTCHEM database, or those entered by the user as needed.

7.4 NAPL Mixture Viscosity

Microemulsion viscosities are modeled as:

$$\mu_\ell = C_{1\ell}\mu_1 e^{\alpha_1(C_{2\ell}+C_{3\ell})} + C_{2\ell}\mu_{2\ell} e^{\alpha_2(C_{1\ell}+C_{3\ell})} + C_{3\ell}\alpha_3 e^{\alpha_4(C_{1\ell}+\alpha_5 C_{3\ell})} \tag{7.23}$$

where $C_{2\ell}$ is the total organic concentration, $C_{2\ell} = \sum_{k=1}^{n_o} C^o_{k\ell}$, and $\mu_{2\ell}$ is the organic mixture viscosity. Grumberg and Nissan's correlation is used to calculate the NAPL viscosity as a function of organic species concentration.

$$\ln \mu_{2\ell} = \sum_{k=1}^{n_o} x^o_{k\ell} \ln \mu^o_k \tag{7.24}$$

7.5 Density of NAPL Mixtures

Hydrostatic pressure gradients for the microemulsion ($\gamma=\rho g$) are calculated as:

$$\gamma_\ell = C_{1\ell}\gamma_{1\ell} + C_{2\ell}\gamma_{2\ell} + C_{3\ell}\gamma_{3\ell} + 0.02535C_{5\ell} - 0.001299C_{6\ell} + C_{8\ell}\gamma_{8\ell} \tag{7.25}$$

For a NAPL mixture, the overall organic hydrostatic pressure gradient is obtained by assuming ideal mixing

$$C_{2\ell}\gamma_{2\ell} = \sum_{k=1}^{n_o} C^o_k \gamma^o_{k\ell} \tag{7.26}$$

UTCHEM allows two different hydrostatic pressure gradients for the organic species, one for the microemulsion phase and the other for the organic phase.

7.6 Adsorption of Organic Species

The organic adsorption is modeled as a linear adsorption isotherm. A constant partition coefficient with respect to the organic fraction is used for each organic component as

$$\hat{C}^o_k = f_{oc} K^o_{oc,k} C^o_{k\ell} \quad \ell \text{ is the water-rich phase} \tag{7.27}$$

7.7 Nomenclature

c_k = Compressibility of species k

C_k, C^o_k = Overall fluid concentration of species k and organic species k

$C_{k\ell l}$, $C^o_{k\ell l}$ = Concentration of species k and organic species k in phase ℓ

$\hat{C}_k$, $\hat{C}^o_k$ = Adsorbed concentration of species k and organic species k

C_{SE} = Effective salinity

C_{SEL} = Lower effective salinity

C_{SEOP} = Optimal effective salinity

C_{SEU} = Upper effective salinity

$\bar{\bar{D}}_{k\ell}$ = Dispersion flux of species k in phase ℓ

f_{oc} = Organic carbon fraction in soil

$K^{o}_{oc,k}$ = Adsorption of organic species k per unit weight of organic carbon in soil

n_o = Total number of organic species

P_R = Reference pressure

Q_k, Q^{o}_{k} = Source/sink term for species k and organic species k

R_k = Reaction rates for species

t = Time

$\vec{u}_{\ell}$ = Darcy flux of phase ℓ

ϕ = Porosity

Section 8
Mathematical Formulation of Reaction Equilibrium

8.1 Introduction

This section describes the geochemistry model in UTCHEM and is based on work by Bhuyan [1989] and Bhuyan *et al*. [1990]. The geochemical model is based on local thermodynamic equilibrium assumption to compute the detailed chemical composition of the reservoir rock and fluids in the presence of chemical reactions among the injected chemical species and reservoir rock and fluids. The reaction chemistry includes aqueous electrolytes chemistry, precipitation/dissolution of minerals, ion-exchange reactions with the matrix, and reaction of acidic components of oil with the bases in the aqueous solution.

A program called EQBATCH was developed to perform batch reaction equilibrium calculations. The algorithm used for this program is essentially the same as described in this section. EQBATCH can be used as a preprocessor for UTCHEM to calculate the initial equilibrium state of the reservoir. EQBATCH writes the output data in a format similar to the geochemical input data of UTCHEM so it can be directly pasted into an input file for UTCHEM. Other uses of EQBATCH include: determination of compatibility between injection water and resident water; equilibrium composition and compatibility of mixing injection water from different sources; and equilibrium composition and the resulting pH of the injection water after addition of various electrolytes. Appendix C contains the user's guide for EQBATCH along with sample input and output files.

8.2 Basic Assumptions

The following assumptions have been made in developing the reaction equilibrium model:

1. All reactions attain thermodynamic equilibrium.
2. Activity coefficients of all reactive species are unity so that molar concentrations replace activities in reaction equilibria calculations.
3. No redox reactions are present.
4. The reservoir is isothermal. Temperature changes resulting from chemical reactions are negligibly small.
5. Pressure and volume changes resulting from chemical reactions are negligibly small.
6. The water present in any phase has the same chemical composition and is in equilibrium with matrix minerals.
7. The active acid species in the crude oil can be represented collectively by a single pseudo acid component, HA. HA is highly soluble in oil and partitions between oil and water with a constant partition coefficient.
8. Supersaturation of aqueous species is not allowed.
9. The activity of water is equal to unity.

8.3 Mathematical Statement of the Problem of Reaction Equilibrium

Let the reactive system be comprised of J fluid species, K solid species, I matrix-adsorbed cations and M micelle-associated cations all made up of N elements. There are then (J+K+I+M) unknown equilibrium concentrations. To determine the equilibrium state of the system, therefore, one needs (J+K+I+M) number of independent equations. These equations are given below.

8.3.1 Mass Balance Equations

Elemental mass balances provide N equations of the form

$$C_n^T = \sum_{j=1}^{J} h_{nj} C_j + \sum_{k=1}^{K} g_{nk} \hat{C}_k + \sum_{i=1}^{I} f_{ni} \overline{C}_i + \sum_{m=1}^{M} e_{nm} \overline{\overline{C}}_m \qquad \text{for } n = 1,\ldots,N \tag{8.1}$$

Electrical neutrality in the bulk fluid phase gives one more equation

$$0 = \sum_{j=1}^{J} z_j C_j + \sum_{m=1}^{M} \overline{\overline{z}}_m \overline{\overline{C}}_m \tag{8.2}$$

However, Eq. 8.2 is actually a linear combination of the set of mass balance equations given by Eqs. 8.1. This equation is, therefore, not an independent equation , but can be used in place of any one of the elemental material balance equations.

8.3.2 Aqueous Reaction Equilibria Relations

Out of the J fluid chemical species, we can arbitrarily select N independent species such that the concentrations of the remaining (J-N) fluid species can be expressed in terms of the concentrations of these N independent species through equilibrium relationships of the form

$$C_r = K_r^{eq} \prod_{j=1}^{N} C_j^{w_{rj}} \qquad \text{for } r = (N+1),\ldots,J \tag{8.3}$$

8.3.3 Solubility Product Constraints

For each solid there is a solubility product constraint given

$$K_k^{sp} \geq \prod_{j=1}^{N} C_j^{w_{kj}} \qquad \text{for } k = 1,\ldots,K \tag{8.4}$$

where the solubility product constants K_k^{sp} are defined in terms of the concentrations of the independent chemical species only. If a solid is not present, the corresponding solubility product constraint is the inequality; if the solid is present, the constraint is an equality.

8.3.4 Ion Exchange Equilibrium on Matrix Substrate

For each substrate allowing exchange among I cations, there is one electroneutrality condition given by

$$Q_v = \sum_{i=1}^{I} \overline{z}_i \overline{C}_i \tag{8.5}$$

Additionally, for these I adsorbed cations there will be (I-1) independent exchange equilibria relations of the form

$$K_p^{ex} = \prod_{j=1}^{N} C_j^{y_{pj}} \prod_{i=1}^{I} \overline{C}_i^{x_{pi}} \qquad \text{for } p = 1,\ldots,(I-1) \tag{8.6}$$

8.3.5 Ion Exchange Equilibrium with Micelles

For M cations associated with surfactant micelles there will be (M-1) cation exchange (on micelle) equilibria relations of the form

$$K_q^{exm} = \prod_{j=1}^{N} C_j^{y_{qj}} \prod_{m=1}^{M} \overline{\overline{C}}_m^{x_{qm}} \qquad \text{for } q = 1,\ldots,(M-1) \tag{8.7}$$

It has been shown that an electrostatic association model where the mass action equilibria constants are not really constants, but are functions of total anionic surfactant concentration, adequately describes these ion exchange equilibria relations (Hirasaki, 1982b). Thus, these equilibria constants are given by

$$K_q^{exm} = \beta_q^{exm}\left(C_{A^-} + C_{S^-}\right) \tag{8.8}$$

Additionally, the electroneutrality conditions for the micelles as a whole provide one more equation as

$$C_{A^-} + C_{S^-} = \sum_{m=1}^{M} \overline{\overline{z}}_m \overline{\overline{C}}_m \tag{8.9}$$

8.3.6 Partitioning Equilibrium of Acid Component Between Crude Oil and Water

For cases where partitioning of an acidic component between oil and water is considered, the acid component remaining with the oil (HA_o) but available for partitioning into the water is selected as one of the independent chemical species as described in Sec. 8.3.2. Since all aqueous reaction equilibria calculations are done on a unit water volume basis, the concentration of HA_o also needs to be expressed on the same basis. Let a unit volume of pore space at a given time and position have v_1 fraction filled by water and v_2 fraction filled by oil. Now defining the concentration of HA_o as

$$C_{HA_o} = \frac{\text{moles of } HA_o}{\text{liter water}}$$

and the partition coefficient constant, K_D as

$$K_D = \frac{\text{Concentration of HA in water}}{\text{Concentration of HA in oil}}$$

$$= \frac{\text{moles of } HA_w}{\text{moles of } HA_o} \times \frac{\text{liter oil}}{\text{liter water}}$$

gives the concentration of the dependent variables HA_w as

$$C_{HA_w} = \frac{\text{moles of } HA_w}{\text{liter water}}$$

$$= K_D \frac{\text{moles of } HA_o}{\text{liter oil}}$$

$$= K_D \frac{\text{liter water}}{\text{liter oil}} C_{HA_o}$$

$$= K_D \frac{v_1}{v_2} C_{HA_o}$$

and that of A^- as

$$C_{A^-} = \frac{\text{moles of } A^-}{\text{liter water}}$$

$$= K_a \frac{C_{HA_w}}{C_{H^+}}$$

$$= K_D K_a \frac{\text{liter water}}{\text{liter oil}} \frac{C_{HA_o}}{C_{H^+}}$$

$$= K_D K_a \frac{v_1}{v_2} \frac{C_{HA_o}}{C_{H^+}}$$

Thus, it is seen that for these two dependent chemical species, the reaction equilibria constants as defined in Sec. 8.3.2 are actually functions of the relative amounts of water and oil available. For a given water-oil ratio, these two equilibrium constants can be calculated from the partition coefficient and acid dissociation constant. Once calculated, these constants can be treated the same as other reaction equilibria constants in the computation procedure for that position and time.

8.4 Numerical Computation to Determine the Equilibrium State

In Sec. 8.3, it was stated that there are N mass balances (the bulk solution neutrality equation may be used to replace one of these mass balance equations), (J-N) aqueous reaction equilibrium relations, K solubility product constraint equations, 1 matrix surface electroneutrality equation, (I-1) cation exchange (on matrix surface) equilibrium relations, (M-1) cation exchange (on micelle) equilibrium relations and 1 electroneutrality condition for the micelles giving a total of (J+K+I+M) independent equations to calculate the equilibrium concentrations of J fluid chemical species, K solid species, I matrix adsorbed cations and M cations adsorbed on micelle surfaces.

An iterative scheme similar to the one used by Walsh [1983] is used to solve this set of non-linear equations. However, the inclusion of the ion exchange reactions on the micellar surface and the partitioning of the acidic component of the crude oil into water makes the numerical treatment of the procedure slightly different from those reported for the single phase (aqueous) flow equilibrium problem. The computational procedure used to determine the equilibrium state is described in the following sections.

8.4.1 Reducing the Number of Independent Concentration Variables for the Newton-Raphson Iteration

As mentioned in Sec. 8.3.2, N out of the J aqueous chemical species are selected such that concentrations of the remaining (J-N) chemical species can be expressed in terms these N independent species concentrations through reaction equilibria relationships given by Eqs. 8.3. Apart from this requirement, the selection of these N independent concentration variables is arbitrary. This reduces the problem at hand to determination of (N+K+I+M) independent unknown concentrations.

The problem of solving for the above discussed (N+K+I+M) independent unknowns can further be reduced to a series of two smaller problems. In the first problem the concentrations of adsorbed cations on the matrix surface as well as on the micellar surface are treated as independent variables along with the N independent aqueous species concentrations. The second problem has K independent unknowns, the concentrations of the solid species. Thus, the first step of the equilibrium state calculation is made independent of the solid concentrations, though it requires some initial guess about which solids are present. This reduction is possible because the solubility product constraint equations are independent of the solid concentrations. The Newton-Raphson iteration scheme is used to solve these non-linear equations.

In the second step, the solid concentrations are determined from elemental material balance equations. The equations to be solved in this step are linear. These computed solid concentrations along with solubility

product constraints are then used to determine if our initial guess of which solids were present was correct. If not, a new guess is made using this information and the first step is repeated.

8.4.2 Generating a Set of Equations Independent of Solid Concentration for the Newton-Raphson Iteration

For the purpose of using the Newton-Raphson iteration scheme, Eqs. 8.1, and 8.4 through 8.9 are rewritten here as

$$E_n = \sum_{j=1}^{J} h_{nj} C_j + \sum_{k=1}^{K} g_{nk} \hat{C}_k + \sum_{i=1}^{I} f_{ni} \bar{C}_i + \sum_{m=1}^{M} e_{nm} \bar{\bar{C}}_m - C_n^T \quad \text{for } n = 1,\ldots,N \tag{8.10}$$

$$F_k = \prod_{j=1}^{N} C_j^{w_{kj}} - K_k^{sp} \quad \text{for } k = 1,\ldots,K \tag{8.11}$$

$$G_p = \prod_{j=1}^{N} C_j^{y_{pj}} \prod_{i=1}^{I} \bar{C}_i^{x_{pi}} - K_p^{ex} \quad \text{for } p = 1,\ldots,(I-1) \tag{8.12a}$$

$$G_p = \sum_{i=1}^{I} \bar{z}_i \bar{C}_i - Q_v \quad \text{for } p = I \tag{8.12b}$$

$$H_q = \prod_{j=1}^{N} C_j^{y_{qj}} \prod_{m=1}^{M} \bar{\bar{C}}_m^{w_{qm}} - \left(C_{A^-} + C_{S^-}\right)\beta_q^{exm} \quad \text{for } q = 1,\ldots,(M-1) \tag{8.13a}$$

$$H_q = \sum_{m=1}^{M} \bar{\bar{z}}_m \bar{\bar{C}}_m - C_{A^-} - C_{S^-} \quad \text{for } q = M \tag{8.13b}$$

The solution to the set of Eqs. 8.10 through 8.13b are the set of $(C_j : j = 1,\ldots,N)$, $(\bar{C}_i : i = 1,\ldots,I)$ and $(\bar{\bar{C}}_m : m = 1,\ldots,M)$ such that $(E_n : n = 1,\ldots,N) = 0$, $(F_k : k = 1,\ldots,K) = 0$, $(G_p : p = 1,\ldots,I) = 0$ and $(H_q : q = 1,\ldots,M) = 0$.

Now as discussed in Sec. 8.4.1 in the first step of the calculation, (N+I+M) independent equations which are free of solid concentrations are used. The only equations where solid concentrations appear are the set of elemental mass balance equations given by Eqs. 8.10. A set of (N-K) modified equations which are independent of solid concentrations is derived as follows.

In order to make the set of equations independent of the concentration of the first solid, i.e. $\hat{C}_1$, consider the equations where g_{n1} values are non-zero. Since each of the solids considered here is composed of at least two elements, there will be at least two such equations. The maximum number of such equations can be as high as (N-1), depending on the number of elements comprising the particular solid (Bryant *et al.*, 1986). Now, dividing this set of equations by the corresponding g_{n1}, gives a set of equations which have unity as the coefficient of the concentration $\hat{C}_1$. This set of equations can be written as

$$\frac{E_n}{g_{n1}} = \sum_{j=1}^{J} \frac{h_{nj}}{g_{n1}} C_j + \hat{C}_1 + \sum_{k=2}^{K} \frac{g_{nk}}{g_{n1}} \hat{C}_k + \sum_{i=1}^{I} \frac{f_{ni}}{g_{n1}} \bar{C}_i + \sum_{m=1}^{M} \frac{e_{nm}}{g_{n1}} \bar{\bar{C}}_m - \frac{C_n^T}{g_{n1}}$$

Now, subtracting one of these equations from the other similar equations we can eliminate $\hat{C}_1$ from these equations. This procedure is repeated on these and remaining elemental material balance equations to eliminate other solid concentrations. The equation selected for subtraction is excluded in any subsequent elimination steps. When elimination steps are completed, the (N-K) equations are

$$\tilde{E}_n = \sum_{j=1}^{J} \tilde{h}_{nj} C_j + \sum_{i=1}^{I} \tilde{f}_{ni} \bar{C}_i + \sum_{m=1}^{M} \tilde{e}_{nm} \bar{\bar{C}}_m - \tilde{C}_n^T \quad \text{for } n = 1,\ldots,(N-K) \tag{8.14}$$

The set of (N+I+M) equations given by Eqs. 8.11 through 8.14 can now be solved for the same number of unknown concentrations by the Newton-Raphson iteration.

8.4.3 Transformations of Variables and Equations for the Newton-Raphson Iteration

The concentrations of the chemical species participating in the various reactions typically vary over several orders of magnitude. For example, the concentration of the hydrogen ion is 10^{-7} mol/L in a neutral water but will change to 10^{-13} moles/liter in the presence of only 0.4% NaOH in the solution. Following Wolery [1979] and Walsh [1983], the molar concentrations of the independent species were transformed into logarithmic variables as

$$X_n = \log C_n \quad \text{for } n = 1,\ldots,N \tag{8.15a}$$

$$X_{N+i} = \log \bar{C}_i \quad \text{for } i = 1,\ldots,I \tag{8.15b}$$

$$X_{N+I+m} = \log \bar{\bar{C}}_m \quad \text{for } m = 1,\ldots,M \tag{8.15c}$$

The logarithmic transformation has been found to aid the convergence of the Newton-Raphson iterations (Walsh, 1983).

For convenience of representation of equations in the subsequent sections, a set of new names are defined for the independent concentration variables as

$$M_i = 10^{X_i} \quad \text{for } i = 1,\ldots,(N+I+M) \tag{8.16}$$

Also, a general form of the equation for all non-solid species concentrations in terms of the (N+I+M) independent concentrations is:

$$Y_j = K_j \prod_{i=1}^{N+I+M} M_i^{a_{ji}} \quad \text{for } j = 1,\ldots,(J+I+M) \tag{8.17}$$

where

$$Y_j = C_j \quad \text{for } j = 1,\ldots,J \tag{8.18a}$$

$$Y_{J+n} = \bar{C}_n \quad \text{for } n = 1,\ldots,I \tag{8.18b}$$

$$Y_{J+I+m} = \bar{\bar{C}}_m \quad \text{for } m = 1,\ldots,M \tag{8.18c}$$

For each independent chemical species the K_j value equals unity, $a_{ji} = 1$ for $Y_j = M_i$ and $a_{ji} = 0$ for $Y_j \neq M_i$. For the dependent species, the K_j's are the corresponding reaction equilibrium constants and

the a_{ji}'s are the exponents of the independent concentrations in the definitions of the corresponding reaction equilibrium constants.

The set of (N+I+M) equations given by Eqs. 8.11, 8.12, 8.13 and 8.14 in terms of the new concentration variables, Y_j 's, X_j's and M_j's, as defined above, is as follows:

$$\tilde{E}_n = \sum_{j=1}^{J} \tilde{h}_{nj} Y_j + \sum_{i=1}^{I} \tilde{f}_{ni} Y_{J+i} + \sum_{m=1}^{M} \tilde{e}_{nm} Y_{JI+Im} - \tilde{C}_n^T \quad \text{for } n = 1,\ldots,(N-K) \tag{8.19}$$

$$\tilde{F}_k = \sum_{j=1}^{N} w_{kj} X_j - \log_{10} K_k^{sp} \quad \text{for } k = 1,\ldots,K \tag{8.20}$$

$$\tilde{G}_p = \sum_{j=1}^{N+I} d_{pj} X_j - \log_{10} K_p^{ex} \quad \text{for } p = 1,\ldots,(I-1) \tag{8.21a}$$

$$\tilde{G}_p = \sum_{i=1}^{I} \bar{z}_i M_{N+i} - Q_v \quad \text{for } p = I \tag{8.21b}$$

$$\tilde{H}_q = \prod_{j=1}^{N+I+M} M_j^{b_{qj}} - \beta_q^{exm} K_A \prod_{m=1}^{N+I+M} M_j^{a_{Aj}} - \beta_q^{exm} C_{S^-} \quad \text{for } q = 1,\ldots,(M-1) \tag{8.22a}$$

$$\tilde{H}_q = \sum_{m=1}^{M} \bar{\bar{z}}_m M_{N+I+m} - K_A \prod_{j=1}^{N+I+M} M_j^{a_{Aj}} - C_{S^-} \quad \text{for } q = M \tag{8.22b}$$

where d_{pj} 's are same as y_{pj}'s for $1 \le j \le N$ and as x_{pi}'s for $N < j \le (N+I)$ of Eqs. 8.12a; b_{qj} 's are same as y_{qj}'s for $1 \le j \le N$, as x_{pi}'s for $(N+I) < j \le (N+I+M)$ of Eqs. 8.13a and are equal to zero for $N < j \le (N+I)$; K_A and a_{Aj} are the reaction equilibrium constant and a_{ij}'s for the dependent chemical species A^-, respectively.

8.4.4 Computation of the Jacobian Matrix and the Newton-Raphson Iteration

Now, applying the Newton-Raphson method to the set of (N+I+M) equations given by Eqs. 8.19, 8.20, 8.21 and 8.22, we have for the ν^{th} iteration step

$$-\tilde{E}_n^{\nu} = \sum_{j=1}^{N+I+M} Z_{nj}^{\nu} \left(X_j^{\nu+1} - X_j^{\nu} \right) \quad \text{for } n = 1,\ldots,(N-K) \tag{8.23}$$

$$-\tilde{F}_k^{\nu} = \sum_{j=1}^{N+I+M} Z_{N-K+kj}^{\nu} \left(X_j^{\nu+1} - X_j^{\nu} \right) \quad \text{for } k = 1,\ldots,K \tag{8.24}$$

$$-\tilde{G}_p^{\nu} = \sum_{j=1}^{N+I+M} Z_{N+pj}^{\nu} \left(X_j^{\nu+1} - X_j^{\nu} \right) \quad \text{for } p = 1,\ldots,I \tag{8.25}$$

$$-\tilde{H}_q^{\nu} = \sum_{j=1}^{N+I+M} Z_{N+I+qj}^{\nu}\left(X_j^{\nu+1} - X_j^{\nu}\right) \quad \text{for } q = 1,\ldots,M \tag{8.26}$$

where Z_{ij}'s are elements of the Jacobian matrix. Equations 8.23 through 8.26 can be written in matrix form as

$$\begin{bmatrix} Z_{11} & \cdots & Z_{1(N+I+M)} \\ \vdots & & \vdots \\ Z_{(N+I+M)1} & \cdots & Z_{(N+I+M)(N+I+M)} \end{bmatrix} \begin{bmatrix} \Delta X_1 \\ \vdots \\ \Delta X_{(N+I+M)} \end{bmatrix} = \begin{bmatrix} -\tilde{E}_1 \\ \vdots \\ -\tilde{E}_{(N-K)} \\ -\tilde{F}_1 \\ \vdots \\ -\tilde{F}_K \\ -\tilde{G}_1 \\ \vdots \\ -\tilde{G}_I \\ -\tilde{H}_I \\ \vdots \\ -\tilde{H}_M \end{bmatrix}$$

where the Jacobian and the right-side vector are calculated for ν^{th} iteration step and ΔX_j's are given by:

$$\Delta X_j = X_j^{\nu+1} - X_j^{\nu} \tag{8.27}$$

For n = 1,…,(N-K), the elements of the Jacobian i.e. Z_{nj}'s are defined as

$$Z_{ni} = \frac{\partial \tilde{E}_n}{\partial X_i} = \frac{\partial \tilde{E}_n}{\partial M_i}\frac{\partial M_i}{\partial X_i} \quad \text{for } i = 1,\ldots,(N+I+M) \tag{8.28}$$

Equation 8.16 gives

$$\frac{\partial M_i}{\partial X_i} = M_i \ln 10 \tag{8.29}$$

and Eqs. 8.17 and 8.19 give

$$\frac{\partial \tilde{E}_n}{\partial M_i} = \sum_{j=1}^{J+I+M} \frac{\partial \tilde{E}_n}{\partial Y_j}\frac{\partial Y_j}{\partial M_i} \tag{8.30}$$

$$\frac{\partial \tilde{E}_n}{\partial Y_j} = \begin{cases} \tilde{h}_{nj} & \text{for } 1 \le j \le J \\ \tilde{f}_{n(j-J)} & \text{for } (J+1) \le j \le (J+I) \\ \tilde{e}_{n(j-J-I)} & \text{for } (J+I+1) \le j \le (J+I+M) \end{cases} \tag{8.31}$$

Also from Eq. 8.17

$$\frac{\partial Y_j}{\partial M_i} = \frac{K_j a_{ji}}{M_i} \prod_{i=1}^{N+I+M} M_i^{a_{ji}} = \frac{Y_j a_{ji}}{M_i} \tag{8.32}$$

Equations 8.28 through 8.32 can be combined to calculate the first (N-K) rows of elements of the Jacobian matrix as

$$Z_{ni} = M_i \ln 10 \left[\sum_{j=1}^{J} \frac{Y_j \tilde{h}_{nj} a_{ji}}{M_i} + \sum_{j=(J+1)}^{J+I} \frac{Y_j \tilde{f}_{n(j-J)} a_{ji}}{M_i} + \sum_{j=(J+I+1)}^{J+I+M} \frac{Y_j \tilde{e}_{n(j-J-I)} a_{ji}}{M_i} \right] \tag{8.33}$$

For n = (N-K+1),…,N, from Eqs. 8.20, we have

$$Z_{ni} = \frac{\partial \tilde{F}_n}{\partial X_i} = \begin{cases} w_{(n-N+K)i} & \text{for } 1 \le i \le N \\ 0 & \text{for } (N+1) \le i \le (N+I+M) \end{cases} \tag{8.34}$$

Similarly, for n = (N+1),…,(N+I-1), from Eqs. 8.21a, the Z_{ni}'s can be calculated as

$$Z_{ni} = \frac{\partial \tilde{G}_{(n-N)}}{\partial X_i} = \begin{cases} d_{(n-N)i} & \text{for } 1 \le i \le (N+I) \\ 0 & \text{for } (N+I+1) \le i \le (N+I+M) \end{cases} \tag{8.35}$$

For n = (N+I), from Eqs. 8.21b, the Z_{ni}'s are

$$Z_{ni} = \frac{\partial \tilde{G}_{(n-N)}}{\partial X_i} = \begin{cases} 0 & \text{for } 1 \le i \le N \\ \bar{z}_{(i-N)} M_i \ln 10 & \text{for } (N+1) \le i \le (N+I) \\ 0 & \text{for } (N+I+1) \le i \le (N+I+M) \end{cases} \tag{8.36}$$

For n = (N+I+1),…,(N+I+M-1), Eqs. 8.22a give

$$\begin{aligned} Z_{ni} &= \frac{\partial \tilde{H}_{(n-N-I)}}{\partial X_i} = \frac{\partial \tilde{H}_{(n-N-I)}}{\partial X_i} \frac{\partial M_i}{\partial X_i} \\ &= \ln 10 \left[b_{(n-N-I)} \prod_{j=1}^{N+I+M} M_j^{b_{(n-N-I)j}} - \beta^{exm}_{(n-N-I)} K_A a_{Ai} \prod_{j=1}^{N+I+M} M_j^{a_{Aj}} \right] \quad \text{for } i = 1,\ldots,(N+I+M) \end{aligned} \tag{8.37}$$

Finally, for n = (N+I+M), from Eq. 8.22b

$$Z_{ni} = \frac{\partial \tilde{H}_{(n-N-I)}}{\partial X_i} = \ln 10 \left[-k_A a_{Ai} \prod_{j=1}^{N+I+M} M_j^{a_{Aj}} + \bar{\bar{z}}_{(i-N-I)} M_i \right] \tag{8.38}$$

For $i \le (N+I)$, the second term inside the bracket of the above equation is zero since only species adsorbed on the micellar surface are considered in this charge balance equation.

Given the $[X_j : j = 1,\ldots,(N+I+M)]$ for the ν^{th} iteration, the corresponding $[\tilde{E}_n : n = 1,\ldots,(N-K)]$, $[\tilde{F}_k : k = 1,\ldots,K]$, $[\tilde{G}_i : i = 1,\ldots,I]$ and $[\tilde{H}_m : m = 1,\ldots,M]$ can be calculated using Eqs. 8.16, 8.17 and 8.19 through 8.22b. The elements of the Jacobian are then calculated using Eqs. 8.33 through 8.38. Solving the set of Eqs.8.23 through 8.26 simultaneously, gives the X_i's for the $(\nu+1)^{th}$ iteration step.

This iteration procedure continues until the following convergence criteria are met:

$$\begin{aligned}
&\left|\tilde{E}_n\right| \le \varepsilon \quad \text{for } 1 \le n \le (N-K)\\
&\left|\tilde{F}_n\right| \le \varepsilon \quad \text{for } 1 \le n \le K\\
&\left|\tilde{G}_n\right| \le \varepsilon \quad \text{for } 1 \le n \le I\\
&\left|\tilde{H}_n\right| \le \varepsilon \quad \text{for } 1 \le n \le M
\end{aligned} \tag{8.39}$$

8.4.5 Determination of the Assemblage and Concentration of Solids

Once these criteria are met, a check for solubility product constraints for all solid species which were assumed absent in the above iteration process is done. If for any of these solids, the calculated right-side of solubility product constraint (Eq. 8.4) is found to exceed its solubility product, then this solid is assumed present and the iteration process is repeated with this new set of solids. This process is repeated until solubility product constraints for all possible solids are satisfied.

At this point, to calculate the solid concentrations, Eqs. 8.1 are put in the form:

$$T_n = \sum_{k=1}^{K} g_{nk}\hat{C}_k \quad \text{for } n = 1,\ldots,N \tag{8.40}$$

where

$$T_n = C_n^T - \left[\sum_{j=1}^{J} h_{nj}C_j + \sum_{i=1}^{I} f_{ni}\bar{C}_i + \sum_{m=1}^{M} e_{nm}\bar{\bar{C}}_m\right] \tag{8.41}$$

Equations 8.40 are a set of N linear equations. A relevant set of K equations are selected, such that the resulting matrix consisting of g_{nk}'s is non-singular, to determine the solid concentrations $\hat{C}_k$'s by simple Gaussian elimination. If some of the solid concentrations calculated here have negative values smaller than some small negative number, ε_0, then the solid with the smallest negative concentration is assumed absent and whole process of Newton-Raphson iteration and solid assemblage determination is repeated with this new set of solids. If none of the calculated solid concentrations is negative, then that set of the solids represents the correct assemblage and those are the concentrations of the solids in equilibrium.

8.4.6 Dampening of the Newton-Raphson Iteration

Whenever a numerical iterative procedure like the Newton-Raphson method is used, there are circumstances under which the method may fail to converge to a solution. Many times such divergence occurs because one or more of the ΔX_j values calculated in a particular iterative step are unusually large in

their absolute values. This causes the next guess of these variables to be very poor causing failure of the method to converge to a solution.

When such cases of divergence occur, the Newton-Raphson iteration may be repeated by not allowing the absolute values of ΔX_j for any j and any iteration step to be larger than a specified maximum value. Following Walsh [1983], a value of 2 is used for this specified maximum. Recalling that the variables X_j's are logarithmic values of concentration variables, this, then, means that we are restricting our independent concentration variables to change by no more than two orders of magnitude in any given iterative step. This somewhat slows down the convergence rate. This dampening procedure is, therefore, kept as an option to be applied only when the conventional method fails to converge to a solution within a reasonable number of iterative steps.

Section 9
UTCHEM Biodegradation Model Formulation and Implementation

This section begins with an overview of biodegradation reactions as a brief review of basic biodegradation concepts. The biodegradation reaction kinetics incorporated into UTCHEM are then described, followed by the method of solution of the biodegradation equations. Finally, model results are compared to analytical solutions and another published biodegradation model to demonstrate that the biodegradation equations are solved accurately.

9.1 Overview of Biodegradation Reactions

A biodegradation reaction is an oxidation-reduction reaction between an electron donor (the substrate, or chemical contaminant) and an electron acceptor (typically oxygen) catalyzed by a microorganism's enzymes. In the reaction, the electron donor is oxidized and transfers its electrons to the electron acceptor, yielding energy for microbial growth. Most bacteria in groundwater aquifers are chemoheterotrophic microorganisms, obtaining from the substrate not only energy for growth but also carbon for building cellular material (Brock *et al.*, 1984).

In general, chemical contaminants are transformed in one of two ways by biodegradation reactions: as a primary substrate or as a cometabolite (McCarty and Semprini, 1993). A compound is biodegraded as a primary substrate when biodegradation of the compound provides carbon and energy that can be utilized by the microorganism. Most organic groundwater contaminants are degraded as primary substrates. A generic biodegradation reaction in which the substrate is biodegraded as a primary substrate is:

$$\text{substrate} + \text{electron acceptor} + \text{microorganisms} \longrightarrow \text{products} + \text{energy} + \text{more microorgansisms} \quad (9.1)$$

Part of the carbon from the parent substrate molecule is used by the microorganism to create additional biomass. The other part of the substrate carbon is oxidized to provide energy for microbial growth.

A compound is biodegraded as a cometabolite when it is transformed fortuitously by enzymes or cofactors produced by the microorganism for other purposes (McCarty and Semprini, 1993). Most halogenated aliphatic hydrocarbons are biodegraded through cometabolism (McCarty and Semprini, 1993). A generic biodegradation reaction in which a compound is biodegraded through cometabolism is:

$$\text{cometabolite} + \text{microorganisms} \xrightarrow{\text{growth substrate + electron acceptor}} \text{products} \quad (9.2)$$

In this reaction, the transformation of the cometabolite provides neither growth nor energy to the microorganism. In fact, biodegradation of the parent cometabolite may even be detrimental to the cell (McCarty and Semprini, 1993). The product of the cometabolic reaction may be transformed further either by cometabolism or as a primary substrate, depending on its composition and structure.

Biodegradation reactions can be classified as either fermentative or respiratory. In fermentation, substrates are only partially oxidized. Electrons are "internally recycled," generally yielding at least one produce that is more oxidized and one that is more reduced than the original substrate (de Blanc *et al.*, 1995). An example fermentation reaction is the fermentation of toluene under methanogenic conditions to yield carbon dioxide and methane. The energy reaction for this process is (Reinhard, 1993):

$$C_7H_8 \longrightarrow 2.5\,CO_2 + 4.5\,CH_4 \quad (9.3)$$

There is no external electron acceptor in this reaction. Part of the toluene molecule is used as the electron donor and part is used as an "internal" electron acceptor.

In respiration reactions, an external electron acceptor is utilized as a terminal electron acceptor in the biodegradation reaction. Respiration reactions are either aerobic or anaerobic. Oxygen is the terminal

electron acceptor in aerobic reactions, while an electron acceptor other than oxygen is the electron acceptor in anaerobic reactions. Examples of anaerobic respiration energy reactions with various electron acceptors for the transformation of toluene are (Reinhard, 1993):

Aerobic (oxygen):

$$C_7H_8 + 9\ O_2 \longrightarrow 7\ CO_2 + 4\ H_2O \tag{9.4}$$

Anaerobic (nitrate):

$$C_7H_8 + 7.2\ NO_3^- + 7.2\ H^+ \longrightarrow 7\ CO_2 + 3.6\ N_2 + 7.6\ H_2O \tag{9.5}$$

Anaerobic (sulfate):

$$C_7H_8 + 4.5\ SO_4^{2-} + 3\ H_2O \longrightarrow 2.25\ H_2S + 2.25\ HS^- + 7\ HCO_3^- + 0.25\ H^+ \tag{9.6}$$

Anaerobic (ferric iron):

$$C_7H_8 + 36\ Fe^{3+} + 21\ H_2O \longrightarrow 7\ HCO_3^- + 36\ Fe^{2+} + 43\ H^+ \tag{9.7}$$

It is possible for some or even all of these reactions to occur in an aquifer, as redox conditions can vary substantially as a result of contaminant biodegradation or other natural conditions.

9.2 Biodegradation Model Concept and Capabilities

The basic conceptual biodegradation model in UTCHEM is illustrated in Figure 2-1. Biodegradable organic constituents dissolve out of the NAPL into the aqueous phase where they can serve as substrates for unattached bacteria. However, since most bacteria are attached to solid surfaces (Harvey *et al.*, 1984), most of the substrate will be removed from the aqueous phase by biodegradation reactions within attached biomass.

In UTCHEM, the attached biomass exists as small microcolonies, each made up of bacterial cells and extra-cellular material. In this microcolony concept, first proposed by Molz *et al.* (1986), it is assumed that the specific surface area of the microcolonies can be measured or estimated. Each microcolony is separated from the bulk aqueous phase by a stagnant liquid film, or diffusion layer. Substrates, electron acceptors, and other nutrients that attached microorganisms require for growth must diffuse across this liquid layer to become available to attached biomass. The concentration of all chemical species is assumed to be uniform within the attached biomass, so that the attached biomass behaves essentially as a reactive surface.

UTCHEM simulates the destruction of substrates, the consumption of electron acceptors, and the growth of biomass. Substrates can be biodegraded by free-floating microorganisms in the aqueous phase or by attached biomass present as microcolonies in the manner of Molz *et al.* (1986). The model accommodates multiple substrates, electron acceptors, and biological species. Important general assumptions for the biodegradation model are listed below.

- Biodegradation reactions occur only in the aqueous phase.
- Microcolonies are fully penetrated; i.e., there is no internal resistance to mass transport within the attached biomass.
- Biomass is initially uniformly distributed throughout the porous medium.

- Biomass is prevented from decaying below a lower limit by metabolism of naturally occurring organic matter unless cometabolic reactions act to reduce the active biomass concentrations below natural levels.

- The area available for transport of organic constituents into attached biomass is directly proportional to the quantity of biomass present.

- The number of cells per microcolony, biomass density, and microcolony volume are constant, so that mass per microcolony is also constant.

- Biodegradation reactions occur independently without mutual effects unless explicitly linked through competition or inhibition terms.

- Adsorption of biomass onto solids can be described with equilibrium partitioning.

- Chemical species within attached biomass do not adsorb to aquifer solids.

The biodegradation model has the following capabilities and features:

- selection of Monod, first-order, or instantaneous biodegradation kinetics.

- first-order abiotic decay reactions.

- external mass transfer resistances to microcolonies (mass transfer resistances can be ignored by the user if desired).

- enzyme competition between multiple substrates.

- inhibition of biodegradation by electron acceptors and/or toxic substrates.

- formation of biodegradation or abiotic reaction by-products.

- nutrient limitations to biodegradation reactions.

- modeling of aerobic cometabolism with transformation capacities and reducing power limitations using the model of Chang and Alvarez-Cohen (1995).

9.3 Mathematical Model Formulation

The basic conceptual biodegradation model in UTCHEM is illustrated in Figure 9.1. Biodegradable organic constituents dissolve out of the NAPL into the aqueous phase where they can serve as substrates for unattached bacteria. However, since most bacteria are attached to solid surfaces (Harvey *et al.*, 1984), most of the substrate will be removed from the aqueous phase by biodegradation reactions within attached biomass.

The complete set of biodegradation model equations in their most general form is included in Appendix B of the UTCHEM Technical Documentation. These equations are similar to those proposed by Molz *et al.* [1986] and Widdowson *et al.* [1988]. However, the UTCHEM model expands on the Molz *et al.* [1986] model and the formulation differs from that of Molz in several important respects:

1. The UTCHEM model expands the Molz *et al.* (1986) model to accommodate an unlimited number of substrates, electron acceptors, and biological species.

2. The UTCHEM model incorporates rate limitations from competition and lack of nutrients, which are not included in the Molz *et al.* (1986) or Widdowson *et al.* (1988) models.

3. Substrates can be biodegraded by either free-floating or attached microorganisms at different rates, whereas all biomass in the Molz *et al.* (1986) model is attached.

4. Aerobic cometabolism utilizing a transformation capacity and reducing power limitations can be modeled with UTCHEM.

5. In UTCHEM, the biodegradation equations are solved separately from the flow system, whereas they are solved simultaneously in the Molz *et al.* (1986) model.

6. In the Molz *et al.* (1986) model, local steady state conditions are assumed between the bulk aqueous phase and the attached biomass, so that the rate of chemical transport into the attached biomass is equal to the rate of chemical destruction within the biomass. This assumption results in a set of differential and algebraic equations. The steady state assumption is not made in UTCHEM, so that the biodegradation equations consist of a system of only ordinary differential equations.

Other later models also include some of these capabilities. However, to the best of the author's knowledge, no other models combine such a comprehensive treatment of biodegradation reactions with multi-phase flow.

The basic structure of the model equations can be more easily seen when they are simplified to apply to a system of a single substrate, electron acceptor and biological species:

$$\frac{dS}{dt} = -\frac{\beta\kappa\bar{X}}{m_c}(S-\bar{S}) - \frac{\mu_{max}X}{Y}\left(\frac{S}{K_S+S}\right)\left(\frac{A}{K_A+A}\right) - k_{abio}S \tag{9.8}$$

$$\frac{d\bar{S}}{dt} = \frac{\beta\kappa}{V_c}(S-\bar{S}) - \frac{\mu_{max}\rho_x}{Y}\left(\frac{\bar{S}}{K_S+\bar{S}}\right)\left(\frac{\bar{A}}{K_A+\bar{A}}\right) - k_{abio}\bar{S} \tag{9.9}$$

$$\frac{dA}{dt} = -\frac{\beta\kappa\bar{X}}{m_c}(A-\bar{A}) - \frac{\mu_{max}XE}{Y}\left(\frac{S}{K_S+S}\right)\left(\frac{A}{K_A+A}\right) \tag{9.10}$$

$$\frac{d\bar{A}}{dt} = \frac{\beta\kappa}{V_c}(A-\bar{A}) - \frac{\mu_{max}\rho_x E}{Y}\left(\frac{\bar{S}}{K_S+\bar{S}}\right)\left(\frac{\bar{A}}{K_A+\bar{A}}\right) \tag{9.11}$$

$$\frac{dX}{dt} = \mu_{max}X\left(\frac{S}{K_S+S}\right)\left(\frac{A}{K_A+A}\right) - bX \tag{9.12}$$

$$\frac{d\bar{X}}{dt} = \mu_{max}\bar{X}\left(\frac{\bar{S}}{K_S+\bar{S}}\right)\left(\frac{\bar{A}}{K_A+\bar{A}}\right) - b\bar{X} \tag{9.13}$$

where

S = aqueous phase substrate concentration (ML^{-3})

$\bar{S}$ = substrate concentration in attached biomass (ML^{-3})

A = aqueous phase electron acceptor concentration (ML^{-3})

$\overline{A}$ = electron acceptor concentration in attached biomass (ML^{-3})

X = aqueous phase (unattached) biomass concentration (ML^{-3})

$\overline{X}$ = attached biomass concentration; mass of attached cells per volume of aqueous phase (ML^{-3})

β = surface area of a single microcolony (L^2)

κ = mass transfer coefficient (LT^{-1})

μ_{max} = maximum specific growth rate (T^{-1})

m_c = mass of cells in a single microcolony; $m_c = \rho_x V_c$ (M)

E = mass of electron acceptor consumed per mass of substrate biodegraded

ρ_x = biomass density; mass of cells per volume of biomass (ML^{-3})

V_c = volume of a single microcolony (L^3)

Y = yield coefficient; mass of cells produced per mass of substrate biodegraded

K_S = substrate half-saturation coefficient (ML^{-3})

K_A = electron acceptor half-saturation coefficient (ML^{-3})

k_{abio} = first-order reaction rate coefficient (for abiotic decay reactions, T^{-1})

b = endogenous decay coefficient (T^{-1})

t = time (T)

Equation 9.8 describes three mechanisms for loss of substrate in the aqueous phase. The first expression describes diffusion of substrate from the bulk liquid across a stagnant liquid film into attached biomass. The second expression in Eq. 9.8 describes the biodegradation of substrate by unattached microorganisms in the bulk liquid. The rate of substrate loss is affected by the substrate and electron acceptor concentrations through the Monod terms. Substrate competition, nutrient limitations, inhibition, and reducing power limitations can also be incorporated into this second expression as described in the following sections. The third expression accounts for abiotic loss of the substrate through first-order reactions. One equation of the same form as Eq. 9.8 is written for each substrate.

Equation 9.9 describes the loss of substrate within attached biomass and is written for a single microcolony (Molz *et al.*, 1986). This equation describes the diffusion of substrate into attached biomass, biodegradation of the substrate within the biomass, and abiotic decay of the substrate. As in Eq. 9.8, expressions accounting substrate competition, nutrient limitations, inhibition, and reducing power limitations can be incorporated into the expression for biodegradation of the substrate.

Equations 9.10 and 9.11 describe the loss of the electron acceptor. These equations are of the same form as Eqs. 9.8 and 9.9 in that they describe diffusion across a liquid film and loss in biodegradation reactions. The second expressions in these equations are multiplied by the factor E, the mass of electron acceptor consumed per mass of substrate biodegraded. Equations similar to Eqs. 9.8 and 9.9 are written for all other chemical species participating in biodegradation reactions. For other chemical species, the factor E is the mass of the chemical species generated or consumed per mass of substrate biodegraded.

Equations 9.12 and 9.13 describe the growth and decay of unattached and attached biomass, respectively. The relationship between the attached biomass concentration $\overline{X}$ appearing in Eqs. 9.8, 9.10, and 9.13 to the biomass density, microcolony volume and microcolony mass is

$$\overline{X} = \frac{C_c \rho_b m_c}{n \phi} \tag{9.14}$$

where C_c is the number of cells per mass of solid, ρ_b is the bulk density of the porous medium, n is the number of cells per microcolony (a constant), and ϕ is the porosity. Since the biomass density, number of cells per microcolony, porosity, and mass per microcolony are assumed to be constant, changes in $\overline{X}$ actually correspond to changes in C_c, or alternately, to C_c/n, the number of microcolonies (Molz *et al.*, 1986). The area available for transport of species from the aqueous phase to the biomass is directly proportional to $\overline{X}$ because the surface area per microcolony is constant.

The assumption that the surface area available for mass transfer is directly proportional to the biomass concentration is not valid if the area covered by biomass exceeds the surface area of the porous medium. This is a limitation of the model that could be overcome in the future by altering the model to limit the maximum mass transfer area to the surface area.

If external mass transport is ignored, then Eqs. 9.8 and 9.10 are not required. If all biomass is assumed to be attached, then the system of equations is reduced to three equations consisting of Eq. 9.13 and a single equation each for loss of the substrate and electron acceptor:

$$\frac{dS}{dt} = -\frac{\mu_{max} \overline{X}}{Y} \left(\frac{S}{K_S + S} \right) \left(\frac{A}{K_A + A} \right) - k_{abio} S \tag{9.15}$$

$$\frac{dA}{dt} = -\frac{\mu_{max} \overline{X} E}{Y} \left(\frac{S}{K_S + S} \right) \left(\frac{A}{K_A + A} \right) \tag{9.16}$$

where $\overline{X}$ is the concentration of attached biomass and all other concentrations are aqueous phase concentrations.

When biodegradation reactions that involve more than one substrate are being modeled, equations of the same form as Eqs. 9.8 and 9.9 (or 9.15) are solved for each additional substrate. Similarly, equations of the form of Eqs. 9.10 and 9.11 (or 9.16) are solved for each additional electron acceptor. Substrates can be biodegraded by microorganisms using more than one electron acceptor, and each electron acceptor can be used for biodegradation of multiple substrates. Multiple biological species can also be simulated by solving additional equations similar to Eqs. 9.12 and 9..13 for each biological species.

9.3.1 Substrate Utilization Options

The substrate loss term in UTCHEM is always structured as the second term in Eqs. 9.8 or 9.9. However, by manipulating the variables in the substrate loss term, many different types of biodegradation kinetics can be simulated. Six of the most common models of substrate utilization and biomass growth are:

1. multiplicative Monod kinetics
2. Monod kinetics with no biomass growth
3. second-order kinetics (pseudo first order; i.e., first-order in both biomass and substrate)
4. first-order kinetics
5. zero-order kinetics
6. instantaneous kinetics (stoichiometric reaction)

With multiplicative Monod kinetics, it is assumed that the substrate, electron acceptor, and other limiting nutrients all limit microbial growth. The substrate utilization expression in Eqs. 9.8 and 9.9 are an example of multiplicative Monod kinetics. When other chemical species or nutrients such as nitrogen or phosphorous limit the reaction, the substrate utilization expression is modified to account for the additional limitations in substrate utilization rate:

$$r_S = \frac{dS}{dt} = -\frac{\mu_{max} X}{Y}\left(\frac{S}{K_S + S}\right)\left(\frac{A}{K_A + A}\right)\left(\frac{N}{K_N + N}\right) \tag{9.17}$$

where

r_S = rate of substrate utilization ($ML^{-3}T^{-1}$)

N = concentration of a limiting nutrient (ML^{-3})

K_N = limiting nutrient half-saturation coefficient concentration (ML^{-3})

If substrate utilization through Monod kinetics and a constant biomass population is desired, then μ_{max} can be set to a very small value, and Y can be set to a value such that the ratio μ_{max}/Y is equal to the desired rate of maximum substrate utilization.

If first-order degradation of the substrate is desired and biomass growth is considered (second-order kinetics overall), then K_S can be set to very large value, and the ratio of μ_{max}/K_S can be set to the desired maximum biomass growth rate. This parameter selection will result in approximate first-order destruction of the substrate and approximate first-order growth of biomass. K_A must also be set to a very small value if electron acceptor Monod limitations are not desired.

First-order decay of the substrate without consideration of biomass growth or the electron acceptor can be simulated by setting μ_{max} to 0 and using the abiotic decay option to decay the substrate.

Zero order kinetics can be approximated by specifying small value of μ_{max}, K_S and K_A, such that the expression $\mu_{max}X/Y$ is equal to the desired 0 order rate constant.

Instantaneous kinetics can be selected by the user as an option, and are modeled with the superposition method in the manner described by Borden and Bedient [1986] in the Bioplume II model:

Substrate limiting:

$$A = ES;\ S = 0 \tag{9.18}$$

Electron acceptor limiting:

$$S = \frac{A}{E};\ A = 0 \tag{9.19}$$

Equations 9.18 and 9.19 mean that when the substrate is the limiting reactant in a particular grid block, all of the substrate is consumed, while the mass of electron acceptor consumed is the stoichiometric ratio of the mass of electron acceptor consumed per mass of substrate biodegraded. When the electron acceptor is the limiting reactant, all of the electron acceptor is consumed, while the mass of substrate consumed is the mass of electron acceptor consumed divided by the stoichiometric ratio of the mass of electron acceptor consumed per mass of substrate biodegraded. Instantaneous kinetics can only be used to describe the biodegradation of a single substrate by a single electron acceptor in UTCHEM. The concentration of biomass is implicitly assumed constant when instantaneous kinetics are used.

9.3.2 Biomass Growth and Adsorption

The basic biomass growth expression of Eqs. 9.12 and 9.13 contains an additional term to limit the volume of the biomass. With this limitation, the general form of the biomass growth expression is:

$$\frac{dX}{dt} = \mu_{max} X \left(\frac{S}{K_A + S} \right) \left(\frac{A}{K_A + A} \right) \left(\frac{0.9(1 - X)}{\rho_X} \right) - bX \tag{9.20}$$

where ρ_X is the biomass density (typically about 0.1 g/cm^3). The linear biomass growth expression limits the total volume of biomass to 90% of the aqueous phase volume. At low biomass concentrations typical of many in situ remediation systems and most intrinsic bioremediation environments, the growth limiting expression has a negligible effect on biomass growth and substrate utilization rates because the biomass occupies such a small volume of the total pore space. For example, using typical sizes of bacterial cells, a biomass density of 0.09 g/cm^3 and a typical initial biomass population of 1×10^6 cells per gram of soil, the biomass pore volume fraction is about 4×10^{-6}. The biomass volume would have to increase by over five orders of magnitude before the biomass saturation approached 1.

When the biomass concentration begins to occupy a significant fraction of the pore volume, as might be expected near in-situ bioremediation injection wells and laboratory column experiments, the key model assumption that biofilms in the pore space are thin and fully penetrated is likely to be violated. The reduction (or near cessation) of biomass growth becomes less important than biofilm mass transport effects, which are not considered in the model. Thus, using the linear growth limitation expression, the model only crudely approximates biological growth in grid blocks occupied by a substantial volume of biomass. At low biomass concentrations, the term has an insignificant effect.

The biodegradation model also limits the minimum attached biomass concentration to a user-defined concentration. Naturally occurring organic matter in the aquifer is assumed to support this minimum microbial population. The user can set the minimum biomass concentration to 0 if desired.

Adsorption of biomass is simulated using equilibrium partitioning, except that a minimum concentration of biomass is assumed to exist on the aquifer solids. Only the biomass that is not part of this minimum population partitions between the aqueous phase and the aquifer solids. The total biomass in the aquifer consists of the attached biomass and the unattached biomass:

$$X_T = X + \overline{X} \tag{9.21}$$

where X_T is the total biomass, X is the aqueous phase biomass, and $\overline{X}$ is the attached biomass. The attached biomass is composed of the minimum biomass population ($\overline{X}_{min}$, which does not partition between the solid and the aqueous phase) and the biomass in equilibrium with the aqueous phase biomass:

$$\overline{X} = \overline{X}_{min} + K_X X \tag{9.22}$$

Substituting the equilibrium relationship of Eq. 9.22 into the mass balance . 9.21 results in the following equilibrium concentration of aqueous phase biomass:

$$X = \frac{X_T - \overline{X}_{min}}{K_X + 1} \tag{9.23}$$

The attached biomass concentration is then calculated from Eq. 9.22. A K_X of infinity would mean that all of the biomass is attached, while a K_X of 0 would mean that all of the biomass, except for $\overline{X}_{min}$, would exist in the aqueous phase.

9.3.3 Substrate Competition

When substrate competition is considered, the half-saturation coefficient of each substrate Monod term is decreased based on the concentration and half-saturation coefficient of the other competing substrates. For example, if substrate 1 and substrate 2 compete for the same enzyme, then the Monod expressions for the two substrates would be (Bailey and Ollis, 1986):

Substrate 1:

$$\frac{S_1}{K_{S,1}\left(1+\frac{S_2}{K_{S,2}}\right)+S_1}$$

Substrate 2:

$$\frac{S_2}{K_{S,2}\left(1+\frac{S_1}{K_{S,1}}\right)+S_2}$$

where:

S_1, S_2 = concentration of substrates 1 and 2, respectively (ML^{-3})

$K_{S,1}$, $K_{S,2}$ = half-saturation coefficients of substrates 1 and 2, respectively (ML^{-3})

This formulation is extended to include the number of substrates that compete for the pertinent enzyme. When modeled in this manner, substrate competition reduces the effective rate of biodegradation over the rate that would exist in the absence of competition. The competitive effect on substrate 1 is most significant when the ratio $S_2/K_{S,2}$ is large relative to $K_{S,1}$ and increases as S_1 decreases relative to S_2.

9.3.4 Inhibition

Inhibition effects are taken into account by multiplying the substrate biodegradation rate expression by an inhibition factor of the form (Widdowson *et al.*, 1988):

$$\left(\frac{I}{I+C_{ihb}}\right)$$

where I is an experimentally determined inhibition constant. The inhibition factor approaches 0 as the concentration of the inhibiting substance C_{ihb} increases. Inhibition can be used to simulate the sequential use of any number of electron acceptors or to simulate a lowering of biodegradation rates due to the presence of a toxic or otherwise inhibitory compound. The expressions for substrate utilization and biomass growth are multiplied by one inhibition factor for each inhibiting substance.

9.3.5 Aerobic Cometabolism

Aerobic cometabolism is simulated using the model of Chang and Alvarez-Cohen [1995] for the cometabolic biodegradation of trichloroethylene (TCE). The model accounts for both a finite transformation capacity (the maximum possible mass of substrate biodegraded per mass of biomass) and loss of reducing power by the cells. The reducing power limitation occurs because the cells must invest NAD(P)H in the first step of TCE biodegradation, but since the cells derive no energy benefit from the reaction, the NAD(P)H is not regenerated. As a result, cells can become deactivated through reducing power loss when biodegrading TCE in the absence of a growth substrate from which they can replace the NAD(P)H lost from the reaction.

When aerobic cometabolic reactions are considered, the equations describing the loss of cometabolite and attached biomass growth are, in the case of no mass transfer resistances, no inhibition, and no substrate competition (Chang and Alvarez-Cohen, 1995):

$$\frac{dC_C}{dt} = -k_C X\left(\frac{C_C}{K_C + C_C}\right)\left(\frac{A}{K_A + A}\right)\left(\frac{R}{K_R + R}\right) \tag{9.24}$$

$$\begin{aligned}\frac{dX}{dt} = {} & \frac{\mu_{max,S} X}{Y}\left(\frac{S}{K_S + S}\right)\left(\frac{A}{K_A + A}\right)\left(\frac{R}{K_R + R}\right)\left(\frac{0.9(1 - X)}{\rho_x}\right) \\ & - \frac{k_C X}{T_c}\left(\frac{C_C}{K_C + C_C}\right)\left(\frac{A}{K_A + A}\right)\left(\frac{R}{K_R + R}\right) - b\overline{X}\end{aligned} \tag{9.25}$$

where:

k_C = maximum specific cometabolite biodegradation rate ($ML^{-3}T^{-1}$)

C_C = aqueous phase cometabolite concentration (ML^{-3})

R = reducing power (NAD(P)H) concentration within the cells (mass NAD(P)H/mass biomass)

K_R = NAD(P)H half-saturation constant (mass NAD(P)H/mass biomass)

K_C = cometabolite half-saturation coefficient (ML^{-3})

$\mu_{max,S}$ = maximum specific growth rate on growth substrate (T^{-1})

T_c = transformation capacity (mass cells deactivated/mass cometabolite biodegraded)

When reducing power losses are considered, a mass balance equation is needed to describe the production and consumption of reducing power within the cell:

$$\begin{aligned}\frac{dR}{dt} = {} & -k_C E_{Rc}\overline{X}\left(\frac{C_C}{K_C + C_C}\right)\left(\frac{A}{K_A + A}\right)\left(\frac{R}{K_R + R}\right) \\ & + \frac{\mu_{max} E_{Rp}\overline{X}}{Y}\left(\frac{S}{K_S + S}\right)\left(\frac{A}{K_A + A}\right)\left(\frac{R}{K_R + R}\right)\end{aligned} \tag{9.26}$$

where E_{Rc} is the mass of NAD(P)H consumed per mass of cometabolite biodegraded and E_{Rp} is the mass of NAD(P)H produced per mass of growth substrate biodegraded.

The aerobic cometabolism model in UTCHEM differs slightly from the model of Chang and Alvarez-Cohen [1995] in two respects. First, the reducing power concentration is expressed as a mass of reducing power per mass of biomass, instead of as a mass of reducing power per unit volume of the pore space. By defining the reducing power concentration on a biomass-specific basis, very small biomass populations do not necessarily result in very low reducing power concentrations. The reducing power concentration per cell when the cell population is small could be just as great as the reducing power concentration when the cell population is large. In a second departure from the Chang and Alvarez-Cohen [1995] model, the reducing power concentration is limited to 30% of the microbial mass. As a result, the amount of NAD(P)H stored in the biomass cannot increase without bound.

9.3.6 Mass Transfer

In the UTCHEM biodegradation model, the user can specify whether or not mass transfer limits the rate of biodegradation reactions. If mass transfer is not considered, then equations for bulk phase biodegradation

of substrate and electron acceptor utilization (Eqs. 9.9 and 9.13) are not solved. Instead, Eqs. 9.15 and 9.16 are solved for the substrate and electron acceptor participating in biodegradation reactions.

If mass transfer is considered, then equations similar to Eqs. 9.9 and 9.13 are solved for each species. All mass transfer resistance is assumed to be caused by a stagnant liquid layer adjacent to the biomass across which all chemicals must diffuse to become available to attached microorganisms. The rate of transport of chemical species from the aqueous phase into the biomass is a function of the biomass concentration, the surface area of each microcolony, and the mass transfer coefficient. Since a key assumption of the model is that the surface area available for mass transfer is proportional to the biomass concentration, mass transfer increases linearly with increasing biomass. The surface area per microcolony is a key parameter that must be estimated based on an assumed microcolony geometry or calculated. The mass transfer coefficient of each species *i* is calculated using the correlation of Wilson and Geankoplis (1966):

$$\kappa_i = 1.09 v_1 Re^{-2/3} Sc_i^{-2/3} \tag{9.27}$$

where:

Re = Reynolds number: $Re = \dfrac{d_p \phi S_1 v_1 \rho_1}{\mu_1}$

Sc_i = Schmidt number of component i: $Sc_i = \dfrac{\mu_1}{\rho_1 D_i}$

v_1 = aqueous phase velocity (L/T)

d_p = average soil particle diameter (L)

ϕ = porosity

S_1 = aqueous phase saturation

μ_1 = viscosity (M/L^2T)

ρ_1 = aqueous phase density (M/L^3)

D_i = molecular diffusivity of species i (L^2/T)

Subscript 1 designates the aqueous phase.

As the velocity increases, the mass transfer coefficient also increases as $v^{1/3}$. The Wilson and Geankoplis correlation is valid for $0.0016 < Re < 55$ and $0.35 < \phi S_1 < 0.75$. Since Reynolds numbers are frequently less than 0.0016 for groundwater flow, there is often considerable uncertainty about the true value of the mass transfer coefficient.

If the velocity of the aqueous phase is 0 (in batch simulations, for example), then the mass transfer coefficient cannot be computed using Eq. 9.27. In this case, the mass transfer coefficient is approximated by D_i/d_p, where D_i is the molecular diffusivity of the compound and d_p is the particle diameter.

Mass transfer may be important in only some areas of the modeling domain. The user can select an option to allow UTCHEM to dynamically select the set of equations that include mass transfer only when mass transfer is estimated to be important. The solution of mass transfer equations can be controlled through either a Damköhler number or an effectiveness factor. The Damköhler number (Da_{4M}) is ratio of the maximum rate of biodegradation reaction and the maximum rate of diffusion into attached biomass, and is defined as follows (de Blanc, 1998):

$$Da_{4M} = \frac{\mu_{max} m_c}{\beta \kappa Y S_0}\left(\frac{S}{K_S + S}\right)\left(\frac{A'}{K_A + A}\right) \tag{9.28}$$

Damköhler numbers smaller than about 0.1 generally indicate that mass transfer is not important in biodegradation reactions and can be ignored (de Blanc, 1998).

The effectiveness factor is the rate of reaction when mass transfer is included in biodegradation kinetics divided by the rate of reaction in the absence of mass transfer. The effectiveness factor in UTCHEM is defined as (de Blanc, 1998):

$$\eta = \frac{\bar{S}(K_S + S)\left(\frac{\bar{A}}{K_A + \bar{A}}\right)}{S(K_S + \bar{S})\left(\frac{A}{K_A + A}\right)} \tag{9.29}$$

This definition is the same effectiveness factor reported by Bailey and Ollis [1986] modified by the ratio of bulk phase and intra-biomass electron acceptor concentrations. In the simulation of one-dimensional systems, an effectiveness factor of 0.9 or greater kept the error from neglecting mass transfer to 6 % or less.

Some experimentation is necessary to determine values of the Damköhler number and effectiveness factor that result in an accurate solution of biodegradation problems for each simulation case.

9.4 Porosity and Permeability Reduction

If significant biomass growth occurs in the modeling domain, then the aquifer porosity will be reduced, with a concomitant reduction in aquifer permeability. Porosity and permeability reductions are most likely to occur near the column entrance in laboratory biodegradation systems and near injection wells in field systems. UTCHEM accounts for both porosity and permeability reductions. However, if mass transfer is considered, then the UTCHEM solution will be inaccurate when biomass growth is significant because intra-biomass diffusion is not taken into account, and because the area available for mass transfer is assumed to be directly proportional to the biomass concentration.

Because biological growth is limited to the aqueous phase, porosity reduction occurs at the expense of only the aqueous phase. It is assumed that the biomass boundary grows without simultaneous diffusion of chemical species across the biomass boundary. This is a simplifying assumption that could be modified in the future. If biomass growth is small at each time step, however, the error created by this assumption is small. Because biological growth is limited to 90% of the aqueous phase, the maximum porosity reduction is equal to 90% of the aqueous phase volume.

Permeability in the *x* direction is recalculated at every grid block and time step according to the Carmen-Kozeny equation (Wilkins *et al.*, 1995):

$$k_x = \frac{d_p^2 \phi^3}{300(1-\phi)^2} \tag{9.30}$$

where the units of d_p and k_x are cm. Because y and z permeabilities can be specified by the user independent of the *x* permeability in UTCHEM, they are adjusted using the Carmen-Kozeny porosity functionality:

$$k_2 = k_1 \frac{\phi_2^3 (1-\phi_1)^2}{\phi_1^3 (1-\phi_2)^2} \tag{9.31}$$

where:

k_2 = y or z permeability based on newly calculated porosity

k_1 = y or z permeability based on old porosity

ϕ_1, ϕ_2 = current and newly calculated porosity, respectively

9.5 Biodegradation Model Equation Solution

9.5.1 Solution of the Combined Flow and Biodegradation System

The combined flow and biodegradation system is solved through operator splitting, in which the solution to the flow equations is used as the initial conditions for the biodegradation reactions. This approach is convenient because modifications can be made to the system of biodegradation equations without having to reformulate the partial differential equations that describe advection and dispersion. The operator splitting approach is also attractive from a computational viewpoint because a separate numerical method designed to achieve high accuracy can be applied to each stage (flow stage and biodegradation stage) of the problem solution (Valocchi and Malmstead, 1992).

Operator splitting can create errors in the solution of the combined flow and reaction system that are the result of the operator splitting technique itself (Valocchi and Malmstead, 1992). A method of controlling the error caused by the operator splitting solution technique has been incorporated into UTCHEM. The method uses the product of a dimensionless reaction rate and Courant number to determine how often to call the subroutines that solve the biodegradation equations. This product is equivalent to average over all grid blocks of the rate of substrate loss from the bulk liquid divided by the mass of substrate in the modeling domain. The form of the dimensionless parameter differs with the type of biodegradation kinetics being simulated. When mass transfer is neglected, the parameter is the product of the Courant number and a Damköhler number, designated, $Da_{B,g}Cr_{OS}$. For a one-dimensional simulation, this parameter is (de Blanc, 1998):

$$\begin{aligned} Da_{B,g}Cr_{OS} &= \frac{\mu_{max}\overline{X}\Delta x}{vY(K_S+S)}\left(\frac{A}{K_A+A}\right)\times\frac{v\Delta t_{OS}}{\Delta x} \\ &= \frac{\mu_{max}\overline{X}\Delta t_{OS}}{Y(K_S+S)}\left(\frac{A}{K_A+A}\right) \end{aligned} \tag{9.32}$$

where:

Δx = length of grid block (L)

Δt_{OS} = operator splitting (biodegradation) time step (T^{-1})

When mass transfer is included in the simulation, the dimensionless parameter is the product of the Courant number and the inverse of a Peclet number Cr_{OS}/Pe_2'. For a one-dimensional simulation, the parameter is (de Blanc, 1998):

$$\begin{aligned} \frac{Cr_{OS}}{Pe_2'} &= \frac{\beta\kappa_S\overline{X}_0\Delta x}{vm_cS_0}(S-\overline{S})\times\frac{v\Delta t_{OS}}{\Delta x} \\ &= \frac{\beta\kappa_S\overline{X}_0\Delta t_{OS}}{m_cS_0}(S-\overline{S}) \end{aligned} \tag{9.33}$$

The relative mass error of a simulation resulting from operator splitting has been shown to be approximately one half the value of the dimensionless parameter (Valocchi and Malmstead, 1992; de Blanc, 1998) when the relative mass error due to operator splitting is 10% or less. As implemented in

UTCHEM, this relationship is used together with dimensionless parameter values calculated from the average of the time derivatives of the substrates to determine the maximum allowable time step that will keep the relative mass error of the simulation below the user-specified value rme (de Blanc, 1998):

$$\Delta t_{OS} = 2\text{rme} \times \left[\frac{1}{\frac{1}{S}\frac{dS}{dt}} \right]_{\text{mass-weighted average}} \tag{9.34}$$

Control of the operator splitting error minimizes simulation execution time by solving the biodegradation subroutines only as often as required to maintain the relative mass error in the system. As an example of the execution time savings that can be realized, use of the automatic time step option reduced simulation times of a one-dimensional simulation by 50 to 80 percent (de Blanc, 1998). Greater savings in execution time could be realized for different problems.

9.5.2 Solution of the Biodegradation Equations

The biodegradation equations comprise a system of ordinary differential equations that must be solved at each grid block and each time step after the advection and dispersion terms are calculated. The selection of an appropriate solution method for the system of equations is provided below. The characteristics and numerical solution of this system of equations is discussed in greater detail by de Blanc *et al.* [1996b].

With typical biodegradation and mass transfer parameters, the characteristic times for diffusion into the biomass and reaction within the biomass differ by several orders of magnitude, suggesting that the system of equations may be stiff. A system of equations is considered stiff if at least one eigenvalue of the Jacobian matrix (matrix of partial derivatives) has a large negative real part, and the solution is slowly varying on most of the integration interval of interest (Kahaner, 1989). To determine if the system of equations is stiff, the eigenvalues were calculated for the set of mass transfer and biodegradation kinetic parameters determined for benzene in laboratory columns by Chen *et al.* [1992]. Eigenvalues were determined for the grid block at the column entrance. The real part of the largest negative eigenvalue for this system was approximately -10^6, indicating that the equations are stiff.

An investigation was made to determine whether the stiffness of the equations was likely to change with time and space, so that the equations might be solved more easily in different parts of the modeling domain. To test the stiffness behavior of the system, batch simulations were run with varying substrate and biomass concentrations. The real part of the largest negative eigenvalue for these batch runs varied between -10^6 and -10^8, indicating that the equations were stiff under all conditions. In addition, the eigenvalues for all simulations increased with time. This secondary investigation indicated that a stiff equation solver such as Gear's method (Gear, 1971) is required at all grid blocks and all times during the simulation when mass transfer is included in the model.

The numerical method selected for the solution of the biodegradation equations was SDRIV2 (or DDRIV2 for double precision calculations) published by Kahaner *et al.* (1989). These subroutines use Gear's method to solve the system of ordinary differential equations at each grid block and time step.

9.6 Model Testing

The biodegradation component of UTCHEM was extensively tested to ensure that correct solutions to the biodegradation equations are produced. Two types of testing were performed: 1) batch biodegradation simulations, in which the solutions to the equations provided by the model for simple systems were compared to solutions calculated in spreadsheets, and 2) comparisons of UTCHEM simulation results to analytical solutions and results of other biodegradation models published in the literature.

9.6.1 Batch Testing

UTCHEM can be run in "batch" mode to facilitate comparison of UTCHEM solutions of biodegradation problems to solutions calculated in spreadsheets. UTCHEM is run in batch mode by specifying a

modeling domain of only one grid block. Spreadsheet solutions were calculated using a fully explicit (Euler method) with a very small time step. The UTCHEM model was compared to spreadsheet solutions to test the proper functioning of substrate competition, inhibition, nutrient limitations, product generation, and cometabolism.

A comparison of a UTCHEM simulation and a spreadsheet solution to a simple biodegradation problem is shown in Fig. 9.2. In this batch simulation, a single substrate, electron acceptor, and biological species react for 1 day. The biodegradation parameters are shown in Table 9.1. The UTCHEM solution and spreadsheet solution match exactly, indicating that the UTCHEM biodegradation model correctly solves the biodegradation equations.

Figure 9.3 is a comparison of a batch UTCHEM simulation with results from spreadsheet calculations of the model published by Chang and Alvarez-Cohen [1995]. The biodegradation parameters for this figure are provided in Table 9.2. UTCHEM matches the curves calculated from the spreadsheet exactly. However, the spreadsheet solution of the model differs slightly from the results published by Chang and Alvarez-Cohen for the case in which there is no growth substrate. The reason for the differences between the spreadsheet model solutions and the solution published by Chang and Alvarez-Cohen could not be determined.

9.6.2 Comparison of UTCHEM to Analytical Solutions and Other Models

Complete flow and biodegradation model solutions were also compared to analytical and literature solutions to ensure that the simultaneous transport and biodegradation of substrates and electron acceptors produced reasonable results. Because Monod kinetics is nonlinear, only first-order (in substrate only) kinetics could be compared to analytical solutions. Figure 9.4 compares the UTCHEM solution to the analytical solution for the first-order decay of a substrate injected at a constant rate and concentration in a laboratory column. The analytical solution is solution number C14 of van Genuchten and Alves [1982], with a third-type boundary condition at the column entrance and a semi-infinite second-type boundary condition at the column exit. The flow and reaction rate parameters for this simulation are shown in Table 9.3. UTCHEM very closely matches the analytical solution.

One-dimensional, single-phase simulations were compared to biodegradation model solutions published by Molz *et al.* [1986]. The flow and biodegradation reaction parameters for these simulations are given in Table 9.4. Figure 9.5 illustrates the comparison. The model predictions are not exactly the same because of slightly different assumptions about biomass decay, electron acceptor utilization, and adsorption. The boundary conditions are also different in the two models. However, UTCHEM is able to generally reproduce the results of the Molz model, indicating that the combined UTCHEM flow and biodegradation model is functioning properly.

9.7 Biodegradation Model Computer Code

The biodegradation model incorporated into UTCHEM consists of four FORTRAN subroutines that formulate the biodegradation equations and control their solution (BIOSOLVE, BIOREAD, F and G), two biodegradation model utility subroutines (THIRDD and PHABIO), and the ordinary differential equation solver package (DDRIV2 for double precision and SDRIV2 for single precision) published by Kahaner *et al.* [1989]. The name and function of the six biodegradation subroutines are listed in Table 9.5. Subroutines BIOREAD, BIOSOLVE, F, G, and THIRDD were written by the author in their entirety. Subroutine PHABIO was modified by the author to calculate porosity and permeability reductions due to biological growth.

9.8 Example Simulations

The multi-phase flow and biodegradation capabilities of the model are demonstrated through the simulation of hypothetical LNAPL and DNAPL spills. In these simulations, the modeling domain consists of a homogeneous, initially uncontaminated, confined aquifer that is 125 m long by 54 m wide by 6 m thick (see Fig. 9.1). The domain is simulated with 25 grid blocks in the x direction, 11 grid blocks in the y direction, and 5 grid blocks in the z direction. Groundwater is flowing in the positive x direction (left to

right in all figures) with an average velocity of 0.1 m/day. Other flow and physiochemical parameters are listed in Table 9.6. The spills are modeled by injecting NAPL into the center of grid block (x = 5, y = 6, z = 1), which is approximately 22 meters from the left boundary. All chemical species are assumed to be non-adsorbing. There is no air phase in these simulations; the top boundary is a no-flow boundary.

For both of these examples, local equilibrium is assumed between the NAPL and the aqueous phase, so that the concentration of organic constituents in the aqueous phase is calculated by the partitioning relationship:

$$C_{i,aq} = C_{i,sol} x_{i,NAPL} \tag{9.35}$$

where $C_{i,aq}$ is the aqueous phase concentration of component i, $C_{i,sol}$ is the aqueous phase solubility of component i, and $x_{i,NAPL}$ is the volume fraction of component i in the NAPL.

9.8.1 LNAPL Simulation Example

Sequential use of electron acceptors and equilibrium partitioning of multiple components into the aqueous phase are illustrated with an example LNAPL simulation. The LNAPL example simulates a leak of 3.8 m^3 of gasoline containing approximately 1% by volume of benzene and 6% by volume of toluene into a shallow, confined aquifer. The leak is assumed to occur over a four-day period. The groundwater initially contains 8 mg/L oxygen and 10 mg/L nitrate. Parameters used for this simulation are listed in Table 9.7.

Figure 9.7 shows the NAPL saturation history in a vertical slice down the center of the aquifer in the x-z plane. As seen in Fig. 9.7, the NAPL moves little once the NAPL lens is established. The NAPL lens gradually decreases in size as the organic constituents dissolve into the flowing groundwater.

As the benzene and toluene partition out of the gasoline into the aqueous phase, they become available to microorganisms as substrates. For simplicity, a single population of microorganisms capable of biodegrading the benzene and toluene is assumed to exist in the aquifer. This biological species biodegrades both benzene and toluene aerobically and biodegrades toluene anaerobically with nitrate as the electron acceptor. Abiotic decay and biodegradation by free-floating microorganisms are assumed to be negligible (k_{abio} and X are 0). Biodegradation kinetic parameters used for the simulation were obtained from Chen *et al.* [1992].

Figure 9.8 compares the concentration of benzene in the aqueous phase at 500 days to the concentration of benzene that would exist if no biodegradation reactions were occurring. This figure shows that significant biodegradation of dissolved benzene has occurred. The toluene plume is also shown in Fig. 9.8. Although the toluene solubility is three times less than the benzene solubility, the maximum toluene concentration in the aqueous phase is higher than the maximum benzene concentration because its concentration in the gasoline is six times the benzene concentration of the gasoline. Toluene concentrations are nearly as low as benzene concentrations at the fringes of the plume because toluene is biodegraded both aerobically and anaerobically, where oxygen is exhausted, but the benzene is not.

The concentrations of benzene, toluene, oxygen and nitrate at 500 days are compared in Fig. 9.9. Oxygen immediately downgradient of the spill is practically exhausted. Nitrate is also nearly exhausted from the area immediately downgradient of the spill because sufficient time has elapsed since oxygen depletion to allow denitrification to occur. However, at the forward edge of the plume, relatively high nitrate concentrations still exist in areas where oxygen has been depleted, but not exhausted.

9.8.2 DNAPL Simulation Example

Different model capabilities are illustrated with a DNAPL simulation in which trichloroethylene (TCE) is biodegraded through cometabolism. In this simulation, 0.028 m^3 of TCE are spilled in a single day. The cometabolic process is illustrated by injecting water containing methane through five injection wells located approximately 24 meters downgradient of the spill. The injected water contains 20 mg/L methane and 8

mg/L oxygen. The water injection rate is 1.4 m^3 per day per well. The groundwater is assumed to contain 8 mg/L oxygen. Parameters used for the DNAPL simulation example are listed in Table 9.8.

A population of methanotrophic microorganisms, capable of biodegrading TCE aerobically through cometabolism, is assumed to exist in the aquifer. The methanotrophs use methane as the primary substrate and oxygen as the electron acceptor. TCE biodegradation is assumed to reduce the active biomass and consume reducing power of the methanotrophs, so that TCE biodegradation both reduces the active biomass concentration and reduces the active biomass's biodegradation effectiveness. Once biomass has become deactivated, it does not become active again. Biodegradation rate parameters were obtained from Chang and Alvarez-Cohen [1995]. External mass transport of chemical species from the aqueous phase to the biomass was ignored for this example.

The effect of the methane injection wells is illustrated in Fig. 9.10, where concentrations of TCE, a hypothetical TCE tracer, oxygen and methane are shown at 170 days. The TCE tracer is simply TCE that is not allowed to biodegrade in the model so that the effects of biodegradation can be seen. Concentration contours of the different constituents are shown in the top 1.2-m layer of the aquifer. Oxygen is depleted downgradient of the plume, but only a small fraction of the oxygen is consumed upgradient of the methane injection wells. Most of the oxygen upgradient of the wells remains because the high TCE concentrations deactivate the biomass and consume reducing power, preventing the TCE from biodegrading. Even with a small TCE spill, TCE concentrations in the aquifer are so high that most biomass immediately downgradient of the spill is rapidly deactivated. Significant TCE biodegradation occurs only where appreciable methane is present to regenerate the microorganism's reducing power and where TCE concentrations are low. These effects can be seen in Fig. 9.10. The high concentration contours of the TCE and TCE tracer are nearly the same, but biodegradation of the TCE causes a slight retardation in the progress of the TCE plume at low concentrations.

9.9 Tables and Figures

Table 9.1. Biodegradation Kinetic Parameters Used in the Simulation of a Simple Batch Biodegradation Problem

Parameter	Value
Initial substrate concentration, S_0 (mg/L)	10
Initial electron acceptor concentration, A_0 (mg/L)	8
Initial biomass concentration, X_0 (mg/L)	1.53
Biomass maximum specific growth rate, μ_{max} (d^{-1})	1.0
Biomass endogenous decay coefficient, b (d^{-1})	0.02
Biomass yield coefficient , Y (mass X/mass S)	0.5
Electron acceptor utilization coefficient, E (mass A/mass S)	2.0

Table 9.2. Kinetic Parameters for the Batch Biodegradation of TCE by Methanotrophs

Parameter	Value
Initial biomass concentration, X (mg/L)	4.31
Maximum biodegradation rate of TCE, k_c (mg TCE/mg cells-d)	4.2
Maximum specific growth rate for methane, $\mu_{max,me}$ (d^{-1})	0.31
Yield coefficient for methane, Y (mg cells/mg methane)	0.33
TCE transformation capacity, T_c (mg TCE/mg cells)	0.1
Half-saturation coefficient for TCE, K_C (mg/L)	7.0
Half-saturation coefficient for methane, K_S (mg/L)	1.1
Half-saturation coefficient for reducing power, K_R (mmol of e^-/L)	0.54
Reducing power production coefficient, E_{rp} (mmol e^- produced/mg methane biodegraded)	0.5
Reducing power consumption coefficient, E_{rc} (mmol e^- consumed/mg TCE biodegraded)	0.15
Initial reducing power concentration in cells, R_0 (mmol e^-/mg cells)	0.0005

Table 9.3. Flow Parameters for the Solution of the One-Dimensional Advection-Dispersion Equation

Parameter	Value
Average velocity, v (m/d)	1.0
Porosity, ϕ	0.38
Bulk soil density, ρ_b (g/cm^3)	1.64
Longitudinal dispersivity, α_L (m)	0.1
Substrate injection concentration, S_0 (mg/L)	1.0
Column length, L (m)	2.0
Number of grid blocks	25
Numerical time step (d)	0.0001
Simulation time (d)	0.5
Pe	1
Cr	1×10^4

Table 9.4. Simulation Parameters for the Comparison of the UTCHEM Model to the Model of Molz *et al.* [1986]

Parameter	Value
Flow and porous medium parameters	
Column length, L (m)	1.0
Average velocity, v (m/d)	0.5
Porosity, ϕ	0.30
Bulk soil density, ρ_b (g/cm^3)	1.67
Longitudinal dispersivity, α_L (m)	0.0056
Numerical simulation parameters:	
Number of grid blocks	100
Numerical time step (d)	0.001
Simulation time (d)	4
Pe	1.79
Cr	2.2×10^{-2}
Biodegradation kinetic parameters	
Initial concentration of all chemical species (mg/L)	5.0
Substrate injection concentration, S_0 (mg/L)	15.0
Electron acceptor injection concentration, A_0 (mg/L)	5.0
Initial attached biomass population, C_b (cells/g-solid)	6.0×10^{-6}
Biomass density, ρ_X (g/cm^3)	0.09
Colony radius , r_c (cm)	5.0×10^{-4}
Colony thickness , τ_c(cm)	5.0×10^{-4}
Cells/colony, n	100
Substrate retardation coefficient, R_f	1.12
Biomass maximum specific growth rate, μ_{max} (d^{-1})	4.34
Biomass endogenous decay coefficient, b (d^{-1})	0.02
Biomass yield coefficient , Y (mass X/mass S)	0.278
Substrate half-saturation coefficient, K_S (mg/L)	120
Electron acceptor half-saturation coefficient, K_S (mg/L)	0.77
Electron acceptor utilization coefficient, E (mass A/mass S)	0.3892
Substrate mass transfer coefficient, κ_S (cm/d)	1.2
Electron acceptor mass transfer coefficient, κ_A (cm/d)	14.2

Table 9.5. Name and Function of Biodegradation Subroutines Incorporated into UTCHEM

Subroutine Name	Function(s)
BIOREAD	1) Read biodegradation parameters from input file. 2) Initialize biodegradation subroutine variables. 3) Calculate some biodegradation subroutine variable values.
BIOSOLVE	1) Convert UTCHEM volume fraction aqueous phase concentrations to mg/L for use in biodegradation equation solver routine. 2) Determine whether or not the concentration of species participating in biodegradation reactions is large enough to justify solving the reaction system. 3) Calculate mass transfer coefficients. 4) Calculate biomass partitioning. 5) Calculate operator splitting time step required to keep error below user-specified value. 6) Partition aqueous phase concentrations of all species between bulk liquid and biomass. 7) Determine whether or not to solve mass transfer equations based on user option selected. 8) Call subroutine to solve biodegradation equations. 9) Calculate first-order reaction and biomass decay that did not go to completion in biodegradation solution routine. 10) Reset biomass concentration to the minimum biomass concentration if the biomass concentration has fallen below the minimum. 11) Calculate mass of biodegradation species consumed or created through biodegradation reactions.
F	Calculate biodegradation reaction equation derivatives.
G	Determine whether or not to exit biodegradation equation solver subroutine early.
THIRDD	Estimate intra-biomass concentrations of substrates and electron acceptors for each metabolic combination.
PHABIO	Adjust porosity and permeability of each grid block based on the amount of attached biomass growth, and recalculate concentrations.
SDRIV2 or DDRIV2	Solve ordinary differential equations describing biodegradation reactions for the Cray version of UTCHEM (SDRIV2) or the double precision version of UTCHEM (DDRIV2).

Table 9.6. Flow Parameters for All Simulations

average velocity, v (m/d)	0.1
porosity, ϕ	0.38
bulk soil density, ρ_b (g/cm^3)	1.64
longitudinal dispersivity, α_L (m)	5
transverse dispersivity, α_T (m)	0.625
initial oxygen concentration, A_o (mg/L)	8.0
initial nitrate concentration, A_n (mg/L)	10.0

Table 9.7. Parameters for LNAPL Simulation Example

Parameter	Value
Simulation parameters	
Spill volume (m^3)	3.8
Spill duration (d)	4
Physiochemical parameters	
Density of gasoline (g/cm^3)	0.87
Density of benzene (g/cm^3)	0.87
Density of toluene (g/cm^3)	0.86
Solubility of benzene (mg/L)	1,778
Solubility of toluene (mg/L)	500
Initial benzene concentration in NAPL (volume %)	1.1
Initial toluene concentration in NAPL (volume %)	6.1
Mass transfer coefficient for benzene, κ_b (m^2/d)	4.60×10^{-1}
Mass transfer coefficient for toluene, κ_t (m^2/d)	4.26×10^{-1}
Mass transfer coefficient for oxygen, κ_o (m^2/d)	7.92×10^{-1}
Mass transfer coefficient for nitrate, κ_n (m^2/d)	6.52×10^{-1}
Microbial parameters (from Chen *et al*., 1992)	
Initial cell concentration, C_c (cells/g soil)	3.8×10^5
Colony population density, n (cells/microcolony)	100
Biomass density, ρ_x (g/cm^3)	1.0
Microcolony surface area, β (m^2/microcolony)	1.19×10^{-10}
Microcolony volume, V_c (m^3/microcolony)	1.0×10^{-16}
Initial attached biomass concentration, $\overline{X}$ (mg/L)	1.64
Maximum specific growth rate on benzene, $\mu_{max,b}$ (d-1)	4.15
Maximum specific growth rate on toluene, $\mu_{max,t}$ (d-1)	4.95
Yield coefficient for benzene, Y_b (g cells/g benzene)	0.5
Yield coefficient for toluene, Y_t (g cells/g toluene)	0.5
Half-saturation coef. of benzene for oxygen respiration, K_s^{bo} (mg/L)	12.2
Half-saturation coef. of toluene for oxygen respiration, K_s^{to} (mg/L)	17.4
Half-saturation coef. of toluene for nitrate respiration, K_a^{tn} (mg/L)	17.4
Half-saturation coef. of oxygen for benzene biodeg., K_a^{bo} (mg/L)	0.1
Half-saturation coef. of oxygen for toluene biodeg., K_a^{to} (mg/L)	0.01
Half-saturation coef.of nitrate for toluene biodeg., K_a^{tn} (mg/L)	2.6
Endogenous decay coefficient, b (d^{-1})	0.1

Table 9.8. Parameters for DNAPL Simulation Example

Parameter	Value
Simulation parameters	
Spill volume (m3)	0.028
Spill duration (d)	1
Physiochemical parameters	
Density of NAPL (g/cm3)	1.46
Density of TCE (g/cm3)	1.46
Solubility of TCE (mg/L)	1,100
Initial TCE concentration in NAPL (volume %)	50
Microbial parameters	
Initial biomass concentration, X (mg/L)	4.31
Maximum biodegradation rate of TCE, kc (mg TCE/mg cells-d)	4.2
Maximum specific growth rate for methane, _max,m (d-1)	0.31
Yield coefficient for methane, Y (mg cells/mg methane)	0.33
TCE transformation capacity, Tc (mg TCE/mg cells)	0.1
Half-saturation coefficient for TCE, Kc (mg/L)	7.0
Half-saturation coefficient for methane, Ks (mg/L)	1.1
Half-saturation coefficient for reducing power, Kr (mmol of e^-/L)	0.54
Reducing power production coefficient, E_{rp} (mmol e^- produced/mg methane biodegraded)	0.5
Reducing power consumption coefficient, E_{rc} (mmol e^- consumed/ mg TCE biodegraded)	0.15
Initial reducing power concentration in cells, (mmol e^-/mg cells)	0.0005

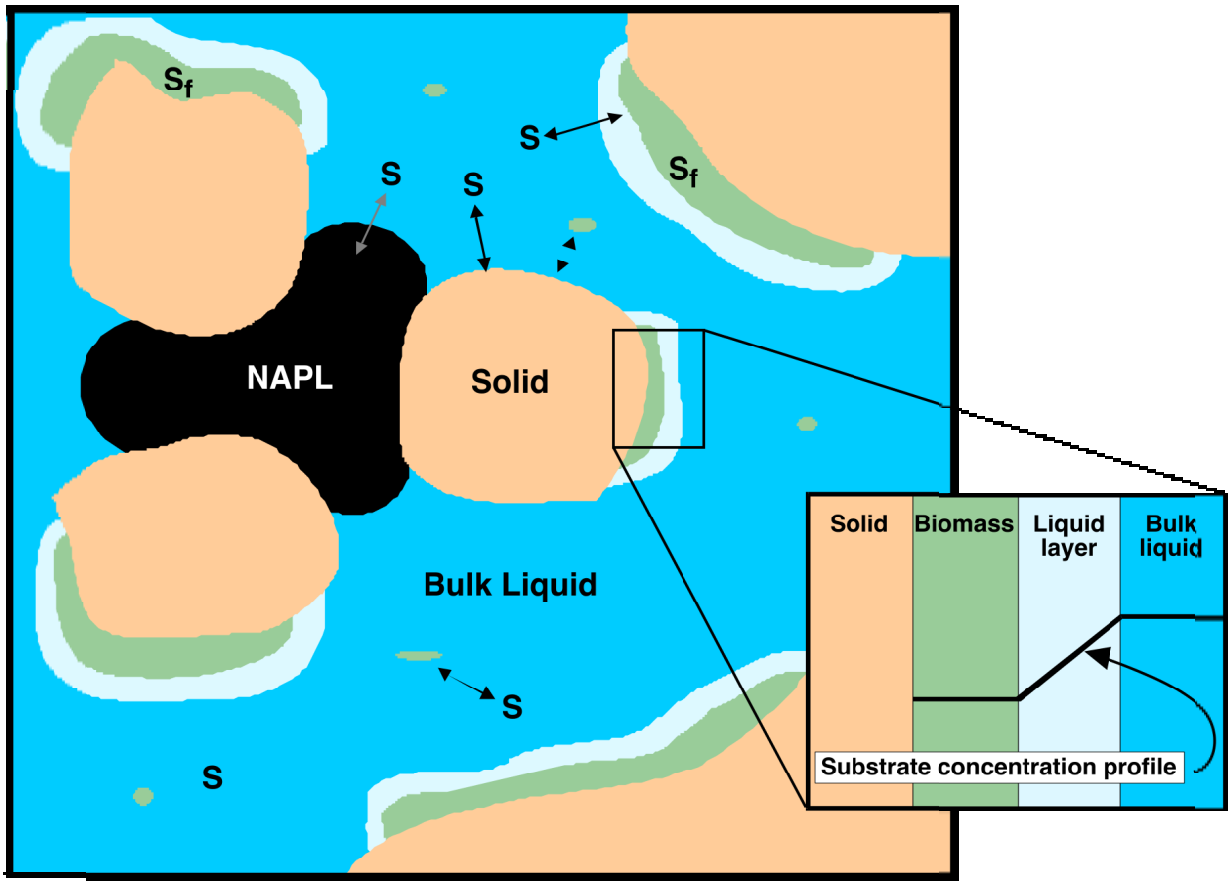

Figure9.1. Conceptual model of biodegradation process. S represents substrate molecules in the bulk liquid that must diffuse across a stagnant liquid layer to become available to attached biomass. The subscript *f* refers to intra-biomass concentrations.

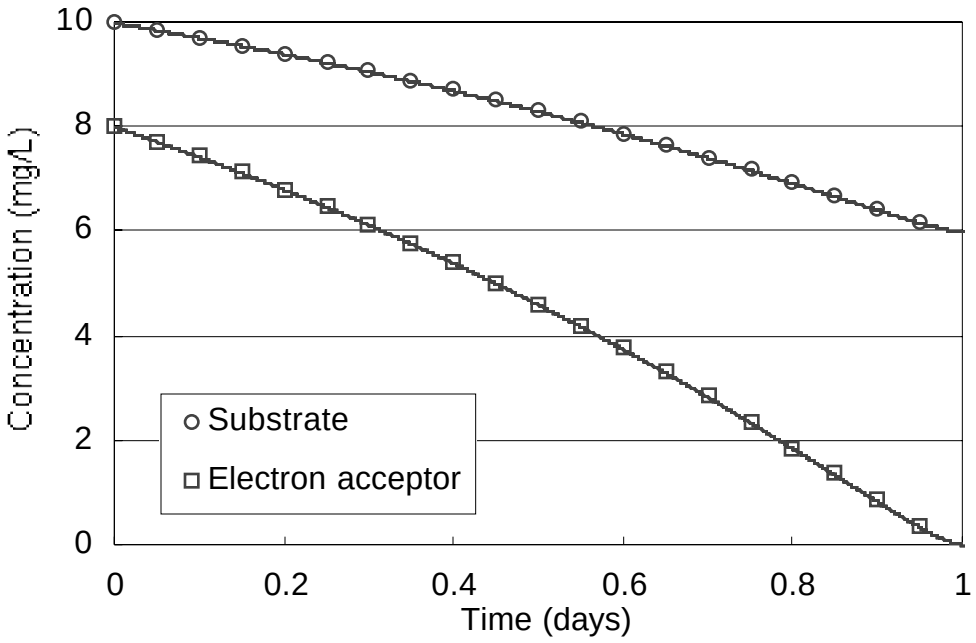

Figure 9.2. Comparison of UTCHEM solution and spreadsheet solution to a simple batch biodegradation problem. Kinetic parameters are given in Table 9.1. The symbols are the UTCHEM solution and the lines are the solution computed in the spreadsheet.

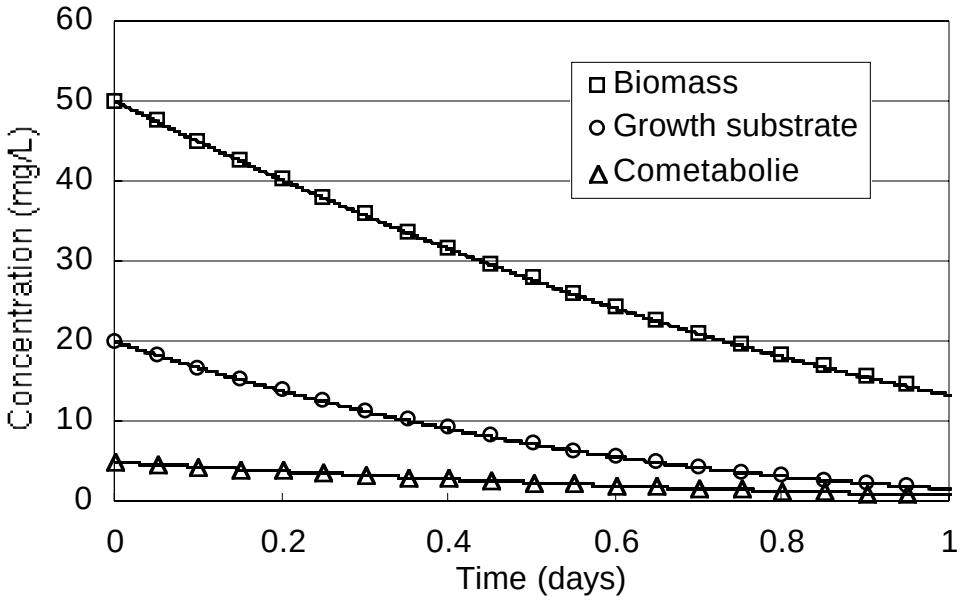

Figure 9.3. Comparison of UTCHEM and spreadsheet solution for the methanotrophic cometabolism of TCE (cometabolite) in a batch system. The symbols are the UTCHEM solution and the solid lines are the solution calculated in a spreadsheet. Kinetic parameters are given in Table 9.2.

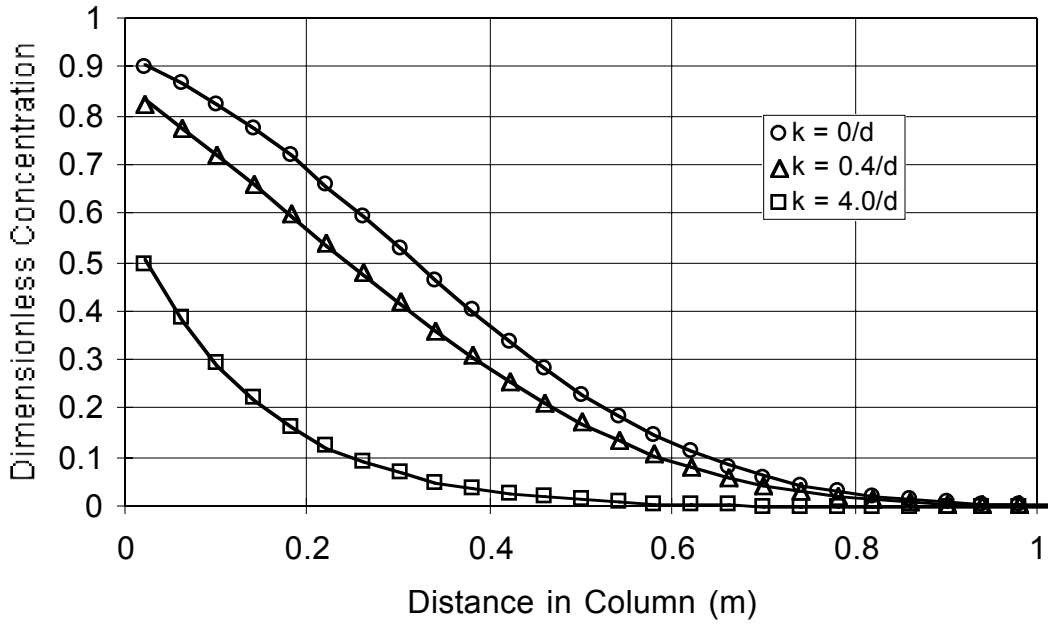

Figure 9.4. Comparison of the UTCHEM and analytical solution of the one-dimensional advection-dispersion equation. The UTCHEM solution is represented by the symbols, and the analytical solution is represented by the solid line. Flow parameters are given in Table 9.3.

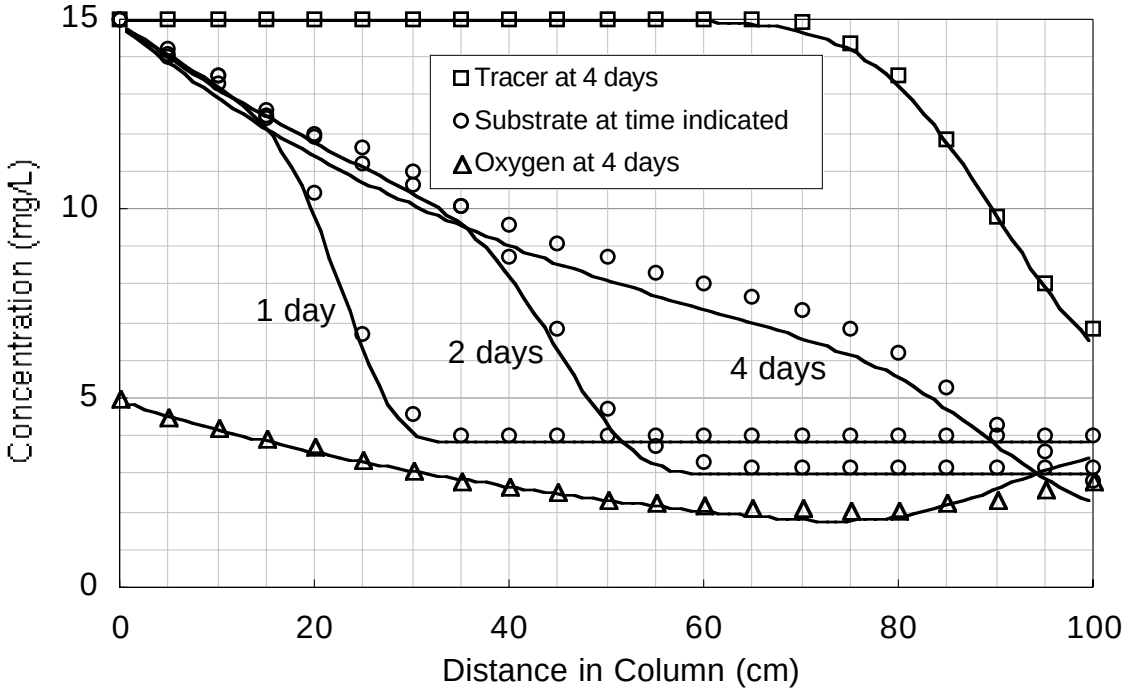

Figure 9.5. Comparison of UTCHEM and Molz *et al.* [1986] solution of the biodegradation of a single substrate by a single microbial species using a single electron acceptor in a 1 m long column. Flow and kinetic parameters are given in Table 9.4.

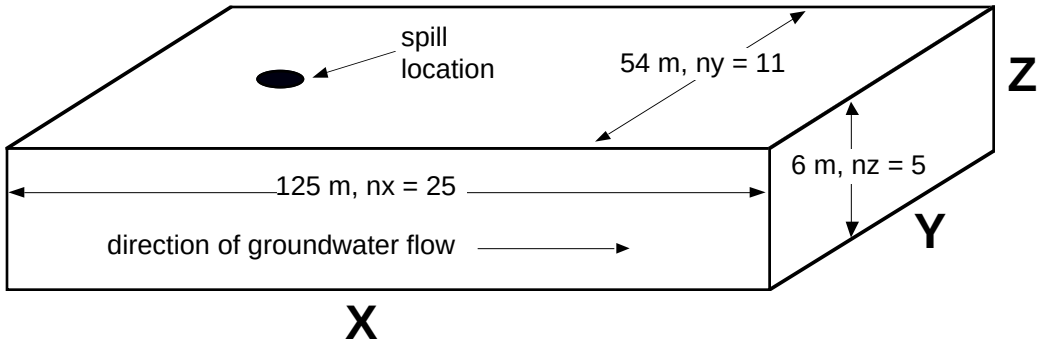

Figure 9.6. Modeling domain size and discretization.

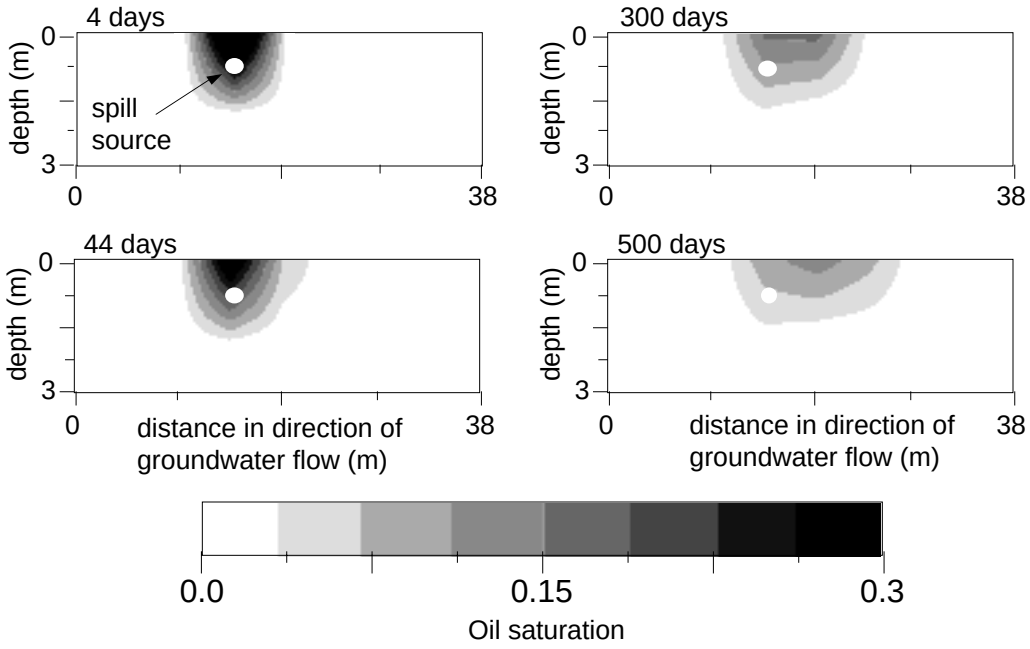

Figure 9.7. NAPL saturation history in the vicinity of a hypothetical gasoline spill. The figure shows a vertical section along the x axis in the center of the aquifer. This gasoline spill is simulated by injecting 3.8 m^3 of gasoline at a depth 0.6 m below the top of the confined aquifer.

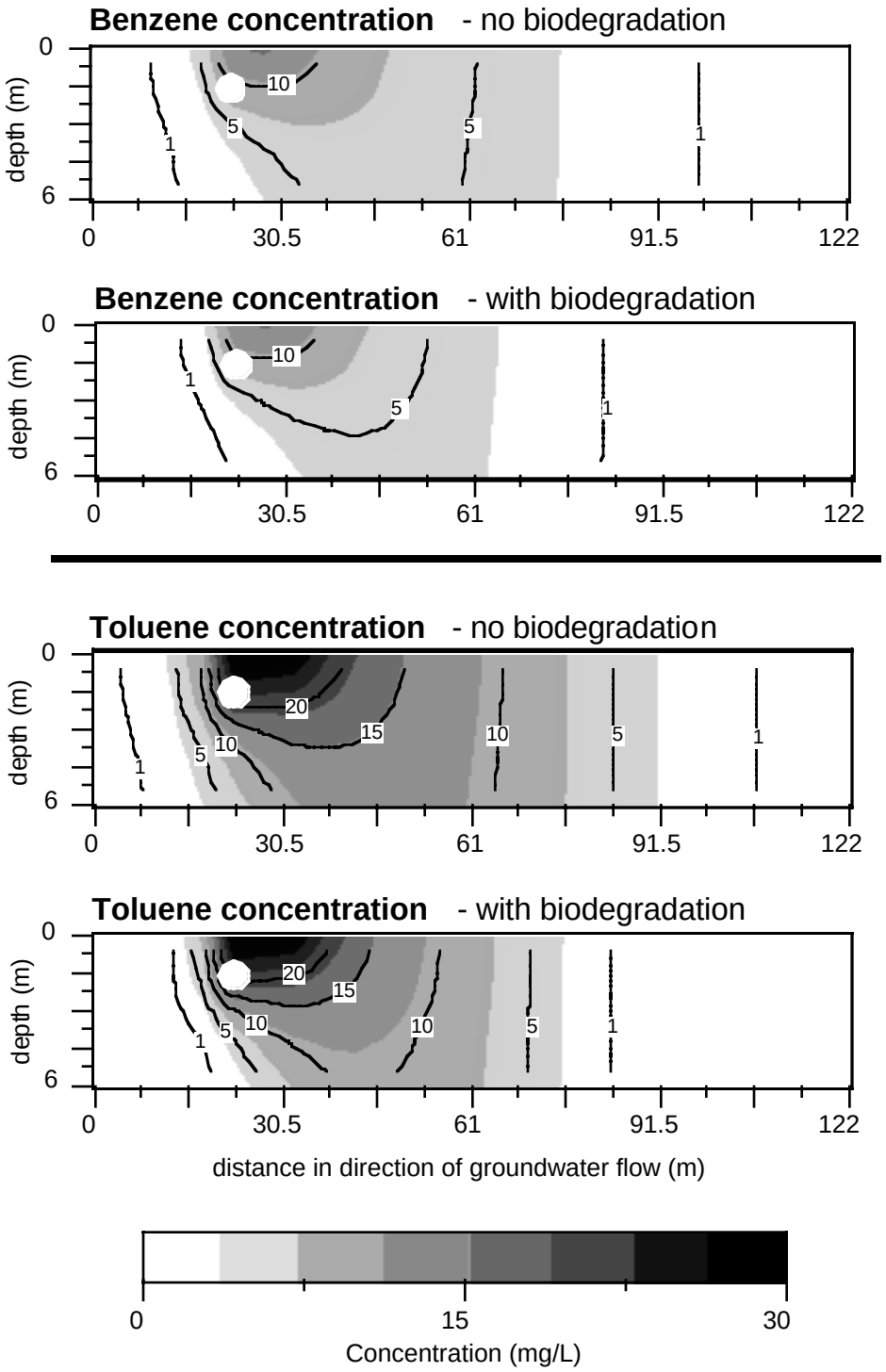

Figure 9.8. Comparison of benzene and toluene concentrations in the aqueous phase 500 days after a gasoline spill. The figure shows a vertical section along the x axis in the center of the aquifer. Gasoline was injected at the location of the white circle. Concentrations of benzene and toluene are compared for the assumptions of no biodegradation and biodegradation of the two compounds.

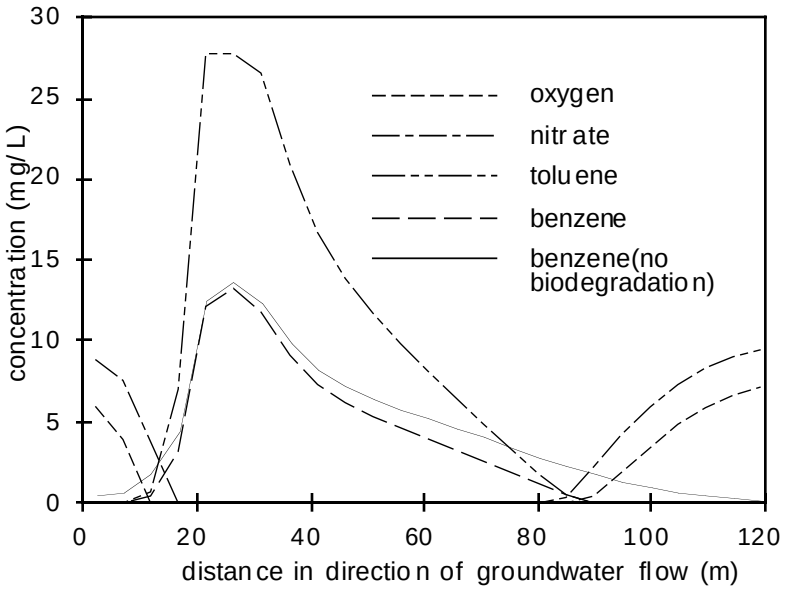

Figure 9.9. Concentrations of benzene without biodegradation, benzene with biodegradation, toluene, oxygen, and nitrate in upper 1.2 m of aquifer along aquifer center line at 500 days.

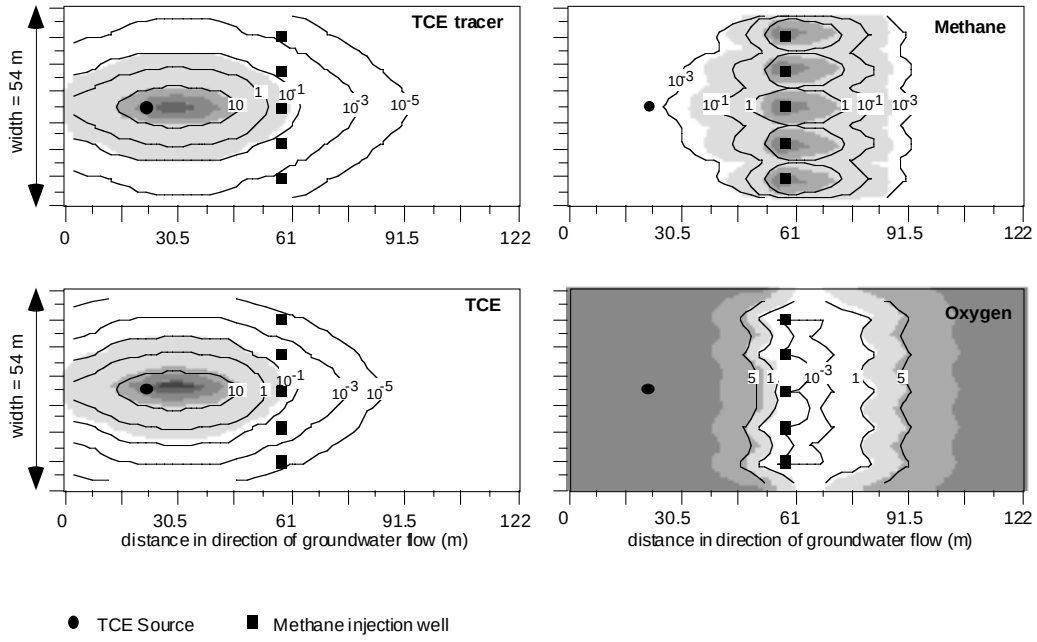

Figure 9.10. Plan view of TCE, a hypothetical TCE tracer, methane and oxygen concentrations in the upper 1.2 m of a confined aquifer 170 days after a TCE spill. All concentrations are mg/L. Groundwater is flowing from left to right at 0.1 m/d. Shading is present for visualization purposes only and does not correspond to specific chemical concentrations. Assumptions are: TCE solubility = 1,100 mg/L; initial oxygen concentration = 8 mg/L; methane concentration in injected water = 20 mg/L. Biodegradation rate parameters are from Chang and Alvarez-Cohen [1995].

Section 10
Well Models

10.1 Introduction

In this section, the well models in the UTCHEM simulator are described. The options available are:

- An arbitrary number of producers in any grid block can be specified (Cartesian grid option only).
- Skin factor (S) and completion interval can be specified.
- Both the injection wells and the producers can be shut in or opened at anytime during the simulation. The well type can also be changed during the simulation (e.g., an injector changed to a producer).
- Each injection well can inject multiple slugs with different component concentrations.
- Wells can be completed in any direction parallel to the axes (Cartesian and Curvilinear grid options only).

10.2 Vertical Wells with Cartesian or Curvilinear Grid Options

Two basic well conditions of constant flow rate or constant flowing bottomhole pressure are implemented. Application of Darcy's law to a wellblock (i,j,k) results in:

$$Q = \sum_{\ell=1}^{n_p} Q_\ell = \sum_{\ell=1}^{n_p} PI_\ell \left(P_{wf} - P_\ell\right) \tag{10.1}$$

where $P_\ell = P_1 + P_{c1\ell}$ and PI is the productivity index. For two-dimensional areal (x-y) and three-dimensional simulation, the PI is given by:

$$PI_\ell = \frac{2\pi\sqrt{k_x k_y}\,\Delta z}{(0.15802)\left(\ln\dfrac{r_o}{r_w} + S\right)}\lambda_{r\ell} \tag{10.2}$$

and for one-dimensional and cross-sectional (x-z) simulation by:

$$PI_\ell = \frac{k_x \Delta y \Delta z}{0.15802\,\dfrac{\Delta x}{2}}\lambda_{r\ell} \tag{10.3}$$

where the constant in the above equations is the unit conversion factors where the permeability is in Darcy and gridblock size in ft and $\lambda_{r\ell} = \dfrac{k_{r\ell}}{\mu_\ell}$ in cp^{-1} to result PI in $(psi)^{-1}$.

The equivalent radius, r_o, is calculated using Peaceman's model (Peaceman, 1983):

$$r_o = 0.28\frac{\left(\left(\frac{k_x}{k_y}\right)^{1/2}\Delta y^2 + \left(\frac{k_y}{k_x}\right)^{1/2}\Delta x^2\right)^{1/2}}{\left(\frac{k_x}{k_y}\right)^{1/4} + \left(\frac{k_y}{k_x}\right)^{1/4}} \tag{10.4}$$

The well bottomhole following pressure in any layer k, $P_{wf,k}$ is given by:

$$(P_{wf})_k = (P_{wf})_{k-1} + \bar{\gamma}_k \qquad k = 2,..., nbz \tag{10.5}$$

where n_{bz} is the number of layers perforated and

$$\bar{\gamma}_k = \gamma_k \frac{\Delta z_k}{2} + \gamma_{k-1}\frac{\Delta z_{k-1}}{2} \tag{10.6}$$

γ_k are calculated from:

$$\gamma_k = \frac{\sum_{\ell=1}^{n_p}\gamma_\ell PI_\ell}{\sum_{\ell=1}^{n_p} PI_\ell} \tag{10.7}$$

For the producer wellblock, specific weights of the produced fluids, γ_ℓ, are used in the above calculations while for the injection wells, the specific weights of the injected phases are calculated using:

$$\gamma_\ell = \sum_{k=1}^{n_c}\left((C_{inj})_{k,\ell}\right)\gamma_k \tag{10.8}$$

10.2.1 Well Constraints for Injection Wells

10.2.1.1 Rate Constraint

When the phase injection rates, $Q_{inj,\ell}$, are specified, the positive injection rates are allocated to the individual layer k that is perforated according to:

$$Q_\ell = Q_{inj,\ell}\frac{\sum_{\ell=1}^{n_p} PI_\ell}{\sum_{k=1}^{n_{bz}}\sum_{\ell=1}^{n_p} PI_\ell} \tag{10.9}$$

The total injection rate for the ijk block is given by:

$$Q = \sum_{\ell=1}^{n_p} Q_\ell \tag{10.10}$$

The above term is then added to the constant vector of the pressure equation at the ijk block. In Eq. 10.9, it is assumed that the potential gradient between the wellbore and the gridblock pressure is the same for all the layers in the reservoir model. Nolen and Berry [1972] have shown that including the potential differences in Eq. 10.9 may result in stability problems. Equation 10.9 may give erroneous results in the case of large vertical heterogeneity and especially when noncommunicating layers exist. However, in the absence of a very low permeability zone or small crossflow, the above formulation does not produce a significant error.

10.2.1.2 Pressure Constraint

When bottomhole injection pressure for the first perforated layer, $(P_{wf})_{ij,k=1}$, is specified, Eq. 10.1 is used. The term $\sum_{\ell=1}^{n_p} PI_\ell \left(P_{wf} - P_{c1\ell}\right)$ in Eq. 10.1 is added to the constant vector of the pressure equation for block ijk and term $\sum_{\ell=1}^{n_p} PI_\ell$ to the $(P_1)^{n+1}$ term (diagonal element in the pressure matrix).

After the pressure equation is solved, Eq. 10.1 is used to obtain the total injection rate at the end of the time step, Q. The injected phase cuts for each layer are the same as the total injected cuts:

$$Q_\ell = Q \frac{Q_{inj,\ell}}{\sum_{\ell=1}^{n_p} Q_{inj,\ell}} \tag{10.11}$$

the phase injection rates, $Q_{inj,\ell}$, specified as input values, are treated as phase cuts.

10.2.2 Well Constraints for Production Wells

10.2.2.1 Rate Constraint

When the total production rate, input as a negative value (Q_{prod}) is specified, the withdrawal rate for each layer k is calculated using:

$$Q = Q_{prod} \frac{\sum_{\ell=1}^{n_p} PI_\ell}{\sum_{k=1}^{n_{bz}} \sum_{\ell=1}^{n_p} PI_\ell} \tag{10.12}$$

and the produced phase cuts are then calculated using:

$$Q_\ell = Q \frac{\lambda_{r\ell}}{\sum_{\ell=1}^{n_p} \lambda_{r\ell}} \tag{10.13}$$

10.2.2.2 Pressure Constraint

When bottomhole pressure for a producer is specified, Eq. 10.1 is used to calculate the total production rate (Q) in the same manner as was described above for the injection well on pressure constraint. The produced phase cuts are then obtained from:

$$Q_\ell = Q\frac{PI_\ell}{\sum_{\ell=1}^{n_p} PI_\ell} \tag{10.14}$$

10.3 Vertical Wells with Radial Grid Option

The boundary conditions for the radial option are

- no vertical flow at the upper and lower boundaries
- a rate constraint well at the center of the reservoir,
- a constant pressure outer boundary that is treated the same as a pressure constraint injector/producer well.

The phase productivity index in the gridblock ijk for the injection or production well is calculated as

$$PI_\ell = \frac{k_x \Delta z}{\frac{\Delta x}{2}}\lambda_{r\ell} \tag{10.15}$$

10.3.1 Rate Constraint Injector

Equations 10.9 and 10.10 are used to calculate the rate allocation to each layer.

10.3.2 Rate Constraint Producer

Equations 10.12 and 10.13 are used to calculate the rate withdrawal from each layer.

10.3.3 External Boundary

The amount of fluid that crosses each layer k from the last gridblock at the open boundary is calculated by

$$Q = \sum_{\ell=1}^{n_p} PI_\ell \left((P_1)_e - (P_1)_{i=n_r} \right) \tag{10.16}$$

where the outer boundary aqueous phase pressure $(P_1)_e$ is maintained at the initial pressure for the duration of the simulation as:

$$(P_1)_{e,k} = (P_1)_{e,k-1} + \bar{\gamma}_k \qquad \text{for k = 2,..., nbz} \tag{10.17a}$$

where $\bar{\gamma}_k$ is calculated from Eqs. 10.6 and 10.7. The phase productivity index is calculated as:

$$PI_\ell = 6.3266\frac{2\pi k_x \Delta z}{\ln\frac{r_e}{r_i}}\lambda_{r\ell} \tag{10.17b}$$

where the permeability and radius of the outermost gridblock ($i = n_r$) are used. The calculation is implicit similar to that for the pressure constrained wells discussed above. Once the pressure is known, total rate for each layer is calculated from Eq. 10.16. The phase cuts for the fluids crossing the boundary are calculated from Eq. 10.14.

10.4 Horizontal Well with Cartesian or Curvilinear Grid Options

Horizontal wells use the same well model equations as vertical wells. Only parameters related to the direction of the wellbore were modified. When the wellbore is parallel to the z direction, the calculation of the productivity index uses the gridblock height, Δz, the permeability in the x direction, k_x, and the permeability in the y direction, k_y:

$$PI_\ell = \frac{2\pi\sqrt{k_x k_y}\,\Delta z}{0.15802\left[\ln\left(\frac{r_o}{r_w}\right)+S\right]}\lambda_{r\ell} \tag{10.18}$$

where the constant 0.15802 is a unit conversion factor. k_x and k_y are in Darcy, Δz, r_o, and r_w are in ft, and $\lambda_{r\ell} = k_{r\ell}/\mu_\ell$ is in cp^{-1}. The equivalent wellblock radius, r_o, is based on Peaceman [1983] and uses wellblock properties in the x and y directions such as the dimensions Δx and Δy and the permeability values k_x and k_y:

$$r_o = 0.28\frac{\left[\left(\frac{k_x}{k_y}\right)^{1/2}\Delta y^2+\left(\frac{k_y}{k_x}\right)^{1/2}\Delta x^2\right]^{1/2}}{\left(\frac{k_x}{k_y}\right)^{1/4}+\left(\frac{k_y}{k_x}\right)^{1/4}} \tag{10.19}$$

10.4.1 Productivity Index for Horizontal Wells

The productivity index calculations were generalized for horizontal wells parallel to either the x direction or the y direction by taking into account the pertinent directional properties. When the wellbore is parallel to the x direction, the productivity index calculation uses Δx as the wellblock dimension parallel to the wellbore. Since the wellbore is perpendicular to the y and z directions, the productivity index calculation uses the permeability in the y direction and the permeability in the z direction:

$$PI_\ell = \frac{2\pi\sqrt{k_y k_z}\,\Delta x}{0.15802\left[\ln\left(\frac{r_o}{r_w}\right)+S\right]}\lambda_{r\ell} \tag{10.20}$$

When the wellbore is parallel to the y direction, the productivity index calculation uses Δy as the wellblock dimension parallel to the wellbore. Since the wellbore is perpendicular to the x and z directions, the productivity index calculation uses the permeability in the x direction and the permeability in the z direction:

$$PI_\ell = \frac{2\pi\sqrt{k_x k_z}\,\Delta y}{0.15802\left[\ln\left(\frac{r_o}{r_w}\right)+S\right]}\lambda_{r\ell} \tag{10.21}$$

10.4.1.1 Equivalent Wellblock Radius for Horizontal Wells (Peaceman, 1983)

The calculations of the equivalent wellblock radius were also generalized for horizontal wells by taking into account reservoir properties perpendicular to the direction of the wellbore. In case the wellbore is parallel to the x direction, the equivalent wellblock radius, based on Peaceman [1983], uses wellblock

properties in the y and z directions such as the dimensions Δy and Δz and the permeability values k_y and k_z:

$$r_o = 0.28 \frac{\left[\left(\frac{k_y}{k_z}\right)^{0.5} \Delta z^2 + \left(\frac{k_z}{k_y}\right)^{0.5} \Delta y^2\right]^{0.5}}{\left(\frac{k_y}{k_z}\right)^{0.25} + \left(\frac{k_z}{k_y}\right)^{0.25}} \tag{10.22}$$

In case the wellbore is parallel to the y direction, the equivalent wellblock radius uses wellblock properties in the x and z directions such as the dimensions Δx and Δz and the permeability values k_x and k_z:

$$r_o = 0.28 \frac{\left[\left(\frac{k_x}{k_z}\right)^{0.5} \Delta z^2 + \left(\frac{k_z}{k_x}\right)^{0.5} \Delta x^2\right]^{0.5}}{\left(\frac{k_x}{k_z}\right)^{0.25} + \left(\frac{k_z}{k_x}\right)^{0.25}} \tag{10.23}$$

10.4.1.2 Equivalent Wellblock Radius (Babu *et al.*, 1991)

In addition to Peaceman's formulation [1983], a formulation of the equivalent wellblock radius based on the paper by Babu *et al.* [1991] was implemented in the simulator (Dakhlia *et al*, 1995). As published, the gridblock sizes were assumed uniform and the equations depended on gridblock numbering. However, numerical reservoir simulation is often carried out with non-uniform gridblock sizes. The equations were therefore rearranged so that gridblock sizes were no longer required to be uniform and the equations no longer depended on the gridblock numbering. $\frac{h}{\Delta z}$ was substituted for n_z and $\frac{a}{\Delta x}$ was substituted for n_x. In case an integer was needed, such as in the summation limits, the FORTRAN function NINT was used to calculate the nearest integer to the argument. Therefore, NINT($\frac{h}{\Delta z}$) was substituted for n_z in the summation limit used in S_{xz}. In addition, $\frac{2x_w}{\Delta x}$ was substituted for ν and $\frac{2z_w}{\Delta z}$ was substituted for λ. As a result, the applicability of the formulation was extended to non-uniform grids. The assumption for these substitutions was that away from the wellbore, the effect of a coarse and non-uniform grid was equivalent to the effect of a fine and uniform grid on the pressure behavior near the wellbore.

The resulting formulation is given below for a wellbore parallel to the y direction. In case the wellbore was parallel to either the x or z direction, the pertinent directional variables were modified accordingly.

$$\ln\left(\frac{r_o}{h}\right) = \left[\frac{\pi a}{6h\left(\frac{a}{\Delta x}\right)^2}\sqrt{\frac{k_z}{k_x}}\right] + 0.25\ln\left[\frac{k_x}{k_z}\right] - \ln\left[\sin\left(\frac{\pi z_w}{h}\right)\right] - 1.84 - B_E - S_{xz} \tag{10.24}$$

where the boundary term, B_E, is computed by

$$B_E = \ln(1 - E_1) + 0.5\ln\left[1 - 2\cos\left(\frac{2\pi z_w}{h}\right)E_1 + E_1^2\right] \tag{10.25}$$

and

$$E_1 = \exp\left[-\frac{2\pi \min(x_w, a - x_w)}{h}\sqrt{\frac{k_z}{k_x}}\right] \tag{10.26}$$

and the summation term, S_{xz}, is

$$S_{xz} = \frac{\pi}{\left(\frac{h}{\Delta z}\right)} \sum_{n=1}^{\mathrm{NINT}\left(\frac{h}{\Delta z}\right)-1} \frac{\cos^2\left[\frac{\pi n z_w}{h}\right]\left[1+x_n^{-\left(\frac{2x_w}{\Delta x}\right)}\right]\left[1+x_n^{-2\left(\frac{a-x_w}{\Delta x}\right)}\right]}{\sin\left[\frac{\pi n}{2\left(\frac{h}{\Delta z}\right)}\right]\sqrt{1+\alpha_n^2}\left[1-x_n^{-\left(\frac{2a}{\Delta x}\right)}\right]} \tag{27}$$

with α, α_n, and x_n defined as

$$\alpha = \frac{\Delta x}{\Delta z}\sqrt{\frac{k_z}{k_x}} \tag{10.28}$$

$$\alpha_n = \alpha \sin\left[\frac{\pi n}{2\left(\frac{h}{\Delta z}\right)}\right] \tag{10.29}$$

$$x_n = \left(\alpha_n + \sqrt{1+\alpha_n^2}\right)^2 \tag{10.30}$$

For symmetry purposes, the wellbore location (x_w, z_w) was temporarily adjusted so that

$$x_w = \min(x_w, a - x_w) \tag{10.31}$$

and

$$z_w = \min(z_w, a - z_w) \tag{10.32}$$

Section 11
Effect of Alcohol on Phase Behavior

11.1 Introduction

This section is based on the Ph.D. dissertation by Saad [1989]. The phase behavior calculation for a mixture of water, oil, and surfactant is discussed in Section 2. The effect of alcohol on the phase behavior is discussed here. The presence of alcohol affects the effective salinities and causes a shift in the phase boundaries. The effect of alcohol on the solubility is accounted for by shifting the maximum height of binodal curve. The amount of alcohol that partitions in the excess phase(s) is modeled either by constant partitioning coefficients as in Hirasaki's model (Hirasaki, 1982) or as a function of total composition with the concept of pseudocomponent and pseudophase as in Provoust's model (Prouvost *et al.*, 1984a,b, 1985). Following is a discussion of the UTCHEM phase behavior model in the presence of alcohol (Pope and Nelson, 1978; Prouvost *et al.*, 1984a,b, 1985; Camilleri *et al*., 1987c; Saad, 1989).

The phase behavior is modeled as a tetrahedric diagram at a fixed salinity. Four pseudocomponents are surfactant, alcohol, oil, and water represented in a tetrahedric diagram. Tielines and binodal curves are located on the ternaries sliced through tetrahedrons. The pseudophases are (1) the aqueous consists of water and alcohol(s), (2) oleic consists of oil and alcohol(s), and (3) microemulsion consists of surfactant and alcohol(s). Similar to the no alcohol mixture, the phase behavior parameters such as binodal curve, plait point and invariant point are calculated as a function of effective salinity using Hand's rule (Hand, 1939).

11.2 Alcohol Partitioning

The two options available in UTCHEM to calculate the alcohol partitioning are based on the models of Hirasaki and Prouvost. Hirasaki's model assumes a constant partition coefficient whereas experimental results show that alcohol partition coefficients vary with total composition. Prouvost extended the pseudophase model to calculate variable alcohol partition coefficients and to be applicable to two alcohols. The following intensive composition parameters are defined in the model:

$$\lambda_j = \frac{C_\kappa^1}{C_1} \tag{11.1}$$

$$\gamma_j = \frac{C_\kappa^2}{C_2} \tag{11.2}$$

$$\sigma_j = \frac{C_\kappa^3}{C_3} \tag{11.3}$$

where for $\kappa = 7$, the value of subscript $j = 1$ and for $\kappa = 8$, $j = 2$. C_1, C_2, and C_3 are the overall water, oil, and surfactant volume fractions, respectively. Superscripts 1, 2, and 3 represent the association of alcohol with aqueous, oleic, and microemulsion pseudophases. Therefore, C_7^1 is the volume of alcohol 7 (component 7 in UTCHEM) in the aqueous phase, and C_8^1 is the volume of alcohol 8 (component 8) in the aqueous phase. The partition coefficients used in Hirasaki's model can be defined using the above parameters:

$$K_\kappa^2 = \frac{\gamma_j}{\lambda_j} \tag{11.4}$$

$$K_\kappa^3 = \frac{\sigma_j}{\lambda_j} \tag{11.5}$$

where for $\kappa = 7$, the value of subscript $j = 1$ and for $\kappa = 8$, $j = 2$. In Prouvost's model, monomeric alcohol reactions are considered. The following thermodynamic constants are used in the model:

k_{w1} = partition coefficient of monomeric alcohol 7 between aqueous and oleic pseudophases
k_{m1} = partition coefficient of monomeric alcohol 7 between interfacial and oleic pseudophases
k_1 = self-association constant of monomeric alcohol 7 in oleic pseudophase
a = ratio of molar volume of monomeric alcohol 7 to equivalent molar volume of surfactant

k_{w2}, k_{m2}, k_2, and b are similar constants for alcohol 8.

The above parameters are input to the simulator. A material balance gives the following relationships:

$$C_\kappa = \frac{A_j C_1}{D_j + \gamma_j C_2} + \frac{B_j C_3}{E_j} \quad \text{for } \kappa = 7,\ j = 1\ ;\ \kappa = 8,\ j = 2 \tag{11.6}$$

where

$$\begin{aligned}
A_1 &= \gamma_1 k_{w1}\left[1 + \gamma_1 + \gamma_2(1 + k_2)\right] \\
B_1 &= a\gamma_1 k_{m1}\left[1 + \gamma_1 + \gamma_2(1 + k_2)\right] \\
D_1 &= \left\{\left[1 + \gamma_2 + \gamma_1(1 + k_1)\right]\left[1 + \gamma_1 + \gamma_2(1 + k_2 - k_{w2})\right] - \gamma_1 k_{w1}\left[1 + \gamma_1 + \gamma_2(1 + k_2)\right]\right\} \\
E_1 &= \left\{\left[1 + \gamma_2 + \gamma_1(1 + k_1)\right]\left[1 + \gamma_1 + \gamma_2(1 + k_2 - k_{m2})\right] - \gamma_1 k_{m1}\left[1 + \gamma_1 + \gamma_2(1 + k_2)\right]\right\}
\end{aligned} \tag{11.7}$$

$$\begin{aligned}
A_2 &= \gamma_2 k_{w2}\left[1 + \gamma_2 + \gamma_1(1 + k_1)\right] \\
B_2 &= b\gamma_2 k_{m2}\left[1 + \gamma_2 + \gamma_1(1 + k_1)\right] \\
D_2 &= \left\{\left[1 + \gamma_1 + \gamma_2(1 + k_2)\right]\left[1 + \gamma_2 + \gamma_1(1 + k_1 - k_{w1})\right] - \gamma_2 k_{w2}\left[1 + \gamma_2 + \gamma_1(1 + k_1)\right]\right\} \\
E_2 &= \left\{\left[1 + \gamma_1 + \gamma_2(1 + k_2)\right]\left[1 + \gamma_2 + \gamma_1(1 + k_1 - k_{m1})\right] - \gamma_2 k_{m2}\left[1 + \gamma_2 + \gamma_1(1 + k_1)\right]\right\}
\end{aligned} \tag{11.8}$$

C_7 and C_8 are the overall volume fractions of alcohol 7 and alcohol 8 in the gridblock and are known values from the solution of species conservation equations. Knowing C_7 and C_8, Eqs. 11.7 and 11.8 are solved for γ_1 and γ_2 using the Newton Raphson iteration method, and then the other four intensive parameters are calculated:

$$\lambda_j = \frac{A_j}{D_j} \quad \text{for } j = 1, 2 \tag{11.9}$$

$$\sigma_j = \frac{B_j}{E_j} \quad \text{for } j = 1 , 2 \tag{11.10}$$

Once λ_j, γ_j, and σ_j are determined, alcohol partition coefficients K_κ^2, and K_κ^3 are calculated using Eqs. 11.4 and 11.5. When only a single alcohol is used, Eq. 11.6 reduces to the following cubic equation:

$$A' \gamma^3 + B' \gamma^2 + C' \gamma + D' = 0 \tag{11.11}$$

where

$$A' = (1 + k - k_m)(1 + k - k_w) \tag{11.12}$$

$$B' = k_w(1+k-k_m)\frac{C_1}{C_2} + ak_m(1+k-k_m)\frac{C_3}{C_2} - (1+k-k_m)(1+k-k_w)\frac{C_1}{C_2} + 2 + 2k - k_m - k_w \tag{11.13}$$

$$C' = k_w \frac{C_1}{C_2} + ak_m \frac{C_3}{C_2} - (2 + 2k - k_m - k_w)\frac{C_1}{C_2} + 1 \tag{11.14}$$

$$D' = \frac{C_7}{C_2} \tag{11.15}$$

Then the partition coefficients are calculated using:

$$K_7^2 = \frac{1+\gamma(1+k-k_w)}{k_w} \tag{11.16}$$

$$K_7^3 = \frac{a\,k_m[1+g(1+k-k_w)]}{k_w[1+g(1+k-k_m)]} \tag{11.17}$$

For two alcohols, the overall alcohol volumes are related to the overall volumes of water (C_1), oil (C_2), and surfactant (C_3) pseudocomponents by:

$$C_\kappa = \lambda_j C_1 + \gamma_j C_2 + \sigma_j C_3 \quad \text{for } \kappa = 7, j = 1 \; ; \; \kappa = 8, j = 2 \tag{11.18}$$

The above equations, can be written in terms of the alcohol partition coefficients as:

$$C_\kappa = \lambda_j C_1 + \lambda_j K_\kappa^2 C_2 + \lambda_j K_\kappa^3 C_3 \quad \text{for } \kappa = 7, j = 1 \; ; \; \kappa = 8, j = 2 \tag{11.19}$$

From above equations the parameters λ_j are defined as:

$$\lambda_j = \frac{C_\kappa}{C_1 + K_\kappa^2 C_2 + K_\kappa^3 C_3} \quad \text{for } j = 1, 2 \tag{11.20}$$

λ_j is then used in calculating the pseudocomponents that are the apexes of the pseudoternary diagram.

C_{P1}= (water volume) + (alcohol volumes associated with water) = $C_1 (1 + \lambda_1 + \lambda_2)$ (11.21)

C_{P2} = (oil volume) + (alcohol volumes associated with oil)

$$= C_2(1+\gamma_1+\gamma_2) = C_2(1+\gamma_1 K_7^2 + \lambda_2 K_8^2) \tag{11.22}$$

C_{P3} = (water volume) + (alcohol volumes associated with water)

$$= C_3(1+\sigma_1+\sigma_2) = C_3(1+\gamma_1 K_7^3 + \lambda_2 K_8^3) \tag{11.23}$$

The calculation of the pseudocomponent volumes is summarized below:

1. Using Newton Raphson iteration, calculate γ_1 and γ_2 from Eqs. 11.3 and 11.4.

2. Calculate λ_j and σ_j using Eqs. 11.9 and 11.10.

3. a) Calculate K_κ^2 and K_κ^3 using Eqs. 11.4 and 11.5. If there is only one alcohol, use Eq. 11.11 to calculate γ. Then calculate the partition coefficients using Eqs. 11.16 and 11.17.
   b) If constant partition coefficient option is used, K_κ^2 and K_κ^3 are input parameters.
   c) Calculate λ_j using Eq. 11.20.

4. Calculate the volume of the pseudocomponents, C_{P1}, C_{P2}, and C_{P3}, using Eqs. 11.21-11.23.

Above calculations are made in Subroutines ALCPTN and TWOALC.

11.3 Effective Salinity

Hirasaki [1982] introduced a model to account for the change in optimal salinity with respect to changes in the concentration of alcohol and calcium. Camilleri *et al.* [1987c] extended Hirasaki's model to entire salinity space to define an effective salinity for the case with one alcohol:

$$C_{SE} = \frac{C_{51}}{(1-\beta_6 f_6^S)(1-\beta_\kappa f_\kappa^S)} \tag{11.24}$$

C_{SE} is the effective salinity, and β_6 and β_κ are the slope parameters for calcium and alcohol dilution effects. f_6^S is the fraction of calcium cations associated with surfactant micelles and is given in Section 2. f_κ^S is defined as:

$$f_\kappa^S = \frac{\text{total volume of alcohol associated with surfactant}}{\text{total volume of surfactant pseudocomponent}} = \frac{\sigma}{1+\sigma} \tag{11.25}$$

β_6 and β_κ are determined by matching an experimental salinity requirement diagram such as those reported by Nelson [1982] or equivalent diagrams (Satoh, 1984). For formulations containing only one alcohol, C_{SEL} and C_{SEU} are constant for a fixed chemical formulation and are determined using Eq. 11.24. If there is no calcium present, Eq. 11.24 represents a group of straight lines which pass through the fixed point $(0, -1/\beta_\kappa)$. If calcium is present, then it represents a group of planes which pass through the three fixed points $(0, -1/\beta_\kappa, 0)$, $(0, 0, 1/\beta_\kappa)$, and $(0, -1/\beta_\kappa, 1/\beta_6)$. Due to the fact that Eq. 11.24 is nonlinear, these planes are not flat . The calculated effective salinity becomes negative when $f_6^S > 1/\beta_6$ or β_κ is negative and $f_\kappa^S > 1/|\beta_\kappa|$.

Since different alcohols give different salinity limits, the following effective salinity is defined for the case when there are two alcohols present:

$$C_{SE} = \frac{C_{51}}{(1-\beta_6 f_6^S)(1+\beta_7 f_7^S+\beta_8 f_8^S)} \tag{11.26}$$

where the effective salinity limits are not constant in this case and are calculated by:

$$C_{SEL}\frac{C_{SEL7}\left|\beta_7 f_7^S\right| + C_{SEL8}\left|\beta_8 f_8^S\right|}{\left|\beta_7 f_7^S\right| + \left|\beta_8 f_8^S\right|} \tag{11.27}$$

$$C_{SEU}\frac{C_{SEU7}\left|\beta_7 f_7^S\right| + C_{SEU8}\left|\beta_8 f_8^S\right|}{\left|\beta_7 f_7^S\right| + \left|\beta_8 f_8^S\right|} \tag{11.28}$$

C_{SEL7}, C_{SEL8}, C_{SEU7}, and C_{SEU8} are effective salinity limits for alcohol 7 and 8. C_{SEL7} and C_{SEU7} are determined when alcohol 7 is the only alcohol present and are calculated using Eq. 11.24. Similar independent calculations are made for alcohol 8. For the two alcohol case, f_7^S and f_8^S are defined as:

$$f_\kappa^S = \frac{\text{total volume of alcohol k associated with surfactant}}{\text{total volume of surfactant pseudocomponent}}$$

$$= \frac{\sigma_1}{1+\sigma_1+\sigma_2} = \frac{\lambda_j K_\kappa^3}{1+\lambda_1 K_7^3 + \lambda_2 K_8^3} \qquad \text{for } \kappa = 7,\ j = 1\ ;\ \kappa = 8,\ j = 2 \tag{11.29}$$

K_κ^3 and λ_j are calculated as outlined in the previous section.

Once effective salinity is calculated, the phase environment (Fig. 11.1) for each gridblock is determined according to:

$C_{SE} < C_{SEL}$	Type II(-)
$C_{SEL} \le C_{SE} \le C_{SEU}$	Type III
$C_{SE} > C_{SEU}$	Type II(+)

Effective salinity is calculated in Subroutine CSECAL.

11.4 Flash Calculations

A binodal curve is an intercept of a binodal surface and a pseudoternary plane. The original simulator introduced by Pope and Nelson [1978] could treat nonsymmetric binodal curves; however, the present simulator can treat only a symmetric binodal curve. The effects of alcohol on the height of the binodal curve was included which can increase as the total chemical increases. The following linear relationship between the height of the binodal curve (C_{3max}) and f_κ^S is used for the case with one alcohol (Fig. 11.2):

$$C_{3max,\kappa m} = m_{\kappa m}\ f_\kappa^S + C_{\kappa m} \qquad \text{for } m = 0, 1, 2;\ \ \kappa = 7 \tag{11.30}$$

where m = 0 means at zero salinity, 1 means at optimal salinity, and 2 means at two times the optimal salinity. $m_{\kappa m}$ is the slope for maximum height of binodal curve vs. fraction of alcohol (alcohol 7 or alcohol 8 for the two alcohol case) associated with the surfactant pseudocomponent at salinity m. $C_{\kappa m}$ is the intercept of maximum height of the binodal curve at zero fraction of alcohol (alcohol 7 or alcohol 8 for the two alcohol case) associated with the surfactant pseudocomponent at salinity m. Parameters $m_{\kappa m}$ and $C_{\kappa m}$ are obtained by matching the volume fraction diagrams corresponding to at least three different total chemical (alcohol + surfactant) compositions. For the first iteration, the slope parameters are set to zero and the intercept parameters are adjusted in order to obtain a reasonable match of the volume fraction diagrams; then the slope parameters are obtained. Having obtained the slope parameters, the matching procedure is repeated for further improvements. This matching is done using single alcohol experiments independently for alcohol 7 and alcohol 8 using Eq. 11.30. The variables HBNC70, HBNC71, HBNC72

in Fig. 11.2 are the UTCHEM input parameters for $C_{\kappa m}$ at three values of m. The variables HBNS70, HBNS71, HBNS72 in Fig. 11.2 are the UTCHEM input parameters for $m_{\kappa m}$ at three values of m.

The following equations are used for calculating the height of the binodal curve for the two alcohol case:

$$C_{3max,\kappa m} = m_{\kappa m}\left(f_7^S + f_8^S\right) + C_{\kappa m} \quad \text{for } \kappa = 7 \text{ and } 8 \tag{11.31}$$

$$C_{3maxm} = C_{3max,8m} + \left(C_{3max,7m} - C_{3max,8m}\right)\frac{f_7^S}{f_7^S + f_8^S} = \left(m_{7m} + \frac{C_{7m}}{f_7^S + f_8^S}\right)f_7^S + \left(m_{8m} + \frac{C_{8m}}{f_7^S + f_8^S}\right)f_8^S \tag{11.32}$$

The following Hand equations are used for phase behavior calculations:

$$\frac{C_{P3}}{C_{P2}} = A\left(\frac{C_{P3}}{C_{P1}}\right)^B \tag{11.33}$$

$$\frac{C_{P3\ell}}{C_{P2\ell}} = E\left(\frac{C_{P3\ell'}}{C_{P1\ell}}\right)^F \tag{11.34}$$

Equation 11.33 defines the binodal curve for all types of phase behavior, and Eq. 11.34 defines the distribution curve (tielines) when two phases exist (Type II(-) or Type II(+)). C_{P1}, C_{P2}, and C_{P3} represent pseudocomponents defined by Eqs. 11.21-11.23. $C_{P2\ell}$, $C_{P3\ell}$, $C_{P1\ell'}$, and $C_{P3\ell'}$ represent phase concentrations of the pseudocomponents in the two pseudophases ℓ and ℓ'. Because pseudocomponent concentrations are in volume fractions, they must add up to one; therefore the following constraints are used:

$$C_{P1} + C_{P2} + C_{P3} = 1 \tag{11.35}$$

$$C_{P1\ell} + C_{P2\ell} + C_{P3\ell} = 1 \tag{11.36}$$

$$C_{P1\ell'} + C_{P2\ell'} + C_{P3\ell'} = 1 \tag{11.37}$$

The total composition, C_{P1}, C_{P2}, and C_{P3}, is known. Therefore there are five equations and six unknowns ($C_{P\kappa\ell}$, κ = 1, 2, 3, ℓ = 1, 2). Any phase concentration can be chosen and varied between 0 and 1 to sweep the phase diagram. Since only symmetric binodal curves are modeled in the simulator, parameter B is equal to -1 and parameter F is equal to 1. Parameter A in Eq. 11.33 is related to the height of the binodal curve by:

$$A = \left(\frac{2C_{3\max}}{1 - C_{3\max}}\right)^2 \tag{11.38}$$

Linear interpolation is then used to determine the A parameter for arbitrary effective salinity values. The reason for interpolating A instead of the maximum height of the binodal curve, C_{3max}, is that, at high salinity, C_{3max} exceeds unity, which means the binodal curve is outside the ternary diagram. To avoid this problem, the interpolation is done on A. The following linear interpolation equations are used:

$$A = (A_0 - A_1)\left(1 - \frac{C_{SE}}{C_{SEOP}}\right) + A_1 \quad \text{for } C_{SE} \le C_{SEOP} \tag{11.39}$$

$$A = (A_2 - A_1)\left(1 - \frac{C_{SE}}{C_{SEOP}}\right) + A_1 \quad \text{for } C_{SE} > C_{SEOP} \tag{11.40}$$

where C_{SEOP} is the optimum effective salinity (CSEOP = 1/2 (CSEL+CSEU)).

Parameter E is calculated from the location of the plait point. From the phase distribution equation (Eq. 11.34) and the plait point P:

$$\frac{C_{P3P}}{C_{P2P}} = E\left(\frac{C_{P3P}}{C_{P1P}}\right)^F \tag{11.41}$$

and since the plait point is also on the binodal curve:

$$\frac{C_{P3P}}{C_{P2P}} = A\left(\frac{C_{P3P}}{C_{P1P}}\right)^B \tag{11.42}$$

Also:

$$C_{P1P} + C_{P2P} + C_{P3P} = 1 \tag{11.43}$$

For the case when B = -1 and F = 1 (symmetric binodal curve), all phase concentrations can be calculated explicitly. From Eq. 11.36:

$$C_{P11} = 1 - C_{P21} - C_{P31} \tag{11.44}$$

Now substituting Eq. 11.44 in Eq. 11.33, C_{P31} can be calculated as a function of C_{P21}:

$$C_{P31} = \frac{1}{2}\left(-AC_{P21} + \sqrt{(AC_{P21})^2 + 4AC_{P21}(1 - C_{P21})}\right) \tag{11.45}$$

and from Eq. 11.42:

$$E = \frac{C_{P1P}}{C_{P2P}} \tag{11.46}$$

where C_{P2P}, the oil pseudocomponent concentration at the plait point, is an input parameter in the simulator, and

$$C_{P3P} = \frac{1}{2}\left(-AC_{P2P} + \sqrt{(AC_{P2P})^2 + 4AC_{P2P}(1 - C_{P2P})}\right) \tag{11.47}$$

Then from Eq. 11.36:

$$C_{P1P} = 1 - C_{P2P} - C_{P3P} \tag{11.48}$$

knowing C_{P1P}, parameter E can be calculated from Eq. 11.46. Having calculated C_{P31} and C_{P11} from Eqs. 11.44 and 11.45, C_{P22} is calculated from the following:

$$C_{P22} = \frac{A}{h^2 + A\,h + A} \tag{11.49}$$

where

$$h = E\frac{C_{P31}}{C_{P11}} \tag{11.50}$$

Then C_{P32} is calculated from

$$C_{P32} = h\, C_{P22} \tag{11.51}$$

and

$$C_{P12} = 1 - C_{P22} - C_{P32} \tag{11.52}$$

The above calculations are performed when there are only two phases present, for Type II(-) or Type II(+) phase behavior. The only difference between the two cases is that for Type II(-) phase behavior C^*_{P2PR} and for Type II(+) phase behavior C^*_{P2PL}, are used for C_{P2P} in the above equations. The distribution of the three pseudocomponents in the two phases for Type II(-) and Type II(+) phase behavior are summarized below:

11.4.1 For Type II(-) Phase Behavior, $C_{SE} < C_{SEL}$

Known values for this case are C_{3max0}, C_{3max1}, C_{3max2}, C_{SE}, C_{SEL}, C_{SEU}, C^*_{P2PR} and overall concentration of the pseudocomponents, C_{P1}, C_{P2}, and, C_{P3}.

1. Calculate parameter A from Eq. 11.39.
2. Using C^*_{P2PR} calculate C^*_{P3PR} and C^*_{P1PR} using Eqs. 11.47-11.48.
3. Calculate parameter E using Eq. 11.46 and C^*_{P1PR} and C^*_{P2PR}.
4. Vary the value of C_{P21} from 0 to C^*_{P2PR}, calculate C_{P11} and C_{P31} using Eqs. 11.44-11.45.
5. Calculate h from Eq. 11.50.
6. Calculate C_{P22}, C_{P32}, and C_{P12} using Eqs. 11.49-11.52.
7. If $(C_{P32} - C_{P3})(C_{P21} - C_{P2}) - (C_{P31} - C_{P3})(C_{P22} - C_{P2}) \le \varepsilon$, where ε is a sufficiently small number (10^{-4}), then stop; otherwise increment C_{P21} using the half interval method and go to step 4.

11.4.2 For Type II(+) Phase Behavior, $C_{SE} > C_{SEU}$

Known values for this case are C_{3max0}, C_{3max1}, C_{3max2}, C_{SEL}, C_{SE}, C_{SEU}, C^*_{P2PL} and overall concentration of the pseudocomponents, C_{P1}, C_{P2}, and .C_{P3}.

1. Calculate parameter A from Eq. 11.40.
2. Using C^*_{P2PL} calculate C^*_{P3PL} and C^*_{P1PL} from Eqs. 11.47-11.48.
3. Calculate parameter E using Eq. 11.46 and C^*_{P1PL} and C^*_{P2PL}.

4-7. Steps 4-7 as in the Type II(-) described above.

For Type III phase behavior, the tie lines for the left (Type II(+)) and the right (Type (-)) lobes are calculated separately. Because of the symmetric binodal curve assumption, the binodal curve is calculated in the same manner as in the Type II(-) and Type II(+) cases. The invariant point M is calculated as follows:

$$a = \frac{C_{SE} - C_{SEL}}{C_{SEU} - C_{SEL}} \tag{11.53}$$

where

$$\frac{a - C_{P2M}}{C_{P3M}} = \text{Cos } 60^\circ \tag{11.54}$$

Therefore, $C_{P3M} = 2(a - C_{P2M})$.

Since the invariant point M is on the binodal curve, Eq. 11.33 can be used to calculate C_{P3M} as a function of C_{P2M} using Eq. 11.45:

$$C_{P3M} = \frac{1}{2}\left(-AC_{P2M} + \sqrt{(AC_{P2M})^2 + 4AC_{P2M}(1 - C_{P2M})}\right) \tag{11.55}$$

Solving Eqs. 11.54-11.55 for C_{P2M}, the following is obtained:

$$C_{P2M} = \frac{2a(4 - A) + A \pm \sqrt{(2a(4 - A) + A)^2 - 16a^2(4 - A)}}{2(4 - A)} \tag{11.56}$$

The invariant point should disappear when C_{SE} approaches C_{SEL} (C_{P2M} = 0, a = 0) and when C_{SE} approaches C_{SEU} (C_{P2M} = 1, a = 1). These conditions hold only for the negative sign in Eq. 11.56. Therefore, the composition at the invariant point is determined by Eq. 11.55, Eq. 11.56 with the negative sign, and by

$$C_{P1M} = 1 - C_{P3M} - C_{P2M} \tag{11.57}$$

The plait point for the left lobe of the Type III phase environment must vary between zero and the plait point for the Type II(+) value, C^*_{P2PL}. The plait point is calculated by salinity interpolation:

$$C_{P2PL} = C^*_{P2PL} + \frac{C_{P2PL}}{C_{SEU} - C_{SEL}}(C_{SE} - C_{SEU}) \tag{11.58}$$

In order to apply the Hand equations to the left lobe, a coordinate transformation is made (Fig. 11.3). The Hand distribution equation in the new coordinate system is :

$$\frac{C'_{P32}}{C'_{P22}} = E\left(\frac{C'_{P31}}{C'_{P11}}\right) \tag{11.59}$$

where

$$C'_{P\,2\ell} = C_{P2\ell} \text{ Sec } \theta \tag{11.60}$$

$$C'_{P\,3\ell} = C_{P3\ell} - C_{P2\ell} \tan \theta \tag{11.61}$$

$$C'_{P\,1\ell} = 1 - C'_{P\,2\ell} - C'_{P\,3\ell} \tag{11.62}$$

Now let

$$\beta = \text{Sec}\,\theta = \frac{\sqrt{(C_{P2M})^2 + (C_{P3M})^2}}{C_{P2M}} \tag{11.63}$$

$$\alpha = \tan\theta = \frac{C_{P3M}}{C_{P2M}} \tag{11.64}$$

Because of the symmetric binodal curve assumption (F=1), E can be calculated explicitly from:

$$E = \frac{C'_{P1P}}{C'_{P2P}} \frac{1-(\beta-\alpha)C_{P2P} - C_{P3P}}{\beta C_{P2P}} \tag{11.65}$$

where C_{P2P} is equal to C_{P2PL} calculated using Eq. 11.58, and C_{P3P} and C_{P1P} are calculated from Eqs. 11.47 and 11.48.

C_{P11} and C_{P31} are calculated by Eqs. 11.44-11.45. Now Eq. 11.59 can be solved as before:

$$C_{P22} = \frac{A}{h'^2 + A\,h' + A} \tag{11.66}$$

where

$$h' = \frac{b\,E\,C'_{P31}}{C'_{P11}} \tag{11.67}$$

and

$$C_{P32} = h'\,C_{P22} \tag{11.68}$$

$$C_{P12} = 1 - C_{P22} - C_{P32} \tag{11.69}$$

Therefore all phase concentrations for the two phases in the left lobe have been determined.

The calculations for the right lobe are very similar to the above calculations for the left lobe. The C_{P2P} value for the plait point in this case varies between 1 and the input value for the Type II(-) case, C^*_{P2PR}, and is calculated by:

$$C_{P2PR} = C^*_{P2PR} + \left(\frac{1-C^*_{P2PR}}{C_{SEU} - C_{SEL}}\right)(C_{SE} - C_{SEL}) \tag{11.70}$$

Then C_{P32} is calculated using Eq. 11.45 but as a function of C_{P12} instead of C_{P21}:

$$C_{P32} = \frac{1}{2}\left(-AC_{P12} + \sqrt{(AC_{P12})^2 + 4AC_{P12}(1-C_{P12})}\right) \tag{11.71}$$

and

$$C_{P22} = 1 - C_{P12} - C_{P32} \tag{11.72}$$

Now let

$$h' = \frac{b\,C'_{P32}}{E\,C'_{P11}} + a \tag{11.73}$$

Then

$$C_{P11} = \frac{A}{h'^{\,2} + A\,h' + A} \tag{11.74}$$

$$C_{P31} = h'\,C_{P11} \tag{11.75}$$

$$C_{P21} = 1 - C_{P11} - C_{P31} \tag{11.76}$$

where

$$\alpha = \frac{C_{P3M}}{C_{P1M}} \tag{11.77}$$

$$\beta = \frac{\sqrt{C_{P3M}^2 + C_{P1M}^2}}{C_{P1M}} \tag{11.78}$$

$$C'_{P1\ell} = \beta\,C_{P1\ell} \tag{11.79}$$

$$C'_{P3\ell} = C_{P3\ell} - \alpha\,C_{P1\ell} \tag{11.80}$$

$$C'_{P2\ell} = 1 - C'_{P3\ell} - C'_{P1\ell} \tag{11.81}$$

$$E = \frac{C'_{P1P}}{C'_{P2P}} = \frac{\beta C_{P1P}}{1-(\beta-\alpha)C_{P1P} - C_{P3P}} \tag{11.82}$$

C'_{P1P} and C'_{P2P} are calculated using Eqs. 11.79-11.81 and Eqs. 11.47-11.48.

When three phases exist, the water and oil pseudocomponents are assumed to contain no surfactant pseudocomponent. This assumption is a consequence of the choice of phase behavior in the three phase region which assumes that the two phase region below the three phase tie triangle is very small; therefore, any composition in the three phase region will have three phases comprising of the surfactant-rich pseudophase with the composition of the invariant point, water-rich pseudophase with the composition of the water pseudocomponent apex, and oil-rich pseudophase with the composition of the oil pseudocomponent apex. Therefore:

$$C_{P11} = C_{P22} = 1 \tag{11.83}$$

$$C_{P21} = C_{P31} = C_{P12} = C_{P32} = 0 \tag{11.84}$$

The composition of the third phase, C_{P13}, C_{P23}, and C_{P33}, is calculated using Eqs. 11.55-11.57. Phase concentrations in the single phase region are the same as the overall composition, $C_{P13} = C_{P1}$, $C_{P23} = C_{P2}$, $C_{P33} = C_{P3}$. The other phase concentrations are zero.

The distribution of the three pseudocomponents in the two or three pseudophases for Type III phase behavior are summarized below:

11.4.3 For Type III Phase Behavior, $C_{SEL} \leq C_{SE} \leq C_{SEU}$

Known values for this case are: C_{3max0}, C_{3max1}, C_{3max2}, C_{SE}, C_{SEL}, C_{SEU}, C^*_{P2PR}, C^*_{P2PL} and overall concentration of the pseudocomponents, C_{P1}, C_{P2}, and .C_{P3}.

1. Calculate parameter A from Eq. 11.39-11.40.
2. Calculate C_{P2M} from Eqs. 11.56.
3. Calculate C_{P3M} and C_{P1M} from Eqs. 11.55-11.57.
4. <u>If the total composition is in the three phase region:</u>
   - Calculate water and oil pseudophase concentrations from Eqs. 11.83-11.84.
   - $C_{P23} = C_{P2M}$ calculated in step 2. $C_{P33} = C_{P3M}$ and $C_{P13} = C_{P1M}$ calculated in step 3.
5. <u>If the total composition is in Type II(+) lobe of Type III:</u>
   - Calculate C_{P2PL} from Eq. 11.58.
   - Calculate a and b from Eqs. 11.63-11.64.
   - Calculate C_{P3PL} and C_{P1PL} from Eqs. 11.47-11.48 using C_{P2PL}.
   - Calculate parameter E from Eq. 11.65.
   - * Using a value of C_{P21} from 0 to C_{P2PL}, calculate C_{P11} and C_{P31} using Eqs. 11.44-11.45.
   - Calculate C'_{P31} and C'_{P11} from Eqs. 11.61-11.62.
   - Calculate h' from Eq. 11.67.
   - Calculate C_{P22}, C_{P32}, and C_{P12} using Eqs. 11.66, 11.68, and 11.69.
   - If $(C_{P33} - C_{P3})(C_{P21} - C_{P2}) - (C_{P31} - C_{P3})(C_{P23} - C_{P2}) \leq \varepsilon$, where ε is a sufficiently small number (10^{-4}), then stop; otherwise increment C_{P21} using the half interval method and go back to step *****.
6. <u>If the total composition is in Type II(-) lobe of Type III:</u>
   - Calculate C_{P2PR} from Eq. 11.70.
   - Calculate α and β from Eqs. 11.77-11.78.

- Calculate C_{P3PR} and C_{P1PR} from Eqs. 11.47-11.48 using C_{P2PR}.
- Calculate parameter E from Eq. 11.82.

** Using a value of C_{P12} from 0 to C_{P1PR}, calculate C_{P32} and C_{P22} using Eqs. 11.71-11.72.

- Calculate C'_{P31} and C'_{P11} from Eqs. 11.79-11.80.
- Calculate h' from Eq. 11.73.
- Calculate C_{P11}, C_{P31}, and C_{P21} using Eqs. 11.74-11.76.
- If $(C_{P32} - C_{P3})(C_{P23} - C_{P2}) - (C_{P33} - C_{P3})(C_{P22} - C_{P2}) \leq \varepsilon$, where ε is a sufficiently small number (10^{-4}), then stop; otherwise increment C_{P12} using the half interval method and go back to step **.

After the phase composition in the pseudoternary diagram and saturations are determined, the phase concentrations are converted back to the pseudoquaternary diagram using Eqs. 11.21-11.23. Phase compositions are calculated in Subroutine PHCOMP.

11.5 Figures

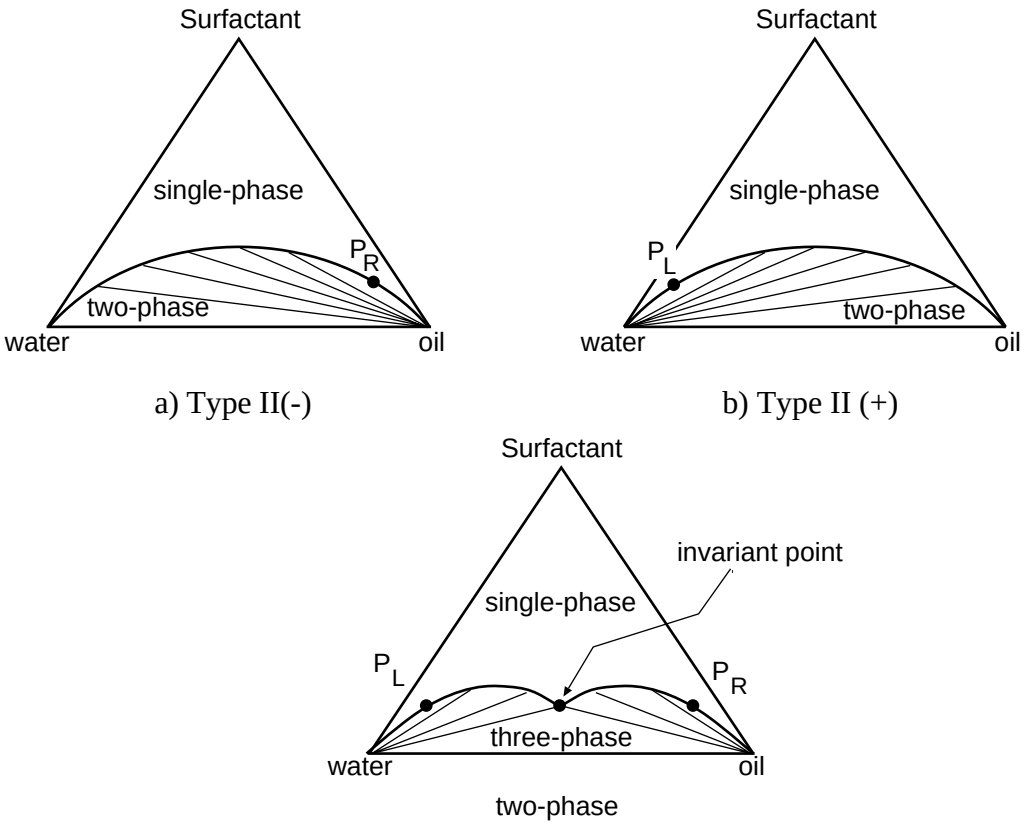

Figure 11.1. Schematic representations of a) Type II(-), b) Type II(+), and c) Type III.

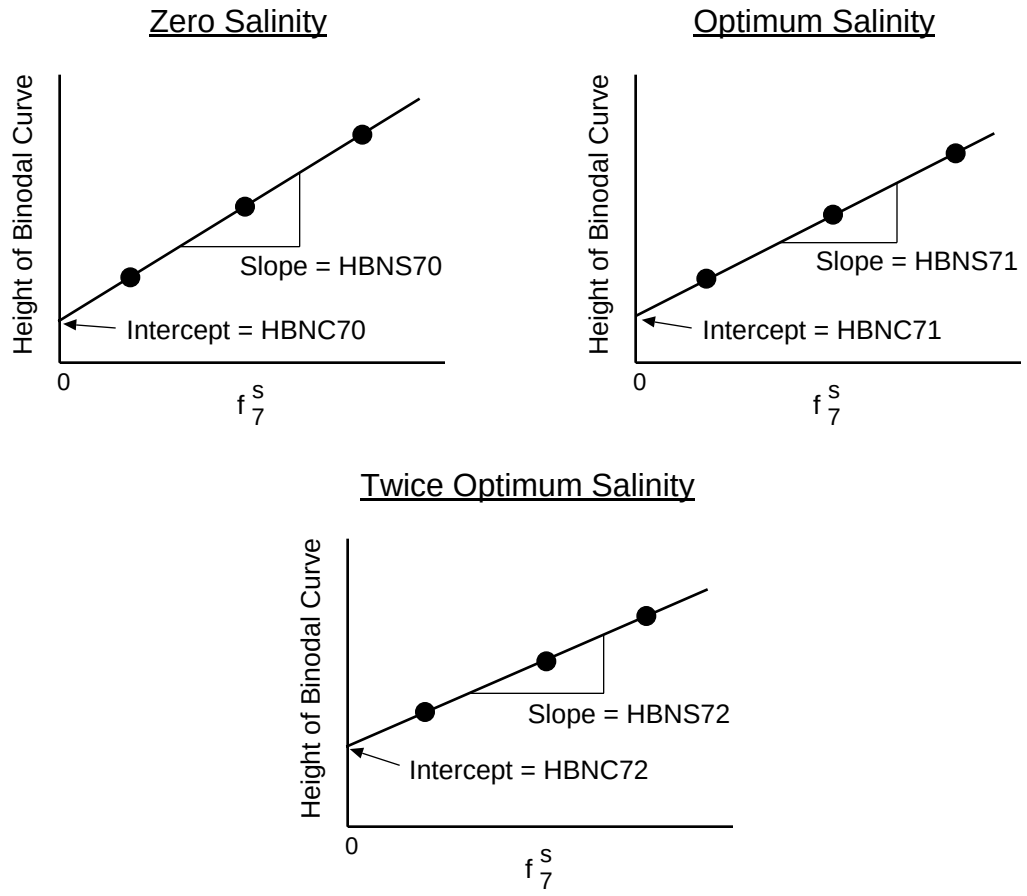

Figure 11.2. Effect of alcohol on the maximum height of binodal curve.

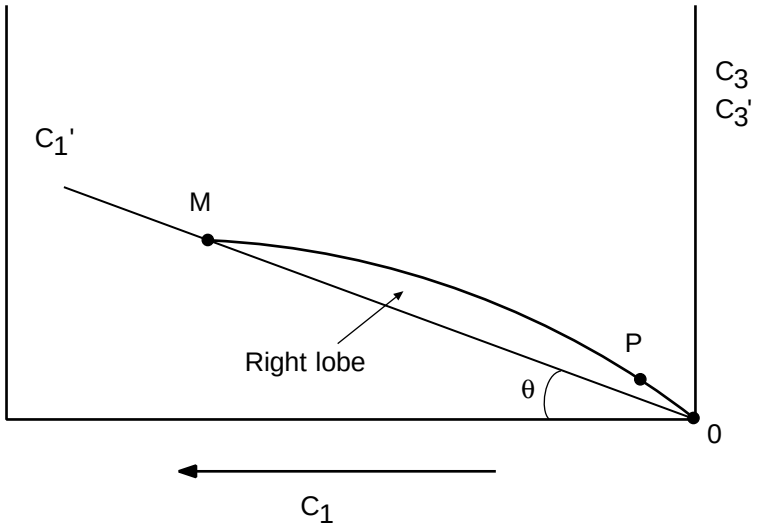

Figure 11.3. Coordinate transformation for Type III.

Section 12
Organic Dissolution Model in UTCHEM

12.1 Introduction

Both equilibrium and rate limited nonequilibrium solubility of organic component in the aqueous phase are modeled in UTCHEM. The rate limited mass transfer equations are used for the enhance solubility of oil in the presence of surfactant. The current implementation in UTCHEM is for under optimum Type II(-) surfactant formulation. However, it can be applied to the Type III phase environment. This section discusses the formulation and the method of solution for the case of single component oil phase. The formulation of the multiple organic oleic phase is given in Section 7.

12.2 Saturated Zone (Gas Phase Is Not Present)

The overall component concentrations for water ($\kappa = 1$), oil ($\kappa = 2$), and surfactant ($\kappa = 3$) in two-phase flow of water/oil or microemulsion/oil from the conservation equations are

$$C_1 = C_{11}S_1 + C_{12}S_2 \tag{12.1a}$$

$$C_2 = C_{21}S_1 + C_{22}S_2 \tag{12.1b}$$

$$C_3 = C_{31}S_1 + C_{32}S_2 \tag{12.1c}$$

where phase 2 refers to the oil phase and phase 1 in this section refers to either water or surfactant rich microemulsion phase.

The overall concentrations for oil, water, and surfactant are obtained solving the conservation equations as below

$$\frac{\partial(\phi C_\kappa)}{\partial t} + \vec{\nabla}\cdot\left(\tilde{F}_{\kappa 1} + \tilde{F}_{\kappa 2}\right) = Q_{\kappa 1} + Q_{\kappa 2} \qquad \text{for } \kappa = 1, 2, 3 \tag{12.2}$$

where the flux term is the sum of the convective and dispersive fluxes as

$$\begin{aligned} \tilde{F}_{\kappa 1} &= C_{\kappa 1}\vec{u}_1 - \phi S_1 \vec{\vec{K}}_{\kappa 1}\cdot\vec{\nabla}C_{\kappa 1} \\ \tilde{F}_{\kappa 2} &= C_{\kappa 2}\vec{u}_2 - \phi S_2 \vec{\vec{K}}_{\kappa 2}\cdot\vec{\nabla}C_{\kappa 2} \end{aligned} \qquad \text{for } \kappa = 1 \text{ or } 2 \tag{12.3}$$

The definitions of the dispersion tensor and the flux are given in Section 2. The nonequilibrium concentration of oil in the aqueous phase is computed from the mass balance on oil species in the aqueous phase and using the first order mass transfer rate equation for oil dissolution as

$$\frac{\partial(\phi S_1 C_{21})}{\partial t} + \vec{\nabla}\cdot\tilde{F}_{21} = Q_{21} + M\left(C_{21}^{eq} - C_{21}\right) \tag{12.4}$$

where C_{21}^{eq} is the known limit of solubility for oil in the aqueous phase. In the absence of the surfactant, the C_{21}^{eq} is the limit of solubility for the specific organic contaminant and when surfactant is present the equilibrium solubility is calculated from the Hand's equations (Section 2). M is the mass transfer coefficient for the dissolution of organic species in the water phase and is assumed to be a constant. Equation 12.4 is solved either explicitly or implicitly as described below.

12.2.1 Organic Solubility

12.2.1.1 Explicit Solution

The new time level, (n+1), concentration of oil solubilized in water is

$$\left(\phi S_1 C_{21}\right)^{n+1} = \left(\phi S_1 C_{21}\right)^{n} + (Q_{21} - \vec{\nabla}\cdot\tilde{F}_{21})\Delta t + M\Delta t\left(C_{21}^{eq} - C_{21}^{n}\right) \quad \text{for } C_{21}^{n} < C_{21}^{eq} \tag{12.5}$$

where the right-hand side of the equation is a known quantity. Therefore,

$$\left(S_1 C_{21}\right)^{n+1} = \frac{\left(\phi S_1 C_{21}\right)^{n+1}}{\phi^{n+1}} \tag{12.6}$$

since the porosity is known either as a constant or is calculated based on the new time step pressure if rock compressibility is not negligible.

12.2.1.2 Implicit Solution

$$\left(\phi S_1 C_{21}\right)^{n+1} = \left(\phi S_1 C_{21}\right)^{n} + (Q_{21} - \vec{\nabla}\cdot\tilde{F}_{21})\Delta t + M\Delta t\left(C_{21}^{eq} - C_{21}^{n+1}\right) \tag{12.7}$$

where we define $\text{RHS} = \left(\phi S_1 C_{21}\right)^{n} + (Q_{21} - \vec{\nabla}\cdot\tilde{F}_{21})\Delta t + M\Delta t\left(C_{21}^{eq} - C_{21}^{n+1}\right)$.

Substituting for S_1^{n+1} from overall concentration for oil component (Eq. 12.1b) and noting that ***C_{22} = 1 for the flow conditions of oil/water and the Type II(-) with corner plait point*** and the sum of the saturations is equal to one ($S_1 + S_2 = 1$), we have

$$\left(\phi C_{21}\frac{C_2 - 1}{C_{21} - 1}\right)^{n+1} = \text{RHS} \tag{12.8}$$

The above equation can then be rearranged in terms of oil concentration in the aqueous phase (C_{21}) as

$$M\,\Delta t\,C_{21}^2 + \text{bterm}\,C_{21} + \text{cterm} = 0 \tag{12.9}$$

where

$$\text{bterm} = \phi C_2 - \phi - M\Delta t - \text{cterm} \tag{12.10}$$

$$\text{cterm} = \left(\phi S_1 C_{21}\right)^{n} + \Delta t\left(Q_{21} - \vec{\nabla}\cdot\tilde{F}_{21}\right) + M\,\Delta t\,C_{21}^{eq} \tag{12.11}$$

The solution to the quadratic equation (Eq. 12.9) is

$$\begin{cases} C_{21} = \dfrac{2\text{cterm}}{-\text{bterm} + \sqrt{(\text{bterm})^2 - 4M\,\Delta t(\text{cterm})}} & \text{for bterm} < 0 \\ C_{21} = \dfrac{2\text{cterm}}{-\text{bterm} - \sqrt{(\text{bterm})^2 - 4M\,\Delta t(\text{cterm})}} & \text{for bterm} > 0 \end{cases} \tag{12.12}$$

12.2.2 Phase Saturations

12.2.2.1 Oil/Water Phases (No Surfactant)

Substituting $C_{12} = 0.0$ and $C_{22} = 1.0$, Eqs. 12.1a and 12.1b become

$$C_1 = C_{11} S_1$$
$$C_2 = C_{21} S_1 + S_2 \tag{12.13}$$

The equilibrium saturations and concentrations are computed first as

$$S_2^{eq} = \frac{C_2 - \min(C_2, K_{ow})}{1 - \min(C_2, K_{ow})} \tag{12.14}$$

$$S_1^{eq} = 1. - S_2^{eq} \tag{12.15}$$

where K_{ow} is the limit of solubility of oil in water at equilibrium in the absence of surfactant or cosolvent and is an input parameter. The minimum in Eq. 12.14 is taken to ensure that the input solubility is not greater than the total oil available in a gridblock.

The nonequilibrium phase saturations and concentrations are computed as described below once the equilibrium organic concentration is solved for from Eq. 12.4.

Explicit Method

Since the product of water saturation times the oil concentration is known using the explicit solution (Eq. 12.6), the new time step oil saturation from Eq. 12.1b is

$$S_2 = C_2 - (C_{21} S_1)^{n+1} \quad \text{and} \quad S_1 = 1 - S_2 \tag{12.16}$$

The overall oil concentration (C_2) is computed from the oil material balance equation. The phase compositions are then as follows

$$C_{11} = \frac{C_1}{S_1}$$
$$C_{21} = \min\left(C_{21}^{eq} , \frac{(C_{21} S_1)^{n+1}}{S_1} \right) \tag{12.17}$$
$$C_{22} = 1.0$$

If the calculated nonequilibrium concentration is greater than the equilibrium value ($C_{21} > C_{21}^{eq}$), the saturations are then set to the equilibrium values calculated from Eqs. 12.14 and 12.15.

Implicit Method

From the implicit solution of the mass balance equation for oil component in the aqueous phase, we could obtain the nonequilibrium organic dissolution in the aqueous phase (Eq. 12.12). The phase saturations and phase compositions are then calculated as

$$\begin{cases} C_{21}^{noneq} = \min(C_{21}^{eq}, C_{21}) \\ S_1 = \dfrac{C_1}{1 - C_{21}^{noneq}} \\ S_2 = 1 - S_1 \end{cases} \tag{12.18}$$

and

$$C_{11} = \frac{C_1}{S_1}$$
$$C_{12} = 0.0 \qquad (12.19)$$
$$C_{22} = 1.0$$

12.2.2.2 Oil/Aqueous Phases (Surfactant Below CMC)

The phase concentrations and saturations are calculated as above and surfactant concentration is

$$C_{31} = \frac{C_3}{S_1} \qquad (12.20)$$

12.2.2.3 Oil /Microemulsion Phases (Type II (-) With Corner Plait Point)

For the case of corner plait point we have

$C_{22} = 1.0$, $C_{12} = 0.0$, and $C_{32} = 0.0$

and the equilibrium concentrations of surfactant, oil, and water in microemulsion phase $\left(C_{11}^{eq}, C_{21}^{eq}, C_{31}^{eq}\right)$ are calculated from Hand's equations described in Section 2. Substituting these in the overall component concentrations, we have

$$C_1 = C_{11}S_1$$
$$C_2 = S_2 + C_{21}S_1 \qquad (12.21)$$
$$C_3 = C_{31}S_1$$

The equilibrium saturations are then computed as

$$S_2^{eq} = \frac{C_2 - C_{21}^{eq}}{1 - C_{21}^{eq}} \qquad (12.22)$$
$$S_1^{eq} = 1 - S_2^{eq}$$

The nonequilibrium concentration of oil (C_{21} for the implicit solution or S_1C_{21} for the explicit solution) is computed from Eq. 12.4 using an explicit or implicit method. The following section gives the phase saturations and phase compositions for both the implicit and explicit solutions of the organic mass balance equation.

Explicit Method

The phase saturations are computed using the overall oil concentration and the product of microemulsion saturation times organic concentration in the microemulsion phase from Eq. 12.12.

$$S_2 = C_2 - \left(C_{21}S_1\right)^{n+1}$$
$$S_1 = 1. - S_2 \qquad (12.23)$$

The phase compositions are then computed as

$$
\begin{aligned}
C_{11} &= \frac{C_1}{S_1} \\
C_{21} &= \min\left(C_{21}^{eq}, \frac{(C_{21}S_1)^{n+1}}{S_1} \right) \\
C_{31} &= 1. - C_{11} - C_{21} \\
C_{22} &= 1.0 \\
C_{12} &= 0.0 \\
C_{32} &= 0.0
\end{aligned}
\tag{12.24}
$$

If the calculated nonequilibrium concentration is greater than the equilibrium value ($C_{21} > C_{21}^{eq}$), the saturations are then set to the equilibrium values.

Implicit Method

From the implicit solution of mass balance equation for oil component in the microemulsion phase, we could obtain the nonequilibrium organic dissolution (Eq. 12.12). The phase saturations and phase compositions are calculated as

$$
\begin{cases}
C_{21} = \min(C_{21}^{eq}, C_{21}^{n+1}) \\
S_2 = \dfrac{C_2 - C_{21}}{1 - C_{21}} \\
S_1 = 1 - S_2
\end{cases}
\tag{12.25}
$$

and

$$
\begin{aligned}
C_{11} &= \frac{C_1}{S_1} \\
C_{31} &= 1 - C_{11} - C_{21} \\
C_{12} &= 0.0,\ C_{22} = 1.0,\ C_{32} = 0.0
\end{aligned}
\tag{12.26}
$$

12.3 Vadose Zone

The solubility of organic species in three-phase flow of water/oil/gas in the vadose zone in the absence of surfactant is modeled in UTCHEM. Similar to the previous section, the overall concentrations for oil, water, and gas are obtained solving the conservation equations.

$$
\frac{\partial(\phi C_\kappa)}{\partial t} + \vec{\nabla} \cdot \left(\tilde{F}_{\kappa 1} + \tilde{F}_{\kappa 2} \right) = Q_{\kappa 1} + Q_{\kappa 2} \qquad \text{for } \kappa = 1, 2, 8 \tag{12.27}
$$

The nonequilibrium concentration of oil in the aqueous phase is calculated from the mass balance on oil species in the aqueous phase and using the first order mass transfer equation for oil solubility as

$$
\frac{\partial(\phi S_1 C_{21})}{\partial t} + \vec{\nabla} \cdot \tilde{F}_{21} = Q_{21} + M\left(C_{21}^{eq} - C_{21} \right) \tag{12.28}
$$

where the flux term is defined as

$$\tilde{F}_{21} = C_{21}\vec{u}_1 - \phi S_1 \vec{\vec{K}}_{21} \cdot \vec{\nabla} C_{21} \tag{12.29}$$

Equation 12.29 is solved explicitly to obtain the rate-limited solubility of contaminant in the aqueous phase in the vadose zone. The new time level, (n+1), concentration of oil solubilized in water is

$$(\phi S_1 C_{21})^{n+1} = (\phi S_1 C_{21})^n + (Q_{21} - \vec{\nabla} \cdot \tilde{F}_{21})\Delta t + M\Delta t\left(C_{21}^{eq} - C_{21}^n\right) \quad \text{for } C_{21}^n < C_{21}^{eq} \tag{12.30}$$

where the right-hand side of the equation is a known quantity. Therefore,

$$(S_1 C_{21})^{n+1} = \frac{(\phi S_1 C_{21})^{n+1}}{\phi^{n+1}} \tag{12.31}$$

since the porosity is known and the new time step oil saturation from Eq. 12.1b is

$$S_2 = C_2 - (C_{21} S_1)^{n+1} \tag{12.32}$$

$$S_1 = C_1 - (S_1 C_{21})^{n+1} \tag{12.33}$$

and

$$S_4 = 1 - S_1 - S_2 \tag{12.34}$$

where the overall concentrations (C_1 and C_2) are computed from the species conservation equations. The phase compositions are then as follows

$$C_{11} = \frac{C_1}{S_1}$$

$$C_{21} = \min\left(C_{21}^{eq}, \frac{(C_{21} S_1)^{n+1}}{S_1}\right) \tag{12.34}$$

$$C_{22} = 1.0$$

If the calculated nonequilibrium concentration is greater than the equilibrium value ($C_{21} > C_{21}^{eq}$), the saturations and phase concentrations are set back to those at the equilibrium.

12.4 Mass Transfer Coefficient

The mass transfer coefficient can either be a constant or can be calculated using an empirical correlation based on the work of Imhoff *et al.* [1995]. The correlation relates the mass transfer coefficient (M) to the Sherwood number (Sh) as below.

$$Sh = [929.03]\frac{M d_{50}^2}{D_a} \tag{12.35}$$

where D_a is the molecular diffusion coefficient of NAPL in the aqueous phase (ft^2/d), d_{50} is the mean grain size diameter (cm) and M is the mass transfer coefficient (1/day). The constant in the bracket is the unit conversion.

The Sherwood number is calculated as a function of Reynolds number, NAPL content, and Schmidt number as follows.

$$Sh = \beta_0 \, Re^{\beta_1} \, \theta_n^{\beta_2} \, Sc^{\beta_3} \tag{12.36}$$

where β_0, β_1, β_2, and β_3 are input parameters and are based on the best fit of the experimental data. The dimensionless numbers are defined as below.

$$\theta_n = \frac{S_2}{\phi} \tag{12.37}$$

$$Re = [0.0353] \frac{\rho_a \, d_{50} \, u_a}{\mu_a \, \phi \, S_a} \tag{12.38}$$

where the constant in the bracket is the unit conversion factor. u_a is the darcy flux (ft/d), μ_a is the aqueous phase viscosity (cp), S_a is the aqueous phase saturation, and ρ_a is the aqueous phase density (g/cc).

$$Sc = [0.93] \frac{\mu_a}{D_a \, \rho_a} \tag{12.39}$$

The mean grain size diameter is calculated using Carmen-Kozeny correlation as below

$$d_{50} = [0.0001] \sqrt{300 \, k_x \frac{(1-\phi)^2}{\phi^3}} \tag{12.40}$$

where horizontal permeability (k_x) is in Darcy and d_{50} is in cm.

12.5 Nomenclature

$C_{i,\kappa}$ = Total concentration of species κ in gridblock i, L^3/L^3 PV

C_κ = Overall concentration of species κ in the mobile phases, L^3/L^3

C_κ^{eq} = Equilibrium concentration of species κ, L^3/L^3

$C_{\kappa\ell}$ = Concentration of species κ in phase ℓ, L^3/L^3

K = Dispersion coefficient, L^2t^{-1}

$\vec{\vec{K}}_{\kappa\ell}$ = Dispersion tensor for species κ in phase ℓ, L^2

M = Mass transfer coefficient, t^{-1}

Q_κ = Source/sink for species κ, L^3/T

S_ℓ = Saturation of phase ℓ, L^3/L^3 PV

t = Time, t

Δt^n, Δt^{n+1} = Time-step size at n^{th} and $n+1^{th}$ time level, t

$\vec{u}_\ell$ = Darcy flux, Lt^{-1}

Greek Symbols

ϕ = Porosity, fraction

Subscripts

κ = species number

- 1 = Water
- 2 = Oil
- 3 = Surfactant
- 8 = air

ℓ = Phase number

- 1 = Aqueous
- 2 = Oleic
- 3 = Microemulsion
- 4 = Air

Section 13
Organic Adsorption Models

13.1 Introduction

We have incorporated both a linear adsorption isotherm and a nonlinear Freundlich isotherm in UTCHEM model (Means *et al.*, 1980; Travis and Etnier, 1981; Rao and Jassup, 1982; Miller and Weber, Jr., 1984; Kinniburgh, 1986, Brusseau and Rao, 1989; Ball and Roberts, 1991). The linear model was already available in UTCHEM. Since both of these models are only valid for small concentrations of organic species and introduce large errors if extrapolated beyond the range of validity, the Langmuir isotherm was also implemented in UTCHEM.

13.2 Linear Isotherm

There are several versions of the linear isotherm with respect to the coefficient and there are empirical correlations for the solute partition coefficient as a function of either solubility or water-octanol partition coefficient (Means *et al.*, 1980; Schwarzenbach and Westall, 1981; Chiou *et al.*, 1983; Karickhoff, 1984; Sabljic, 1987). The current UTCHEM implementation allows for either distribution coefficient (K_d) or fraction of organic carbon (f_{oc}) and partition coefficient (K_{oc}) as input parameters for the linear isotherm.

$$\hat{C}_\kappa = K_{d,\kappa} \min\left(C_{\kappa 1}^{eq}, C_{\kappa\ell}\right) \qquad \kappa = 1,\ldots, N_O \tag{13.1}$$

where

$\hat{C}_\kappa$ = adsorbed organic species, g adsorbed organic/g soil,

$K_{d,\kappa}$ = distribution coefficient for species κ, cc solution/g soil,

$C_{\kappa\ell}$ = concentration of organic species κ in the aqueous (phase ℓ) or surfactant-rich aqueous solution (phase 3 in the Type II(-)), g organic/cc solution,

$C_{\kappa 1}^{eq}$ = equilibrium solubility of organic species κ in water, g organic/cc solution, and

N_O = number of organic species.

The minimum in the above equation is taken to introduce the organic solubility as the upper limit concentration for extrapolation of linear isotherm. We will further investigate this aspect of the model.

$K_{d,\kappa}$ can be input directly or it can be calculated from $K_{d,\kappa} = f_{oc}\, K_{oc,\kappa}$ if the user prefers to input f_{oc} and $K_{oc,\kappa}$, where

f_{oc} = fraction of organic carbon in soil, g organic carbon in soil/g soil, and

$K_{oc,\kappa}$ = partition coefficient for organic species κ, $\dfrac{\text{g adsorbed/g organic carbon in soil}}{\text{g organic/cc solution}}$.

There are several empirical correlations available to calculate the partition coefficient (Lyman *et al.*, 1982; Chiou *et al.* , 1983). Examples of these correlations for nonionic organic species are given by Chiou *et al.* (1983) as

$$\begin{aligned} \log K_{oc} &= -0.729 \log S + 0.001 \\ \log K_{oc} &= 0.904 \log K_{ow} - 0.779 \end{aligned} \tag{13.2}$$

where S is the molar water solubility of the compound and K_{ow} is the octanol-water partition coefficient. We may implement a few of these empirical correlations as a function of solubility as options in UTCHEM in order to reduce the number of adsorption model input parameters since the organic solubility is already one of the UTCHEM input parameters.

13.3 Freundlich Isotherm

The nonlinear Freundlich isotherm was implemented in UTCHEM. The Freundlich sorption isotherm is one that has been widely used to calculate the sorption of organic species and various metals by soils.

$$\hat{C}_\kappa = K_{f,\kappa}\left[\min\left(C_{\kappa 1}^{eq}\ ,\ C_{\kappa\ell}\right)\right]^n \qquad \kappa = 1,\ldots,\ N_O \tag{13.3}$$

where

$K_{f,\kappa}$ = constant related to sorption capacity, cc solution/g soil, and

n = constant related to sorption intensity.

As for the case of linear isotherm, we assume that the Freundlich isotherm is valid for concentrations below and at the equilibrium water solubility. We will further investigate how to introduce an upper limit to the amount of sorbed solute. This is especially important for the surfactant enhanced remediation processes where the injected surfactant will greatly enhance the organic solubility.

13.4 Langmuir Isotherm

The Langmuir sorption isotherm is the only model chosen that assumes a finite number of sorption sites and once all the sorption sites are filled, the surface will no longer sorb solute from solution. The Langmuir isotherm implemented in UTCHEM is expressed as

$$\hat{C}_\kappa = \frac{a_\kappa b_\kappa \max\left(C_{\kappa 1}, C_{\kappa 3}\right)}{1 + b_\kappa \max\left(C_{\kappa 1}, C_{\kappa 3}\right)} \qquad \kappa = 1,\ldots,\ N_O \tag{13.4}$$

where

b_κ = constant related to the rate of adsorption, cc solution/g soil, and

a_κ = the maximum amount of solute that can be adsorbed by the solid, g adsorbed/g soil.

The maximum is taken to use the higher concentration of solute in the aqueous or surfactant-rich phase.

13.5 Implementation

The implementation of the organic sorption models in UTCHEM involves tracking of the adsorbed amount for each organic compound. The organic species are considered as volume occupying components in UTCHEM and thus the adsorbed amount is calculated in every time step and is taken into account when computing the overall species concentrations as

$$\tilde{C}_\kappa = \left(1 - \sum_{\kappa=1}^{n_{cv}} \hat{C}_\kappa\right)\sum_{\ell=1}^{n_p} S_\ell C_{\kappa\ell} + \hat{C}_\kappa \qquad \kappa = 1,\ldots,\ n_c \tag{13.5}$$

where

$\tilde{C}_\kappa$ = overall volume of component κ per unit pore volume, vol./ pore vol.,

S_ℓ = saturation of phase ℓ, vol./ pore vol.,

$C_{\kappa\ell}$ = concentration of species κ in phase ℓ,

n_{cv} = volume occupying components such as surfactant, organic species, and co-solvents, and

n_c = number of components.

Organic Adsorption Models

The adsorption calculations for the organic components are done in a new subroutine called ADOIL. This routine is called only if the input flag IADSO is not equal to zero. The unit of adsorption can take on a variety of forms, but mass of oil per mass of soil is most common. Since we use the unit of volume of species per pore volume for the concentrations in the species conservation equations in UTCHEM, a unit conversion for the adsorbed quantity from mass/mass to vol./pore volume is included in the subroutine ADOIL. The unit conversion, the quantity in the bracket, is

$$\frac{\text{vol. of adsorbed organic}}{\text{Pore volume}} = \frac{\text{mass of adsorbed organic}}{\text{mass of soil}}\left[\frac{\rho_s(1-\phi)}{\phi\rho_\kappa}\right]$$

where

ρ_s = soil bulk density, g/cc,

ρ_κ = density of organic species, g/cc, and

ϕ = porosity.

The calculated amount of adsorbed organic species from Eqs. 13.1, 13.3, and 13.4 after the conversion to the unit of vol./pore vol. is checked against the overall concentration ($\tilde{C}_\kappa$) from Eq. 13.5 to guarantee that the adsorption is no greater that the total organic concentrations.

Both reversible and irreversible organic adsorption models are implemented. The user can specify each model by an input flag IREV. A report of the material balance on each organic species is written to the output files at the end of the simulation with a consistent unit of volume per pore volume. The amount of sorbed organic is also written to the output files in g/g soil for the comparison with the experimental data.

Section 14
Hysteretic Capillary-Pressure and Relative-Permeability Model for Mixed-Wet Rocks

14.1 Introduction

This section describes the formulation of the hysteretic two-phase oil/water relative-permeability, saturation, capillary-pressure relations (k-S-P) incorporated in UTCHEM for mixed-wet media.

Lenhard [1997] developed a hysteretic k-S-P model for two-phase flow of oil-water in a mixed-wet porous medium based on pore-scale processes. Key features of the capillary pressure-saturation model are that 1) the main drainage curve can be modeled with either a power curve (Brooks and Corey, 1966) or an S-shape function (Lenhard, 1996), 2) the scanning curves are modeled using an S-shaped function that approaches asymptotes at either end, and 3) the model is capable of predicting relations between negative capillary pressures and saturations observed in mixed-wet rocks. The relative permeability-saturation function (k-S) is based on Burdine's pore-size-distribution model (Burdine, 1953) using the main drainage capillary-pressure parameter, λ. The wettability effects in the k-S relations are accounted for by using an index that is used to distinguish those pore sizes that are water-wet from those that are oil- or mixed-wet. The capillary-pressure model tested against experimental data indicated that the model is capable of capturing the capillary-pressure behavior in mixed-wet rocks. A trapped-oil-saturation relation has also been developed that takes into account the size of the pores that are oil-wet. The mixed-wet model has successfully been implemented in UTCHEM.

14.2 Model Description

Lenhard [1996] developed a hysteretic k-S-P model for two-phase flow of oil-water in a mixed-wet porous medium based on pore-scale processes. The main drainage capillary pressure-saturation relation can be described by either Brooks-Corey (Brooks and Corey, 1966) or van Genuchten functions [1980], whereas the scanning curves are modeled by a modified van Genuchten function (Lenhard, 1996) to account for the negative capillary pressure data in mixed-wet rocks. The relative permeability-saturation function (k-S) is based on Burdine's pore-size-distribution model using the main drainage capillary pressure parameter, λ. The wettability effects in the k-S relations are accounted for by using an index (M_{ow}) that is used to distinguish those pore sizes that are water-wet from those that are oil- or mixed-wet.

14.2.1 Capillary Pressure

The capillary pressure for any drying or wetting scanning curve is calculated using the modified van Genuchten function as follows:

$$P_c = P_{neg} + \frac{1}{\alpha}\left[\frac{1}{\left(\bar{S}_w\right)^{1/m}} - 1\right]^{1/n} \tag{14.1}$$

where $\bar{S}_w = \dfrac{S_w - S_{wr}}{1 - S_{wr} - S_{or}}$, P_{neg} is the maximum negative capillary pressure at which the water saturation reaches a maximum value on the main imbibition path, and α, m, and n are model fitting parameters. The residual water saturation, S_{wr}, is commonly assumed to be a function of only the pore-size geometry because it is always associated with the smallest pores. However, the residual oil saturation, S_{or}, in mixed-wet media is likely to be a function of the pore geometry as well as the sizes of the pores that are oil-wet. The smaller the oil-wet pores, the larger S_{or} is going to be. To index the smallest of the oil-wet pores, Lenhard used a saturation index, M_{ow} that characterizes the smallest pores in which oil has displaced water for the required residence time to transform the water-wet pores to oil-wet pores. M_{ow}, is

likely to be the initial water saturation in the reservoir before oil production. In many reservoirs this may be equal to the residual water saturation.

To develop a relation to calculate the residual oil saturation, it is assumed that S_{or} has a maximum value when $M_{ow} = S_{wr}$ and is zero when $M_{ow} = 1$. The proposed relationship (Lenhard, 1997) between S_{or} and M_{ow} is

$$S_{or} = S_{or}^{max}\left(1 - \overline{M}_{ow}\right)^2 \tag{14.2}$$

where S_{or}^{max} is the residual oil saturation at $M_{ow} = S_{wr}$ and

$$\overline{M}_{ow} = \left(\frac{M_{ow} - S_{wr}}{1 - S_{wr} - S_{or}}\right) \tag{14.3}$$

The substitution of Eq. 14.3 into Eq. 14.2 and re-arrangement of the resulting equation gives a cubic equation. The implementation in UTCHEM involves the analytical solution to the cubic equation with the root that meets all the imposed constraints to be the residual oil saturation.

14.2.2 Relative Permeabilities

Lenhard obtained analytical expressions for water and oil relative permeabilities using Burdine's relative-permeability model and the Brooks-Corey main drainage capillary pressure-saturation function.

For $\overline{S}_w \le \overline{M}_{ow}$:

$$k_{rw} = \overline{S}_w^{(2+3\lambda)/\lambda} \tag{14.4}$$

$$k_{ro} = \left(1 - \overline{S}_w\right)^2\left(1 - \overline{S}_w^{(2+\lambda)/\lambda}\right) \tag{14.5}$$

For $\overline{S}_w > \overline{M}_{ow}$:

$$k_{rw} = \overline{S}_w^2\left(1 + \overline{M}_{ow}^{(2+\lambda)/\lambda} - \Omega^{(2+\lambda)/\lambda}\right) \tag{14.6}$$

$$k_{ro} = \left(1 - \overline{S}_w\right)^2\left(\Omega^{(2+\lambda)/\lambda} - \overline{M}_{ow}^{(2+\lambda)/\lambda}\right) \tag{14.7}$$

where

$$\Omega = \overline{M}_{ow} + \overline{S}_o$$

$$\overline{S}_o = \frac{S_o - S_{or}}{1 - S_{wr} - S_{or}}$$

and

$$\overline{M}_{ow} = \frac{M_{ow} - S_{wr}}{1 - S_{wr} - S_{or}}$$

M_{ow} is an index that is used to distinguish those pore sizes that are water-wet from those sizes that are oil- or intermediate-wet. The assumption is that the largest pores will be oil- or intermediate-wet in mixed-wet oil reservoirs.

14.2.3 Saturation Path

As stated earlier, the main drainage branch can be modeled using either the Brooks-Corey or van Genuchten functions. However, all the scanning paths are modeled with an S-shaped function to capture the capillary-pressure asymptotes at the lower and upper saturation limits. To model an imbibition path with reversal from the main drainage, Lenhard [1996] developed the following equation:

$$\bar{S}_w(P_c) = 1 + \frac{\left(\bar{S}_w^{\,I}(P_c) - 1\right)\left(\bar{S}_w^{\,DI}\right)}{\bar{S}_w^{\,I}\left(P_c^{\,DI}\right) - 1} \tag{14.8}$$

where P_c is the capillary pressure of the point being calculated and $P_c^{\,DI}$ is the capillary pressure at the reversal from main drainage. $\bar{S}_w^{\,I}(P_c)$ and $\bar{S}_w^{\,I}\left(P_c^{\,DI}\right)$ are effective water saturations of the hypothetical main drainage branch at the capillary pressure P_c and the capillary pressure at the reversal point, respectively. $\bar{S}_w^{\,DI}$ is the effective water saturation at the most recent reversal from main drainage to imbibition.

Section 15
Groundwater Applications Using UTCHEM

15.1 Introduction

A subsurface numerical model of surfactant enhanced aquifer remediation must simulate the advection, dispersion, and transformation of the different species (contaminants, surfactant, water, electrolytes, co-solvent, polymer) in the aquifer under various pumping and injection strategies. UTCHEM is a three-dimensional chemical compositional simulator. Variations in density, interfacial tension, capillary pressure, relative permeability, adsorption, viscosity, diffusion and dispersion, biodegradation of organic contaminants and aqueous geochemistry among many other properties and phenomena are modeled. Surfactant floods performed at Hill AFB, DOE Portsmouth, and MCB Camp Lejeune were all modeled and designed with UTCHEM. Many NAPL sites have been modeled with UTCHEM during the past few years as shown in Fig. 15.1.

In addition to the surfactant enhanced aquifer remediation (SEAR) modeling, UTCHEM has also been used extensively to model groundwater tracers including both conservative and partitioning tracers for NAPL characterization (PITT). Still other applications have included modeling both laboratory and field demonstrations of co-solvent remediation, thermally enhanced chemical remediation processes, the flow and transport of radionuclides, spills of NAPL in both vadose and saturated zones, the migration of dissolved plumes in the subsurface, the bioremediation chlorinated solvents, and the natural attenuation of organic contaminants in groundwater. The EPA recognizes UTCHEM as an approved numerical simulator to model fate and transport of NAPLs. EPA has been one of several major sponsors including DOE and WES of the research and development effort at UT over the past ten years. The UTCHEM code and documentation is public domain and can be downloaded from the EPA web site. An even more recent and versatile version of UTCHEM is being incorporated into the Groundwater Modeling System of WES and will be available on the Web later this year and will for the first time make many of the related GMS features such as visualization tools available with UTCHEM. We have also developed a very user-friendly stand alone Graphical User Interface for use with Windows PCs.

The subsurface environment is complex and it is necessary to accurately characterize the subsurface in order to accurately and efficiently design and perform surfactant enhanced aquifer remediation (SEAR) tests. Numerical models provide a tool for understanding how variations in subsurface properties can impact a SEAR design on a field-scale, so that the design can be made more robust to withstand the uncertainties in site characterization. Thus, the primary objectives of SEAR modeling are to aid in the scale-up and optimization of the design of SEAR by assessing the performance of the design at the laboratory and field scales and by exploring alternative strategies and approaches to remediation. The modeling results are used not only to establish the operating parameters for the SEAR test, but also to demonstrate to regulators that hydraulic capture can be accomplished and to predict the effluent concentrations of contaminant and injected chemicals requiring surface treatment.

The SEAR process is inherently multiphase and compositional due to mass transfer between the aqueous, microemulsion and NAPL phases. Field scale problems are always three-dimensional and involve heterogeneities in both the porous media and the DNAPL saturation and in some cases the DNAPL composition. While surfactants can be selected to promote solubility enhancements only without mobilization of the DNAPL, reduction in interfacial tension can cause partial mobilization of NAPL. When the NAPL is a DNAPL, this possibility should be carefully investigated with the model in each and every case taking into account the uncertainty in the subsurface parameters and what impact this might have on the mobilization and its consequences. For example, local heterogeneities in the aquifer make the local velocity field variable. The only recourse to guaranteeing a SEAR design that maintains hydraulic control and avoids any mobilization of DNAPL is 3-D simulation of the heterogeneous aquifer with a model that can allow for two or three-phase flow as a function of the interfacial tension via the trapping number. Recently, a new variation of SEAR known as neutral buoyancy SEAR has been developed specifically to eliminate the risk of downward migration of dense contaminants during the remediation process and accurate 3-D modeling is a key component of this new technology.

All other SEAR models are limited in their applicability in one aspect or another (e.g., one or two-dimensional, inadequate numerical accuracy, simplified surfactant phase behavior and properties, etc.). As far as we know, UTCHEM is the only SEAR model that accounts for all of the significant SEAR phenomena such the effect of surfactant on interfacial tension, microemulsion phase behavior, trapping number, rate-limited dissolution of the NAPL, and surfactant adsorption in three dimensions with up to three fluid phases flowing simultaneously. These critical advantages plus the fact that it is also used in many other subsurface environmental applications makes it the most versatile and useful flow and transport model available for general use. Furthermore, we continue to add new features, new applications, more validation and better interfaces among other improvements and enhancements.

Here we give a few examples of UTCHEM applications for processes such as SEAR, PITT, bioremediation, and geochemical. Each example is fully described and the corresponding UTCHEM input file is provided on the UTCHEM distribution CD.

15.2 Example 1: Surfactant Flooding of an Alluvial Aquifer Contaminated with DNAPL at Hill Air Force Base Operational Unit 2

Two field tests at Hill Air Force Base Operational Unit 2 were completed in May and September of 1996 to demonstrate surfactant remediation of an alluvial aquifer contaminated with DNAPL (dense nonaqueous phase liquid). The DNAPL at Hill OU2 consists primarily of trichloroethene (TCE), 1,1,1-trichloroethane (1,1,1-TCA) and tetrachloroethene (PCE). Sheet piling or other artificial barriers were not installed to isolate the 6.1 x 5.4 m test area from the surrounding aquifer. Hydraulic confinement was achieved by: (1) injecting water into a hydraulic control well south of the surfactant injectors (2) designing the well pattern to take advantage of the alluvial channel confined below and to the east and west by a thick clay aquiclude and (3) extracting at a rate higher than the injection rate within the well pattern. An extensive program of laboratory experimentation, hydrogeological characterization, effluent treatment and predictive modeling was critical in the design of these tests and the success of the project. Simulations were conducted to determine test design variables such as well rates, injected chemical amounts and test duration, and to predict the recovery of contaminants and injected chemicals, degree of hydraulic confinement and pore volume of the aquifer swept by the injected fluids. Partitioning interwell tracer tests were used to estimate the volume and saturation of DNAPL in the swept volume and to assess the performance of the surfactant remediation. Analysis of the Phase I and Phase II results showed high recoveries of all injected chemicals, indicating that hydraulic confinement was achieved without sheet pile boundaries. Approximately 99% of the DNAPL within the swept volume was removed by the surfactant in less than two weeks, leaving a residual DNAPL saturation of about 0.0003. The concentration of dissolved contaminants was reduced from 1100 mg/l to 8 mg/l in the central monitoring well during the same time period.

The conventional method of treating DNAPL-contaminated aquifers to-date is 'pump and treat', where contaminant dissolved in groundwater and, possibly, DNAPL itself are pumped to the surface and treated. This method can be quite effective at removing the more mobile DNAPL within the drainage area of the pumping wells and also at minimizing the migration offsite of the contaminated groundwater plume. Unfortunately, conventional pump and treat methods have proved totally ineffective at removing the DNAPL saturation remaining as less-mobile, more isolated ganglia within the groundwater aquifer, sometimes referred to as trapped, bypassed, or residual DNAPL (Mackay and Cherry, 1989).

Surfactants have recently shown great promise in remediating this trapped DNAPL, in laboratory experiments (Soerens *et al*., 1992; Pennell *et al*., 1994; Dwarakanath *et al*., 1998), small-scale field tests (Hirasaki *et al*., 1997; Knox *et al*., 1996; Fountain *et al*., 1996), and aquifer simulation studies (Abriola *et al*., 1993; Brown *et al*., 1994). The addition of surfactants to water injected into aquifers has the potential to greatly enhance the remediation efficiency by: (1) increasing the solubility of the solvent contaminants in groundwater up to several orders of magnitude ('solubilization') and (2) by decreasing the interfacial tension between the DNAPL and the water, thereby reducing the capillary forces 'trapping' the DNAPL in the pore spaces and making the residual DNAPL more mobile ('mobilization'). Which one of these two processes dominate, or indeed which is most desirable, is a function of the characteristics of the site, the contaminant, and the surfactant.

Partitioning tracer tests are conducted before surfactant remediation to estimate the volume of DNAPL in the swept volume of the demonstration area and again after remediation for performance assessment of the remediation. Partitioning tracer tests have been used for this purpose at several sites recently. These tests include the saturated zone tests at Hill Air Force Base Operable Unit 1 (Annable *et al*., 1998) and at a Superfund site in Arizona (Nelson and Brusseau, 1996) and an unsaturated zone test in the Chemical Landfill Waste site near Sandia National Laboratory (Studer *et al*., 1996).

Among the most important new achievements of this field demonstration of surfactant flooding were the following:

1. Demonstrated that surfactant flooding can remove almost all of the residual DNAPL from the swept volume of an alluvial aquifer in a very short time period. In less than two weeks, 99% of the DNAPL was removed from the volume swept by the surfactant. The final DNAPL saturation was 0.0003, which corresponds to 67 mg/ kg of soil. The goal was to remove the source of the contaminant plume rather than the contaminants dissolved in the water; however, the dissolved contaminants were reduced from 1100 mg/l to 8 mg/l at the central monitoring well and were still declining when the pumping was stopped.

2. Demonstrated the use and value of partitioning tracer tests before and after the remediation to determine the amount of DNAPL present before and after remediation. This was the first such test at a DNAPL site.

3. Demonstrated the use and value of predictive modeling to design the test and to address issues critical to gaining approval for a surfactant flood of a DNAPL source zone in an unconfined aquifer, such as hydraulic confinement, injected chemical recovery, DNAPL recovery, and final concentrations of injected chemicals and contaminants.

This example focuses on the analysis and simulations needed to design surfactant remediation field tests and briefly summarizes the key results of the Phase I and Phase II field tests.

Spent degreaser solvents and other chemicals were disposed of in shallow trenches at the Hill Air Force Base Operational Unit 2 (Hill AFB OU2) Site, located north of Salt Lake City, Utah, from 1967 to 1975. These disposal trenches allowed DNAPL to drain into an alluvial aquifer confined on its sides and below by thick clay, resulting in the formation of a DNAPL pool. The DNAPL at Hill OU2 consists primarily of three chlorinated solvents or VOCs (volatile organic compounds). These are trichloroethene (TCE), 1,1,1-trichloroethane (1,1,1-TCA), and tetrachloroethene (PCE).

In 1993, Radian installed a Source Recovery System (SRS) consisting of extraction wells and a treatment plant. More than 87,000 L of DNAPL have been recovered and treated by this system (Oolman *et al*., 1995). This still leaves much DNAPL source remaining at the site in the form of residual or bypassed DNAPL not recovered by pump and treat operations that will continue to contaminate the groundwater.

The primary objectives for the Phase I test were to: (1) determine the amount of DNAPL initially present using partitioning tracers (2) achieve and demonstrate hydraulic control of the surfactant solution at the site (3) test both the surface treatment and subsurface injection-extraction facilities (4) obtain data for the design of the Phase II remediation test and for regulatory purposes (5) measure the swept volume of each well pair using tracers (6) validate tracer selection and performance (7) measure the hydraulic conductivity during injection of surfactant solution in one well and (8) optimize the sampling and analysis procedures.

The primary objectives for the Phase II test were to: (1) use commercially available biodegradable chemicals to remove essentially all DNAPL in the swept volume of the well pattern (2) recover a high percentage of all injected chemicals and leave only very low concentrations of these chemicals in the groundwater at the end of the test (3) use partitioning tracers to accurately assess remediation performance (4) maintain hydraulic control (5) use existing surface treatment facilities on site to treat the effluent during the test and (6) complete the entire test including before and after tracer tests within 30 days.

The Phase II test of August, 1996, lasted approximately one month and consisted of the initial water flood, a pulse of tracer injection, water flooding (NaCl was added to the water during the final day of this flood), the surfactant flood, water flooding, a second pulse of tracer injection, water flooding and finally a short period of extraction only.

Approximately one hundred simulation predictions were conducted to design tests that would achieve the Phase I and Phase II objectives in the shortest time and within budget. These simulations used an aquifer model based on Hill AFB site characterization including field hydraulic testing and well data, and extensive laboratory experiments using Hill AFB soil, DNAPL, groundwater and injected tap water.

15.2.1 Design of the Field Tests

The Hill AFB OU2 site characterization included the following: aquifer stratigraphy and aquiclude topography; porosity and permeability distribution; soil, groundwater, and contaminant constituents and distribution; hydraulic gradient direction, magnitude and seasonal variation; aquifer temperature and seasonal variation. This site characterization was based on the following site data: soil borings, well logs, seismic data, water levels, soil contaminant measurements, DNAPL and groundwater sampling and analysis, hydraulic testing, and historical pumping data.

15.2.1.1 Site Description and Characterization

Figure 15.2 shows the OU2 Site at Hill AFB and the locations of the test area wells and nearby wells. Within the test area, there are a line of extraction wells (U2-1, SB-1, SB-5) to the north 3.1 m apart and a line of injection wells (SB-3, SB-2, SB-4) 3.1 m apart and located 5.4 m south of the line of extraction wells. This 6.1 m x 5.4 m approximately square test area well configuration is also referred to as a 3x3 line drive pattern. A monitoring well, SB-6, is located in the center of the test area. Additional monitoring wells (for fluid levels and water samples) are located to the north and south of the mapped area. The site's abandoned chemical disposal trenches, used for disposal of spent degreasing solvents, are located to the south of U2-1; the exact location is unknown.

A hydraulic control well, SB-8, was located 6.1 m south of the line of injection wells. The injection wells within the test area inject water and various chemicals while the hydraulic control well is located outside of the test area and injects water only. The purpose of the hydraulic control well is to prevent the migration of injected chemicals to the south of the test area. The pattern is confined by the aquiclude to the east and west, by extraction wells to the north, and by the hydraulic control well to the south. The choice of appropriate locations and rates of the seven wells are critical in achieving this confinement and are key design parameters. More than one hydraulic control well would likely be needed in most surfactant floods, but in this case one was sufficient due to the favorable channel geometry of the aquiclude. The injection and extraction rates are high enough that the forced gradient completely dominates the hydraulic gradient between wells during the test. This is an essential part of a successful surfactant flood.

The depth to the water table, approximately 1423 m above mean sea level (AMSL), is 6 to 8 m below ground surface in the U2-1 area, and varies seasonally. The depth to the Alpine clay underlying the aquifer is contoured on Fig. 15.2 to this same depth of 1423 m AMSL. The Alpine Formation is on the order of a hundred meters thick and bounds the aquifer below and to the east and west and forms a very effective aquiclude for the aquifer. The aquifer is in a narrow channel with a north to south trend. A more complete site description may be found in (Radian, 1992; Intera, 1996; Radian, 1994). From October 1993 to June 1994, 87,000 L of DNAPL and over 3,800,000 L of contaminated groundwater were produced from these areas (Oolman *et al.*, 1995).

Groundwater flow is towards the northeast, and varies in direction and magnitude seasonally. In the test area, the hydraulic gradient is around 0.002 (Radian, 1994). This natural hydraulic gradient is approximately two orders of magnitude less than the forced gradients induced during the field tests.

Many pumping tests have been conducted in the OU2 area over the past eight years, with resulting hydraulic conductivities ranging from 3.5×10^{-5} to 4.1×10^{-4} m/s, and, assuming only water is present in the zone, equivalent to a permeability of 3.6 to 44 μm^2 (3.6 to 44 Darcy) (Radian, 1994). In Oct. 1996, a series of pump tests were conducted for wells in the test area, yielding hydraulic conductivities ranging

from $9.5x10^{-6}$ to $1.4x10^{-4}$ m/s, equivalent to a permeability of 1 to 14 μm^2 (Intera, 1996). Because the soil is unconsolidated, obtaining representative in-situ permeability measurements from the cores is difficult but column values of hydraulic conductivity are on the order of 10 μm^2.

15.2.1.2 Contaminant Characterization

It is very important to know the volume and distribution of DNAPL before remediation is started, yet this is usually very poorly known. The purpose of a partitioning tracer test is estimate the volume and saturation of DNAPL throughout the test volume and provides a spatially integrated value with a minimum of disturbance of the soil or DNAPL. Some estimate of the DNAPL volume was needed for the Phase I tracer test design simulations. This initial DNAPL saturation distribution was estimated based upon: (1) soil contaminant concentrations measured from soil samples collected when the wells were drilled (2) aquiclude structure, (3) measured DNAPL volumes produced from some wells (4) and produced contaminant concentration history from extraction wells within and outside the test pattern. Although the uncertainty using these data is high, it turned out to be a sufficiently good estimate of DNAPL volume for tracer test design purposes.

Contaminant measurements in the soil samples acquired before any production from the test area showed DNAPL in the lower two meters of a narrow channel filled with sand and gravel. For the Phase I design simulations, the DNAPL saturation was approximated as 0.20 in the bottom three layers of the six-layer aquifer simulation model (excluding aquiclude regions), representing the lowest 2 meters of the aquifer. The upper 4 meters of the aquifer (the upper three model layers) were assumed to contain no DNAPL in the test area. By volumetrically averaging the initial saturations throughout the test volume, the initial aquifer DNAPL saturation was estimated to be approximately 0.03.

15.2.1.3 Surfactant Phase Behavior

Extensive laboratory experiments were conducted to establish an effective surfactant formulation. This involved batch phase behavior tests, measurements of viscosity, interfacial tension, tracer partition coefficients and numerous tracer and surfactant column floods (Dwarakanath *et al*., 1998; Dwarakanath, 1997). These experiments used soil, DNAPL, groundwater, and tap water from the site. The phase behavior experiments were used to identify and characterize suitable surfactants that form classical microemulsions and to identify the need for co-solvent to eliminate problems with liquid crystals, gels or emulsions, which can cause soil plugging. Co-solvent also promotes rapid equilibration and coalescence to the desired equilibrium microemulsions. The phase behavior of the surfactant was measured as a function of electrolyte concentrations, temperature, co-solvent concentration and other key variables. The soil column experiments were used to evaluate the tracers, to assess the effectiveness of surfactants at removing DNAPL from the soil, to measure surfactant adsorption on the soil, to assess any problems with reduction in hydraulic conductivity and to evaluate the use of co-solvents in improving the test performance.

The anionic surfactant used in these tests was sodium dihexyl sulfosuccinate obtained from CYTEC as Aerosol MA-80I. Extensive testing of this surfactant was done and the results can be found in (Dwarakanath *et al*., 1998; Baran et al., 1994; Dwarakanath, 1997). The solubility of the Hill DNAPL in a microemulsion containing 8% dihexyl sulfosuccinate and 4% co-solvent (isopropyl alcohol, IPA) was determined as a function of NaCl added to the Hill tap water. The solubility of the three principal Hill chlorinated DNAPL constituents in groundwater is about 1,100 mg/L. Adding 7000 mg/L NaCl to the mixture at 12.2 °C increases the contaminant solubility to approximately 620,000 mg/L of microemulsion, or a solubility 560 times greater than that in groundwater.

15.2.1.4 Partitioning Tracer Experiments

Seven tracers were selected for use as conservative and partitioning tracers at the Hill OU2 site (Dwarakanath, 1997). In order to use the partitioning tracer tests to estimate DNAPL saturations, it is essential to know the partition coefficients of the tracers between DNAPL and water accurately. Batch equilibrium partition coefficient tests were performed to measure the partition coefficients of the alcohol tracers. The partition coefficient is the ratio between the concentration of the tracer species in the DNAPL and the concentration of the tracer species in the aqueous phase. The optimum injection rates, in terms of

desired retention times for both surfactant and tracer tests, were determined through column experiments. These experiments indicated that a retention time greater than about 20 hours is needed to achieve local equilibrium, essential for obtaining good estimation of residual DNAPL saturations using partitioning tracer tests, and this same constraint was assumed to apply to the field test. Partitioning tracers for estimation of DNAPL contamination is described in detail by Dwarakanath (1997), Jin *et al*. (1995), Jin (1995), and Pope *et al*. (1994).

15.2.1.5 Surfactant Column Experiments

Extensive surfactant flood experiments were conducted using columns packed with soil from the OU2 site test area, as well as DNAPL from the site. The surfactant mixture used in the final design had been shown by these column experiments to reduce the DNAPL saturation in the soil to less than 0.001 as estimated from both the partitioning tracers and mass balance. Although our goal was to remove the DNAPL rather than the dissolved contaminant in this unconfined aquifer system, laboratory column data showed that the TCE concentration in the effluent water could be reduced to less than 1 mg/L after surfactant flooding of the soil. The concentration of TCE and other VOCs and tracers was measured using a Gas Chromatograph (GC) with an FID mechanism with straight liquid injection. The minimum detection of TCE concentration was 1 mg/L.

Surfactant adsorption was measured in column experiments using Hill soil by comparing the response of a conservative tracer (tritiated water) to that of the surfactant labeled with carbon 14. The retardation factor for the surfactant was 1.00094. The surfactant adsorption calculated from this value is 0.16 mg/g of soil, which is zero within experimental error of the retardation factor. All of these and other experimental results are described and discussed in detail in (Dwarakanath *et al*., 1998; Dwarakanath, 1997).

15.2.1.6 Surface Treatment

Existing groundwater treatment facilities at Hill AFB OU2, including phase separators and a steam stripper (Oolman *et al*., 1995), were utilized to treat all of the groundwater and DNAPL recovered during the Phase I and II field tests. The high levels of surfactant, co-solvent and contaminant in the recovered groundwater presented significant challenges for steam stripper operation. Prior to the field tests, the ASPEN model was used to model the treatment facilities to determine if and how the existing steam stripper could achieve required contaminant removal levels. The predicted composition of the effluent from the UTCHEM modeling described below was used as the input to ASPEN. Actual operation of the steam stripper during the field tests demonstrated that predicted performance levels could be achieved. It was also shown that steam stripping is a favorable technology for the treatment of the highly contaminated groundwaters recovered during surfactant enhanced remediations. These results can be found in the final report to the Air Force Center for Environmental Excellence (Intera, 1998).

15.2.1.7 Aquifer Model Development and Simulations

UTCHEM was used to design the tests and to predict the performance of the Phase I and Phase II surfactant and tracer tests. Use of this simulator makes possible the study of phenomena critical to surfactant flooding such as solubilization, mobilization, surfactant adsorption, interfacial tension, capillary desaturation, dispersion/diffusion, and the microemulsion phase behavior. The use of the UTCHEM simulator in modeling DNAPL contamination and remediation processes is discussed in Brown *et al*. (1994).

Determining realistic in-situ properties for these unconsolidated soil samples is very difficult, due to grain rearrangement and disruption of the porous media during boring, transport, cutting, and storage. The difficulty is increased for the OU2 site soil samples because the aquifer is composed primarily of gravel interspersed with cobbles, some of them larger than the 6 cm diameter sampling tube. To minimize the core disruption, the sampling tube was frozen upon reaching the laboratory, before the core cutting and until the measurements could be obtained.

The model grid and aquifer properties are summarized in Table 15.1. The steeply dipping lower boundary of the aquifer was modeled by assigning lower permeability (5×10^{-6} μm^2) and porosity to all gridblocks lying within the aquiclude. This aquiclude structure, and the ability to model it accurately, played a key

role in the design of the field test, and combined with the use of a hydraulic control water injection well to the south of the surfactant injection wells, allowed hydraulic control to be achieved without using sheet piling. The sandy/gravelly aquifer soil was modeled using a random correlated permeability field with a standard deviation of ln k of 1.2. The correlation length along the channel was 3 meters, across the channel 1.5 meters and in the vertical direction 0.3 meters. The permeability assigned to individual gridblocks ranged from a low of 0.2 μm^2 to a high of 420 μm^2. These values resulted in a good match of the tracer data taken with the same well field during Phase I.

The natural hydraulic gradient (0.002) is approximately two orders of magnitude less than the induced gradient during the field tests (0.10-0.20), so the natural gradient was assumed to be zero for the simulations. Open boundaries were placed at the north and south sections of aquifer model to allow flow into and out of the aquifer in response to the test area injection and extraction.

In UTCHEM, phase behavior parameters define the solubility of the organic contaminant in the microemulsion as a function of surfactant, co-solvent and electrolyte concentrations and temperature. These parameters were obtained by matching the experimentally determined solubility of the Hill contaminants at various surfactant, co-solvent and electrolyte concentrations. The phase behavior model agrees well with the measured data. Experimentally determined interfacial tensions for DNAPL-groundwater and DNAPL-microemulsion were used to calibrate the UTCHEM correlation for calculating interfacial tension.

Many UTCHEM simulation cases were performed to determine design parameters such as hydraulic control well injection rate, injection and extraction rates, frequency of sampling points, amount of surfactant, composition of injected surfactant solution, amount and composition of tracer solutions, duration of water flooding and extraction needed after the surfactant injection, and the concentrations of contaminants, surfactant and alcohol in the effluent. The high injection rate of water in the hydraulic control well to the south of surfactant injection wells was found to a particularly important design variable.

15.2.2 Results and Discussion

15.2.2.1 Phase I Field Test

The Phase I test, completed in May 1996, lasted approximately two weeks and consisted of an initial water flood, tracer injection, water flooding, injection of a small mass of surfactant in one well only, water flooding, then post-test extraction to recover any remaining injected chemicals. Water flooding consists of injection of water only to sweep the fluids within the test area volume towards the extraction wells where they are pumped and treated at the surface.

Based upon tracer concentrations measured during the test with on-site GCs, about 97% of the tracers injected during the two weeks of the Phase I Field Test were recovered. This high tracer recovery was due to good hydraulic confinement of the test area. This is the primary confirmation and best means of determining the degree of hydraulic control; however, the evaluation that hydraulic control was achieved in the Phase I tests can also be supported by three other sources of information: Firstly, measured piezometric data during the tests indicated that water levels for the three extraction wells were approximately 0.5 meters lower than the surrounding aquifer, creating a large gradient from within the test area towards the extraction wells. Secondly, monitoring wells had very low measured concentrations (at or below the measurement detection level) of the injected tracers throughout the test. These monitoring wells were placed both to the north and south (aquiclude confines aquifer to the east and west) approximately 21 meters away from the test area. Finally, simulation results matched the model very well in predicted tracer recovery (both were 97%).

Figure 15.3 shows Phase I tracer concentrations for the central extraction well SB-1. Four alcohol tracers were injected during the Phase I test, with partition coefficients ranging from 0 to 141. The upper graph compares the predicted tracer concentrations with the field data measured during the Phase I test, for the two tracers used in the moment analysis to estimate the initial DNAPL saturations and volumes. The lower graph in Fig. 15.3 shows the produced concentrations for all four of the injected tracers, plotted on a log

scale to highlight the log-linear behavior typically exhibited during latter part of the tracer tests. There is substantial separation between the nonpartitioning tracer, isopropanol, and the highest partitioning tracer, 1-heptanol, as the latter is retarded by the presence of the DNAPL.

The predicted concentrations shown here are those published in the workplan before the test was undertaken and therefore are not history-matched or calibrated to the field data. Even so, breakthrough times, peaks, and tails for both the partitioning and nonpartitioning tracers are similar to the UTCHEM predictions. Because the simulation predictions agreed with the actual Phase I field performance very well, few modifications were required in the aquifer model for the Phase II design simulations. Approximately 750 L of contaminant was extracted during the Phase I test based upon the partitioning tracer data.

15.2.2.2 Phase II Field Test

Phase II included an initial tracer test, a NaCl preflood, a 2.4 PV surfactant flood, and a final tracer test, followed by a period of extraction only to maximize the recovery of injected chemicals. See Table 15.2 for a summary of the Phase II test. The purpose of the one day NaCl preflood was to increase the salinity of the water to a value closer to the optimal value of 7000 mg/l NaCl before the surfactant was injected. The swept pore volume calculated from the non-partitioning tracer analysis is approximately 57,000 liters for all three well pairs and the injected pore volumes listed in Table 15.1 are based on this total swept pore volume. The saturated pore volume of the alluvium within the line drive well pattern as estimated from the structure of the clay aquiclude below the aquifer was also about 57,000 liters, indicating very little if any unswept soil between the screened intervals of the injection and extraction wells.

Figure 15.4 shows the measured surfactant concentration for the central extraction well SB-1 during Phase II and compares those with UTCHEM predictions. While the breakthrough and peak times are similar, the magnitude of the peak and the 'tail' concentrations are significantly different. The surfactant concentration dropped below the CMC (critical micelle concentration) at around 13 days in the UTCHEM prediction case and around 18 days in the field test. These differences in observed and predicted surfactant concentrations are due in part to differences in the design rates and those actually achieved in the Phase II field test. The lower extraction rates in the field test result in lower extraction/injection ratios, less dilution from groundwater flowing into the extraction wells from the north and higher surfactant concentrations than the model prediction shown in Fig. 15.4. There is an increase in surfactant concentration at 20 days due to the increase in extraction rates at the end of the water flood. These and other factors could be adjusted and would improve the agreement with the field data, but we prefer to show the predictions that we made before the field test and comment that they were more than adequate to meet all of our stated objectives and design purposes. No comparable model predictions can be found in the literature. Thus, it is very worthwhile to show that even with all of the approximations and uncertainties inherent in such modeling, the predictions can be sufficiently accurate to be very useful for a variety of important purposes e.g. in estimating how much surfactant is needed to reduce the DNAPL saturation to a given level.

Over 94% of the surfactant was recovered and the final surfactant concentration in the effluent water was less than 0.05%. Figure 3 shows a normalized plot of the surfactant and isopropanol concentrations in the effluent. Breakthrough of surfactant and IPA occurred at the same time and no measurable separation occurred at any time, which indicates that there was negligible adsorption of the surfactant on the soil, a result consistent with the column studies.

Figure 15.5 shows the contaminant concentrations measured by GC analysis of extraction well fluid samples for the central extraction well SB-1 and compares these with UTCHEM predictions. The measured concentrations during the initial tracer test (first 5 days of the plot) are near the groundwater solubility of 1100 mg/L both in the prediction case and the field measured data. Shortly after surfactant injection begins at 5.5 days, the contaminant concentration increases steeply: to over 10,000 mg/L in the predictions and to over 20,000 mg/L in the field data. The decline in concentrations after surfactant injection ends at 8.7 days (2.4 PV) is slower in the field data than that for the UTCHEM prediction. This difference is at least partially due to the higher extraction rates in the predictive simulations, compared to those actually achieved in the field.

In general, field test results exhibit 'spiky' or non-smooth behavior in produced concentrations due to small scale fluctuations in rates and flow fields, sampling variations, measurement errors, heterogeneities, etc. The simulations similarly show 'spiky' behavior due to aquifer heterogeneities, spatially variable remaining DNAPL saturations, changes in the flow field, phase behavior changes, and the effect of structure upon each streamlines' arrival time at the effluent well. The 'spike' seen in the simulation at Day 20 is a result in a changing flow field, when all injection is stopped in the field and only extraction wells continue pumping, to maximize the recovery of any injected chemicals.

Figure 15.6 compares the difference between the water table depth (or fluid head) between each injection well and extraction well pair during the Phase II test. There was no loss of hydraulic conductivity during the Phase II surfactant flood, based on measured hydraulic gradients before and after surfactant injection. The fluid head levels increased slightly during the surfactant injection period due to the increased viscosity of the surfactant solution compared to water, but quickly returned to the pre-surfactant injection levels during the water flood. These and other laboratory and field data demonstrate that the sodium dihexyl sulfosuccinate surfactant is an extremely good choice for these conditions when used with a co-solvent such as isopropanol, which promotes microemulsions with very fast equilibration times, equilibrium solubilization and minimal surfactant adsorption on the soil.

Figure 15.7 shows the produced tracer concentrations for the final Phase II tracer test, conducted after the surfactant remediation. Even though very high partition coefficient tracers (K=30 and 141) were used for this test, very little retardation of these tracers are seen; in other words, effluent data for the different tracers overlay for the two outside extraction wells SB-5 and U2-1 and the central monitoring well SB-6 and show only a very slight difference in the tail for the central extraction well SB-1. Compare this to the substantial retardation observed for the 1-heptanol tracer (K=141) during the Phase I test in extraction well SB-1, shown in Fig. 15.3 on the semi-log scale.

The DNAPL volumes and saturations determined from the first temporal moment of the effluent tracer concentrations (Jin, 1995; Pope *et al*., 1994) of the Phase II tracer test for the three extraction wells is summarized in Table 15.3. The initial volume of DNAPL within the test pattern was 1310 L (6000 mg/kg of soil). The initial DNAPL volumes and saturations are based on moment analyses of the Phase I tracer test conducted before any surfactant injection. The final DNAPL volumes and saturations are based on moment analyses of the Phase II final tracer test conducted after the surfactant remediation. Values for each of the three extraction/injection well pairs and for the total test pattern are given in Table 15.3. The initial DNAPL saturation ranged from 0.013 to 0.054, with an average of 0.027, equivalent to 6,000 mg/kg of soil averaged over the entire saturated volume of the aquifer.

After surfactant remediation, the average DNAPL saturation was 0.0003, a decrease of 99%, and the DNAPL saturations in the two outside swept volumes are too low to detect (less than 0.0001). This final average DNAPL saturation is equivalent to approximately 67 mg/kg of soil. After surfactant remediation, the amount of DNAPL remaining within the swept volume was only about 19 L. The estimated volume of DNAPL recovered based upon the effluent GC data taken on-site during the test was 1870 L. The estimated volume of DNAPL collected after steam stripping in the treatment plant was 1374 L.

We consider both of these DNAPL recovery estimates from the effluent data to be less accurate than the estimate of 1291 L from the tracer data. The partitioning tracer data do not depend on aquifer characteristics such as porosity and permeability. The estimated error is on the order of 12% of the estimated volume of DNAPL in the swept volume of the aquifer even when the DNAPL volume is very small provided the retardation factor is still sufficiently high. The partition coefficient must be high when the average NAPL saturation is low for the retardation factor to be sufficiently high. The final DNAPL volume estimate of 19 L reported above is based upon the 1-heptanol tracer data. The retardation factor for each well pair is uncertain by about ± 0.035. This results in an uncertainty of 5 L of DNAPL for each well pair and a total of 15 L for the entire swept volume, or about $99 \pm 1\%$ removal of the DNAPL from the swept volume of the aquifer.

The important conclusion is that these results clearly demonstrate that surfactant flooding can be used to remove essentially all of the DNAPL in the contacted volume of an aquifer, which is the source of the

continuing contamination of the water for extended periods of time i.e. the large and mobile dissolved plume. Only three weeks were required to achieve this result. The total contaminant concentration in the central monitoring well at the end of the test was only 8 mg/L. This is a 99% reduction compared to the initial concentrations. While this concentration is still much higher than the 0.005 mg/L maximum concentration limit (MCL) for TCE, a UTCHEM simulation showed that only 55 days of continued water flooding at the same well rates would be sufficient to reduce the aqueous concentration of the contaminants to the MCL (Intera, 1998). Either natural attenuation or some other means such as bioremediation could be used to degrade the contaminants remaining in the water now that almost all of the DNAPL source has been removed. However, the test area is an open geosystem and this final step could not be completed without either remediating the entire OU2 aquifer or isolating the remediated volume to prevent recontamination from outside the demonstration area.

15.3 Example 2: Design of the Surfactant Flood at Camp Lejeune

15.3.1 Introduction

A surfactant-enhanced aquifer remediation (SEAR) demonstration to remove PCE from the groundwater at site 88, below a dry cleaning facility at Marine Corps Base Camp Lejeune in North Carolina, was completed during 1999. The objectives of this demonstration were (1) further validation of SEAR for dense nonaqueous phase liquid (DNAPL) removal and (2) evaluation of feasibility and cost benefits of surfactant regeneration and reuse during SEAR. A total of 288 L of PCE was recovered during the surfactant test. This corresponds to a recovery of about 92% from the upper permeable zone where most of the contaminant source was initially located. Details on the site description, field-test operations, and results are given in Holzmer *et al*. (2000).

The design of the SEAR demonstration was completed after integrating the information obtained during the site characterization activities and the laboratory studies into the numerical model. The site characterization activities included the pre-SEAR tracer tests. The results of the field tracer tests were used to modify the geosystem model for the final design of the surfactant flood. Subsequently, the most important SEAR design variables were identified by selectively changing model parameters and determining effect on the simulation results.

UTCHEM was used for all geosystem model development. We used the model not only to predict the performance but to address issues critical to gaining approval to conduct the demonstration. These issues included: (1) demonstration of hydraulic containment, (2) prediction of recoveries of injected chemicals, (3) prediction of DNAPL recovery, and (4) prediction of the final concentrations of injected chemicals and source contaminant.

Numerous simulations were conducted to develop the recommended design for surfactant flooding at Camp Lejeune. The objectives of the simulation study were to:

- Determine the time required for each test segment: pre-surfactant water injection, surfactant injection, and post-surfactant water injection
- Determine mass of surfactant, alcohol, and electrolytes recommended for each segment of the test
- Determine test design parameters such as number of hydraulic control, injection, and extraction wells, well locations, and well rates.
- Estimate effluent concentrations of contaminant, surfactant, alcohol, and electrolytes during and at the end of the test
- Estimate mass of contaminants, surfactant, alcohol, and electrolytes that remain in the volume of the test zone at the end of the test

- Evaluate the sensitivity of the performance of the proposed design to critical aquifer properties such as permeability and degree of heterogeneity, process parameters such as microemulsion viscosity, and operational parameters such as flow interruption in the middle of the surfactant injection

15.3.2 Design of the Sear Field Test

15.3.2.1 Site Description and Characterization

The site characterization included the following: aquifer stratigraphy and aquiclude topography, porosity and permeability distribution, soil, groundwater, and contaminant constituents and distribution, hydraulic gradient direction and magnitude, aquifer temperature and pH. The field site characterization conduced by Duke Engineering & Services (DE&S, 1999a) was based on the following site data: soil borings, well logs, water levels, soil contaminant measurements, DNAPL and groundwater sampling and analysis, hydraulic testing, and historical pumping data. The DNAPL zone was found to be about 5-6 m below ground surface. The aquifer soil has a relatively low permeability with about an order of magnitude smaller permeability in the bottom 0.3 m of the aquifer. Because of the low aquifer permeability and the limited thickness, each pore volume of the surfactant required about 12 days to inject.

Prior to the installation of the SEAR wellfield, several well patterns with different number of wells were simulated. The most efficient well pattern based on site hydrogeological data was a line of 3 central injection wells and 6 extraction wells arranged in a divergent line-drive pattern as shown in Fig. 15.8. To maintain hydraulic control and to ensure adequate sweep efficiency in the wellfield, each injection and extraction well was spaced about 3 m apart and the distance between any pair of injection and extraction wells was about 4.6 m. A dual injection system was used in the three injectors to prevent upward migration of injectate and to focus the flow paths of injected surfactant through the DNAPL zone along the bottom portion of the aquifer. Water was injected in the upper screen with simultaneous injection of surfactant mixture in the lower screen. Similarly, to provide further hydraulic control of the injected fluids, several scenarios to identify the number of hydraulic control wells and their locations were simulated. Two hydraulic control wells located on each end of the line of injectors (Fig. 15.8) were found to be adequate to achieve hydraulic control of the test zone.

The results of the pre-SEAR partitioning interwell tracer test conducted during May/June 1998 indicated that approximately 280 to 333 L of DNAPL were present in the test zone. The highest average DNAPL saturations found were in the range of 4.5%. The spatial distribution of DNAPL saturation was highly variable in both areal and vertical directions.

15.3.2.2 Surfactant Phase Behavior

In UTCHEM, phase behavior parameters define the solubility of the organic contaminant in the microemulsion phase as a function of surfactant, cosolvent, and electrolyte concentrations. Solubility data for Camp Lejeune DNAPL obtained from laboratory experiments were used to calibrate the phase behavior model parameters (Ooi, 1998). The DNAPL is ~ 99% PCE. In addition to modeling surfactant phase behavior, the physical property model parameters such as microemulsion viscosity and microemulsion-DNAPL interfacial tension were also calibrated against experimental measurements.

A total of 155 surfactant formulations were screened by observing the phase behavior and measuring selected phase properties such as microemulsion viscosity until an optimum mixture was found (Weerasooriya *et al.*, 2000). The target properties of the optimum mixture include (1) high DNAPLs solubilization, (2) fast coalescence to a microemulsion (less than a day), (3) low microemulsion viscosity, and (4) acceptable ultrafiltration characteristics. The surfactant composition used in the field test was a mixture of 4 wt% Alfoterra™ 145-4-PO sodium ether sulfate, 16 wt% isopropyl alcohol (IPA), and 0.16-0.19 wt% calcium chloride mixed with the source water. The alfoterra is made from a branched alcohol with 14 to 15 carbon atoms by propoxylating and then sulfating the alcohol. The contaminant solubilization was about 300,000 mg/L at 0.16 wt% $CaCl_2$ and about 700,000 mg/L at 0.19 wt% $CaCl_2$.

15.3.2.3 Aquifer Model Development and Simulations

The plan view of the three-dimensional grid used for the design of the Camp Lejeune surfactant flood is shown in Fig. 15.8 and described in Table 15.4. A total of 10,000 gridblocks using a 25x25x16 mesh 43

m long and 24.4 m wide was used. The nearly 4 m saturated thickness of the aquifer was divided into 16 nonuniform numerical layers vertically. The top elevation of the numerical grid corresponds to about 5.5 m AMSL. Both layered and stochastic permeability distributions were used for the design simulations. The aquitard gridblocks were identified based on the clay elevation data mapped to the grid and were assigned a very low porosity and permeability. A ratio of horizontal to vertical permeability of 0.1 was used. Design simulations were conducted with permeability fields with different values of average and variance and initial DNAPL volume and saturation distributions.

15.3.3 Results and Discussion

We conducted numerous simulations to design the SEAR test for the Camp Lejeune. Here we only discuss the results of the two predictive simulations conducted prior to the field test to illustrate the sensitivity of variations in the permeability on the contaminant recovery. Simulation ISA7m assumed a lower permeability for the bottom 0.6 m of the aquifer, whereas simulation ISA26m assumed a higher permeability. We also discuss the results of our brief attempt to history match the field data.

15.3.3.1 Simulation No. ISA7m

The injection strategy given in Table 15.5 included 2 days of water preflush followed by 30 days of surfactant solution. A summary of flow rates for various sections of the flood is given in Table 15.6. The hydraulic conductivity was $4x10^{-4}$ cm/s for the top 12 layers (3.3 m) and $8x10^{-5}$ cm/s for the bottom 4 layers (0.6 m) i.e., a permeability contrast of 5:1. The initial DNAPL saturation increased with depth for the bottom 0.6 m of the aquifer. This corresponds to an average DNAPL saturation of 0.02 within the wellfield. A comparison between the predicted and measured dissolved PCE concentration at extraction well EX01 is shown in Fig. 15.9 and agree very well. The peak PCE concentration predicted from the model is 1500 mg/L compared to the field-observed value of 2800 mg/L. The total simulated PCE recovery (dissolved and free-phase) from all the wells at the end of the flood (100 days) was 310 L compared to a recovery of 288 L measured in the field demonstration.

15.3.3.2 Simulation No. ISA26m

The results from simulation ISA26m were reported in the SEAR Work Plan (DE&S, 1999b) and were used as the final basis for the design and operation of the surfactant flood at Camp Lejeune. The aquifer permeability was modeled using a random correlated permeability field with an average hydraulic conductivity of $4x10^{-4}$ cm/s with a standard deviation of log k of 1. The hydraulic conductivity of the bottom 0.3 m was then reduced by a factor of 4 to an average of 10^{-4} cm/s. The injection strategy given in Table 15.5 included 6 days of electrolyte preflush with 0.22 wt% $CaCl_2$ followed by 48 days of surfactant solution. Injection and extraction rates during the preflush and surfactant injection were reduced compared to those used during the field tracer test or postwater flush because of the higher viscosity of surfactant solution (2.5 mPa.s) compared to the water. A summary of flow rates for various sections of the flood is given in Table 15.6. The reduction in the rates will prolong the surfactant injection test, however, it reduces the risk of excessive water buildup near the injection wells or excessive drawdown near the extraction wells. This was especially critical for this shallow aquifer. A comparison of the predicted and measured PCE concentration at extraction well EX01 is shown in Fig. 15.9. The peak PCE concentration in simulation ISA26m was 25,000 mg/L whereas that observed in the field was an order of magnitude smaller of about 2800 mg/L. The predicted surfactant and IPA effluent concentrations in well EX01 are compared with the measured data in Fig. 15.10. The agreement is not as good in the other extraction wells due to highly heterogeneous nature of both permeability and DNAPL saturation distributions not accurately accounted for in the model.

15.3.3.3 Discussion of UTCHEM Predictive Simulations

From Fig. 15.9, it is evident that the match between predicted and measured PCE concentrations for run ISA7m is better than for run ISA26m. This is because in run ISA7m, the hydraulic conductivity of the bottom 0.6 m was $8x10^{-5}$ cm/s which is 5 times lower than that in the upper 4.3 m. In comparison to ISA26m, the hydraulic conductivity of the bottom 0.3 m was 10^{-4} cm/s, which is 4 times lower than that in the upper 4.6 m. The combination of a thicker and less permeable bottom 0.6 m in ISA7m compared to a thinner and more permeable bottom 0.30 m in ISA26m explains overestimate of the effluent PCE solubilities. Based on these results, it was inferred that the permeability contrast between the less

permeable bottom of the aquifer and the other zones is at least a factor of 5. This can also explain a partial remediation of the lower permeability bottom zone as was observed during the field demonstration (Holzmer *et al*., 2000).

15.3.3.4 Field History Match Simulation

A preliminary effort was made to qualitatively match the results of the field test. Adjustment in the UTCHEM input included the well rates and duration of the initial water flush and surfactant injection that were slightly altered during the field test compared to those of the final design simulation ISA26m. The injection and extraction rates and strategies are summarized in Tables 15.5 and 15.6. The rates were altered from the design rates to improve the sweep efficiency of the surfactant solution through the more highly contaminated sections of the test zone. Other adjustments in the model were in the spatial distribution of the DNAPL and permeability and its variation with depth. An attempt was made to approximate the grading of the DNAPL saturation across the wellfield, but the actual variations are more complex. The DNAPL volume is about 265 L within a pore volume of about 22,474 L in this simulation. This is an average DNAPL saturation of about 0.0118 within a swept pore volume similar to that estimated from the pre-SEAR tracer test. The permeability was modeled as three geological layers as given in Table 15.7. A permeability contrast of 20 was used between the upper high permeability zone and the bottom zone right above the clay aquitard. The effluent PCE concentrations compare favorably to those measured at the field in most of the extraction wells. Comparison of measured and history match of dissolved PCE concentrations for extraction well EX01 is shown in Fig. 15.11. The final DNAPL volume within a swept volume of 22,474 L was 76.5 L corresponding to an average DNAPL saturation of 0.0034. This gives a PCE recovery of about 72% for run SEAR5. The simulated surfactant and IPA concentrations and subsequently the recoveries were higher than the field data in most of the extraction wells. The breakthrough times and the peak concentrations of both IPA and surfactant were closely matched in well EX01 as shown in Fig. 15.12. Plausible explanations for the lower field surfactant recoveries are (1) higher surfactant adsorption in the bottom of the aquifer with high clay content and (2) biodegradation of surfactant, and (3) fluctuations in the injected surfactant concentration compared to the design value of 4 wt%.

15.3.4 Summary and Conclusions

The surfactant flood for the Camp Lejeune PCE-DNAPL site was simulated using UTCHEM simulator. The design was based on the available surfactant phase behavior data and geosystem model calibrated against the pre-SEAR tracer test. The results of model predictions provided critical guidelines for the field operation. These include the wellfield design, hydraulic containment, well rates, the frequency of the sampling for effluent analysis, and effluent concentrations necessary for surface treatment and surfactant recycling operations.

15.4 Example 3: Modeling of TCE Biodegradation

15.4.1 Introduction

The transport of NAPLs in soil and groundwater and the destruction of these compounds through biodegradation reactions in in-situ bioremediation systems involve many complex processes. Aquifer properties, contaminant properties, and system operating practices all have a great influence on the performance of an in-situ bioremediation system. As a result, designing bioremediation systems can be very difficult. Because in-situ bioremediation can be expensive and time consuming to test in the field, there is a great need for models that can aid in design or, at a minimum, determine whether or not in-situ bioremediation is feasible at a particular site.

NAPLs can significantly affect the performance of in-situ bioremediation systems. Near NAPL sources, concentrations of NAPL constituents can be toxic to microorganisms, preventing biodegradation from occurring in localized areas. Biodegradation in aquifer locations where NAPL constituent concentrations are high can deplete oxygen, other electron acceptors, or nutrients near the NAPL. As more soluble NAPL constituents leach out of the NAPL phase, the effects of the NAPL on biodegradation processes change with time and space, making prediction of bioremediation performance difficult.

Failure to consider these and other effects of NAPL sources in an aquifer can result in ineffective bioremediation designs and overly optimistic assessments of in-situ bioremediation performance.

15.4.2 Objective

The objective was to use UTCHEM to design a bioremediation system that removes TCE from a shallow aquifer following a surfactant enhanced aquifer remediation (SEAR) demonstration at Hill Air Force Base in Utah. See Section 9 for information on the biodegradation model.

15.4.3 Description of Hill AFB OU2 Site

Shallow groundwater at OU2 exists in an unconfined aquifer consisting of heterogeneous alternating and interlaced deposits of sand, gravel, and clay. Depth to groundwater in this area is 6 to 7.6 m below the existing ground surface, with a general flow direction to the northeast. The shallow aquifer is defined locally by an aquitard of low permeability clay at a depth of approximately 15 m below ground surface. An important characteristic of the aquitard elevation is that it occurs at a greater depth in the area of OU2 than is typical for the surrounding area. The result is a subsurface depression in the aquitard, running in a line roughly north-northwest that is conducive to the pooling of DNAPLs (Intera, 1994; Intera, 1996).

Base records indicate that, from 1967 to 1975, the OU2 site was used to dispose of unknown quantities of TCE bottoms from a solvent recovery unit, and sludge from vapor degreasers. The contaminant mixture consisted of several chlorinated solvents (60% TCE with lesser amounts of tetrachloroethene (PCE), 1,1,1-trichloroethane (TCA), methylene chloride and Freon 113), and with some amount of incorporated oil and grease. TCE, TCA and PCE comprised over 90% of the DNAPL present at the site (Intera, 1994; Intera, 1996; Intera, 1998).

The disposal area consisted of at least two disposal trenches at the site, trending north-northwest and estimated to have been approximately 2 to 2.4 m deep. The trenches were about 3 m wide and had lengths of approximately 15 and 30 m, respectively (Intera, 1994; Intera, 1996).

The chlorinated organic solvents disposed of in these trenches had densities greater than water and relatively low aqueous solubilities. As a result, the contaminants behaved as DNAPL that migrated downward through the vadose zone and aquifer until it stopped at the aquitard. As DNAPL flowed through the aquifer, it left behind a trail of residual DNAPL that remained a persistent source of contamination in the shallow groundwater system. DNAPL was present in sufficiently large quantities from the disposal trenches that it formed pools of DNAPL at the base of the shallow aquifer, in depressions on the surface of the aquitard.

15.4.4 SEAR Demonstration

The SEAR demonstration consisted of two tests. The Phase I test was completed in May 1996, and the Phase II test was completed in September 1996. The goal of the SEAR was to demonstrate the efficacy of surfactant flushing in reducing the saturation of DNAPL in the aquifer. Both SEAR tests consisted of four steps:

1. a pre-flushing tracer test to estimate the DNAPL residual saturation in the aquifer;
2. aquifer flushing with a surfactant solution to mobilize the residual DNAPL;
3. aquifer flushing with water to reduce the in-situ surfactant concentration; and
4. a post-flushing tracer test to estimate the remaining DNAPL saturation.

Phase I was a limited scale test to determine the amount of DNAPL present, assess the injection behavior, test the ability of the treatment system to treat the extracted groundwater, and provide data for the second test. Phase II was a larger-scale test designed to remove DNAPL from the aquifer.

15.4.4.1 SEAR Design

The SEAR treated a portion of the shallow aquifer measuring approximately 6 m square. Water was injected into a hydraulic control well upgradient of the treatment area to isolate injected solutions within the treatment zone from the surrounding groundwater during the test. Surfactant and tracer solutions were injected into three injection wells upgradient of the treatment zone and were recovered in three downgradient extraction wells. Figure 15.13 shows the locations of the injection and extraction wells, and the location of a key monitoring well located within the test area. Details of the SEAR can be found in Section 15.2.

15.4.4.2 Simulated Aquifer Description and SEAR System Configuration

Computer simulations were conducted by Brown *et al*. [1999] using UTCHEM to determine design parameters for the SEAR and estimate performance. A necessary part of the simulation was a numerical representation of the test area and aquifer. The test area was simulated with gridblocks comprising a volume 54 m long, 20 m wide and 5.9 m thick. This aquifer test volume was represented in three dimensions by 2040 gridblocks. The discretization consisted of 20 gridblocks in the x, or longitudinal, direction (N-S, the primary direction of injected solution flow) 17 gridblocks in the transverse direction (E-W), and 6 gridblocks in the vertical direction.

The trench-like configuration of the aquifer was simulated by specifying low permeability and porosity boundaries on the sides and bottom of the aquifer. The low permeability and porosity gridblocks (aquiclude) slope in from the top of the formation in a stadium-like configuration, so that most of the upper part of the formation is relatively permeable, while only a small channel of relatively permeable material exists in the bottom layer. This channel will be referred to as the "flow channel" in later discussions.

A very low permeability of $5x10^{-6}$ Darcy (hydraulic conductivity of $5x10^{-11}$ m/s) and porosity (0.01) was specified for the aquiclude gridblocks along the side slopes and the base of the trench-like aquifer to simulate the aquiclude. The permeability of non-aquiclude gridblocks was simulated using a three-dimensional stochastically generated conductivity field. The mean permeability was 20 Darcy (hydraulic conductivity of $2x10^{-4}$ m/s), and ranged from 0.17 to 417 Darcy (hydraulic conductivity of $1.7x10^{-6}$ m/s to $4.2x10^{-3}$ m/s).

The locations of injection, extraction, and monitoring wells in the test area are shown in Fig. 15.13. Each horizontal slice in Figure 1 represents a vertical layer in the design simulations. The symbols representing the wells indicate the layer in which each injection and extraction well was screened. A row of injection wells spaced 3 m apart is separated by 5.3 m from a row of extraction wells, also 5.3 m apart. Fluids were injected from right to left (south to north) in the figure.

The DNAPL saturation in the gridblocks was assigned a value of either 0.1, 0.2 or 0 for the SEAR design simulations. Most of the DNAPL was assumed to be present in layers 4 and 5 (Fig. 15.13). The composition of the injected fluids and the duration of fluid injection for both SEAR tests are described in Section 15.2. The simulations indicated that most of the DNAPL in the aquifer would be removed by the SEAR.

15.4.4.3 SEAR Execution and Results

The surfactant used for the SEAR was sodium dihexyl sulfosuccinate (CYTEC Aerosol MA-80I). Laboratory testing showed that adding 8% solution of surfactant, 7,000 mg/L of NaCl, and 4% isopropyl alcohol to the groundwater increased the solubility of chlorinated hydrocarbons by a factor of about 560, to approximately 620,000 mg/L, in a microemulsion.

The initial DNAPL saturation was estimated to be 0.03 averaged over the entire test area volume. Based on partitioning tracer tests completed in Phase I, the initial DNAPL volume was estimated to be approximately 1,310 L. Following the SEAR, the final average DNAPL saturation was only 0.0003 in the swept volume, and tracer tests indicated that the estimated DNAPL volume was approximately 19 L, a reduction of approximately 99%. The total VOC concentration in the central monitoring well (M7) was reduced from near the TCE solubility of 1,100 mg/L to only 8 mg/L by the end of the test. Approximately 95% of the surfactant was recovered. It may have been possible to recover more of the surfactant if

groundwater extraction had continued longer. These results closely matched post-SEAR DNAPL volumes predicted by the UTCHEM design simulations.

15.4.4.4 Bioremediation Considerations

The SEAR was extremely effective in reducing the volume of DNAPL present in the aquifer. However, the aqueous phase concentrations of VOCs in the aquifer following the SEAR are still environmentally significant. Also, the aqueous phase concentrations of surfactant and IPA could impact attempts to bioremediate the remaining TCE. Although about 95% of the injected surfactant and co-solvent was flushed out by water and sent to the treatment plant, the remaining aqueous phase concentrations of surfactant and co-solvent, and the fact that pockets of DNAPL remaining can act as continuing sources of VOCs in the groundwater, constitute significant challenges to bioremediation.

Although the DNAPL at Hill AFB consists of a mixture of chlorinated solvents, the DNAPL was assumed to be 100% TCE for bioremediation simulations since TCE comprises the majority of the DNAPL mixture.

Design of a bioremediation system to reduce these SEAR fluid concentrations to background levels requires consideration of several important issues. First, TCE biodegradation by methanotrophs is a suicidal process for the methanotrophs. At the kinetic constants used for these simulations, biomass is reduced by an amount that is ten times the mass of TCE biodegraded. This effect hampers the ability of the bioremediation system to generate and maintain a viable biomass within the aquifer.

Second, the remaining surfactant and IPA create an oxygen demand as these compounds are biodegraded by heterotrophs. This oxygen demand reduces the oxygen available to the methanotrophs for biodegradation of methane and the concomitant destruction of TCE.

Third, low permeability areas of the aquifer that contain NAPL serve as continuing sources of TCE. Because these pockets have a low permeability, it is difficult to bring methane and oxygen into these pockets to biodegrade the TCE there.

15.4.5 TCE/Surfactant Biodegradation Simulation

15.4.5.1 Simulation Conditions

The considerations listed above emphasize the need for a model such as UTCHEM to accurately simulate the physical, chemical and biological factors involved in such a complex groundwater system. The methods used to address the three considerations above were:

1. Inject methanotrophs into the aquifer to replace those destroyed by the TCE biodegradation process.

2. Amend injected fluids with oxygen in the form of hydrogen peroxide to prevent oxygen limitations created by surfactant and IPA biodegradation.

3. Inject fluids continuously to biodegrade TCE that leaches out of the low permeability aquifer areas.

Since adequate biomass is a critical factor in the biodegradation of SEAR compounds, biomass was simply injected into the treatment zone along with methane and oxygen. It was assumed that injected biomass partitions to the aquifer solids at a ratio of 10 parts attached biomass to 1 part unattached biomass. Methanotrophs, methane and oxygen were injected at concentrations of 10 mg/L, 20 mg/L, and 300 mg/L, respectively. Injection began immediately after surfactant flushing ended (day 227). Kinetic parameters and other simulation conditions are described by de Blanc [1998].

To determine the effectiveness of the bioremediation system, a baseline simulation was also run. In the baseline simulation, water was simply circulated through the test area at the same rate as the amended water in the bioremediation simulation. The baseline simulation acted as a "pump and treat" control to which concentrations of all relevant SEAR species could be compared.

15.4.5.2 Simulation Results

Figure 15.14 compares the total mass of TCE, surfactant and IPA in the aquifer as a function of time for both the pump and treat system and the bioremediation system. The total mass of TCE and surfactant remaining in the aquifer as simulated in the bioremediation run do not differ significantly from the total mass simulated in the pump and treat run. Injection of the additional oxygen does reduce the IPA slightly, but the effect is not significant. The IPA reduction occurred because it is highly biodegradable compared with both the TCE and surfactant, so that its biodegradation in the aquifer was oxygen limited. Injection of a solution containing more oxygen enhanced IPA degradation.

When the concentration of TCE in well M7 is compared between the pump and treat run and the bioremediation run (Fig. 15.15), the effect of methane, oxygen and methanotroph injection on the concentration of TCE in the aquifer is evident. The simulated TCE concentration in the flow channel near well M7 is significantly reduced when methanotrophs are injected with methane and oxygen. The simulated TCE concentration in the aquifer as measured at well M7 is approximately 10 times less than the simulated TCE concentration in the pump and treat scenario.

Figure 15.16 indicates that the average TCE concentration in the extracted groundwater simulated by the bioremediation run is not significantly lower than the average TCE concentration when pumping alone is used to remediate the aquifer. Apparently, the beneficial effect of methanotroph injection does not extend through the entire flow channel. TCE leaching from low permeability areas in the center of the test area becomes entrained in the circulating water beyond the point penetrated by injected biomass.

Injection of oxygen did reduce the concentration of surfactant and IPA in the extracted groundwater, since these constituents are more easily biodegraded than TCE.

15.4.6 Conclusions

The design simulation highlights the complexity of a bioremediation system when NAPL is present and many processes occur simultaneously. The fact that the simulation indicates that injection of chemicals to stimulate biodegradation performed no better than simple water flushing in reducing the in-situ mass of TCE emphasizes the importance of considering many different bioremediation designs. A relatively inexpensive way to rule out potentially ineffective bioremediation strategies in such a complex system is through the use of a model such as UTCHEM.

UTCHEM was successfully demonstrated by the simulation of TCE, IPA and surfactant biodegradation in the SEAR treatment area at Hill Air Force Base. To the best of the authors' knowledge, no other simulator can simulate multi-phase flow, surfactant phase behavior, and biodegradation simultaneously in three dimensions. The biodegradation model was able to provide useful information that could be used in future design studies for bioremediation of TCE at Hill AFB and other sites where biodegradation systems are being considered, particularly when NAPL is present. Specific conclusions of the Hill AFB OU2 bioremediation design simulations are:

1. Injection of methane, oxygen and methanotrophs into the SEAR test area does not reduce TCE, surfactant, or IPA mass in the aquifer any faster than circulation of water alone under the particular conditions of these simulations. The reason is that the rate of reduction of these SEAR compounds is limited by the transport of these constituents from low permeability to high permeability zones within the aquifer. Other injection and extraction strategies may be more effective than the particular design discussed in this example.

2. Circulation of methane and oxygen through the aquifer can reduce the concentration of TCE, IPA, and surfactant in the more permeable aquifer zones. Tighter well spacing could result in reduced TCE concentrations in the entire aquifer.

3. Circulation of oxygen through the aquifer can substantially reduce the concentration of IPA in the extraction wells.

4. Residual surfactant and IPA have very little effect on TCE biodegradation because they are rapidly flushed from the flow channel.

15.5 Example 4: Migration of Dissolved Metals Using the Geochemical Option

The geochemical option in UTCHEM allows the modeling of aqueous and solid reactive species. See Section 8 for information on the geochemical model. An application to an acid mine tailing contamination problem is presented here to illustrate the capability of simulating additional components such as chromium, lead, and sulfate that were not included in the original UTCHEM model. The aquifer and site conditions for this one-dimensional example are similar to the conditions at the Nordic site near Elliot Lake, northern Ontario (Walter *et al*., 1994). This is an example of an extensively studied field site where geochemical and physical transport processes combine to control the migration of dissolved metals. A total of 51 aqueous species and 7 solid species are simulated (Table 15.8). The initial and injected component concentrations are similar to those used in the simulation by Walter *et al*. [1994]. Initial concentrations were determined by equilibrating the water and mineral phases using batch equilibrium calculations.

The intention here is not to reproduce the simulation results of Walter *et al*. [1994], but to illustrate the UTCHEM capability in modeling a complex geochemical process. The simulated concentration profiles of selected aqueous and solid species at different fluid throughput in pore volumes are shown in Figs. 15.17 through 15.24. These results show a very similar trend to those presented by Walter *et al*. [1994]. However, the conditions for the two simulations were not identical. For example, species such as K, Mn, and Fe were not included in the UTCHEM simulation example.

There are other geochemical transport models that allow a large number of reactive aqueous species. The advantage of UTCHEM is that up to four fluid phases can be modeled at the same time that geochemical reactions and/or other chemical, microbiological and physical phenomena are modeled. This is what is needed to model the most general contaminant fate and transport problems faced in practice.

15.6 Tables and Figures

Table 15.1. Grid and Aquifer Properties Used in the Phase I Design Simulations

Property	Value	Comments
Mesh	xyz: 20 x 17 x 6 (2040 gridblocks)	
Dimensions	54 x 20 x 5.9 meters	
Mesh size	0.8 x 0.8 x 0.5 meters, (smallest aquifer cell), pore volume of 72 liters 14 x 2.7 x 2.0 meters, (largest aquifer cell), pore volume of 20,100 liters	
Boundary conditions	Impervious top, bottom, east and west boundaries; constant potential boundaries north and south	
Initial pressure	Atmospheric pressure in top layer; hydrostatic distribution in vertical	
Initial DNAPL saturation	20% (the DNAPL residual saturation) in the lower 2 m of the aquifer	Based on core contaminant measurements and measured DNAPL pool depth
Aquifer pore volume	126,000 liters	
Total aquifer DNAPL volume	5090 liters	Including DNAPL in the northern primary DNAPL pool and other DNAPL outside test area

Table 15.2. Summary of Phase II Test

Duration (days)	Cumulative time (days)	Segment	Pore Volumes	Chemicals added to Hill source water
1.7	1.7	water flooding	1.2	
0.4	2.1	tracer injection	0.3	1,572 mg/L 2-propanol (K=0) 1,247 mg/L 1-pentanol (K=3.9) 1,144 mg/L 2-ethyl-1-butanol (K=12.5)
3.7	5.8	water flooding	2.6	
1.0	6.8	NaCl preflood	0.7	7,000 mg/L NaCl
3.4	10.2	surfactant/ alcohol flooding	2.4	7.55% sodium dihexyl sulfosuccinate 4.47 % isopropanol 7,000 mg/L NaCl
11.0	21.2	water flooding	7.8	
1.0	22.2	tracer injection	0.7	854 mg/L 1-propanol (K=0) 431 mg/L bromide (K=0) 798 mg/L 1-hexanol (K=30) 606 mg/L 1-heptanol (K=141)
5.1	27.3	water flooding	3.6	
2.4	29.7	extraction only	--	

Notes: All injected solutions are mixed in Hill tap water. The total injection rate was 1.7 m^3/s (7.5 gpm) for all three injection wells and the total extraction rate was 2.1 m^3/s (9.2 gpm) for all three extraction wells. The water injection rate for the hydraulic control well SB-8 was 1.6 m^3/s (7 gpm).

Table 15.3. Initial and Final DNAPL Volumes and Saturations from Tracer Tests

	Well Pair U2-1/SB-3	Well Pair SB-1/SB-2	Well Pair SB-5/SB-4	Total Swept within Test Area
DNAPL volume, liters				
Initial	250	795	265	1310
Final	0	19	0	19
DNAPL Saturation, %				
Initial	1.7	5.4	1.3	2.7
Final	0.00	0.10	0.00	0.03
Contaminant Soil Content				
Initial, mg/kg of soil	3,800	12,000	2,900	6,000
Final, mg/kg of soil	0	224	0	67

Table 15.4. Grid and aquifer properties for SEAR design.

Dimension	42.97 x 24.38 x 3.96 meters
Mesh	xyz: 25x25x16 (10,000 gridblocks)
Porosity	0.28
Aquifer pore volume	937,146 liters
Smallest gridblock size	0.9144 x 0.6096 x 0.1524 meters
Largest gridblock size	7.312 x 3.657 x 0.6096 meters
Boundary conditions	Impervious top, bottom, north, and south; constant potential west-east boundaries with a hydraulic gradient of 0.0123 m/m
Initial pressure	Atmospheric pressure in top layer, hydrostatic distribution in vertical
Initial electrolyte concentration	0.1 wt% calcium chloride

Table 15.5. Injection strategies used in the SEAR simulations.

Process	Run ISA7m		Run ISA26m		Run SEAR5	
	days	rate	days	rate	days	rate
Water preflush	2	No. A	6	No. B	8	No. B
Surfactant flood	30	No. A	48	No. B	58	No. C
Water postflush	68	No. A	58	No. A	74	No. A

Table 15.6. Well rates (m^3/day) used in SEAR simulations.

Wells	Rate No. A	Rate No. B	Rate No. C
Upper screen injection: IN1, IN2, IN3	0.436	0.436	0.436
Injection: IN01, IN02, IN03	1.09	0.727	0.545 - 0.927
Hydraulic control: HC01, HC02	1.635	1.09	1.09
Extraction: EX01-EX06	1.362	0.908	0.709 to 1.2

Table 15.7. Hydraulic conductivity used in the history match simulation SEAR5.

Simulation Layer number	Thickness, m	Hydraulic conductivity, cm/s
1-12	3.35	$2x10^{-4}$
13-14	0.30	$5x10^{-5}$
15-16	0.30	10^{-5}

Table 15.8. List of Elements and Reactive Species Used in Example 4.

Elements			
Cr	H	Pb	Mg
Ca	Na	Al	Si
Cl	CO_3	SO_4	O
Aqueous Species			
$Cr(OH)^{2+}$	H^+	Pb^{2+}	Mg^{2+}
Ca^{2+}	Na^+	Al^{3+}	H_4SiO_4
Cl^-	CO_3^{2-}	SO_4^{2-}	H_2O
OH^-	$H_3SiO_4^-$	$MgOH^+$	$MgCO_3$ (Aq.)
$MgHCO_3^+$	$MgSO_4$ (Aq.)	$CaOH^+$	$CaHCO_3^+$
$CaCO_3$ (Aq.)	$CaSO_4$ (Aq.)	$NaCO_3^-$	$NaHCO_3$ (Aq.)
$NaSO_4^-$	$AlOH^{2+}$	$Al(OH)_2^+$	$AlSO_4^+$
$Al(SO_4)_2^-$	$PbCl^+$	$PbCl_2$ (Aq.)	$PbCl_3^-$
$PbCl_4^{2-}$	$Pb(CO_3)_2^{2-}$	$PbOH^+$	Pb_2OH^{3+}
$PbSO_4$ (Aq.)	$PbCO_3$ (Aq.)	$Pb(SO_4)_2^{2-}$	$PbHCO_3^+$
HCO_3^-	H_2CO_3 (Aq.)	HSO_4^-	Cr^{3+}
$Cr(OH)^{2+}$	$CrCl^{2+}$	$CrCl_2^+$	$CrSO_4^+$
$CrOHSO_4$ (Aq.)	$Cr_2(OH)_2SO_4^{2+}$	$Cr_2(OH)_2(SO_4)_2$ (Aq.)	
Solid Species			
Calcite ($CaCO_3$)	Gibbsite ($Al(OH)_3$)	Gypsum ($CaSO_4$)	SiO_2
Cerrusite ($PbCO_3$)	Anglesite ($PbSO_4$)	$Cr(OH)_3$	

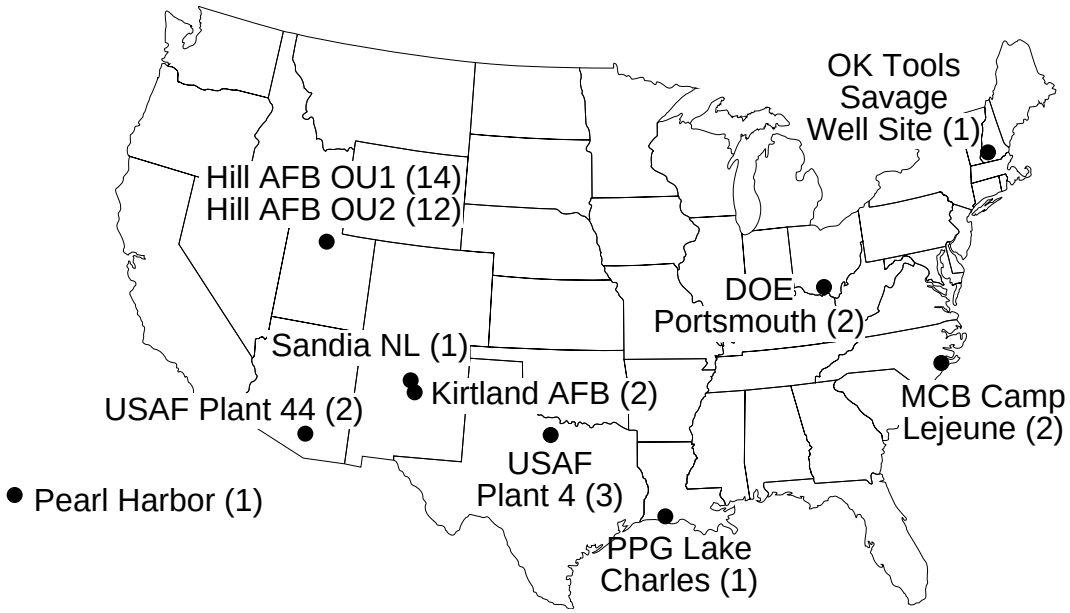

Figure 15.1. NAPL sites modeled with UTCHEM; number of tests in parentheses.

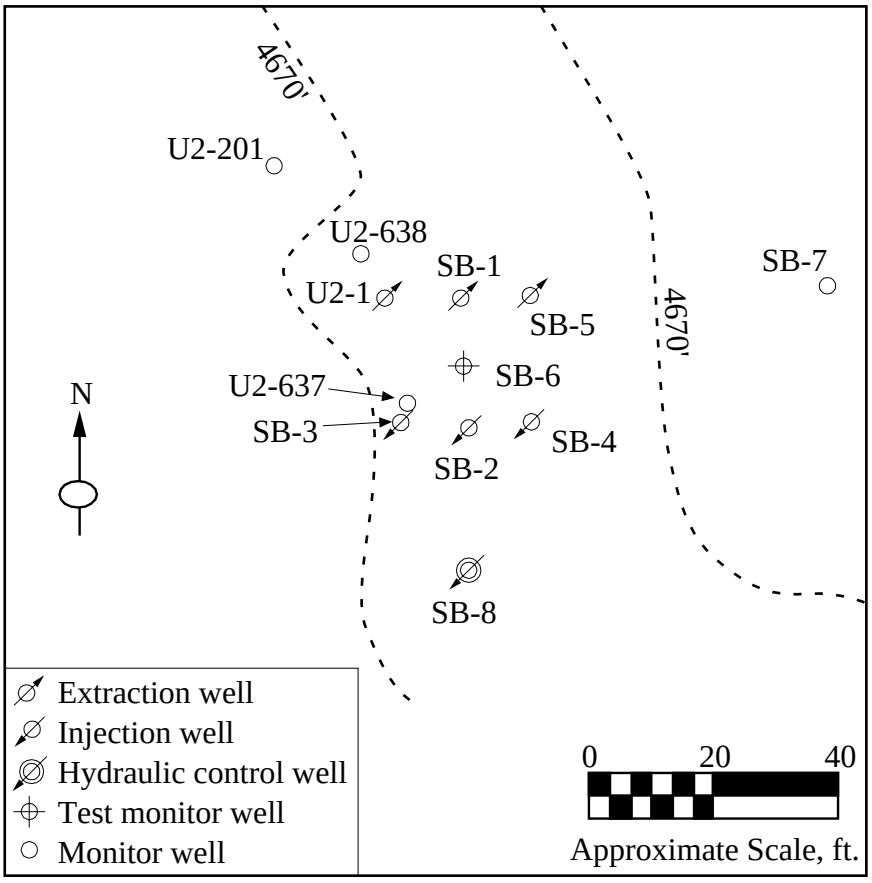

Figure 15.2. Plan view of Hill AFB OU2 site.

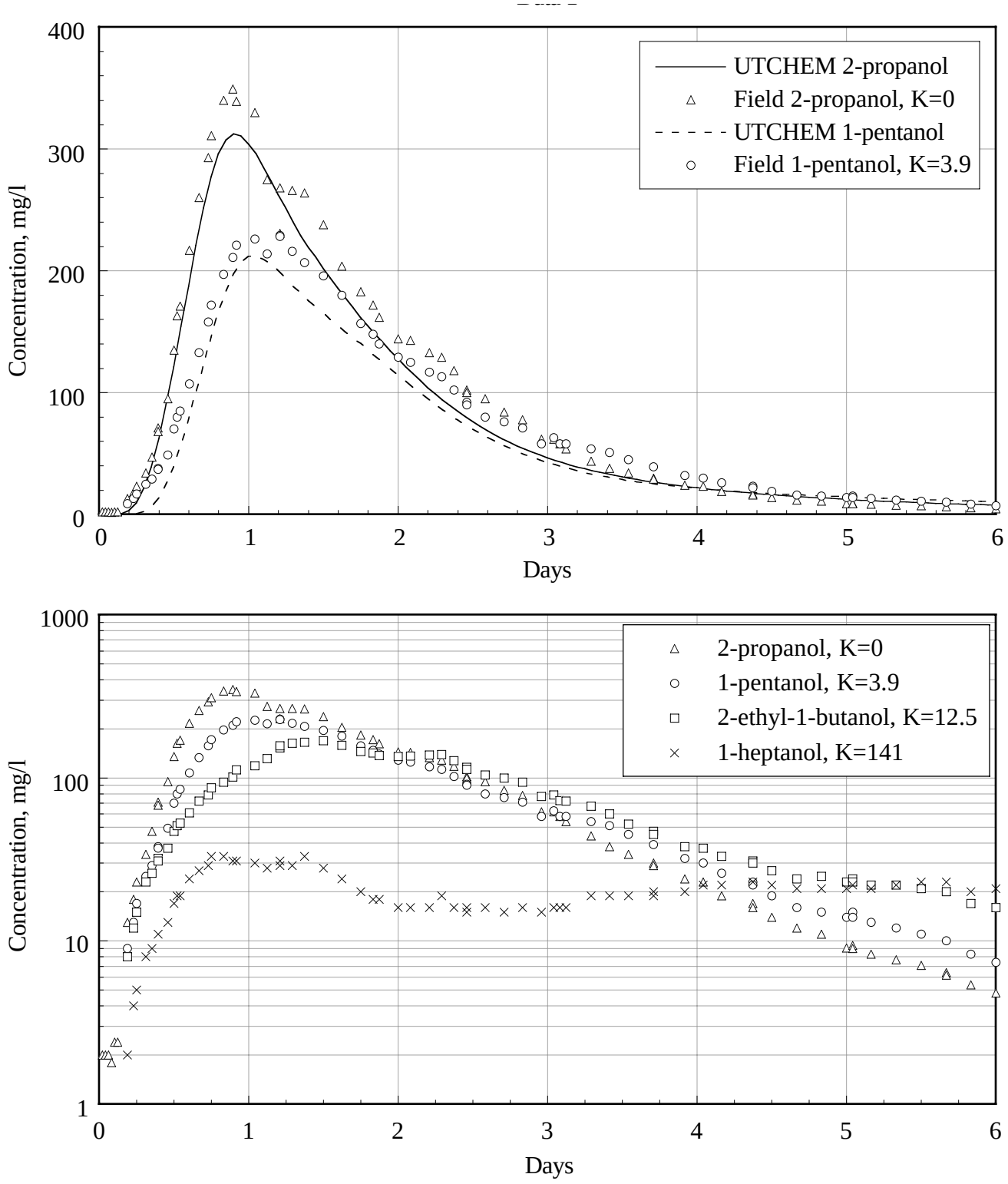

Figure 15.3. Tracer data for extraction well SB-1. Top: comparison of UTCHEM prediction with 2-propanol and 1-pentanol. Bottom: tracer data plotted on a log scale.

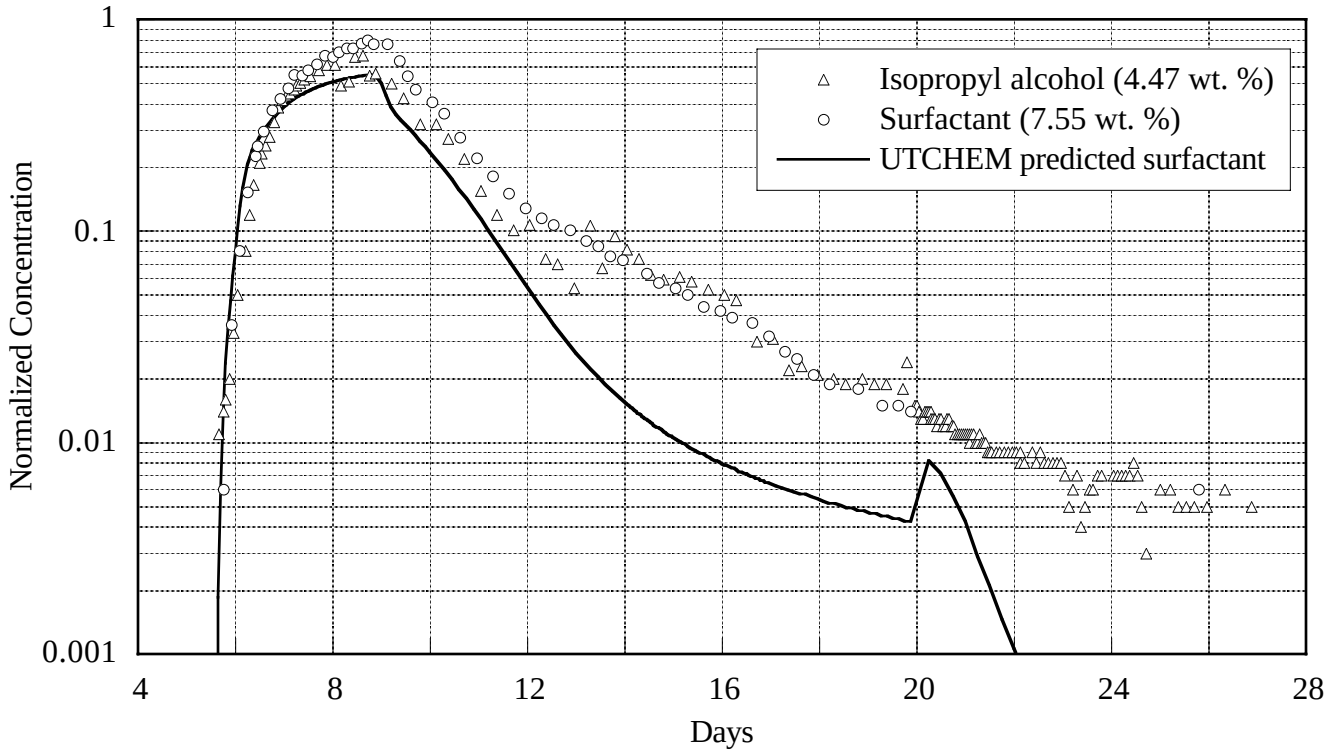

Figure 15.4. Surfactant and IPA concentrations produced at extraction well SB-1 during Phase II test: comparison of UTCHEM prediction with field data.

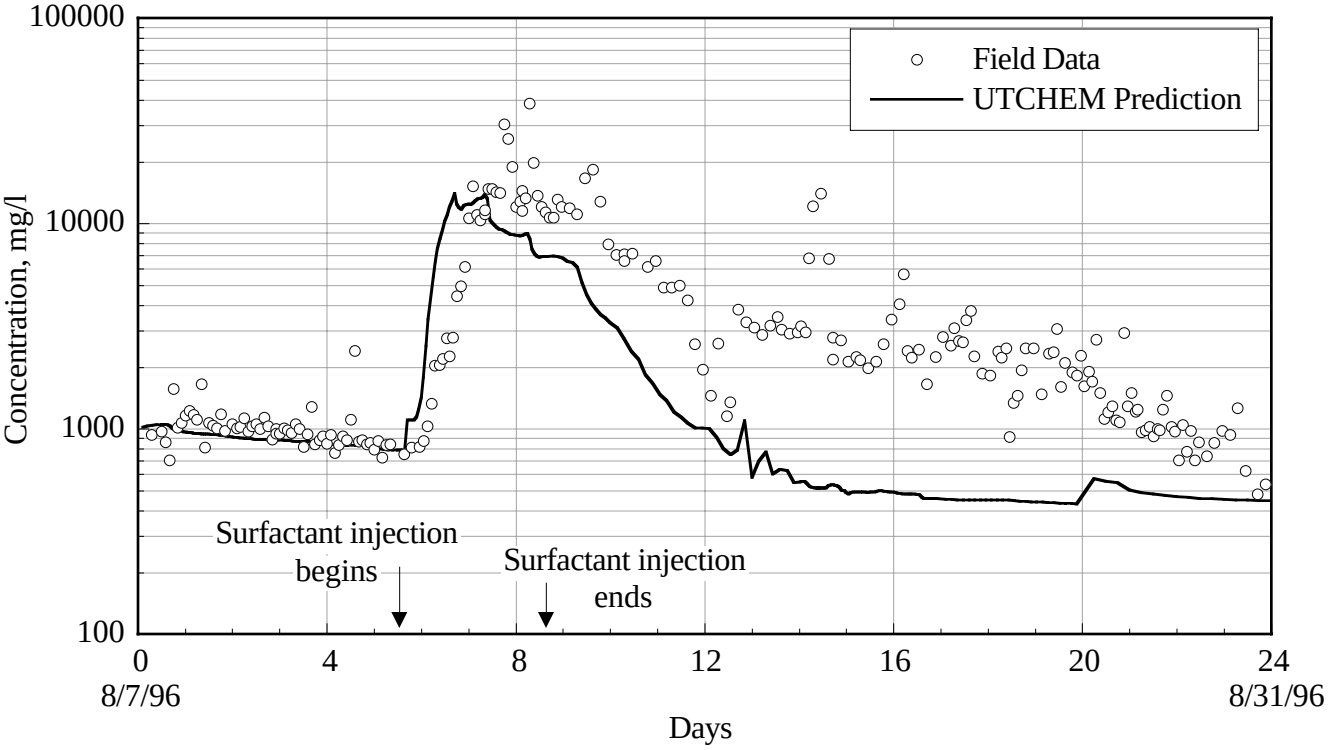

Figure 15.5. Contaminant concentrations produced at extraction well SB-1 during Phase II test: comparison of UTCHEM prediction with field data.

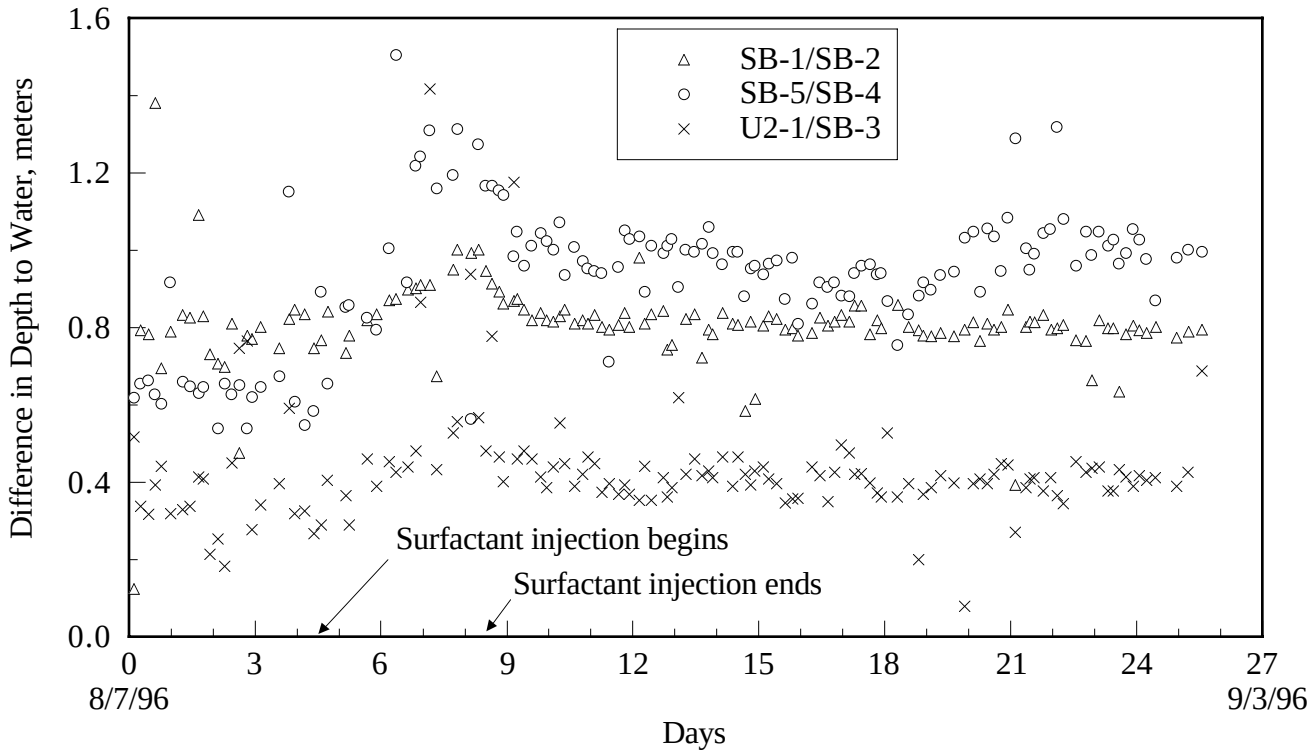

Figure 15.6. Difference in water table depth between test area extraction/injection well pairs.

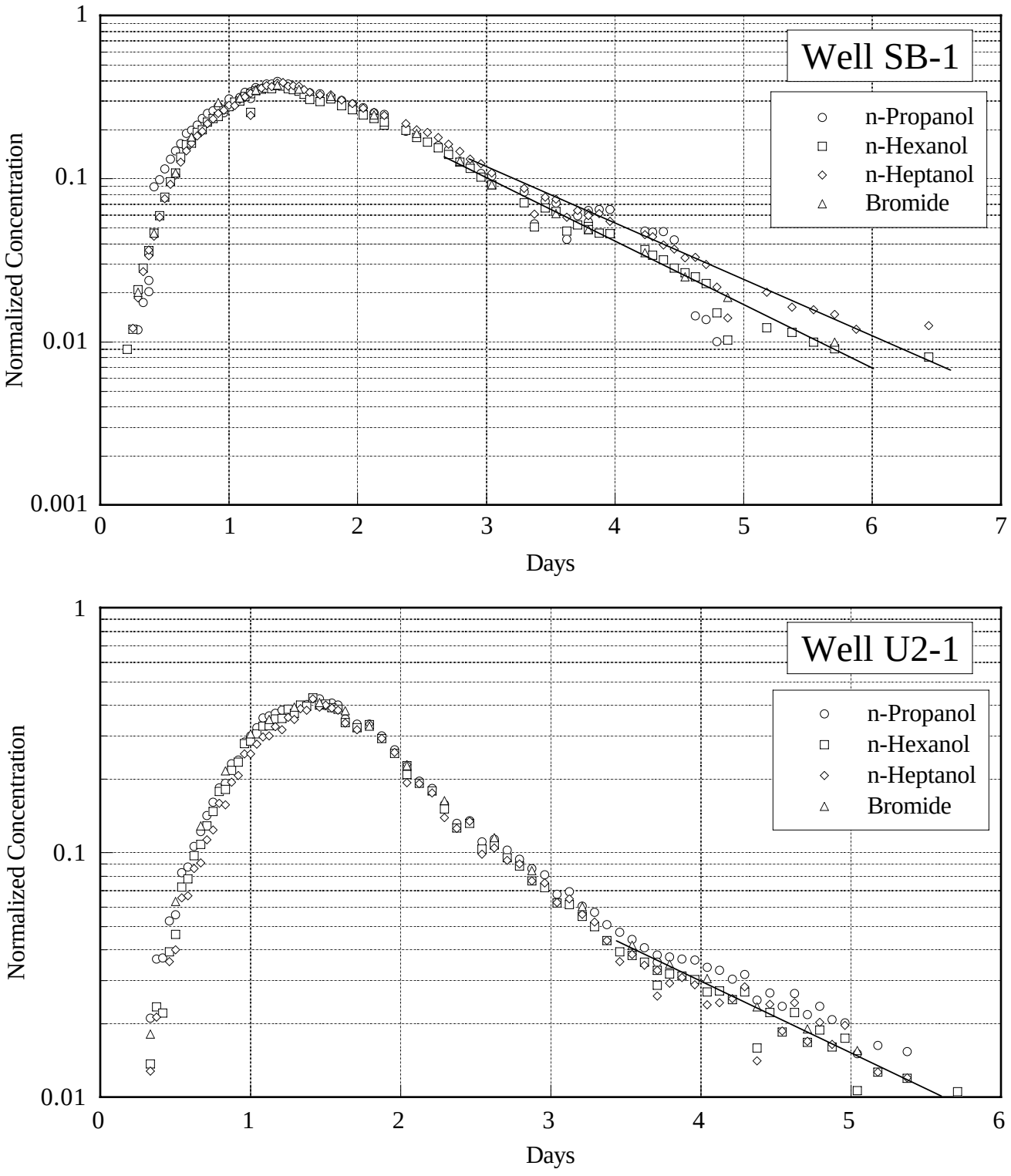

Figure 15.7a. Measured tracer concentrations produced in the three extraction wells and monitoring well during Phase II test, Wells SB-1 and U2-1.

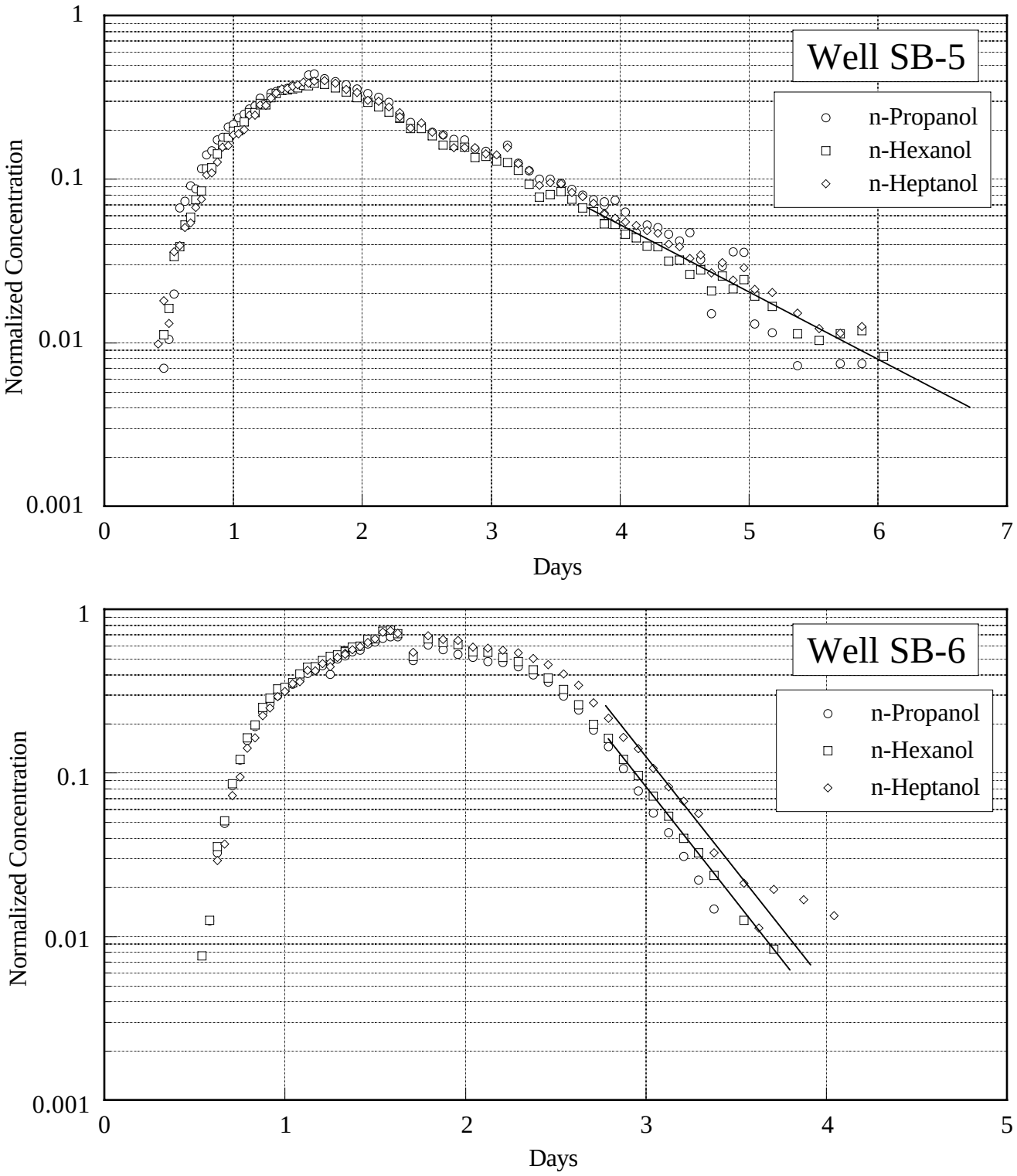

Figure 15.7b. Measured tracer concentrations produced in the three extraction wells and monitoring well during Phase II test, Wells SB-5 and SB-6.

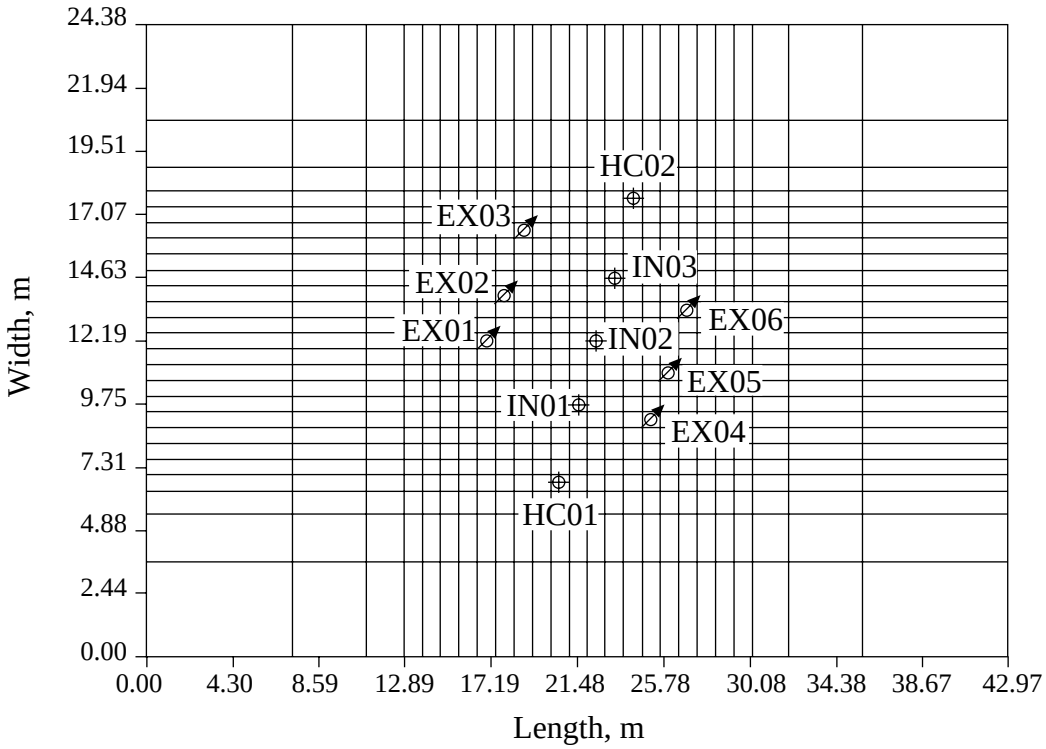

Figure 15.8. Simulation grid and well locations.

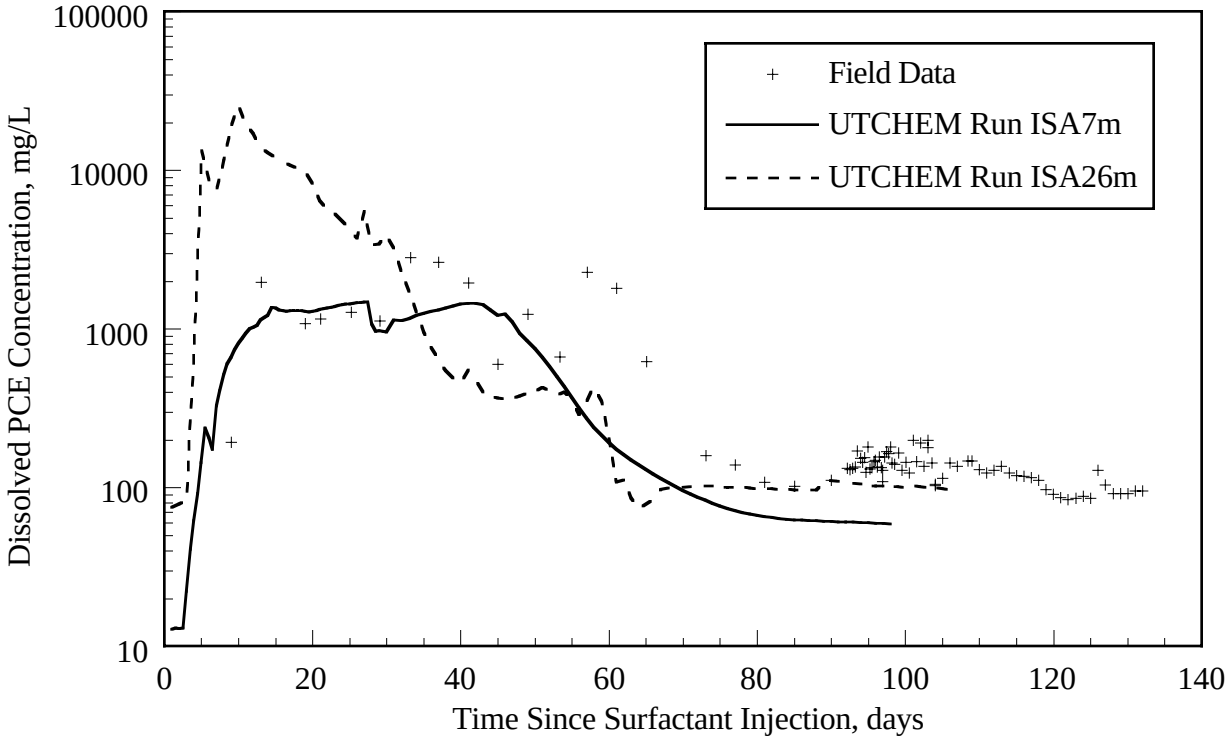

Figure 15.9. Comparison of predicted dissolved contaminant concentration and measured concentration in extraction well EX01.

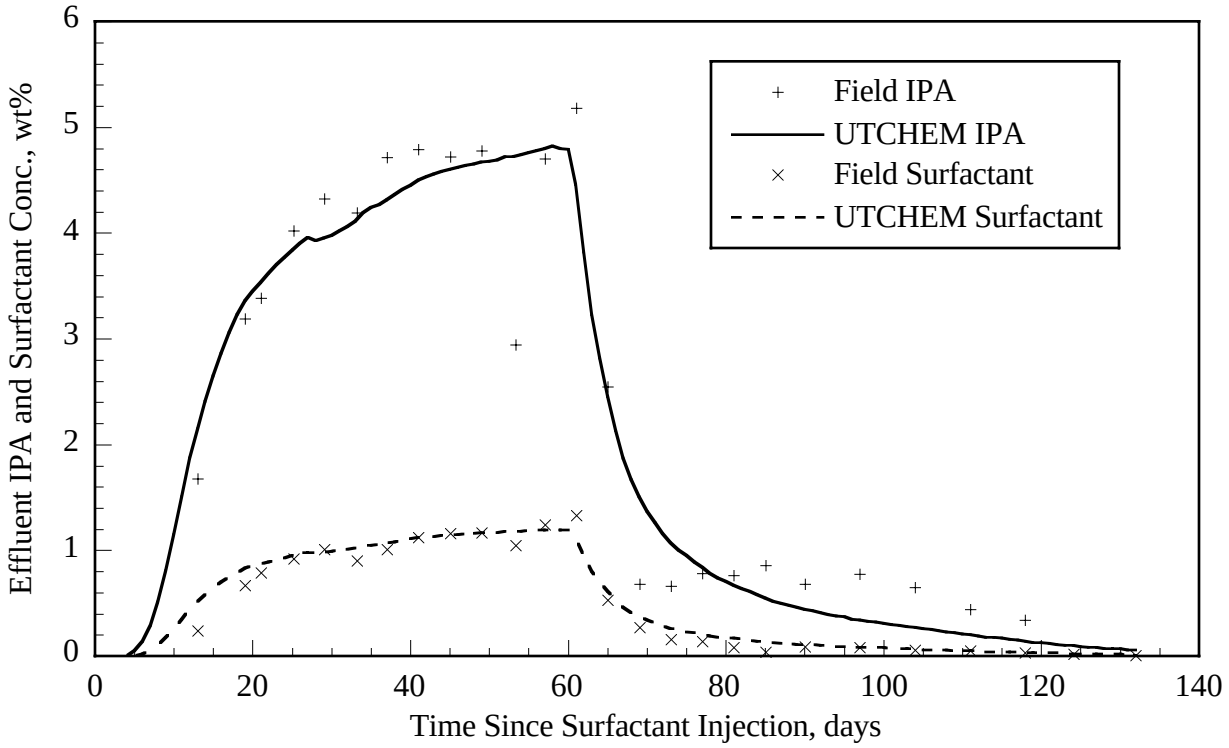

Figure 15.10. Comparison of measured and history match of surfactant and IPA concentrations in extraction well EX01 for simulation SEAR5.

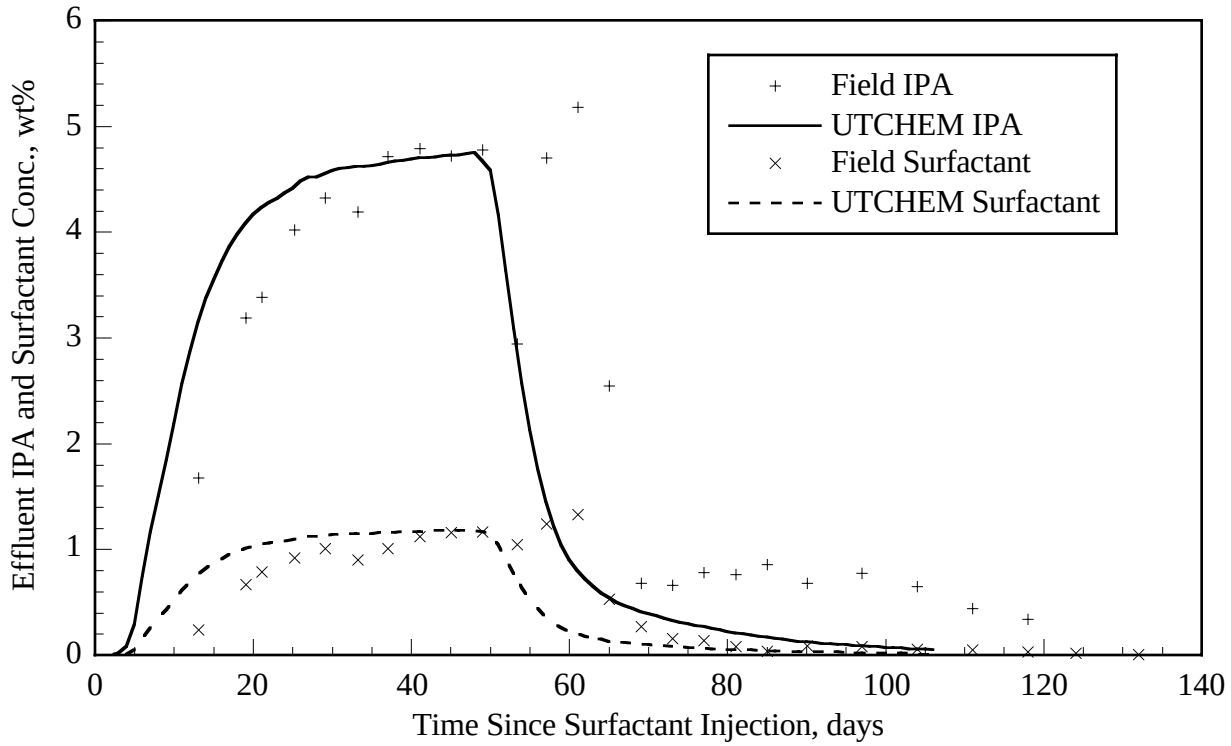

Figure 15.11. Comparison of field and predicted surfactant and IPA concentration at well EX01 for run ISA26m.

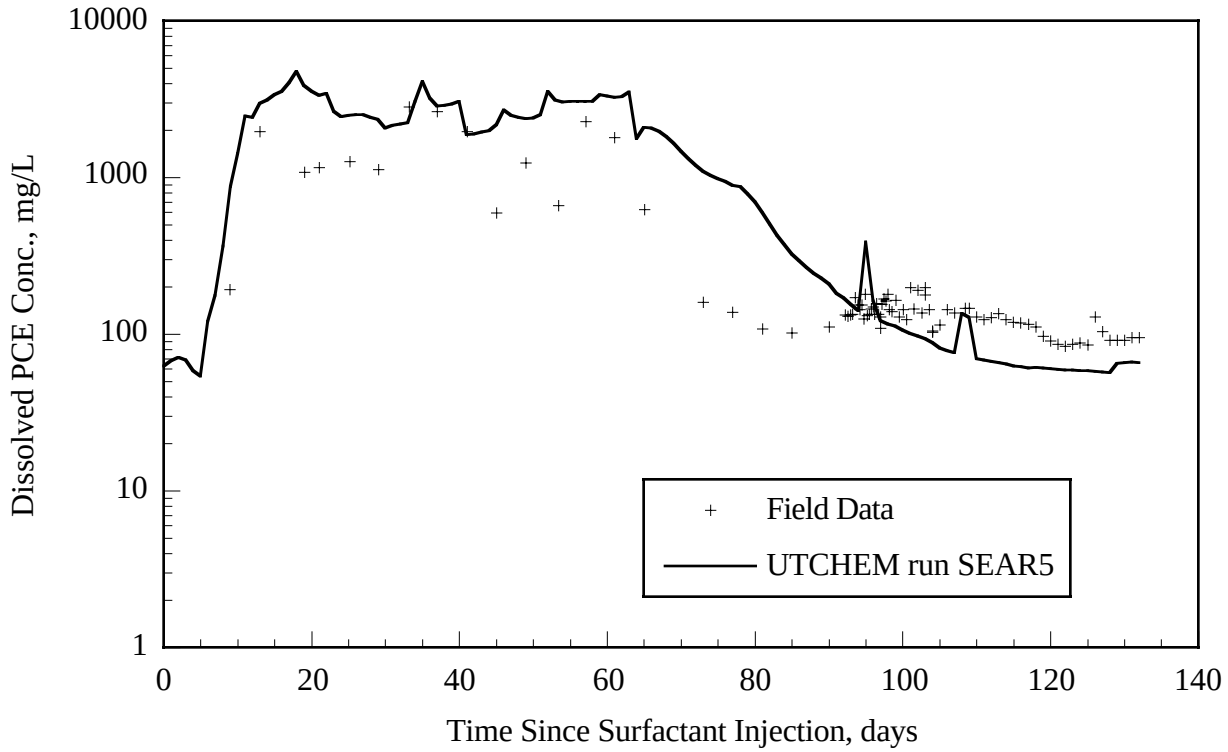

Figure 15.12. Comparison of measured and history match of dissolved PCE concentration in extraction well EX01.

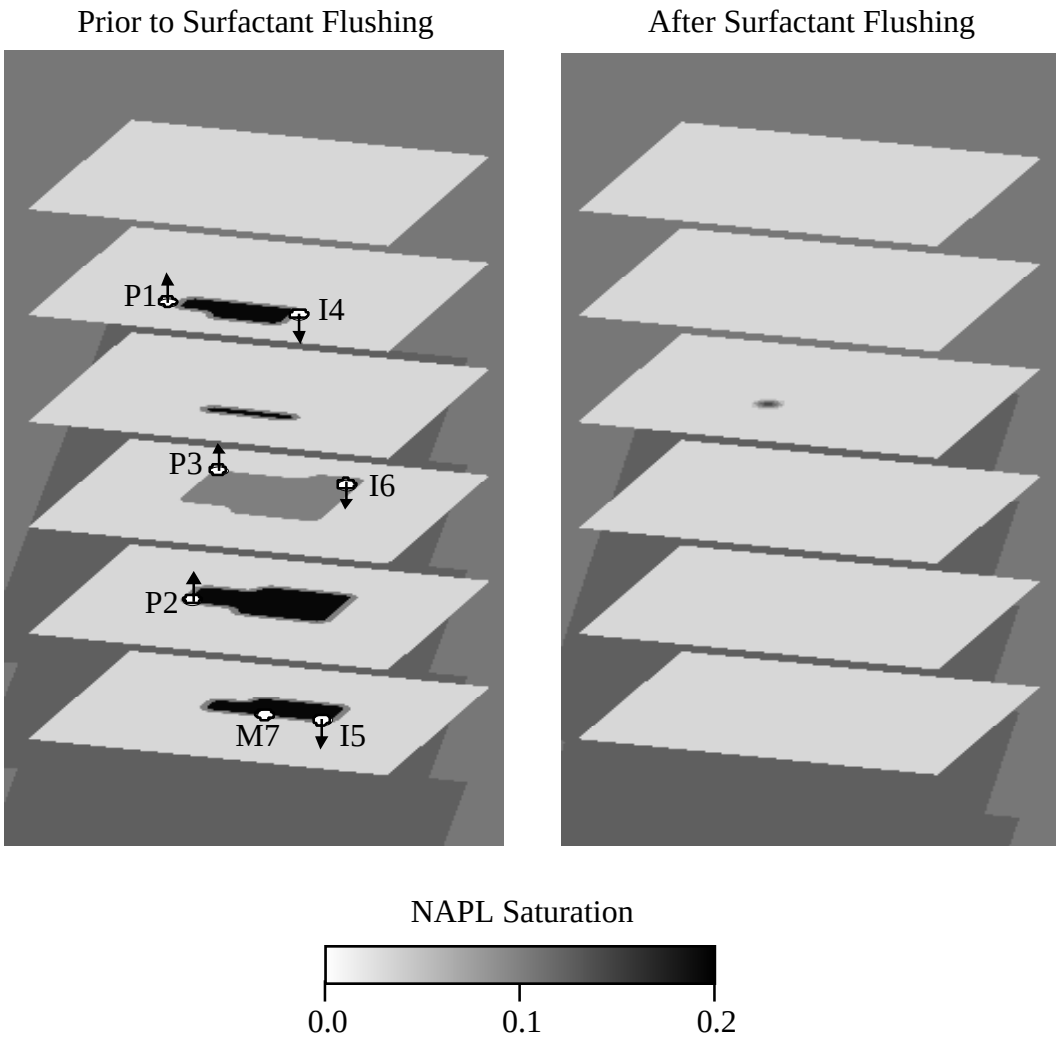

Figure 15.13. NAPL saturation in aquifer and location of injection, extraction, and monitoring wells in the test area by simulation layer. "P" denotes an extraction well, "I" denotes an injection well, and "M" denotes a monitoring well. Surfactant and nutrient solutions were injected from right to left in the figure.

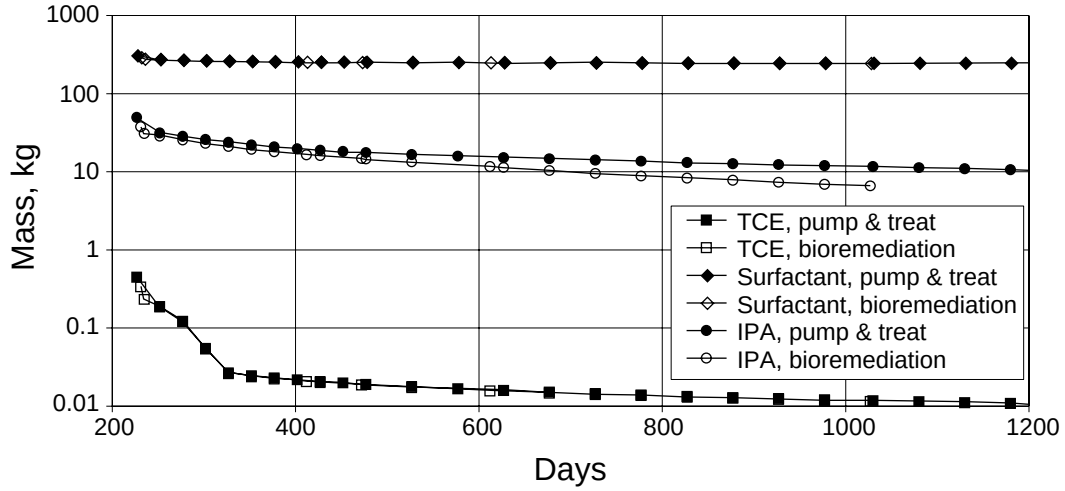

Figure 15.14. Mass of TCE, surfactant, and IPA in aquifer as simulated by a pump and treat scenario and a bioremediation scenario. Injection of methane, oxygen and biomass have an insignificant effect on the total mass of TCE and surfactant in the aquifer, and only a small effect on the mass of IPA.

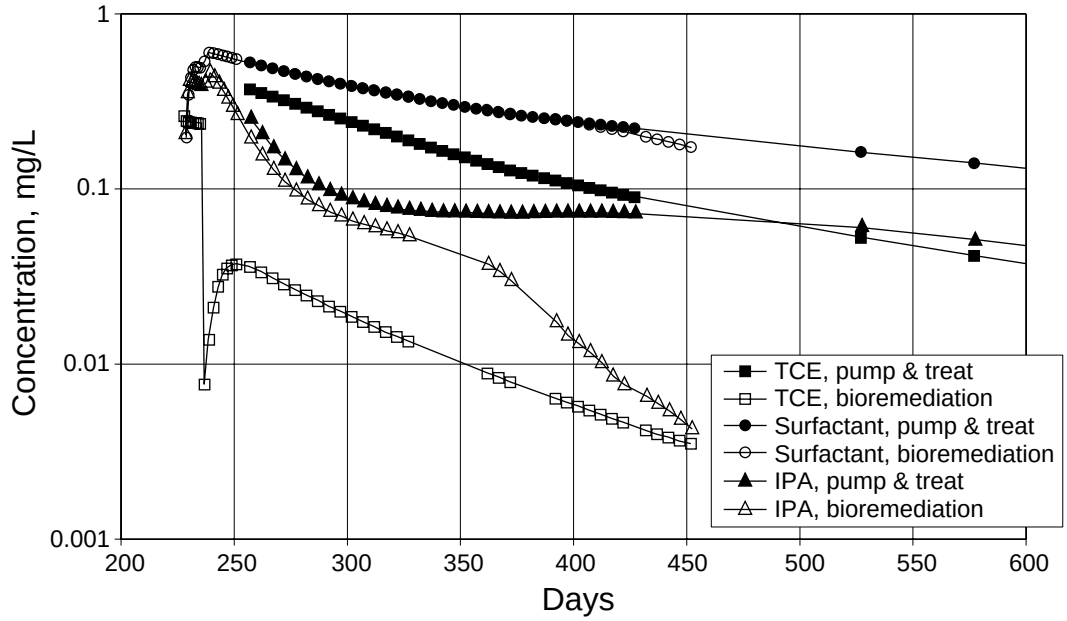

Figure 15.15. Simulated concentration of TCE, surfactant and IPA at central monitoring well M7.

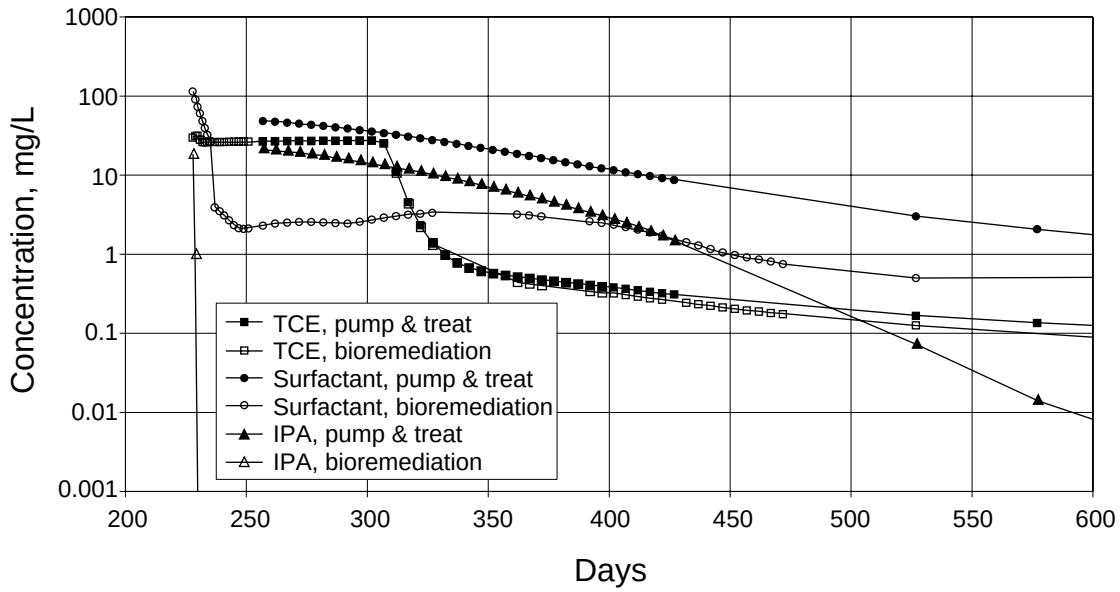

Figure 15.16. Comparison of simulated concentration of TCE, surfactant and IPA in extraction wells between a pump and treat system and a bioremediation system.

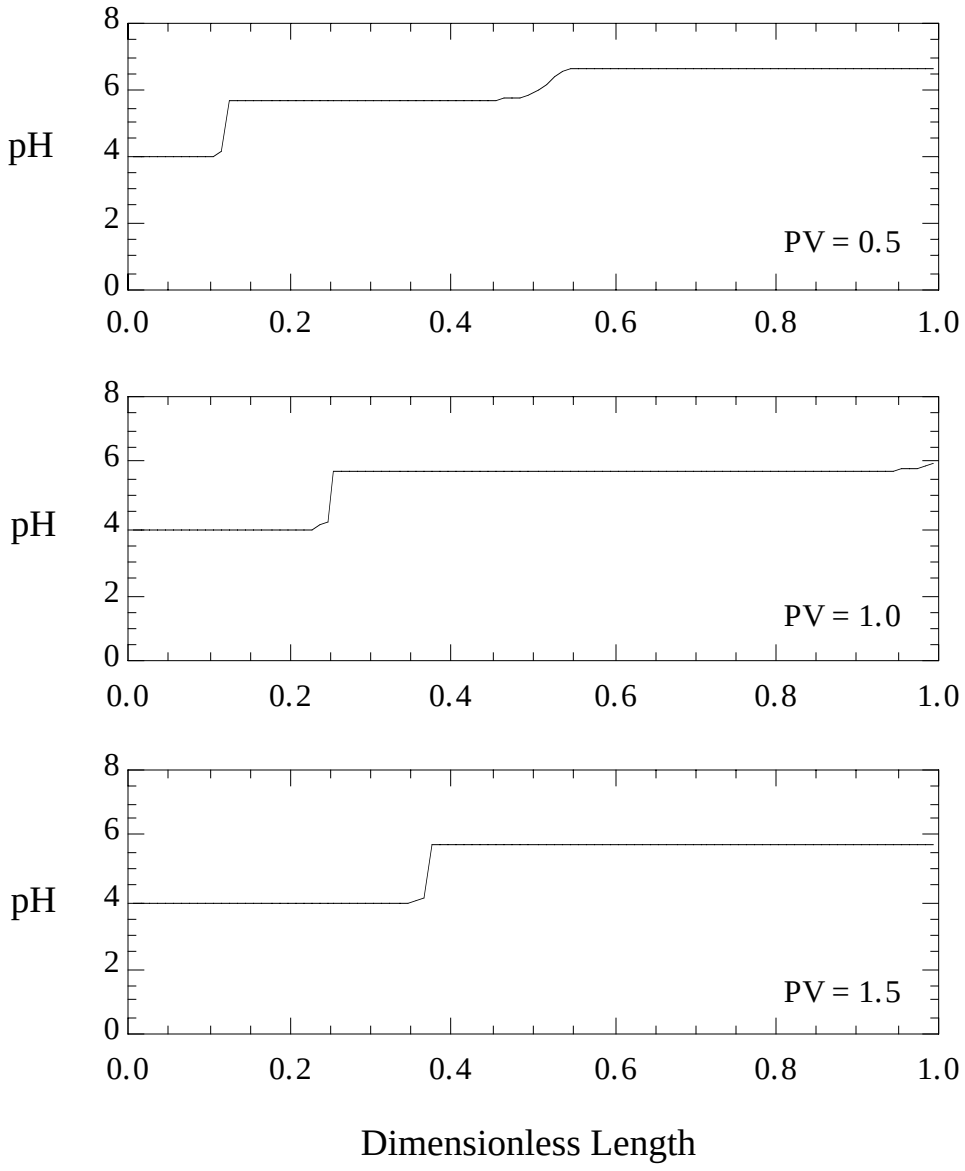

Figure 15.17. pH distribution at 0.5, 1.0, and 1.5 PV injected.

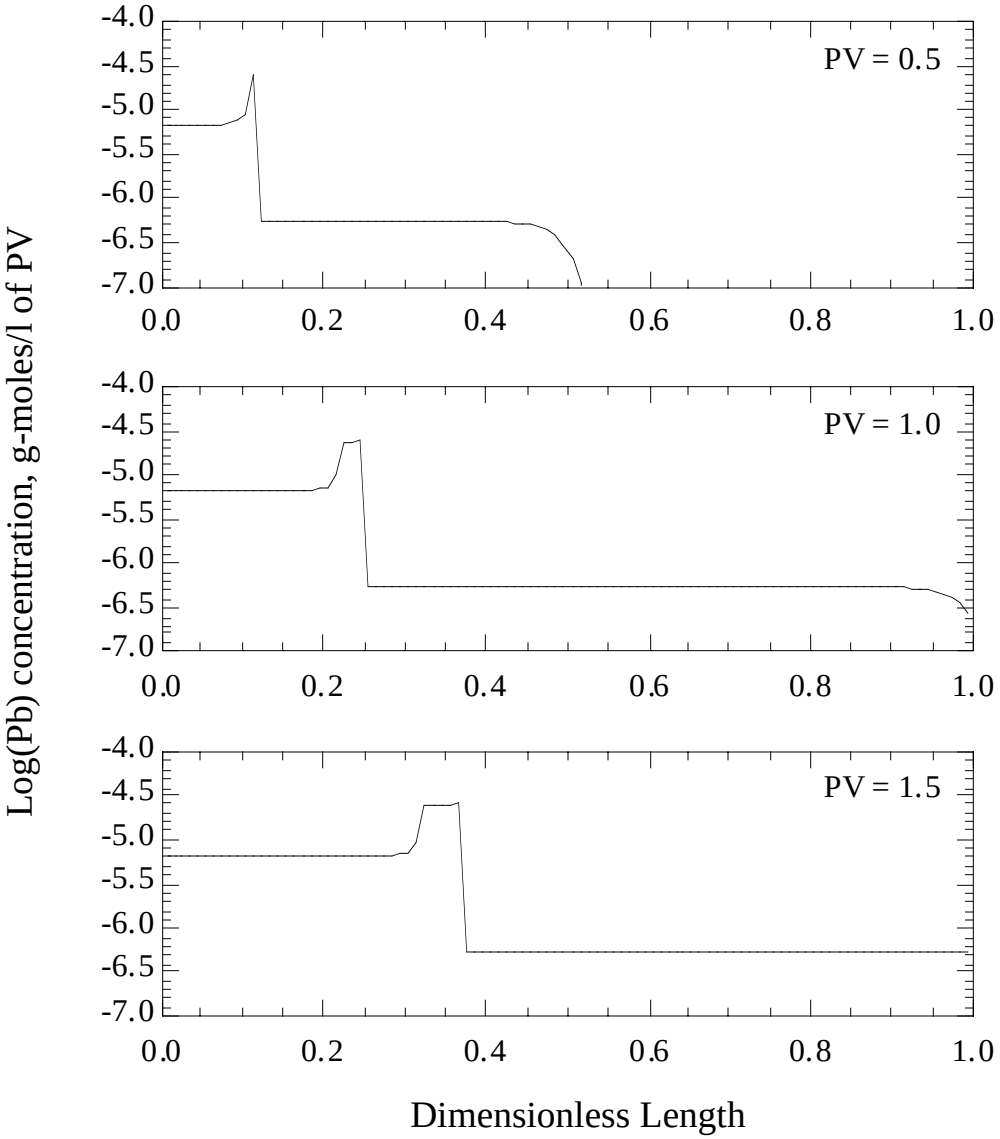

Figure 15.18. Lead concentration distribution at 0.5, 1.0, and 1.5 PV injected.

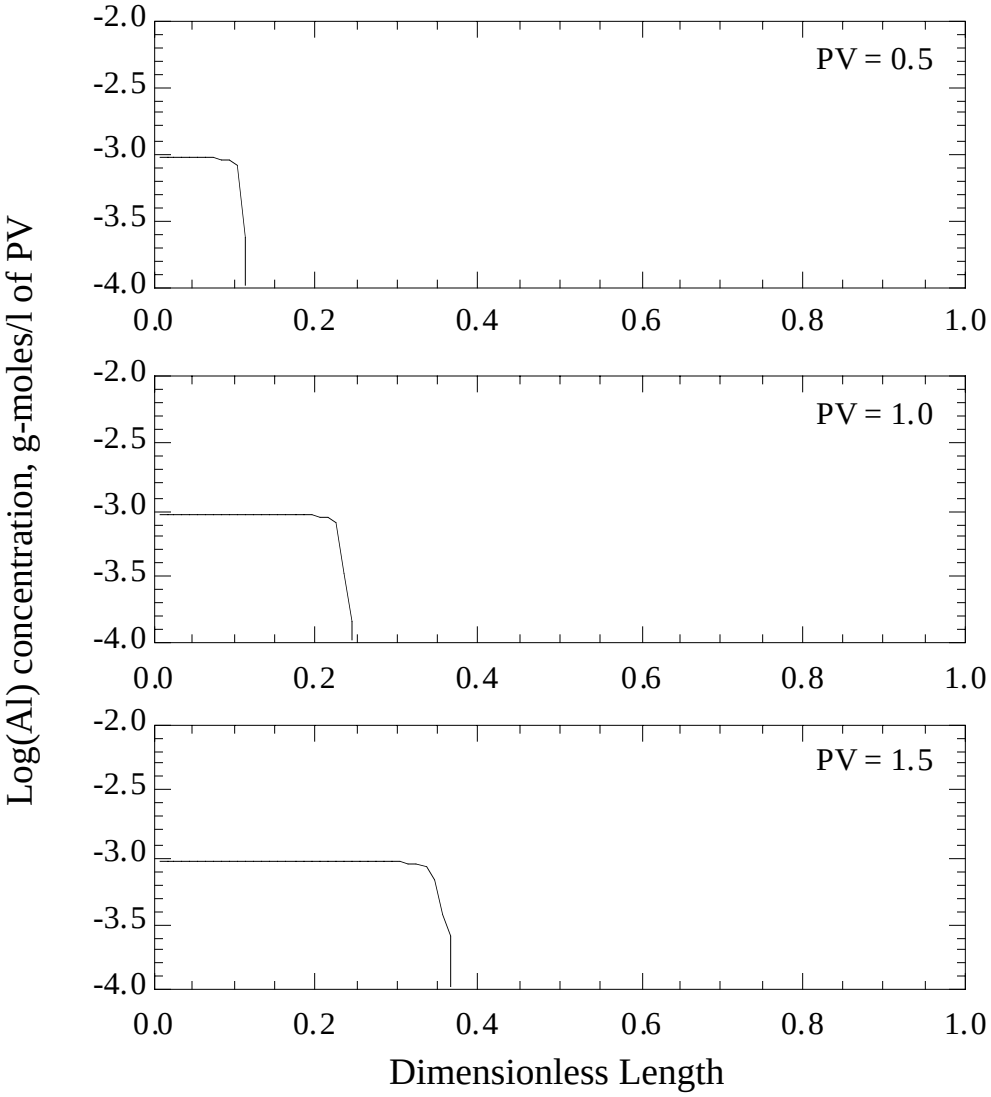

Figure 15.19. Aluminum concentration distribution at 0.5, 1.0, and 1.5 PV injected.

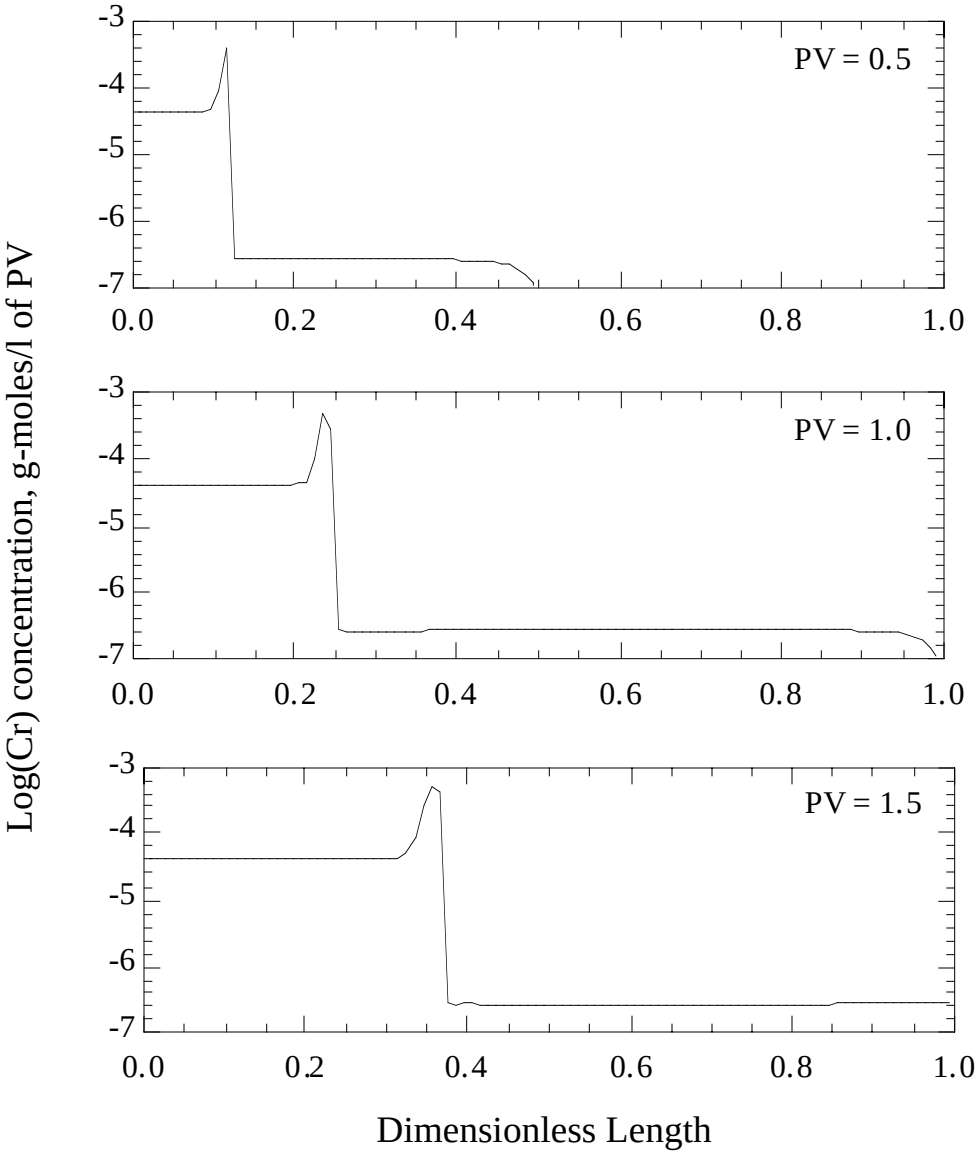

Figure 15.20. Aluminum concentration distribution at 0.5, 1.0, and 1.5 PV injected.

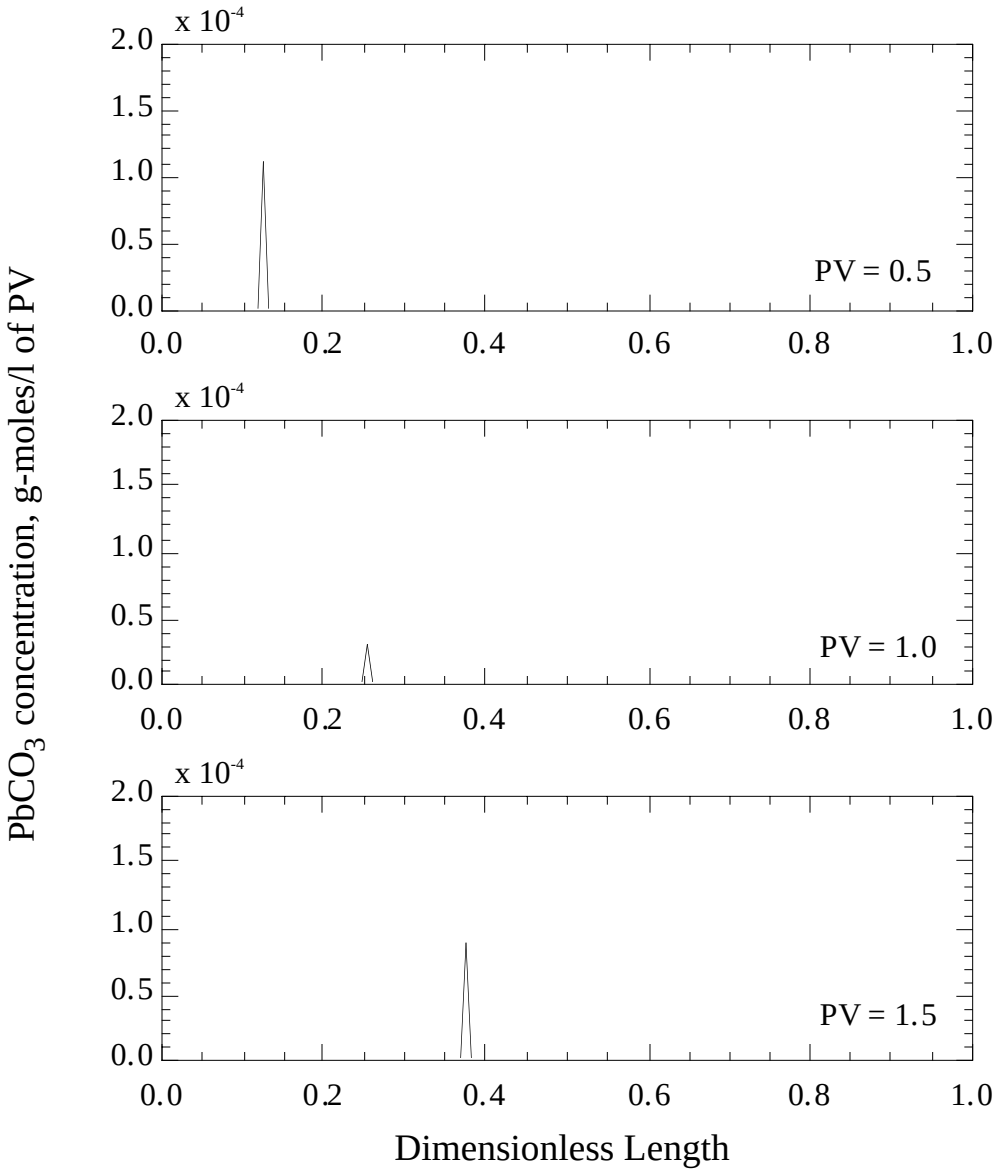

Figure 15.21. $PbCO_3$ concentration distribution at 0.5, 1.0, and 1.5 PV injected.

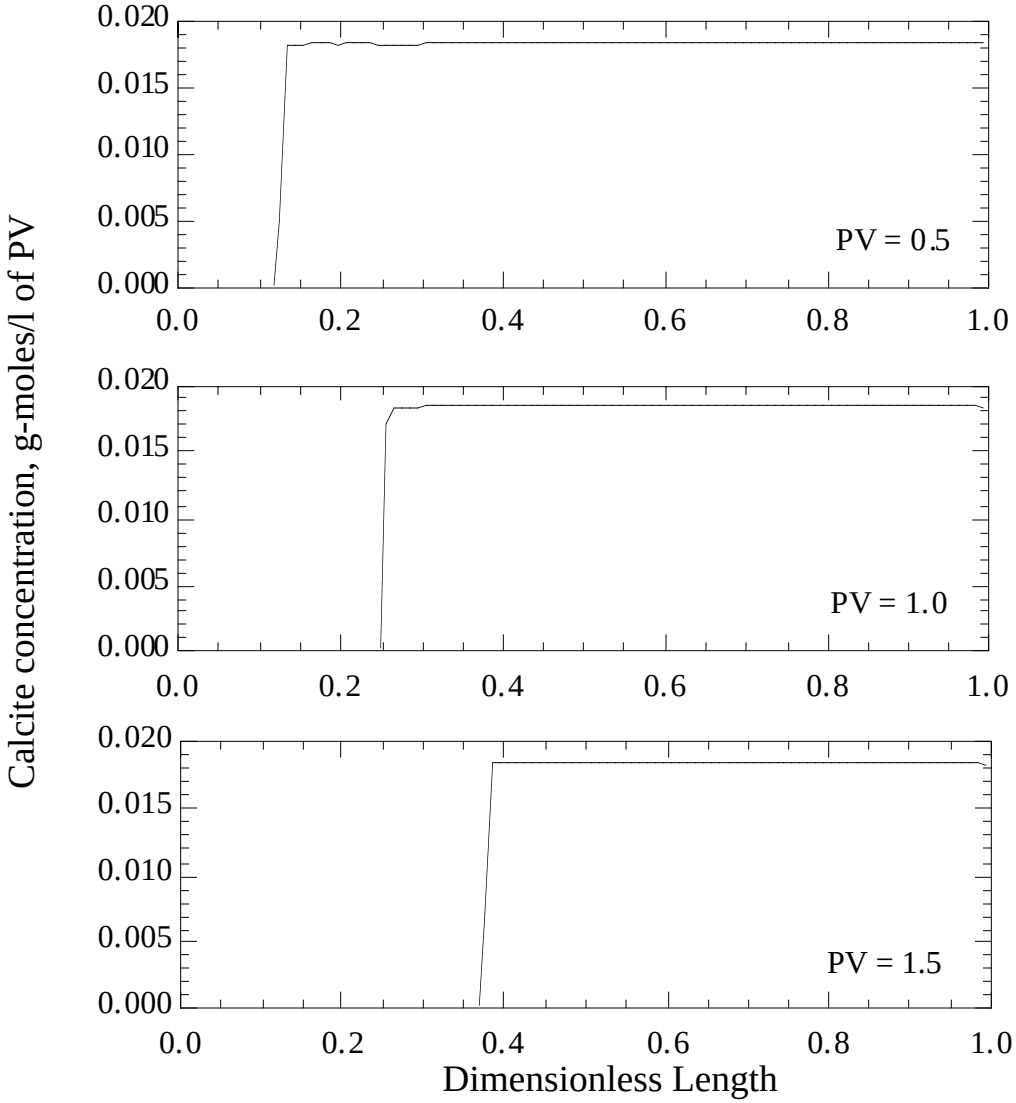

Figure 15.22. Calcite ($CaCO_3$) concentration distribution at 0.5, 1.0, and 1.5 PV injected.

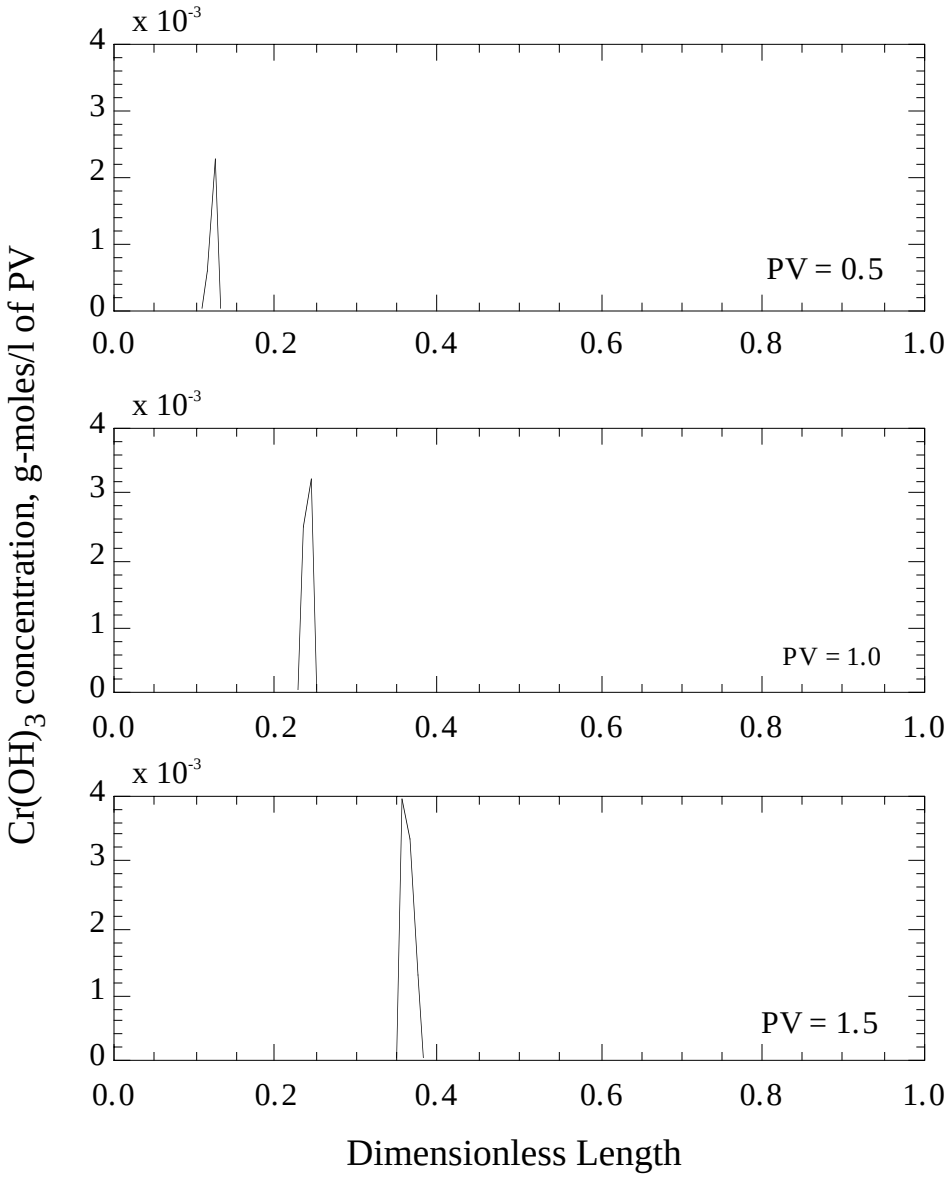

Figure 15.23. $Cr(OH)_3$ concentration distribution at 0.5, 1.0, and 1.5 PV injected.

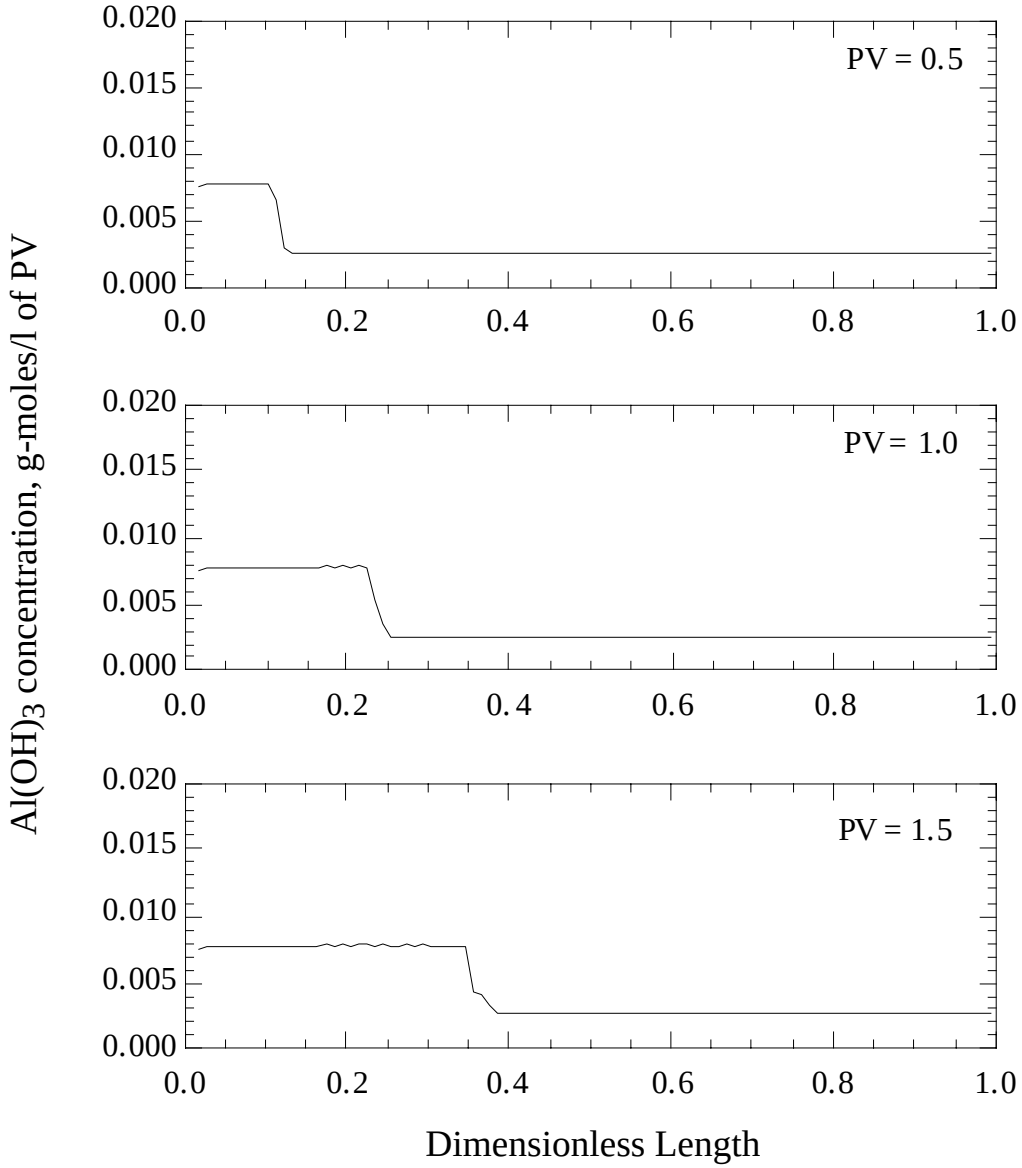

Figure 15.24. $Al(OH)_3$ concentration distribution at 0.5, 1.0, and 1.5 PV injected.

Section 16
Guidelines for Selection of SEAR Parameters

16.1 Introduction

The physics and chemistry of the SEAR process can be quite complicated, and simulation of such processes demands that the user specify more data than are normally required for the simulation of ground water flow for applications such as pump and treat. For example, the presence of surfactant causes multiple phases of liquid to be present, and each has its own flow properties. The viscosity and density of a given phase, properties which affect the fluid flow behavior, are functions of the composition of that phase, the temperature, and the pH. To model all of these phenomena, the surfactant/water/NAPL phase behavior, interfacial tension, viscosity, and density must be known. The fluid property data must have been measured in the laboratory at the temperature and pH conditions of the site. Other critical data that involve the interaction between the surfactant solution and the aquifer soil material include the surfactant adsorption and cation exchange. The usual protocol for surfactant selection followed by many researchers is to measure contaminant solubilization enhancement and interfacial tension. However, microemulsion viscosity and density are equally important properties but only rarely reported in the literature until very recently (Dwarakanath *et al.*, 1999; Kostarelos, 1998; Weerasooriya *et al.*, 1999). Measurement of microemulsion viscosity is critical since low viscosities are required for reasonable flow rates under maximum available hydraulic gradients in most aquifers. The microemulsion density is also important since it has an effect on the vertical migration of a microemulsion plume containing solubilized dense nonaqueous phase liquids. This is especially important in the design of the neutral buoyancy SEAR. We refer the readers to Dwarakanath and Pope (2000) for more details in phase behavior and property measurements.

16.2 Phase Behavior

The most complex property to describe quantitatively is phase behavior because it is influenced by temperature and concentrations of all the species in the system. In UTCHEM, phase behavior parameters define the solubility of the organic contaminant in the microemulsion phase as a function of surfactant, cosolvent, and electrolyte concentrations and temperature using Hand's rule described in Sections 2 and 11. The number of input parameters to define the phase behavior increases with the complexity of the surfactant formulation and conditions. The complexity arises due to the presence of cosolvent, significant temperature variations, NAPL mixtures, and variation in electrolyte concentration because of cation exchange due to possible differences in the electrolyte composition of the injected water and ground water. The phase behavior parameters are calculated based on the volume fraction diagram and the contaminant solubilities measured at different electrolyte and surfactant concentrations at a fixed temperature and pH.

Phase behavior experiments identify surfactants with acceptably high contaminant solubilization, rapid coalescence times, and minimal tendency to form liquid crystals, gels, and emulsions. Volume fraction diagram and ternary diagrams commonly represent the phase behavior. These experiments are described in detail in Dwarakanath and Pope (2000). The volume fraction diagram provides an understanding of the sensitivity of the surfactant solution behavior to additional electrolyte. The volume fraction diagram involves equal volumes of NAPL and surfactant solution to be mixed and allowed to equilibrate. The temperature and concentrations of surfactant, cosolvent, and contaminants are fixed while the concentration for the electrolyte is varied between various samples. Volume fraction diagrams provide information on the electrolyte concentrations at which a transition from Winsor Type I to Type III to Type II is observed. In addition, these diagrams provide information on the solubilization of the contaminants in the microemulsion and the optimum salinity. Ternary phase diagrams represent surfactant phase behavior as a function of varying concentrations of surfactant, contaminant, and water. In these experiments, the electrolyte concentration in the water is fixed and the volume fraction of surfactant, cosolvent, contaminant, and water is varied.

An illustration of a volume fraction diagram is shown in Fig. 16.1 for a mixture of 4 wt.% Alfoterra© 145 $(PO)_4$ sodium ether sulfate, 16 wt.% IPA, and PCE DNAPL and calcium chloride at a temperature of 25 ˚C. From this figure it can be seen that under 0.225 wt.% calcium chloride, the microemulsion and

PCE DNAPL phases coexist, implying Winsor Type I behavior. Above 0.23 wt.% calcium chloride, only the aqueous and microemulsion phases coexist, implying Winsor Type II behavior. Between 0.225% and 0.23% calcium chloride, PCE DNAPL, aqueous and microemulsion phases coexist, implying Winsor Type III behavior. A schematic of change in the phase behavior with the electrolyte concentration is shown in Fig. 16.2.

Volume fraction diagram experiments also provide information on the solubilization of NAPL constituents in microemulsion. The concentration of the NAPL constituents in microemulsion should be measured using a gas chromatograph (GC). The solubility of PCE in water is approximately 240 mg/L. The enhancement in solubilization of PCE by 4 wt.% Alfoterra© 145 $(PO)_4$ sodium ether sulfate over a range of electrolyte concentrations is shown in Fig. 16.3. The solubilization of PCE is observed to increase from approximately 160,000 mg/L at 0.15% calcium chloride to approximately 530,000 mg/L at 0.21% calcium chloride.

16.2.1 Critical Micelle Concentration

Critical micelle concentration (CMC) is the concentration at which a surfactant forms aggregates called micelles. One of the objectives of SEAR is to maintain the surfactant concentration well above the CMC in the target aquifer zones such that the solubilization or mobilization of NAPL is maximized. For a given surfactant this necessitates that either a sufficiently high concentration or alternatively a large slug of surfactant be injected such that the surfactant concentration remains above the CMC after dilution and dispersion in the aquifer. The exact concentration of the injected surfactant and the size of the surfactant slug should be determined after design simulations that quantify dilution and dispersion in the aquifer. The use of a surfactant with a low CMC will lower the mass of surfactant required conversely the use of a surfactant with high CMC will necessitate the injection of a larger mass of surfactant to effect the same level of remediation. It is desirable to use a surfactant with a low CMC as this has the potential to lower costs.

As an illustration, sodium dihexyl sulfosuccinate, which was used in the surfactant flood demonstration at Hill Air Force Base, Utah has a CMC of 0.8 wt.% in fresh water and 0.2 wt.% at optimal salinity. Due to such a high CMC, a higher surfactant concentration is required in the injectate surfactant formulation to overwhelm the effects of dilution and dispersion. Conversely, Alfoterra© I-12-3PO-sulfate, has a CMC on the order 0.01 wt.%. A low CMC also makes the surfactant more amenable to recycling. The important implication of this parameter in UTCHEM is that for surfactant concentration below CMC, there is no solubility enhancement and no interfacial tension reduction and surfactant resides in the water phase and only affects the viscosity and density of the water phase.

16.2.2 Procedure to Obtain Phase Behavior Parameters

As mentioned earlier, the number of input parameters to define the phase behavior increases with the complexity of the surfactant formulation due to the variation in cosolvent concentration, temperature, and electrolyte concentration due to cation exchange. To model all these effects, of course, requires the availability of laboratory data for the model calibration.

Here we give the procedure to match the volume fraction diagram with fixed surfactant and cosolvent concentrations and at a fixed temperature and pH. We use the same volume fraction diagram as Fig. 16.1 measured for 4 wt.% Alfoterra© 145 $(PO)_4$ sodium ether sulfate, 16 wt % IPA, and PCE at a range of calcium chloride concentrations at a temperature of 25 ˚C. The procedure is as follows for each test tube.

1. Calculate Microemulsion Phase Concentrations

$$C_{23} = \frac{\text{volume of dissolved NAPL in microemulsion phase}}{\text{volume of microemulsion phase}}$$

$$C_{33} = \frac{\text{volume of added surfactant in microemulsion phase}}{\text{volume of microemulsion phase}}$$

$$C_{13} = 1 - C_{23} - C_{13}$$

2. Calculate Effective Salinity

The effective salinity is the same as the anion concentration for the special case of fixed cosolvent, fixed temperature, and no cation exchange. The effective salinity as a function of temperature and cosolvent concentration and in the presence of cation exchange is calculated using Eq. 11.26 in Section 11. The lower effective salinity (CSEL7) is the effective salinity at which the transition between Type I and Type III occurs. The upper effective salinity (CSEU7) is the effective salinity at which the transition of Type III to Type II occurs. The lower effective salinity is about 0.225 wt.% and the upper effective salinity is about 0.235 wt.% as shown in Fig. 16.1. Anion and cation concentrations are in meq/ml of water in UTCHEM. Therefore, the commonly used laboratory unit of wt.% should be converted to meq/ml. Please also note that the electrolyte concentrations in the laboratory are commonly expressed in terms of the aqueous phase volume that includes the volume of surfactant and cosolvent in addition to the water. For example, 0.225 wt.% $CaCl_2$ is converted to meq/ml water with 4 vol% surfactant and 19 vol% IPA with the density of 0.84 g/cc in the following manner:

$$\frac{0.225\ \text{g}}{100\ \text{g}} \text{ x } \frac{1\ \text{mole}}{110.99\ \text{g}} \text{ x } \frac{1000\ \text{g}}{1\ \text{liter}} = 0.0203\ \frac{\text{moles } Ca^{++}}{\text{liter of aq. solution}}$$

$$= 0.0406\ \frac{\text{moles } Cl^{-}}{\text{liter of aq. solution}}$$

The calcium concentration in meq/ml of water is

$$0.0203\ \frac{\text{moles } Ca^{++}}{\text{liter of aq. solution}} \times 2 \text{ valence} \times \frac{1}{1 - 0.04 - 0.19} = 0.0527\ \frac{\text{meq } Ca^{++}}{\text{ml of water}}$$

and the chloride concentration in meq/ml of water is

$$0.0406\ \frac{\text{moles } Cl^{-}}{\text{liter of aq. solution}} \times 1 \text{ valence} \times \frac{1}{1 - 0.04 - 0.19} = 0.0527\ \frac{\text{meq } Cl^{-}}{\text{ml of water}}$$

The lower effective salinity (CSEL7) is the same as the anion concentration of 0.0527 meq/ml adjusted for the volume of surfactant and alcohol. Similarly, the upper effective salinity (CSEU7) of 0.235 wt.% is equivalent to 0.055 meq/ml.

3. Calculate Optimum Effective Salinity

$$C_{SEOP} = \frac{CSEL7 + CSEU7}{2} = 0.0539\ \text{meq/ml}$$

4. Calculate Hand's Rule A Parameter

The parameter A is calculated from the binodal curve Eq. 2.28 in Section 2 for microemulsion phase ($\ell = 3$) as

$$\frac{C_{33}}{C_{23}} = A \left(\frac{C_{33}}{C_{13}} \right)^{-1}$$

$$A = \frac{C_{33}^2}{C_{23}\, C_{13}} = \frac{C_{33}^2}{C_{23}\left(1 - C_{33} - C_{23}\right)}$$

5. Plot the Parameter A as a Function of Normalized Effective Salinity

An example of plot of A calculated from the experiments vs. normalized effective salinity is given in Fig. 16.4. The effective salinity calculated for each test tube as in Step 2 is normalized by the optimum salinity obtained in Step 3 as follows:

$$\text{Normalized effective salinity} = \frac{\text{Effective salinity}}{C_{SEOP}}$$

Fit the data with lines as shown in Fig. 16.4. The data are normally sparse with scatter so special cares need to be taken in obtaining the best fit. Next, the values of A at zero (A_0), optimum (A_1), and twice optimum (A_2) salinities are determined. Please note that if the desired phase behavior is that of the Type I (below optimum), then the behavior above the optimum is not important and is irrelevant.

Parameter A for salinities other than those measured can either be read from the best-fit lines or calculated from Eq. 2.31 as

$$A = \left(A_0 - A_1\right)\left(1 - \frac{C_{SE}}{C_{SEOP}}\right) + A_1 \quad \text{for } C_{SE} \le C_{SEOP}$$

$$A = \left(A_2 - A_1\right)\left(\frac{C_{SE}}{C_{SEOP}} - 1\right) + A_1 \quad \text{for } C_{SE} \succ C_{SEOP}$$

For comparison of model with measured data, the Hand Equation (Eq. 2.29 in Section 2) for surfactant concentration in microemulsion phase (C_{33}) is solved by varying the contaminant concentration in the microemulsion phase (C_{23}) between 0 and 1.

$$C_{33} = -\frac{1}{2}AC_{23} + \frac{1}{2}\sqrt{\left(AC_{23}\right)^2 + 4A\left(C_{23} - C_{23}^2\right)}$$

6. Calculate Height of Binodal Curve

The phase behavior calculation in UTCHEM requires the height of binodal curve at three different effective salinities, namely: zero, optimum, and twice optimum. Hand's rule parameters A calculated in Steps 4 and 5 are related to the height of binodal curve by rearranging Eq. 2.30a in Section 2 as

$$C_{3\max,0} = \frac{\sqrt{A_0}}{2 + \sqrt{A_0}} \equiv \text{HBNC70}$$

$$C_{3\max,1} = \frac{\sqrt{A_1}}{2 + \sqrt{A_1}} \equiv \text{HBNC71}$$

$$C_{3\max,2} = \frac{\sqrt{A_2}}{2 + \sqrt{A_2}} \equiv \text{HBNC72}$$

In summary, the UTCHEM input parameters for the case of fixed alcohol concentration and fixed ratio of Ca to Na concentration (no cation exchange) and fixed temperature are given in Table 16.1. The phase behavior parameters that were matched against the volume fraction diagram and corresponding PCE solubility data shown in Figs. 16.1 and 16.3 are also provided in Table 16.1. Fig. 16.5 compares the measured PCE solubility data and the model calculations. The plait point parameters (C_{2PR} and C_{2PL}) in principle can be determined from a detailed phase composition analysis of two-phase samples close to the plait points. In practice, however, this is very difficult and plait points are usually assumed to be in the corners.

16.2.3 Effect of cosolvent

For a more general case where cosolvent concentration varies, additional phase behavior data are required to obtain the model parameters. Cosolvent is normally added to the surfactant formulation to minimize the occurrence of gels/liquid crystals/emulsions, lower the equilibration times, and reduce the viscosity of the contaminant-rich microemulsion. For example, Fig. 16.6 shows that the optimum salinity for a mixture of 8 wt.% sodium dihexyl sulfosuccinate decreases from 1.25 wt.% NaCl to 0.5 wt.% NaCl by addition of 20 wt.% IPA (Dwarakanath and Pope, 2000). In general surfactant is more effective without added cosolvent except for the need to reduce the viscosity and equilibration times. These and other experimental data suggest that the optimal salinity varies linearly with cosolvent concentration. The optimal salinity in terms of the anion concentration in the aqueous phase is then expressed as

$$C_{51,\,opt} = C^{*}_{51,\,opt}\left(1+\beta_7 f_7^s\right)$$

where C^{*}_{51} is the optimum anion concentration in the absence of cosolvent. The parameter β_7 can be estimated from the slope of the straight line of normalized optimum salinity ($C_{51,opt}/C^{*}_{51,opt}$) versus f_7^s. f_7^s is defined as the ratio of the volume of cosolvent associated with surfactant to total volume of surfactant and is estimated as

$$f_7^s = \frac{1}{1+\left(C_{73}\right)^{-1}}$$

The definition of effective salinity in the presence of alcohol is then given by Eq. 11.24 in Section 11 as

$$C_{SE} = \frac{C_{51}}{\left(1+\beta_7 f_7^s\right)}$$

Therefore the additional model input due to the presence of cosolvent include

- Cosolvent partitioning data for water/surfactant and water/contaminant (for example OPSK7O and OPSK7S of the Hirasaki's model of IALC = 0). Refer to Eqs. 11.4 and 11.5 in Section 11.
- Effect of cosolvent on the effective salinity (BETA7) in Eq. 11.24 in Section 11.
- Effect of alcohol on contaminant solubility (HBNS70, HBNS71, HBNS72) in Eq. 11.30 in Section 11.

Kostaleros (1998) performed experiments specifically designed to measure the IPA partition coefficients. The partitioning of IPA with micelle was measured in a three-phase sample (Type III) by mixing 4 cc of TCE and 4 cc of surfactant solution containing 4 wt.% sodium dihexyl sulfosuccinate (on active basis) and 8 wt.% IPA at an optimum salinity of 9400 mg/L NaCl. After the sample came to equilibrium, a sample from each phase was analyzed for IPA concentration. IPA and DNAPL concentrations were measured by

gas chromatography. The volume fraction of IPA in excess TCE DNAPL, excess water, and microemulsion phases were 0.015, 0.093, and 0.046 respectively.

The partitioning coefficient of alcohol to TCE was computed as the ratio of volume fraction of IPA in excess TCE phase to that in the excess water phase as

$$K_7^2 = \frac{\text{Conc. of IPA in excess DNAPL}}{\text{Conc. of IPA in excess water}}$$

With this data and a mass balance of total IPA, the partitioning coefficient of IPA to surfactant micelle (K_7^3) is computed which is the ratio of volume fraction of IPA in surfactant to that in the excess water. The mass balance can be written in terms of the total IPA as

$$V_7 = K_7^2\, C_{71} V_2 + C_{71}\, V_1 + K_7^3\, C_{71}\, V_3$$

where

C_{71} = concentration of IPA in excess water

V_1 = Volume of excess water

V_2 = Volume of excess oil

V_3 = Volume of surfactant

V_7 = Volume of IPA

To obtain the effect of cosolvent on the shift in optimum salinity (β_7), volume fraction diagram needs to be measured for at least two different cosolvent concentrations. The effect of IPA concentration on the optimum salinity of a mixture of 8 wt.% sodium dihexyl sulfosuccinate, Hill DNAPL is demonstrated in Fig. 16.6. Figure 16.7 shows the effect of alcohol on the solubilization parameters at the optimum salinity.

In order to obtain the phase behavior parameters for cosolvent namely HBNS70, HBNS71, and HBNS72, and BETA7, we normally perform batch-calculations with UTCHEM and vary the phase behavior input parameters until a satisfactory match of UTCHEM output data of microemulsion phase concentrations and the measured data is obtained. Each batch run corresponds to one test tube of the phase behavior experiment at a fixed electrolyte concentration. A sample batch input is included in the UTCHEM distribution CD-ROM. Example input parameters for a mixture of sodium dihexyl sulfosuccinate, IPA, Hill AFB DNAPL, and sodium chloride is given in Table 16.2.

Please note that if the alcohol is modeled as a separate component in UTCHEM, the lower and upper effective salinities should be based on experiments with zero cosolvent since the input parameter (BETA7) will be used to shift the optimum salinity.

16.2.4 Cation Exchange and Effect of Calcium

The phase behavior of surfactant formulations with anionic surfactants is strongly affected by electrolyte composition. A difference in electrolyte concentration between the injected water and the resident water can cause ion exchange with the clays and hence an increase in the electrolyte concentration. For example if the source water injected during the SEAR contains a small amount of sodium, the calcium concentration can be increased due to the exchange of Na^+ and Ca^{++} through ion exchange with Ca-rich clays. The total divalent ions (total of calcium and magnesium) is referred here to as "calcium". Additional ion exchange can occur in the surfactant because anionic surfactant forms negatively charged micelles to which sodium and calcium ions associate in a manner similar to the surface of clay. The increase in calcium concentration

of the aqueous solution can cause an unfavorable shift in phase behavior that may not be accounted for during the SEAR design if the ion exchange is significant and is not modeled appropriately. The ion exchange model in UTCHEM allows for calculations of ions that may be free in solution, adsorbed on the soil, and associated with surfactant. Refer to Eqs. 2-19 through 2-26 in Section 2. Any increased calcium concentration picked up by surfactant due to the ion exchange is accounted for in the electrolyte concentration calculations. Consequently, this will affect the phase behavior and ultimately the SEAR performance. Hence, carefully designed soil column experiments with representative aquifer material should be conducted to determine both the cation exchange capacity of the clays as well as to determine the potential for mobilization and migration of fines. Table 16.3 gives the cation exchange parameters for the UTCHEM model. Example input values were determined by Hirasaki (Intera, 1997) for the AATDF surfactant/foam demonstration at Hill AFB.

The effect of calcium concentration on the phase behavior is taken into account by the shift in the optimum salinity similar to that of the cosolvent. Optimum salinity decreases linearly with the fraction of calcium bound to micelles (f_6^s). The optimum salinity is calculated from

$$C_{51,\,opt} = C^*_{51,\,opt}\left(1 - \beta_6 f_6^s\right)$$

where f_6^s is estimated based on the ion exchange measurements with surfactant.

16.2.5 Effect of Temperature

As stated above, the solubility of contaminant and surfactant phase behavior is a strong function of temperature. If the surfactant solubility in water decreases with a decrease in temperature, which is typical of sulfonates, then less electrolyte is needed to achieve equal affinity of the surfactant for the water and the NAPL, thereby reducing the optimum salinity. Low temperatures also tend to result in slower equilibration and more problems with viscous phases. Bourrel and Schechter (1988) have shown that optimum salinity increases linearly with increase in temperature for most anionic surfactants. The phase behavior measurements with Hill OU2 DNAPL and sodium dihexyl sulfosuccinate show an increase in optimum salinity as the temperature is increased from the groundwater value of 12 ˚C as shown in Fig. 16.8. These results emphasis the importance of phase behavior measurements at the representative groundwater temperatures.

16.3 Microemulsion Viscosity

The viscosity of the injected surfactant solution and the microemulsion is one of the primary factors in the surfactant selection study since it influences the injectivity, especially in low permeability or shallow aquifers. Surfactants are highly prone to forming viscous macroemulsions, gels and liquid crystals, under different conditions. A very viscous surfactant and microemulsion will be difficult to pump through shallow aquifers as doing so will require high-induced gradients, and will result in unacceptably slow flow rates and long remediation times. Therefore, both the measurement and accurate modeling of microemulsion viscosity are critical. In general the viscosity of the aqueous surfactant solution and microemulsion should be as close as possible to the viscosity of water and exhibit Newtonian behavior under ambient aquifer conditions.

The viscosity of the microemulsion generally increases with an increasing fraction of solubilized NAPL components. As the viscosity of the solution injected into the subsurface increases, a higher hydraulic gradient is required to sustain the same flow. As such, the benefit of the maximum hydraulic gradient, which can be, sustained between injection and extraction wells decreases as the viscosity of the fluids being moved through the subsurface increases. The viscosity of surfactant solution is also temperature dependent and at low groundwater temperatures a higher viscosity is expected and should be factored into the overall surfactant selection process. Therefore, the laboratory measurements should be performed at the representative groundwater temperature.

Since variation in DNAPL solubilization can have such a dramatic impact on the viscosity of the microemulsion, the numerical simulator used to design the surfactant flood should calculate viscosity

based on composition. In UTCHEM, the viscosity of each phase is modeled in terms of the water and contaminant viscosities and the phase concentration of the water, surfactant, and contaminant in each phase. The measured microemulsion viscosity is generally used to calibrate the microemulsion phase viscosity correlation.

An example comparison of the calculated and measured microemulsion viscosity is given in Fig. 16.9. The microemulsion is a mixture of 4 wt.% Alfoterra© 145 $(PO)_4$ sodium ether sulfate, 16 wt.% IPA, 0.2 wt.% calcium chloride, at varying fractions of solubilized PCE. As points of comparison, the viscosity of the surfactant solution with no DNAPL present is 2.4 cp and the viscosity of PCE-DNAPL is 0.89 cp. The microemulsion viscosity is increased as more contaminant is dissolved. The viscosity of a microemulsion containing 0.19 vol% dissolved DNAPL is about 3 cp.

The viscosity experiments involve different volumes of DNAPL in the range of 0 to 50 % added to an aqueous surfactant solution with a fixed surfactant, alcohol, and electrolyte concentration. Once the samples are equilibrated, a sample of microemulsion phase from each test tube is analyzed for viscosity at different shear rates using an ultra-low shear viscometer.

The microemulsion viscosity is calculated using Eq. 2.77 in Section 2 for phase ℓ =3 as

$$\mu_3 = C_{13}\,\mu_w\, e^{\left[\alpha_1(C_{23}+C_{33})\right]} + C_{23}\,\mu_o\, e^{\left[\alpha_2(C_{13}+C_{33})\right]} + C_{33}\,\alpha_3\, e^{\left[\alpha_4 C_{13}+\alpha_5 C_{33}\right]}$$

where μ_w and μ_o are the water and DNAPL viscosities. The five alpha parameters are adjusted until a satisfactory fit of the measured viscosity and the model is obtained as demonstrated in Fig. 16.9. The microemulsion phase concentrations (C13, C23, C33) are known for each test tube. Table 16.4 gives the list of viscosity model parameters.

The addition of a cosolvent can reduce the viscosity of the microemulsion formed. The concentration of cosolvent should be optimized such that the viscosity of the microemulsion is as low as possible. Fig. 16.10 illustrates the effect of the addition of cosolvent on microemulsion viscosity. In this figure a microemulsion containing 8 wt.% sodium dihexyl sulfosuccinate, 4 wt.% IPA and 163,000 mg/L dissolved Hill AFB-DNAPL constituents has a viscosity of approximately 8 cp. A similar solution with 8 wt.% IPA and 152,000 mg/L dissolved DNAPL constituents has a lower viscosity of approximately 5.2 cp. The lower viscosity is a result of the additional alcohol cosolvent in the microemulsion. The optimal cosolvent concentration should be such that acceptably low microemulsion and surfactant viscosities are achieved in the subsurface.

As mentioned earlier, the addition of cosolvent will affect the phase behavior of the surfactant, e.g., parameters such as the extent of contaminant solubilization and the optimum salinity. If cosolvent is to be used in the surfactant formulation, the phase behavior experiments conducted must include cosolvent.

16.4 Surfactant Adsorption

Surfactant sorption by mineral surfaces can cause substantial loss of surfactant and reduce its performance. In addition to surfactant losses, sorption can also reduce the permeability of the aquifer material. Nonionic surfactants are more likely to be sorbed by mineral surfaces due to the presence of polar groups in the surfactant molecule that may attach to polar groups on mineral surfaces. Anionic surfactants typically exhibit low sorption in the presence of aquifer material and are preferred (Pope and Baviere, 1991). This is because the negatively charged head of the surfactant is repelled by the net negative charge of silica and other typical minerals that make up alluvium aquifers at typical values of groundwater pH. The commonly used anionic surfactants for SEAR include alcohol ether sulfates, alkane sulfonates, and sulfosuccinates, all of which, typically exhibit low adsorption. The tendency of surfactants to sorb to the aquifer solids is evaluated in soil column tests. The sorption experiments should preferably be conducted in uncontaminated soil. A conservative non-sorbing tracer such as IPA or tritium should be used as a conservative tracer. Surfactant adsorption is modeled with a Langmuir isotherm that takes into account both the surfactant and electrolyte concentrations. Fig. 16.11 is an example of the measured adsorption data for sodium dioctyle sulfosuccinate surfactant at the Canadian River Alluvium (Shiau *et al*, 1995).

Also shown is the Langmuir isotherm fitted to these data. The procedure to fit the measured surfactant adsorption data to obtain the UTCHEM input parameters are given as follows.

The Langmuir adsorption isotherm has the form, as given in Eq. 2.14 in Section 2, of:

$$\hat{C}_3^* = \frac{a_3\left(\tilde{C}_3 - \hat{C}_3^*\right)}{1 + b_3\left(\tilde{C}_3 - \hat{C}_3^*\right)}$$

$$\hat{C}_3 = C_1 \hat{C}_3^*$$

where

a_3 = Langmuir fitting parameter, dimensionless

b_3 = Langmuir fitting parameter, vol. of water/vol. of surfactant

C_1 = Water concentration, volume of water/pore volume

$\hat{C}_3$ = Adsorbed surfactant concentration, volume of surfactant/pore volume

$\hat{C}_3^*$ = Adsorbed surfactant concentration, volume of surfactant/volume of water

$\tilde{C}_3 - \hat{C}_3$ = Concentration of surfactant in water, volume of surfactant/volume of water

The ratio of two Langmuir parameters, (a_3/ b_3), determines the horizontal asymptote and the parameter b_3 determines the steepness of the isotherm. Measured surfactant adsorption data are expressed in several different units. The adsorption data given in Fig 16.11 is, for example, in the unit of μmol/g of adsorbed and mmol/L of surfactant concentrations. The reported surfactant concentrations are converted to the UTCHEM unit using a density of 1.10 g/cc and molecular weight of 445 for sodium dioctyle sulfosuccinate surfactant.

$$\tilde{C}_3 - \hat{C}_3\left[\frac{\text{vol. of surfactant}}{\text{vol. of water}}\right] = C_3^{lab}\left[\frac{\text{mmol}}{\text{L}}\right]\left(\frac{\text{MW}}{\text{density}}\right)_{\text{surf.}}$$

Adsorption in volume of surfactant/pore volume is:

$$\hat{C}_3\left[\frac{\text{vol. of adsorbed surf.}}{\text{pore volume}}\right] = \hat{C}_3^{lab}\left[\frac{\mu\text{mole surf.}}{\text{g soil}}\right] \times \text{MW} \times \frac{\rho_r}{\rho_s} \times \frac{1-\phi}{\phi}$$

where for this specific example with the porosity of 0.35 and grain soil density of 2.65 g/cc and the surfactant solution density of 1.10 g/cc, we have

$$\hat{C}_3\left[\frac{\text{cc surf.}}{\text{cc pv}}\right] = \hat{C}_3^{lab}\left[\frac{\mu\text{mole surf.}}{\text{g soil}}\right]\left[\frac{1\text{ mole}}{10^6\mu\text{mole}}\right]\left[\frac{445\text{ g}}{\text{mole}}\right]\left[\frac{1\text{ cc of surf.}}{1.10\text{ g}}\right]\left[\frac{2.65\text{ g soil}}{1\text{ ml of soil}}\right]\left[\frac{1-0.35}{0.35}\right]$$

Assuming no dependency on the salinity (a_{32} = 0.0), the UTCHEM adsorption parameters fitted to the data were found to be a_3 = 12 and b_3 = 1000.

The parameter a_3 can also be adjusted based on salinity and permeability using Eq. 2.15 in Section 2 as follows:

$$a_3 = \left(a_{31} + a_{32} C_{SE}\right)\left(\frac{k}{k_{ref}}\right)^{0.5}$$

Table 16.5 gives the UTCHEM surfactant adsorption input parameters.

16.5 Interfacial Tension

Interfacial tensions (IFTs) depend on the types and concentration of surfactant, cosolvent, electrolyte, contaminant, and temperature. IFTs have been directly correlated with surfactant phase behavior. The published correlations relate the microemulsion/NAPL IFT to the volume fraction of contaminant and surfactant in the microemulsion phase (Lake, 1989; Huh, 1979; Healy and Reed, 1974). IFT measurements are relatively difficult to perform therefore the phase behavior data and a few IFT measurements are all needed to calibrate the IFT correlation for a specific surfactant formulation. IFTs can be measured using a spinning drop tensiometer (Cayais *et al.*, 1975). Model calibration of the DNAPL/microemulsion IFT is critical in SEAR simulation for the assessment of the DNAPL mobilization. Examples of measured and model calculations of IFT using Chun Huh's (IFT = 1) model are shown in Fig. 16.12. Chun Huh (1979) proposed that the interfacial tension and solubility are intrinsically related by the following function.

$$\sigma_{23} = \frac{c}{R_{23}^2}$$

where the contaminant solubilization parameter is defined as

$$R_{23} = \frac{C_{23}}{C_{33}} \equiv \frac{V_o}{V_S}$$

The solubilization ratio (V_o/V_S) is the ratio of volume of contaminant solubilized in the microemulsion phase to the volume of surfactant in the microemulsion phase.

In UTCHEM, we introduced Hirasaki's correction factor and modified Huh's correlation so the IFT reduces to water-oil interfacial tension as the surfactant concentration approaches to zero. For example, Eq. 2.47 in Section 2 can be written for interfacial tension between NAPL and microemulsion as follows.

$$\sigma_{23} = \sigma_{ow} \exp\left(-aR_{23}\right) + \frac{cF_2}{R_{23}^2}\left(1 - \exp\left(-aR_{23}^3\right)\right)$$

where σ_{ow} is the water/DNAPL interfacial tension and the correction factor F_2 is defined as:

$$F_2 = \frac{1 - \exp\left(-\sqrt{\left(C_{12} - C_{13}\right)^2 + \left(C_{22} - C_{23}\right)^2 + \left(C_{32} - C_{33}\right)^2}\right)}{1 - \exp\left(-\sqrt{2}\right)}$$

There are only two calibration parameters in Huh's model namely, c and a. These parameters are adjusted until a satisfactory match of the measured IFT and model calculations are obtained. In order to obtain the calculated IFT curve for a wide range of solubilization ratio, the microemulsion phase concentrations obtained from matching the phase behavior measurements is used for the IFT calculations. Please refer to Brown (1993) for more details on the phase behavior and the IFT model parameters. For either a Type III or Type II phase behavior, the IFT between microemulsion and water is calculated using the solubilization ratio,

$$R_{31} = \left(\frac{V_w}{V_S} \right)$$

and the correction factor F_1 (Eqs. 2.44 and 2.45 in Section 2 for ℓ =1).

Table 16.6 gives the Chun Huh's IFT model parameters with example input parameters based on the data given in Fig. 16.12.

16.6 Microemulsion Density

The accurate modeling of the microemulsion density is critical due to the risk of vertical migration of contaminant solubilized in the denser than water microemulsion phase in aquifers with insufficient capillary barriers such as clay or shale. UTCHEM continually calculates the microemulsion density as a function of the concentration of each component as the flood progresses.

DNAPLs can be removed from aquifers with no capillary barrier using the SEAR at neutral buoyancy (Shook *et al*., 1998; Kostarelos *et al.*, 1998). The concept is to add sufficient amounts of light alcohols, i.e., alcohols with density less than water, to reduce the density of the microemulsion to make it neutrally buoyant with respect to the ground water. This will remediate the site while controlling the spreading of the contaminants downward into the uncontaminated ground water. However, the use of a neutrally buoyant surfactant solution presents another challenge, and that is that it will tend to float when no DNAPL is contacted; thus it is still important in all cases to calculate the microemulsion density.

The density of each phase is calculated as a function of its composition and is adjusted for fluid compressibility. For example, the microemulsion phase density (ρ_3) or specific weight ($g\,\rho_3$) is calculated as a function of the concentration of each component in the microemulsion phase using Eq. 2.48 in Section 2 as follows.

$$\gamma_3 = C_{13}\,\gamma_{13} + C_{23}\,\gamma_{23} + C_{33}\,\gamma_{33} + 0.02533\,C_{53} - 0.001299\,C_{63} + C_{73}\,\gamma_{73}$$

where

$$\gamma_{13} = \gamma_{1R}\left[1 + C_1^0\left(P_3 - P_{R0}\right)\right]$$

$$\gamma_{23} = \gamma_{23R}\left[1 + C_2^0\left(P_3 - P_{R0}\right)\right]$$

$$\gamma_{33} = \gamma_{3R}\left[1 + C_3^0\left(P_3 - P_{R0}\right)\right]$$

$$\gamma_{73} = \gamma_{7R}\left[1 + C_7^0\left(P_3 - P_{R0}\right)\right]$$

The apparent density of each component ($\gamma_{\kappa R}$) is estimated based on the best fit to the measured microemulsion density data. An example of microemulsion density as a function of alcohol and TCE concentrations is given in Fig. 16.13 (Kostarelos *et al.*, 1998). The solution is a 4 wt.% active sodium dihexyl sulfosuccinate, 0.6 wt.% sodium chloride, with alcohol concentrations (ethanol or IPA) ranging from 0 to 8 wt.%, and TCE concentrations ranging from 0 to 6 wt.%, and water. The apparent density of TCE in the microemulsion is about 1.32 g/cc compared to the pure TCE density of 1.46 g/cc.

Table 16.7 gives the phase density model parameters with example input parameters based on the data given in Fig. 16.13.

16.7 Trapping Number

Surfactants have the potential for both mobilizing as well as solubilizing NAPL therefore, we can design either a mobilization or solubilization surfactant flood by adjusting the trapping number (Jin, 1995; Pennell

et al., 1996; Delshad *et al*., 1996). Please refer to Eq. 2.72c in Section 2 for the mathematical definition of trapping number. A lower trapping number is achieved by using a surfactant with relatively low contaminant solubilization and lower interfacial tension reduction. Conversely a higher trapping number is achieved by using a surfactant with ultra-low interfacial tensions and ultra-high contaminant solubilization.

The capillary desaturation curve is the relationship between residual saturation of a nonaqueous or aqueous phase and a local capillary number (or a more general definition of trapping number). The trapping number is a dimensionless ratio of the viscous and gravitational forces to the capillary forces. At low trapping number, residual saturations are roughly constant. At some trapping number designated, as the critical trapping number, the residual saturations begin to decrease. The capillary desaturation curves define the mobilization for each phase as the trapping number is increased primarily because of the reduced interfacial tension.

The most critical capillary desaturation curve in the SEAR design simulations is that of the DNAPL since it defines the degree of DNAPL mobilization or free-phase recovery during the surfactant test. Reduction in interfacial tension due to the injected surfactant or even small changes in hydraulic gradient can cause DNAPL to migrate vertically. If a strong capillary barrier such as a competent clay exists beneath the targeted zone of contamination, vertical mobilization may not be an issue or concern. On the other hand, for the case of aquifers with insufficient or no capillary barrier, the risk of vertical DNAPL migration must be accurately assessed. Vertical DNAPL mobilization can however be minimized by engineering the surfactant solution appropriately, as with the application of SEAR neutral buoyancy or otherwise avoiding the creation of ultra-low IFTs in the subsurface.

Examples of capillary desaturation curves for DNAPLs measured by Dwarakanath (1997) and Pennell *et al*. (1996) are given in Fig. 16.14. Both sets of data were fit to the model as shown in Fig. 16.14. The model calibration parameters for the DNAPL are T_{22}, S_{2r}^{low}, and S_{2r}^{high} as given in Table 16.8. These parameters are obtained by the fit of normalized residual NAPL as a function of trapping number to the following equation as follows:

$$\frac{S_{2r} - S_{2r}^{high}}{S_{2r}^{low} - S_{2r}^{high}} = \frac{1}{1 + T_2 N_{T2}}$$

An example of the capillary desaturation curves for water and microemulsion phases are given in Fig. 16.15. The model parameters for these curves are given in Table 16.8. The trapping parameters for water and microemulsion phases are based on the fit of the model to the published data of Delshad (1990) for mixtures of petroleum sulfonate, decane, and sodium chloride in Berea sandstone.

16.8 Physical Dispersion

Heterogeneity and dispersion both cause mixing in an aquifer and the appropriate longitudinal and transverse dispersivities depend on how the heterogeneities are modeled. When a stochastic heterogeneity field is used with a fine grid, dispersion is not very important since heterogeneity dominates. When homogeneous layers and a coarse grid are used, large effective dispersivities are appropriate. Both molecular diffusions and dispersivities are modeled in UTCHEM. The longitudinal dispersivities can be estimated by the calibration of simulation results against the conservative interwell tracer test (CITT) field data.

Example values of dispersivities used in the SEAR simulations discussed in Section 15 are given in Table 16.9.

16.9 Tables and Figures

Table 16.1. Phase Behavior Parameters

Phase Behavior Parameter	Equation Symbol	UTCHEM Parameter	Parameter Value*
Maximum height of binodal curve at zero salinity	$C_{3max,0}$	HBNC70	0.07
Maximum height of binodal curve at optimum salinity	$C_{3max,1}$	HBNC71	0.04
Maximum height of binodal curve at twice optimum salinity	$C_{3max,2}$	HBNC72	0.171
Lower effective salinity where Type II begins, meq/ml water	CSEL	CSEL	0.0527
Upper effective salinity where Type III ends, meq/ml water	CSEU	CSEU	0.055
Oil concentration at the plait points of the Type I region (right hand side), vol. fraction	C_{2PR}	C2PRC	1
Oil concentration at the plait points of the Type II region (left hand side), vol. fraction	C_{2PL}	C2PLC	0
Critical micelles concentration, vol. fraction	CMC	EPSME	10^{-4}

*4 wt.% Alfoterra© 145 $(PO)_4$ sodium ether sulfate, 16 wt.% IPA, and PCE DNAPL at a range of calcium chloride concentrations at a temperature of 25 ˚C

Table 16.2. Phase Behavior Parameters to Account for Cosolvent

Phase Behavior Parameter	Equation Symbol	UTCHEM Parameter	Parameter Value*
Slope at zero salinity	$m_{7,0}$	HBNS70	0.1
Slope at optimum salinity	$m_{7,1}$	HBNS71	0.15
Slope at twice optimum salinity	$m_{7,2}$	HBNS72	0.3
Effect of cosolvent on effective salinity	β_7	BETA7	-2.08
Partitioning between water/surfactant (IALC=0)	K_7^2	OPSK7S	0.162
Partitioning between water/contaminant (IALC=0)	K_7^3	OPSK7O	2.62

* Mixture of 8 wt.% sodium dihexyl sulfosuccinate, 4 wt.% IPA

Table 16.3. Cation Exchange Parameters

Parameter	Equation Symbol	UTCHEM Parameter	Parameter Value
Cation exchange capacity, meq/ml pore volume	Q_v	QV	0.06
Exchange coefficient with clay, $(meq/ml)^{-1}$	β^c	XKC	0.4
Exchange coefficient with surfactant, $(meq/ml)^{-1}$	β^s	XKS	0.45
Equivalent weight of surfactant	M_3	EQW	388

Table 16.4. Microemulsion Viscosity Parameters

Parameter	Equation Symbol	UTCHEM Parameter	Parameter Value
Water viscosity, cp	μ_w	VIS1	1
Contaminant viscosity, cp	μ_o	VIS2	0.89
Alpha parameters	α_1 α_2 α_3 α_4 α_5	ALPHAV(1) ALPHAV(2) ALPHAV(3) ALPHAV(4) ALPHAV(5)	1 3.6 0.708 5 0.0

Table 16.5. Surfactant Adsorption Model Parameters

Parameter	Equation Symbol	UTCHEM Parameter	Parameter Value*
Surfactant adsorption parameter, dimensionless	a_{31}	AD31	12
Surfactant adsorption parameter, $(meq/ml)^{-1}$	a_{32}	AD32	0.0
Surfactant adsorption parameter, dimensionless	b_3	B3D	1000
Reference permeability, md	k_{ref}	REFK	N/A
Effective salinity, meq/ml	C_{se}	CSE	0.0

* Based on measured data by Shiau *et al*. (1994)

Table 16.6. Interfacial Tension Model Parameters

Parameter	Equation Symbol	UTCHEM Parameter	Parameter Value
Log_{10} water/NAPL IFT, dyne/cm	σ_{ow}	XIFTW	0.68
IFT Model	N/A	IFT	1
Chun Huh constant, c	c	CHUH	0.22
Chun Huh constant, a	a	AHUH	9

Table 16.7. Phase Density Model Parameters

Parameter	Equation Symbol	UTCHEM Parameter	Parameter Value
Water specific weight*, psi/ft	γ_{1R}	DEN1	0.433
NAPL specific weight, psi/ft	γ_{2R}	DEN2	0.632
Constant for contaminant in microemulsion phase, psi/ft	γ_{23R}	DEN23	0.571
Surfactant specific weight, psi/ft	γ_{3R}	DEN3	0.433
Cosolvent IPA specific weight, psi/ft	γ_{7R}	DEN7	0.3637

* Please note that water density of 1g/cc ≡ 0.433 psi/ft

Table 16.8. Trapping Model Parameters

Parameter	Equation Symbol	UTCHEM Parameter	Parameter Value
Trapping parameter for water	T_1	T11	1865
Trapping parameter for DNAPL	T_-	T22	6000
Trapping parameter for microemulsion	T_3	T33	365
Residual saturations at high trapping number for all three phases	S_{1r}^{high} S_{2r}^{high} S_{3r}^{high}	S1RC S2RC S3RC	0.0 0.0 0.0
DNAPL residual saturation at low trapping numbers: Dwarakanath (1997) Pennell *et al*. (1996)	S_{2r}^{low}	S3RW	 0.15 0.11

Table 16.9. Physical Dispersion Parameters

Parameter	Equation Symbol	UTCHEM Parameter	Parameter Value[1]	Parameter Value[2]
Water phase:				
Longitudinal dispersivity, ft	α_{L1}	ALPHAL(1)	0.05	0.01
Transverse dispersivity, ft	α_{T1}	ALPHAT(1)	0.0	0.0
NAPL phase:				
Longitudinal dispersivity, ft	α_{L2}	ALPHAL(2)	0.05	0.01
Transverse dispersivity, ft	α_{T2}	ALPHAT(2)	0.0	0.0
Microemulsion phase:				
Longitudinal dispersivity, ft	α_{L3}	ALPHAL(3)	0.05	0.01
Transverse dispersivity, ft	α_{T3}	ALPHAT(3)	0.0	0.0

[1] Used in SEAR simulation of Camp Lejeune site

[2] Used in SEAR simulation of Hill AFB OU2 site

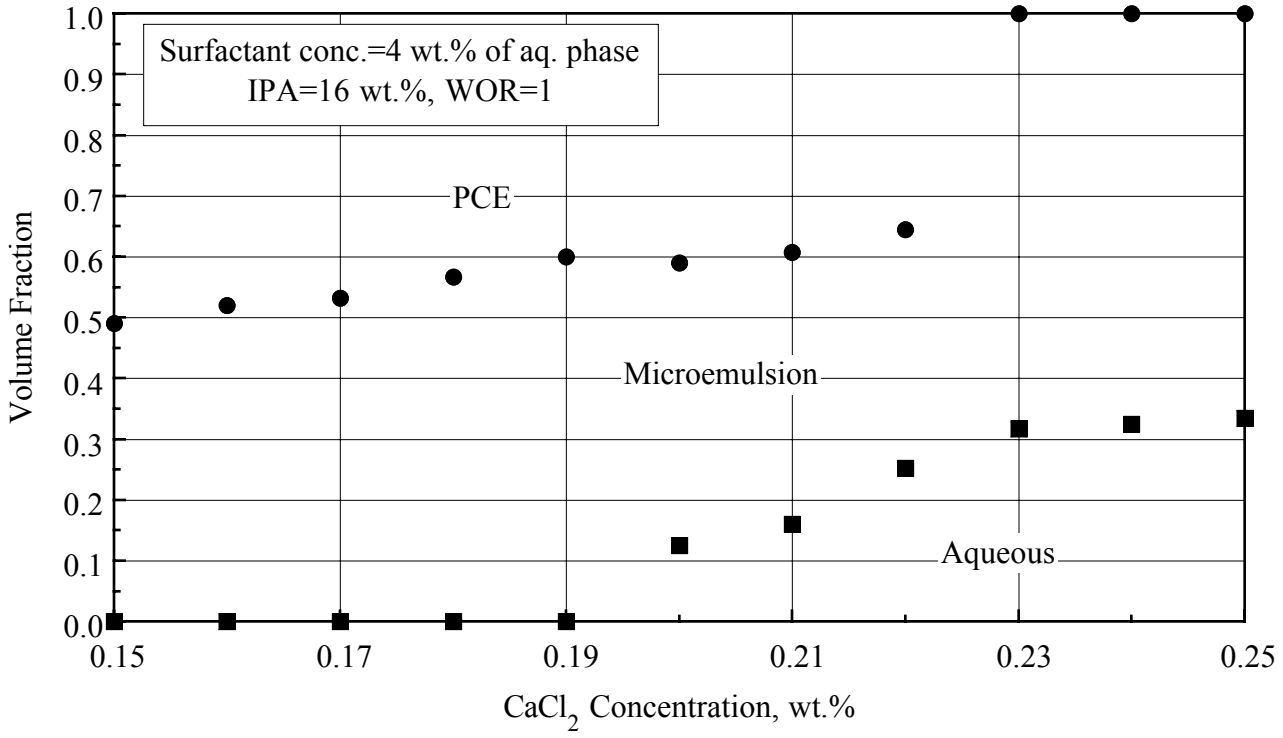

Figure 16.1. Volume Fraction Diagram for 4 wt.% Alfoterra© 145 $(PO)_4$ sodium ether sulfate and 16 wt.% IPA with PCE at 25 °C.

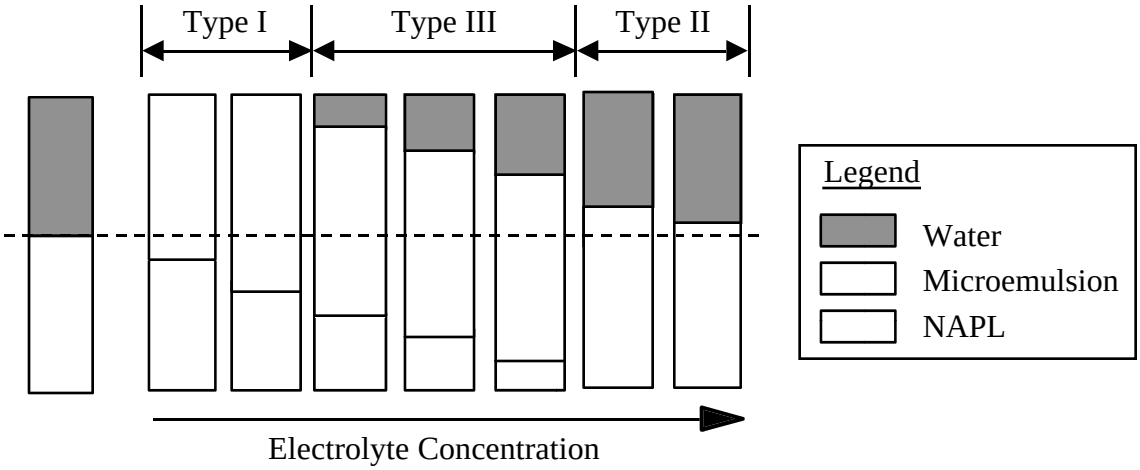

Figure 16.2. Dependence of phase behavior on electrolyte concentration.

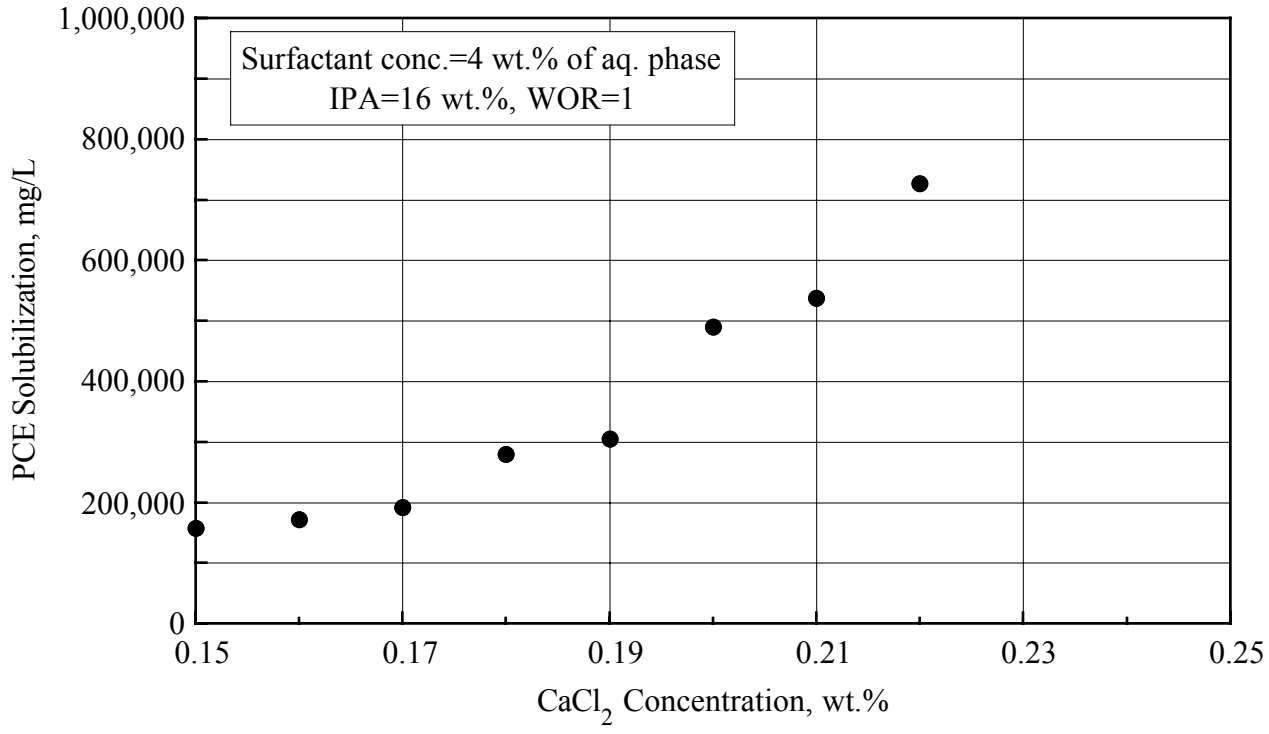

Figure 16.3. PCE solubilization for 4 wt.% Alfoterra© 145 $(PO)_4$ sodium ether sulfate and 16 wt.% IPA at 25 °C.

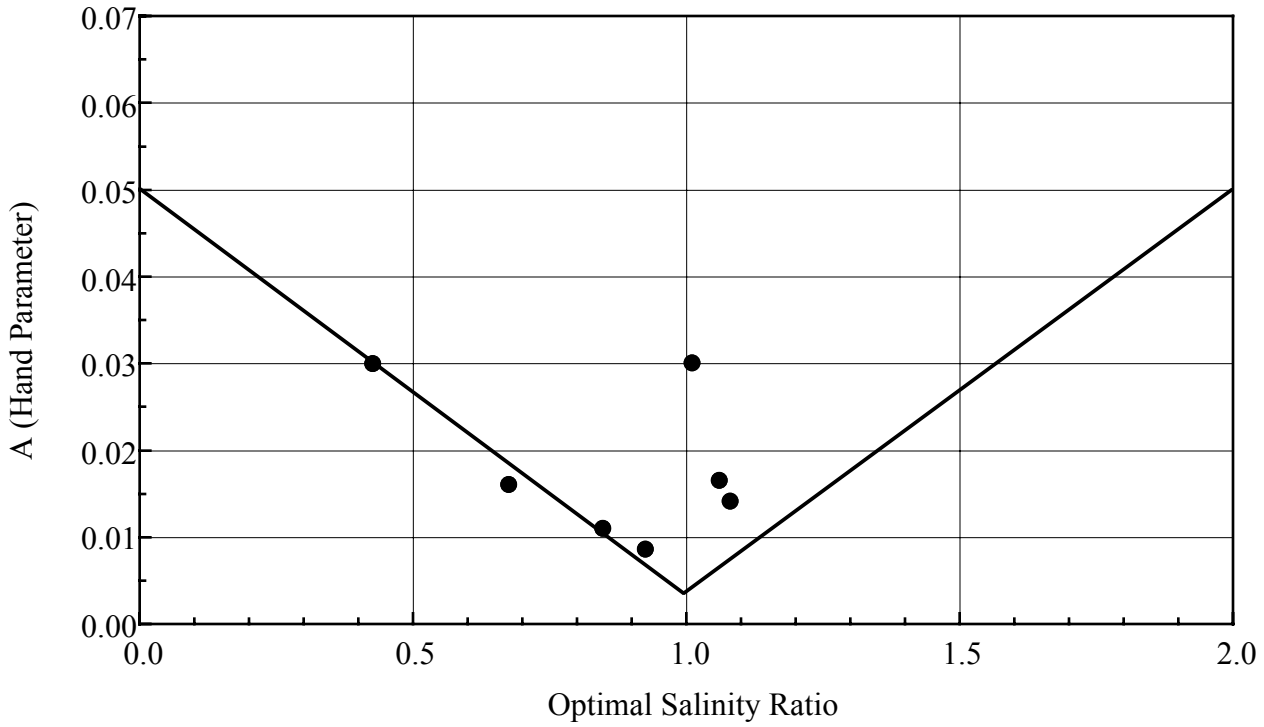

Figure 16.4. Experimentally determined "A" Hand parameter vs. optimal salinity ratio.

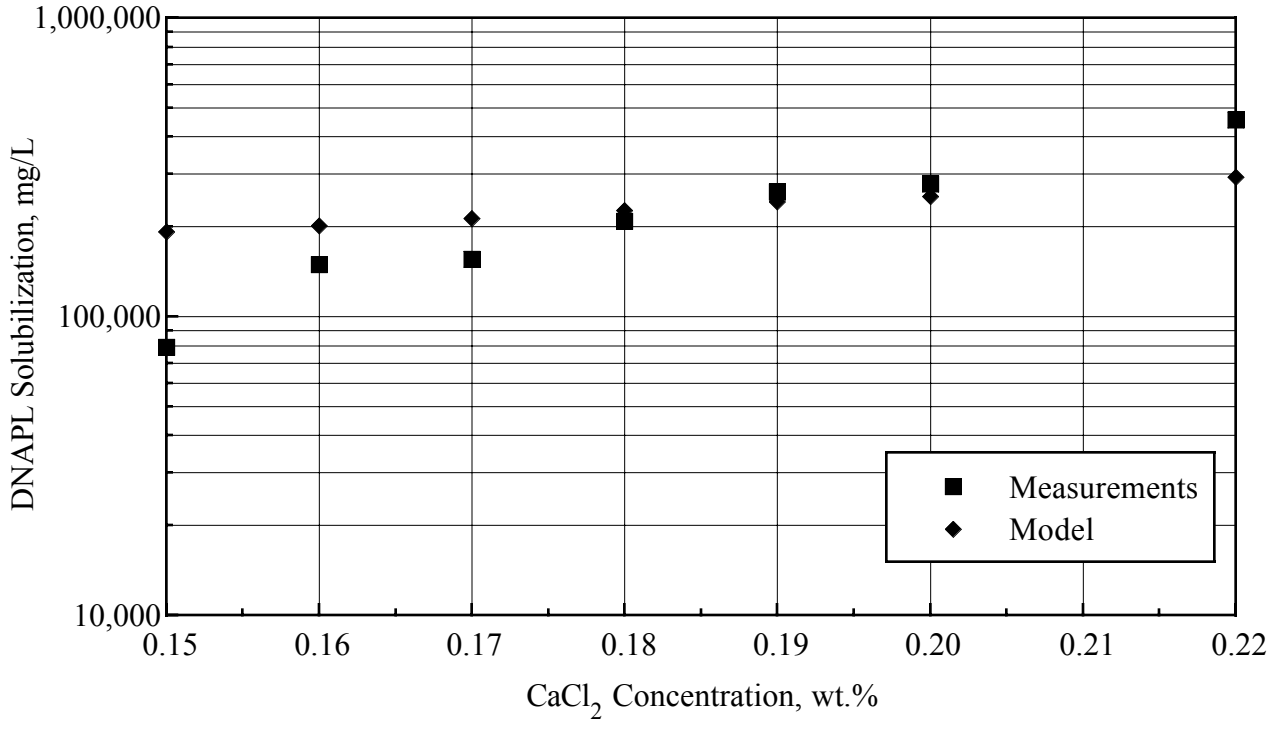

Figure 16.5. Measured and calculated DNAPL solubilization for a mixture of 4 wt.% Alfoterra© 145 $(PO)_4$ sodium ether sulfate, 16 wt.% IPA, and Camp Lejeune DNAPL at different calcium chloride concentrations.

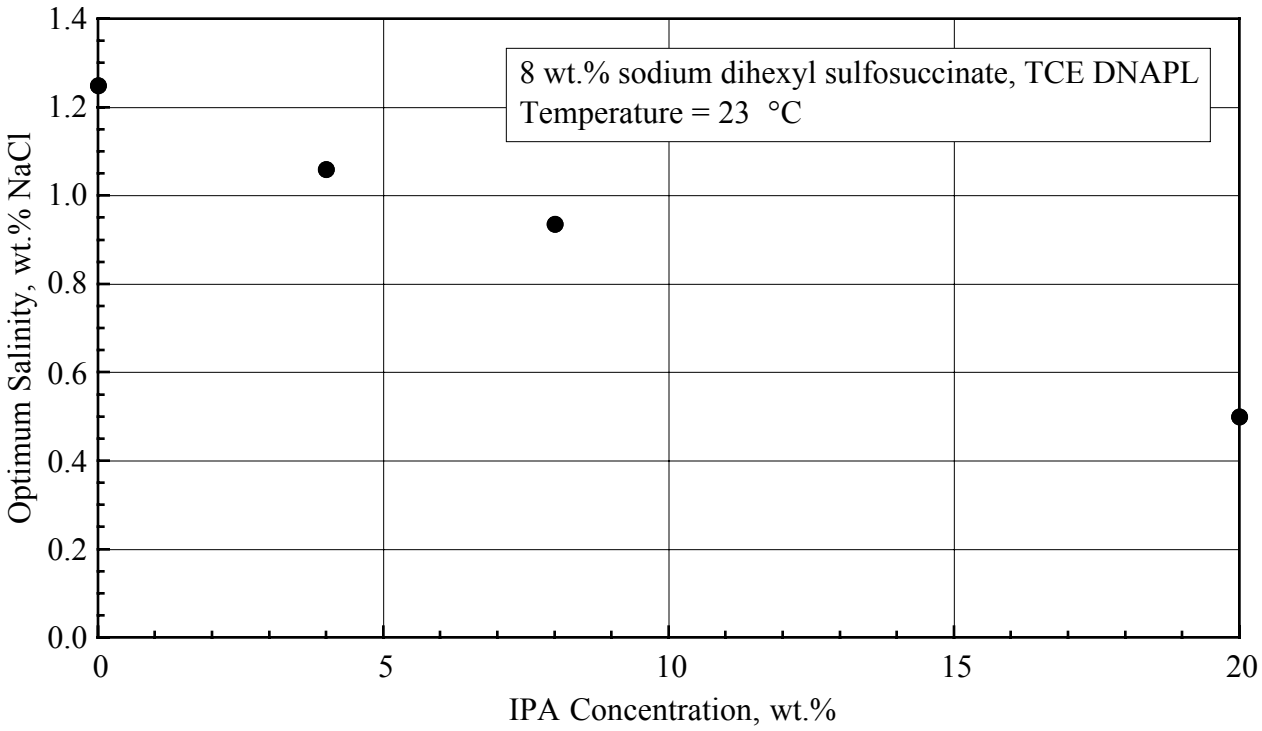

Figure 16.6. Effect of IPA concentration on optimum salinity.

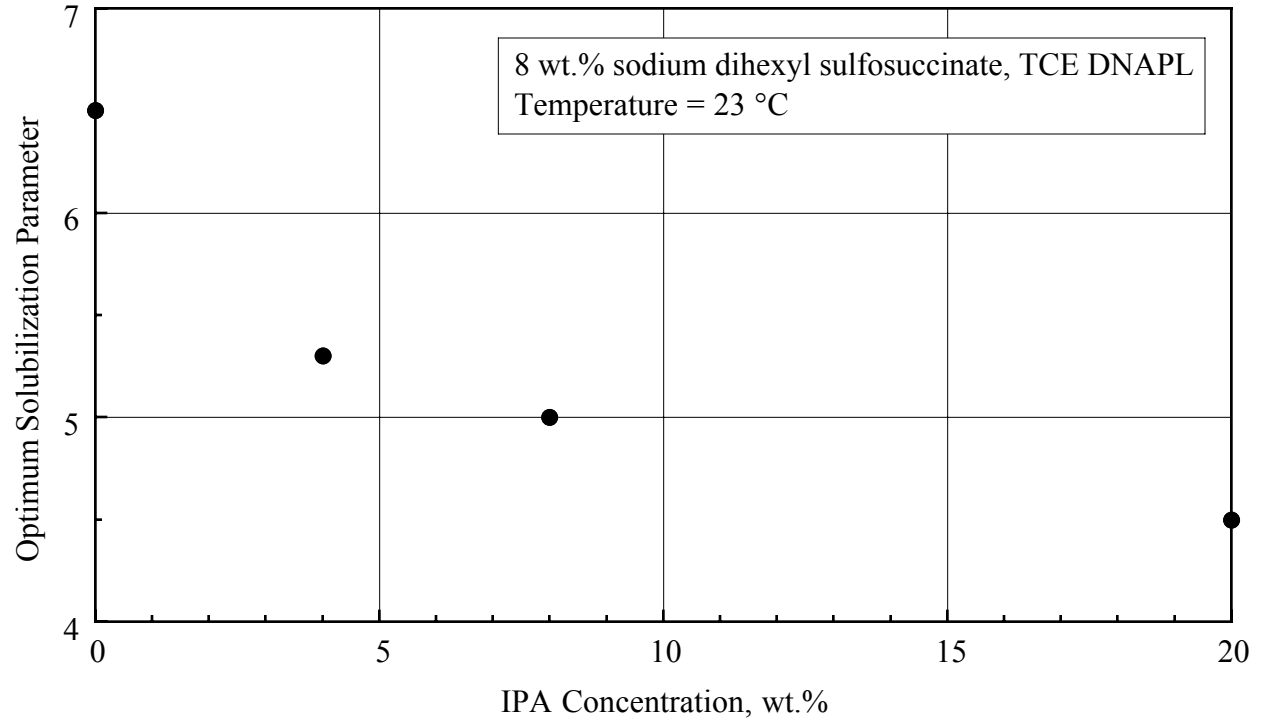

Figure 16.7. Effect of IPA concentration on optimum solubilization parameter.

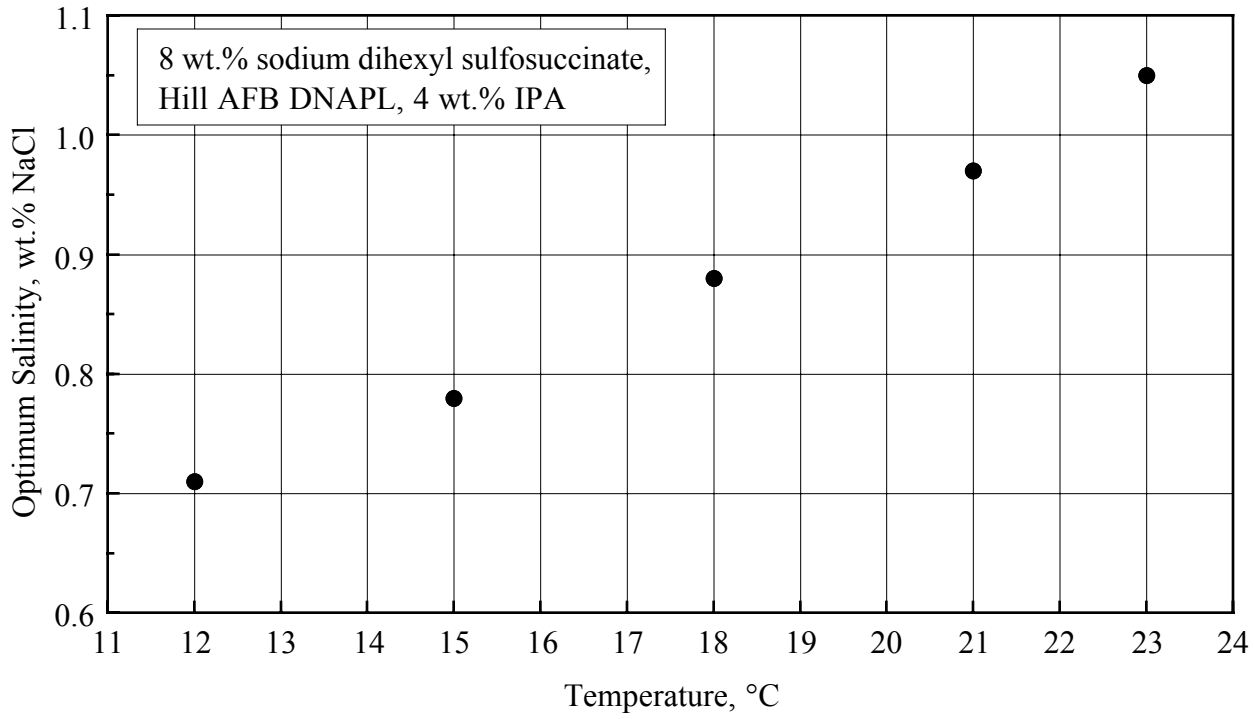

Figure 16.8. Effect of temperature on optimum salinity.

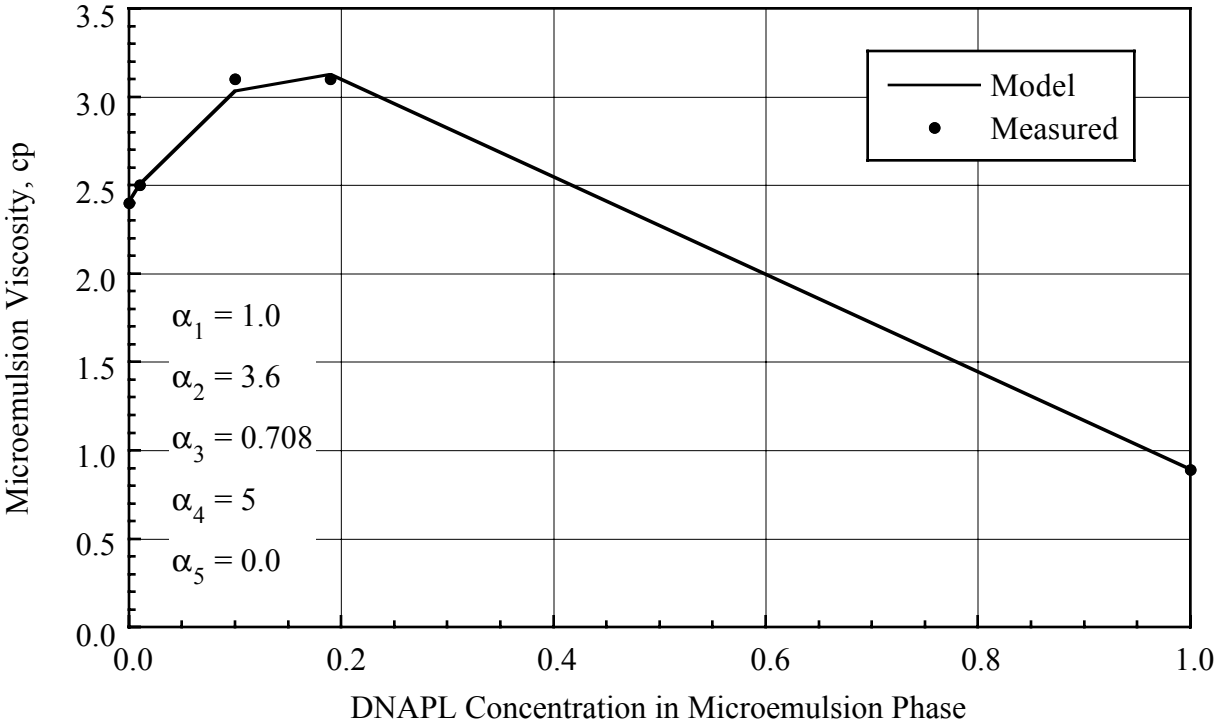

Figure 16.9. Measured and calculated microemulsion viscosity for a 4 wt.% Alfoterra© 145 $(PO)_4$ sodium ether sulfate, 16 wt.% IPA, and 0.2 wt.% calcium chloride at different PCE concentrations.

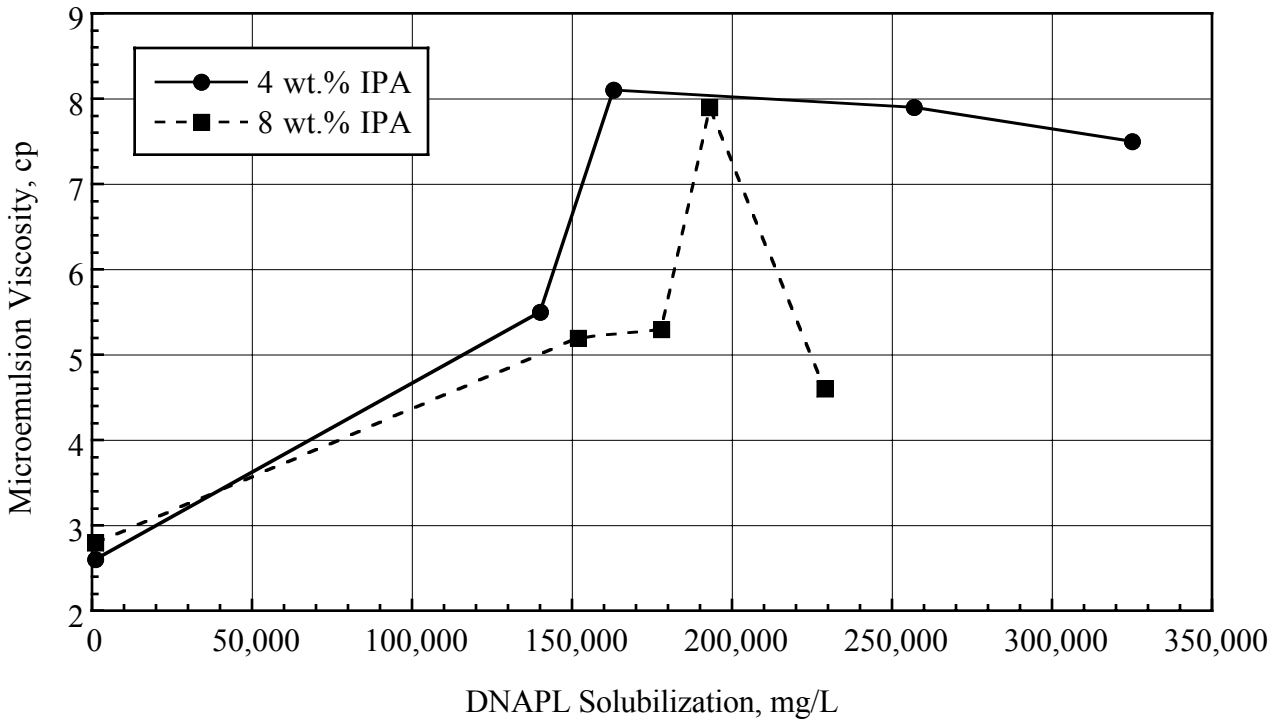

Figure 16.10. Microemulsion viscosities for mixtures of 8 wt.% sodium dihexyl sulfosuccinate, sodium chloride, IPA, and Hill AFB-DNAPL at 12 °C.

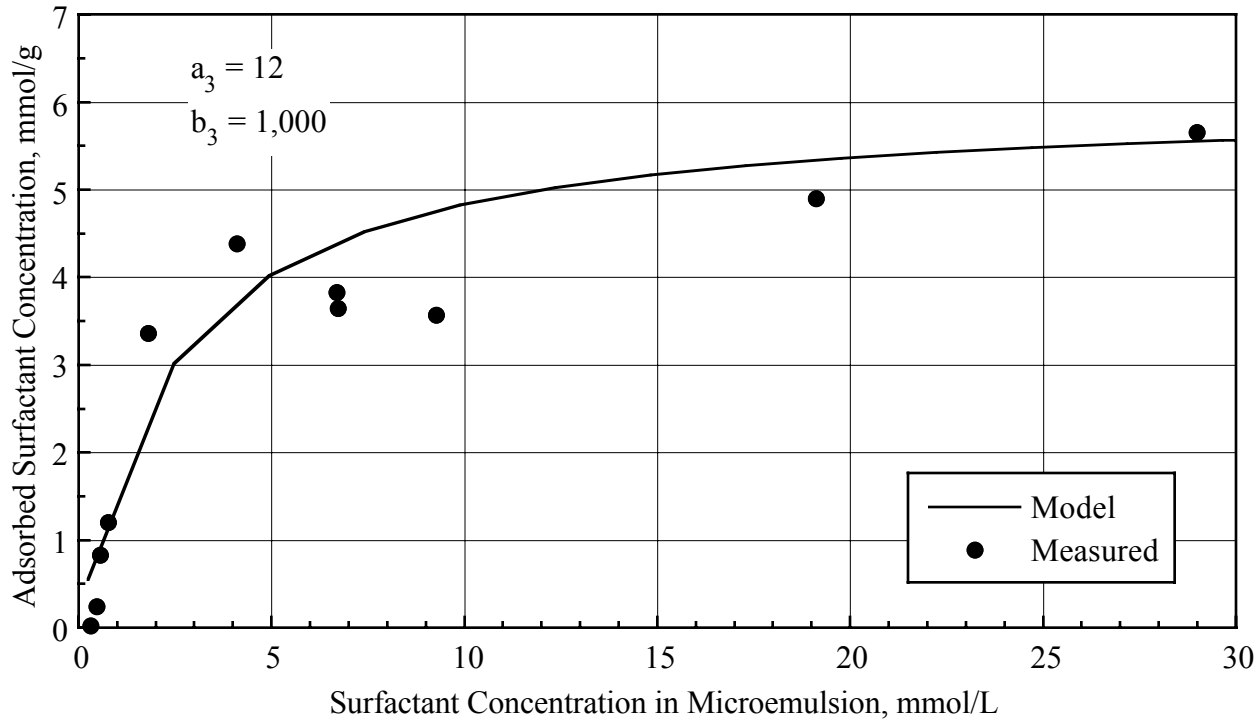

Figure 16.11. Comparison of measured and Langmuir Isotherm model calculations for the adsorbed sodium dioctyle sulfosuccinate (AOT) surfactant on Canadian River Alluvium (Shiau *et al.*, 1994).

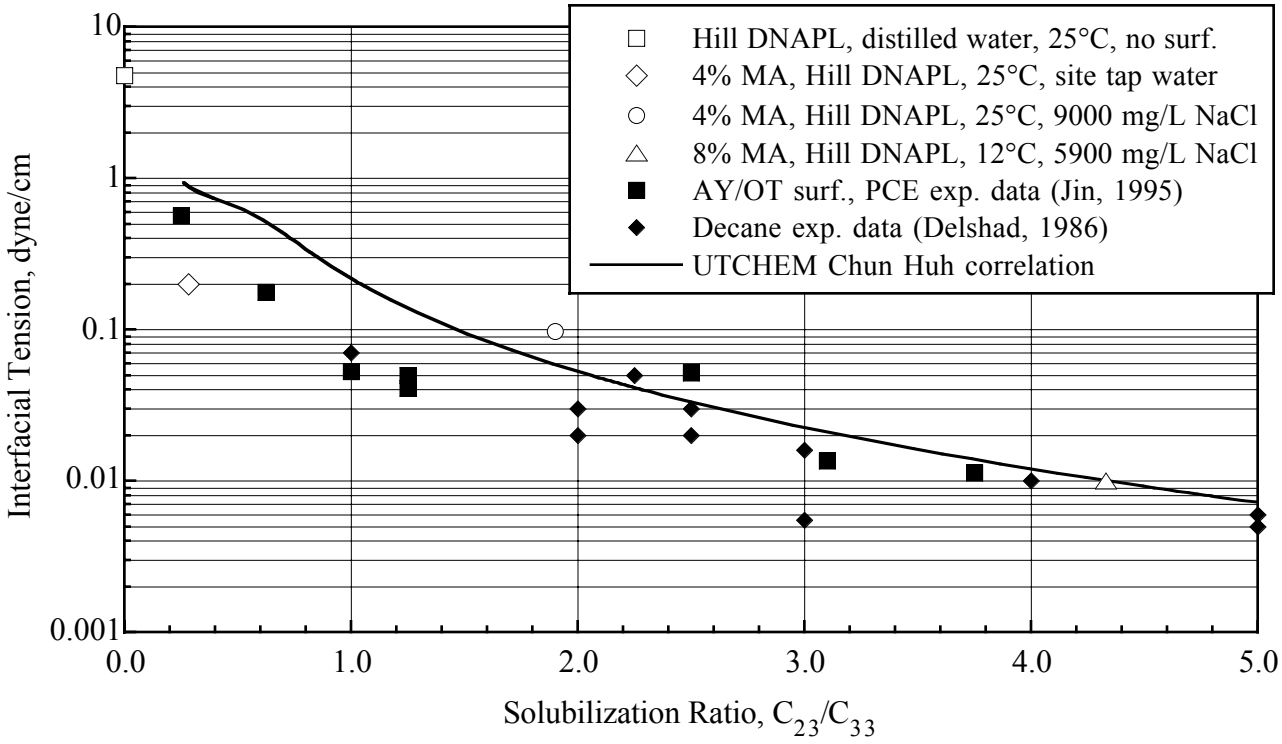

Figure 16.12. Measured and calculated interfacial tension as a function of solubilization ratio.

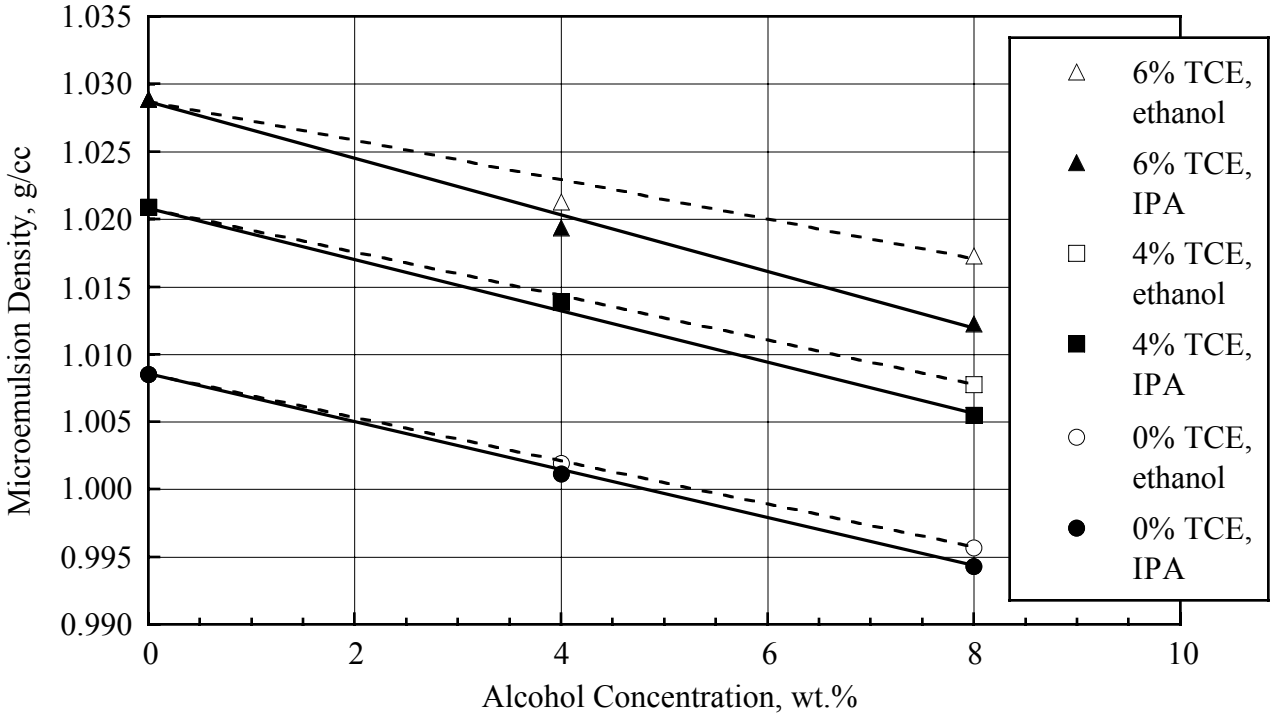

Figure 16.13. Microemulsion density for increasing concentration of alcohol (either ethanol or isopropanol), 4 wt.% sodium dihexyl sulfosuccinate, 0.6 wt.% sodium chloride, and TCE.

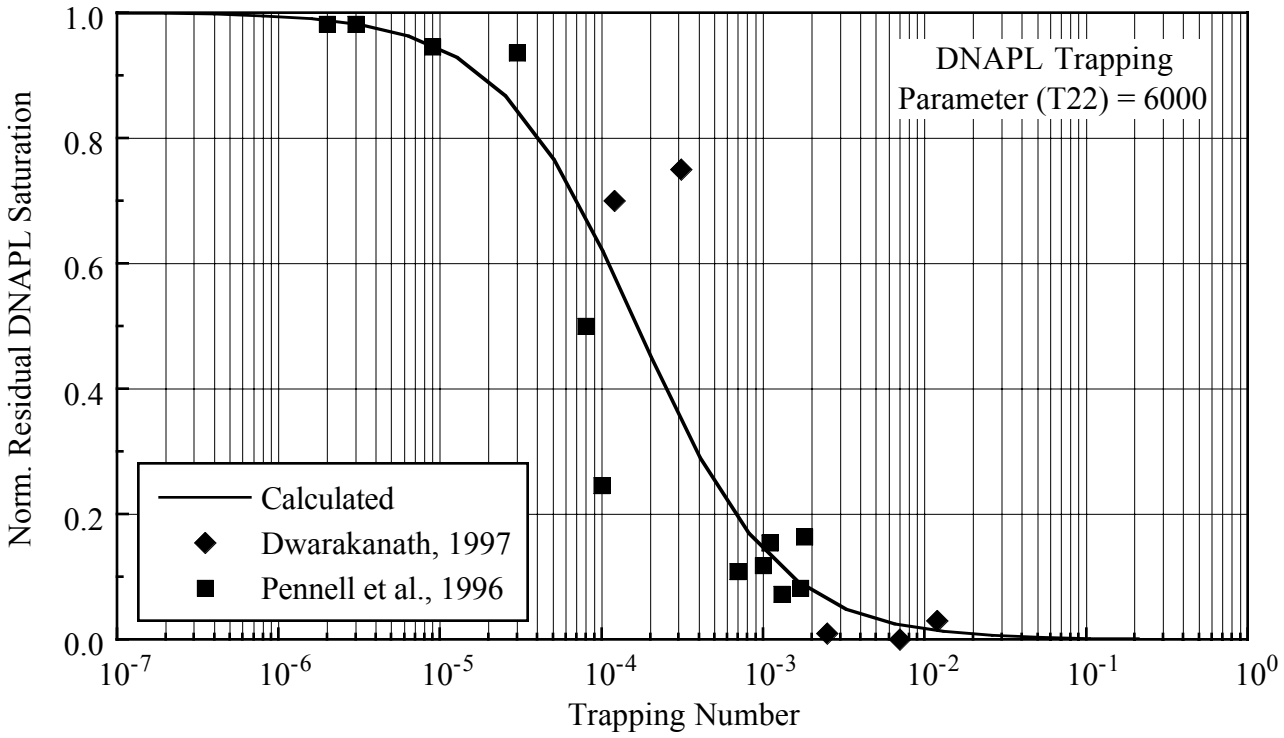

Figure 16.14. Comparison of the calculated and measured capillary desaturation curve for DNAPL.

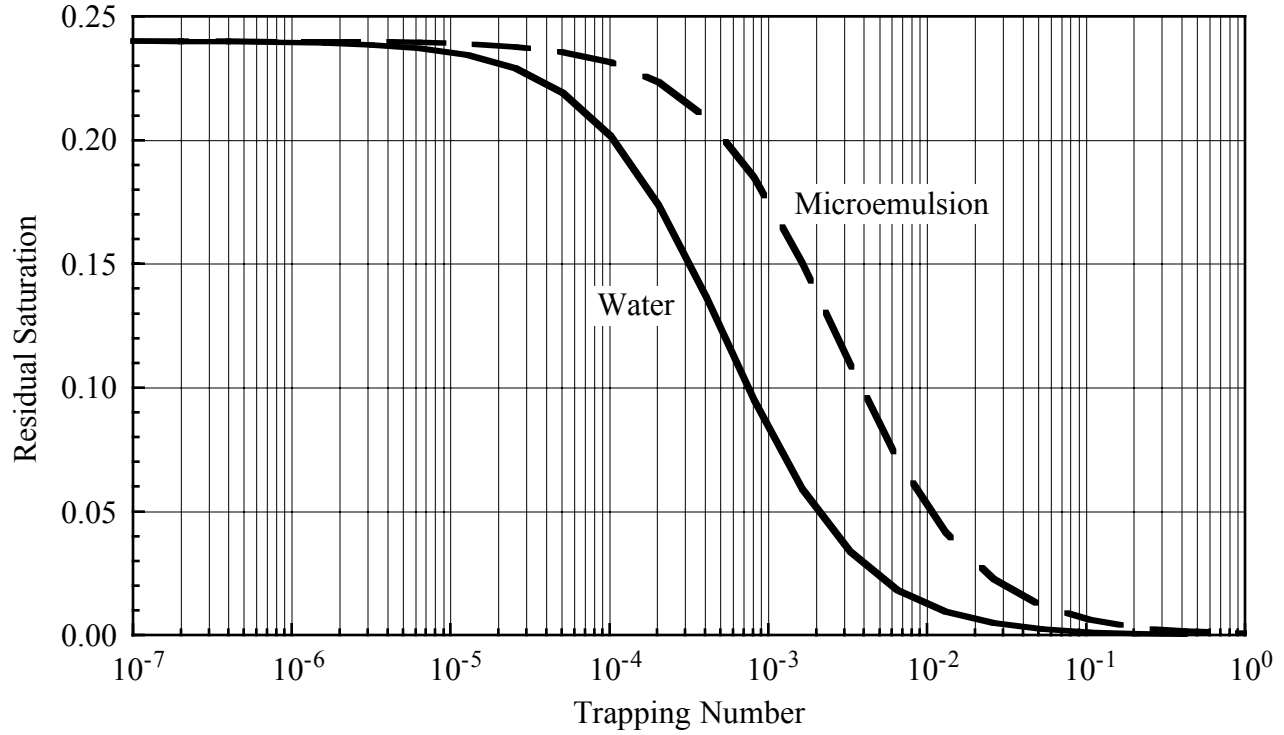

Figure 16.15. Example for capillary desaturation curves for SEAR simulations.

Appendix A
Discretized Flow Equations

The coordinate system can be either cartesian, radial, or curvilinear. The discretized equations presented here are for the cartesian coordinate system referred to as (x, y, z). The finite-difference grid is block-centered and numbered from 1 to $N_x N_y N_z$, where N_x, N_y, and N_z correspond to the number of gridblocks in the x, y, and z directions, respectively. The volume of the m^{th} block (i, j, k) is $\Delta V_m = \Delta x_m \Delta y_m \Delta z_m$ where i, j, and k correspond to the x, y, and z coordinate directions, respectively. The time increment δt is from timestep n to timestep n+1. The delta operator δ denotes discrete differences:

$$\begin{aligned}
&\delta_t f^n = f^{n+1} - f^n \\
&\delta_x f_m = f_m - f_{m-1}, \delta_x f_i = f_i - f_{i-1} \\
&\delta_y f_m = f_m - f_{m-Nx}, \delta_y f_j = f_j - f_{j-1} \\
&\delta_z f_m = f_m - f_{m-NxNy}, \delta_z f_k = f_k - f_{k-1}
\end{aligned} \tag{A.1}$$

Most variables, including pressure, concentrations, adsorbed concentrations, saturations, capillary pressures, phase properties such as density, viscosity, interfacial tension, and relative permeabilities are calculated and stored at gridblock centers. Some variables, such as transmissibilities and phase velocities, are evaluated at the faces between gridblocks. Applying the finite-difference approximations to the species conservation equations (Eq. A.1) and the pressure equation (Eq. A.10), we obtain a system of finite-difference equations. For the purpose of simplicity, the system of equations is illustrated for a two-dimensional problem even though the code is three-dimensional.

The species conservation equation for species κ at gridpoint m is

$$\left(F_{a\kappa}\right)_m^{n+1} = \left(F_{a\kappa}\right)_m^n + \delta_t t^n \left(F_{t\kappa} + F_{q\kappa}\right)_m^{\bar{n}} \tag{A.2}$$

The superscript $\bar{n}$ indicates that the variables are evaluated using both old timestep (n) variables and new timestep (n+1) variables.

$F_{a\kappa}$ is the accumulation term

$$\left(F_{a\kappa}\right)_m = \left\{\phi_R \Delta V \tilde{C}_\kappa \left[1 + \left(C_f + C_\kappa^0\right)\left(P_R - P_{R0}\right)\right]\right\}_m \tag{A.3}$$

$F_{t\kappa}$ is the transport term as

$$
\begin{aligned}
\left(F_{t\kappa}\right)_m^{\bar{n}} \;=\; & -\delta_x\left[1+C_\kappa^0\left(P_R-P_{R0}\right)\right]_m^{n+1}\sum_{\ell=1}^{n_p}\Big\{\left(C_{x\kappa\ell}\right)_m^n\left(\bar{T}_{x\ell}\right)_m^n \\
& \cdot\left[\delta_x\left(P_R^{n+1}+P_{c\ell R}^n\right)_{m+1}-\left(\bar{\gamma}_{x\ell}^n\right)_m\delta_x(D)_{m+1}\right] \\
& +\left(\bar{K}_{xx\kappa\ell}^{\bar{n}}\right)_m\delta_x\left(C_{\kappa\ell}^n\right)_{m+1}+\left(\bar{K}_{xy\kappa\ell}^{\bar{n}}\right)_m\delta_y\left[\left(C_{\kappa\ell}^n\right)_m+\left(C_{\kappa\ell}^n\right)_{m+Nx}\right]\Big\} \\
& -\delta_x\left[1+C_\kappa^0\left(P_R-P_{R0}\right)\right]_m^{n+1}\sum_{\ell=1}^{n_p}\Big\{\left(C_{y\kappa\ell}\right)_m\left(\bar{T}_{y\ell}\right)_m \\
& \cdot\left[\delta_y\left(P_R^{n+1}+P_{c\ell R}^n\right)_{m+Nx}-\left(\bar{\gamma}_{y\ell}^n\right)_m\delta_y(D)_{m+Nx}\right] \\
& +\left(\bar{K}_{yy\kappa\ell}^{\bar{n}}\right)_m\delta_y\left(C_{\kappa\ell}^n\right)_{m+Nx}+\left(\bar{K}_{yx\kappa\ell}^{\bar{n}}\right)_m\delta_x\left[\left(C_{\kappa\ell}^n\right)_m+\left(C_{\kappa\ell}^n\right)_{m+1}\right]\Big\}
\end{aligned}
\tag{A.4}
$$

where $C_{x\kappa\ell}$, $C_{y\kappa\ell}$, $\bar{T}_{x\ell}$, and $\bar{T}_{y\ell}$ are defined by

$$
\begin{aligned}
\left(C_{x\kappa\ell}\right)_m &= \left(C_{\kappa\ell}\right)_m+\varphi_m\left\{r_{xm}\left[\left(C_{\kappa\ell}\right)_m\right]\right\}\delta_x\left(C_{\kappa\ell}\right)_{m+1}/2 \\
\left(C_{y\kappa\ell}\right)_m &= \left(C_{\kappa\ell}\right)_m+\varphi_m\left\{r_{ym}\left[\left(C_{\kappa\ell}\right)_m\right]\right\}\delta_y\left(C_{\kappa\ell}\right)_{m+Nx}/2
\end{aligned}
\tag{A.5}
$$

$$
\begin{aligned}
\left(\bar{T}_{x\ell}\right)_m &= \left\{\left(k_{r\ell}\right)_m\varphi_m\left\{r_{xm}\left[\left(k_{r\ell}\right)_m\right]\right\}\delta_x\left(k_{r\ell}\right)_{m+1}/2\right\}\left(T_x/\mu_\ell\right)_m \\
\left(\bar{T}_{y\ell}\right)_m &= \left\{\left(k_{r\ell}\right)_m\varphi_m\left\{r_{ym}\left[\left(k_{r\ell}\right)_m\right]\right\}\delta_y\left(k_{r\ell}\right)_{m+Nx}/2\right\}\left(T_y/\mu_\ell\right)_m
\end{aligned}
\tag{A.6}
$$

$\left(T_x\right)_m$ and $\left(T_y\right)_m$, given by

$$
\begin{aligned}
\left(T_x\right)_m &= 2(\Delta y\Delta z)_m/\left(\Delta x_m/k_m+\Delta x_{m+1}/k_{m+1}\right) \\
\left(T_y\right)_m &= 2(\Delta x\Delta z)_m/\left(\Delta y_m/k_m+\Delta y_{m+Nx}/k_{m+Nx}\right)
\end{aligned}
\tag{A.7}
$$

are transmissibilities.

φ_m is the flux limiter function defined as follows (Liu *et al.*, 1994):

$$
\varphi_m=\frac{2\left(f_{m+1/2}-f_m\right)}{f_{m+1}-f_m} \tag{A.8}
$$

The magnitude of the limiting depends on the smoothness of the data, measured by the ratio of consecutive cell gradients r:

$$
r_m=\frac{f_m-f_{m-1}}{f_{m+1}-f_m} \tag{A.9}
$$

and $\varphi(r)=\max\left(0,\min\left(\varphi_b,\frac{2+r}{3}\right)\right)$.

$$
\begin{aligned}
r_{xm}\left[\left(C_{\kappa\ell}\right)_m\right] &= \delta_x\left(C_{\kappa\ell}\right)_m / \delta_x\left(C_{\kappa\ell}\right)_{m+1} \\
r_{ym}\left[\left(C_{\kappa\ell}\right)_m\right] &= \delta_y\left(C_{\kappa\ell}\right)_m / \delta_y\left(C_{\kappa\ell}\right)_{m+Nx} \\
r_{xm}\left[\left(k_{r\ell}\right)_m\right] &= \delta_x\left(k_{r\ell}\right)_m / \delta_x\left(k_{r\ell}\right)_{m+1} \\
r_{ym}\left[\left(k_{r\ell}\right)_m\right] &= \delta_y\left(k_{r\ell}\right)_m / \delta_y\left(k_{r\ell}\right)_{m+Nx}
\end{aligned}
\tag{A.10}
$$

$\overline{K}_{xx\kappa\ell}, \overline{K}_{yy\kappa\ell}, \overline{K}_{xy\kappa\ell}, \text{and } \overline{K}_{yx\kappa\ell}$ are the dispersion coefficients defined by

$$
\begin{aligned}
\left(\overline{K}_{xx\kappa\ell}\right)_m &= \Delta y_m \Delta z_m / \left[\left(\Delta x_m + \Delta x_{m+1}\right)/2\right]\left(\phi_R S_\ell K_{xx\kappa\ell} + \delta_t t^n u_{x\ell}^2 / \phi_R\right)_m \\
\left(\overline{K}_{xy\kappa\ell}\right)_m &= \Delta y_m \Delta z_m / \left[\Delta y_m + \left(\Delta y_{m-Nx} + \Delta y_{m+Nx}\right)/2\right]\left(\phi_R S_\ell K_{xy\kappa\ell} + \delta_t t^n u_{y\ell} / \phi_R\right)_m \\
\left(\overline{K}_{yy\kappa\ell}\right)_m &= \Delta x_m \Delta z_m / \left[\left(\Delta y_m + \Delta y_{m+Nx}\right)/2\right]\left(\phi_R S_\ell K_{yy\kappa\ell} + \delta_t t^n u_{y\ell}^2 / \phi_R\right)_m \\
\left(\overline{K}_{yx\kappa\ell}\right)_m &= \Delta y_m \Delta z_m / \left[\Delta x_m + \left(\Delta x_{m-1} + \Delta x_{m+1}\right)/2\right]\left(\phi_R S_\ell K_{yx\kappa\ell} + \delta_t t^n u_{y\ell} u_{x\ell} / \phi_R\right)_m
\end{aligned}
\tag{A.11}
$$

The average specific weight of phase ℓ is calculated from

$$
\begin{aligned}
\left(\bar{\gamma}_{x\ell}\right)_m &= \left[\left(\gamma_\ell E_\ell \Delta x\right)_m + \left(\gamma_\ell E_\ell \Delta x\right)_{m+1}\right] / \left[\left(E_\ell \Delta x\right)_m + \left(E_\ell \Delta x\right)_{m+1}\right] \\
\left(\bar{\gamma}_{y\ell}\right)_m &= \left[\left(\gamma_\ell E_\ell \Delta y\right)_m + \left(\gamma_\ell E_\ell \Delta x\right)_{m+Nx}\right] / \left[\left(E_\ell \Delta y\right)_m + \left(E_\ell \Delta y\right)_{m+Nx}\right]
\end{aligned}
\tag{A.12}
$$

where E_ℓ is the existence index of phase ℓ and is defined as

$$
\left(E_\ell\right)_m = \begin{cases} 0 & \left(S_\ell\right)_m = 0 \\ 1 & \left(S_\ell\right)_m > 0 \end{cases}
\tag{A.13}
$$

$F_{q\kappa}$ is the source and sink term:

$$
\begin{aligned}
\left(F_{q\kappa}\right)_m^{\bar{n}} = \Bigg\{ & \sum_{\ell=1}^{n_p}\left[Q_\ell^n + (PI)_\ell^n\left(P_{wf} - P_R^{n+1} - P_{c\ell R}^n\right)\right] C_{\kappa\ell}^n \\
& + \phi_R \Delta V\left[1 + \left(C_f + C_\kappa^0\right)\left(P_R^{n+1} - P_{R0}\right)\right]\left(\sum_{\ell=1}^{n_p} S_\ell^n r_{\kappa\ell} + r_{\kappa s}\right)\Bigg\}_m
\end{aligned}
\tag{A.14}
$$

which includes wells constrained by either rate or pressure and the production from chemical reactions.

The pressure equation at gridpoint m is

$$
\left(F_a^{n+1} - F_{t1}^{\bar{n}}\right)_m = \left(F_a\right)_m^n + \delta_t t^n \left(F_{t2} + F_q\right)_m^n
\tag{A.15}
$$

F_a is the total accumulation

$$\left(F_a\right)_m = \left(\phi_R \Delta V C_t P_R\right)_m \tag{A.16}$$

F_{t1} is the total transport as a function of reference phase pressure:

$$\begin{aligned}\left(F_{t1}^{\bar{n}}\right)_m = & -\delta_x\left\{\sum_{\ell=1}^{n_p}\left(\bar{T}_{x\ell}\right)_m^n\left[1+\left(P_R-P_{R0}\right)\sum_{\kappa=1}^{n_{cv}}C_\kappa^0 C_{\kappa\ell}\right]_m^n \delta_x\left(P_R^{n+1}\right)_{m+1}\right\} \\ & -\delta_y\left\{\sum_{\ell=1}^{n_p}\left(\bar{T}_{y\ell}\right)_m^n\left[1+\left(P_R-P_{R0}\right)\sum_{\kappa=1}^{n_{cv}}C_\kappa^0 C_{\kappa\ell}\right]_m^n \delta_y\left(P_R^{n+1}\right)_{m+Nx}\right\}\end{aligned} \tag{A.17}$$

Both F_{t2}, the total transport as a function of capillary pressure and gravity, and F_q, the total source or sink, are evaluated using values of the old timestep:

$$\begin{aligned}\left(F_{t2}\right)_m = & -\delta_x\left\{\sum_{\ell=1}^{n_p}\left(\bar{T}_{x\ell}\right)_m\left[1+\left(P_R-P_{R0}\right)\sum_{\kappa=1}^{n_{cv}}C_\kappa^0 C_{\kappa\ell}\right]_m \cdot\left[\delta_x\left(P_{c\ell R}\right)_{m+1}-\left(\bar{\gamma}_{x\ell}\right)_m\delta_x(D)_{m+1}\right]\right\} \\ & -\delta_y\left\{\sum_{\ell=1}^{n_p}\left(\bar{T}_{y\ell}\right)_m\left[1+\left(P_R-P_{R0}\right)\sum_{\kappa=1}^{n_{cv}}C_\kappa^0 C_{\kappa\ell}\right]_m \cdot\left[\delta_y\left(P_{c\ell R}\right)_{m+Nx}-\left(\bar{\gamma}_{y\ell}\right)_m\delta_y(D)_{m+Nx}\right]\right\}\end{aligned} \tag{A.18}$$

$$\left(F_q\right)_m = \sum_{\kappa=1}^{n_{cv}}\sum_{\ell=1}^{n_p}\left\{\left[Q_\ell + (PI)_\ell\left(P_{wf}-P_R-P_{c\ell R}\right)\right]C_{\kappa\ell}\right\}_m \tag{A.19}$$

Coefficients of reference phase pressure P_R on the left-hand side of Eq. A.15 are concentration-dependent and are evaluated using values at the old timestep. The equation written for all gridblocks in the spatial domain results in a system of equations with reference phase pressure P_R as the only unknown and is solved implicitly. The conservation equations (Eq. A.2) are then solved explicitly for overall concentrations. Phase concentrations and saturations are obtained by phase equilibria calculations. Other phase pressures are obtained using capillary pressure relations.

Appendix B
Biodegradation Equations

B.1 Equations

Loss of substrate i in bulk fluid:

$$\frac{dC_i}{dt} = \sum_{k=1}^{nb}\left\{-\frac{\kappa_i\beta_k\overline{X}_k}{m_k}(C_i-\overline{C}_{i,k})-\sum_{j=1}^{na}\left[\frac{\mu_{max}^{ijk}X_k}{Y^{ijk}}\left(\frac{C_i}{K_S^{ijk}\left(1+\sum_{m=1}^{ncs}\frac{C_m}{K_S^{mjk}}\right)+C_i}\right)\cdot\left(\frac{C_j}{K_A^{ijk}+C_j}\right)\left(\frac{C_{R,k}}{K_{R,k}+C_{R,k}}\right)\prod_{n=1}^{nn}\left(\frac{C_n}{K_{N,n}^{ijk}+C_n}\right)\prod_{ih=1}^{nih}\left(\frac{I_{ih}^{ijk}}{I_{ih}^{ijk}+C_{ih}}\right)\right]\right\}-k_{abio,i}C_{i,k}$$

Loss of substrate i in attached biomass k:

$$\frac{d\overline{C}_{i,k}}{dt} = \frac{\kappa_i\beta_k}{V_k}(C_i-\overline{C}_{i,k})-\sum_{j=1}^{na}\left[\frac{\mu_{max}^{ijk}\rho_k}{Y^{ijk}}\left(\frac{\overline{C}_{i,k}}{K_S^{ijk}\left(1+\sum_{m=1}^{ncs}\frac{\overline{C}_{m,k}}{K_S^{mjk}}\right)+\overline{C}_{i,k}}\right)\cdot\left(\frac{\overline{C}_{j,k}}{K_A^{ijk}+\overline{C}_{j,k}}\right)\left(\frac{\overline{C}_{R,k}}{K_{R,k}+\overline{C}_{R,k}}\right)\prod_{n=1}^{nn}\left(\frac{\overline{C}_{n,k}}{K_{N,n}^{ijk}+\overline{C}_{n,k}}\right)\prod_{ih=1}^{nih}\left(\frac{I_{ih}^{ijk}}{I_{ih}^{ijk}+\overline{C}_{ih,k}}\right)\right]-k_{abio,i}\overline{C}_{i,k}$$

Loss of electron acceptor j in bulk fluid:

$$\frac{dC_j}{dt} = \sum_{k=1}^{nb}\left\{-\frac{\kappa_j\beta_k\overline{X}_k}{m_k}(C_j-\overline{C}_{j,k})-\sum_{i=1}^{ns}\left[\frac{\mu_{max}^{ijk}X_kE_j^{ijk}}{Y^{ijk}}\left(\frac{C_i}{K_S^{ijk}\left(1+\sum_{m=1}^{ncs}\frac{C_m}{K_S^{mjk}}\right)+C_i}\right)\cdot\left(\frac{C_j}{K_A^{ijk}+C_j}\right)\left(\frac{C_{R,k}}{K_{R,k}+C_{R,k}}\right)\prod_{n=1}^{nn}\left(\frac{C_n}{K_{N,n}^{ijk}+C_n}\right)\prod_{ih=1}^{nih}\left(\frac{I_{ih}^{ijk}}{I_{ih}^{ijk}+C_{ih}}\right)\right]\right\}-k_{abio,j}C_{j,k}$$

Loss of electron acceptor j in biomass k:

$$\frac{d\overline{C}_{j,k}}{dt} = \frac{\kappa_j\beta_k}{V_k}(C_j-\overline{C}_{j,k})-\sum_{j=1}^{ns}\left[\frac{\mu_{max}^{ijk}\rho_kE_j^{ijk}}{Y^{ijk}}\left(\frac{\overline{C}_{i,k}}{K_S^{ijk}\left(1+\sum_{m=1}^{ncs}\frac{\overline{C}_{m,k}}{K_S^{mjk}}\right)+\overline{C}_{i,k}}\right)\cdot\left(\frac{\overline{C}_{j,k}}{K_A^{ijk}+\overline{C}_{j,k}}\right)\left(\frac{\overline{C}_{R,k}}{K_{R,k}+\overline{C}_{R,k}}\right)\prod_{n=1}^{nn}\left(\frac{\overline{C}_{n,k}}{K_{N,n}^{ijk}+\overline{C}_{n,k}}\right)\prod_{ih=1}^{nih}\left(\frac{I_{ih}^{ijk}}{I_{ih}^{ijk}+\overline{C}_{ih,k}}\right)\right]-k_{abio,j}\overline{C}_{j,k}$$

Loss of nutrient n in bulk fluid:

$$\frac{dC_n}{dt} = \sum_{k=1}^{nb}\left\{-\frac{\kappa_n \beta_k \bar{X}_k}{m_k}(C_n - \bar{C}_{n,k})\right\} - \sum_{ijk=1}^{nmet}\left[\frac{\mu_{max}^{ijk} X_k E_n^{ijk}}{Y^{ijk}}\left(\frac{C_i}{K_S^{ijk}\left(1+\sum_{m=1}^{ncs}\frac{C_m}{K_S^{mjk}}\right)+C_i}\right)\cdot\left(\frac{C_j}{K_A^{ijk}+C_j}\right)\left(\frac{C_{R,k}}{K_{R,k}+C_{R,k}}\right)\prod_{n=1}^{nn}\left(\frac{C_n}{K_{N,n}^{ijk}+C_n}\right)\prod_{ih=1}^{nih}\left(\frac{I_{ih}^{ijk}}{I_{ih}^{ijk}+C_{ih}}\right)\right] - k_{abio,n}C_{n,k}$$

Loss of nutrient n in biomass k:

$$\frac{d\bar{C}_{n,k}}{dt} = \frac{\kappa_n \beta_k}{V_k}(C_n - \bar{C}_{n,k}) - \sum_{ijk=1}^{nmet}\left[\frac{\mu_{max}^{ijk} \rho_k E_n^{ijk}}{Y^{ijk}}\left(\frac{\bar{C}_{i,k}}{K_S^{ijk}\left(1+\sum_{m=1}^{ncs}\frac{\bar{C}_{m,k}}{K_S^{mjk}}\right)+\bar{C}_{i,k}}\right)\cdot\left(\frac{\bar{C}_{j,k}}{K_A^{ijk}+\bar{C}_{j,k}}\right)\left(\frac{\bar{C}_{R,k}}{K_{R,k}+\bar{C}_{R,k}}\right)\prod_{n=1}^{nn}\left(\frac{\bar{C}_{n,k}}{K_{N,n}^{ijk}+\bar{C}_{n,k}}\right)\prod_{ih=1}^{nih}\left(\frac{I_{ih}^{ijk}}{I_{ih}^{ijk}+\bar{C}_{ih,k}}\right)\right] - k_{abio,n}\bar{C}_{n,k}$$

Generation and/or loss of product p in bulk fluid:

$$\frac{dC_p}{dt} = \sum_{k=1}^{nb}\left\{-\frac{\kappa_p \beta_k \bar{X}_k}{m_k}(C_p - \bar{C}_{p,k})\right\} + \sum_{ijk=1}^{nmet}\left[\frac{\mu_{max}^{ijk} X_k E_p^{ijk}}{Y^{ijk}}\left(\frac{C_i}{K_S^{ijk}\left(1+\sum_{m=1}^{ncs}\frac{C_m}{K_S^{mjk}}\right)+C_i}\right)\cdot\left(\frac{C_j}{K_A^{ijk}+C_j}\right)\left(\frac{C_{R,k}}{K_{R,k}+C_{R,k}}\right)\prod_{n=1}^{nn}\left(\frac{C_n}{K_{N,n}^{ijk}+C_n}\right)\prod_{ih=1}^{nih}\left(\frac{I_{ih}^{ijk}}{I_{ih}^{ijk}+C_{ih}}\right)\right] - k_{abio,p}C_{p,k}$$

Generation and/or loss of product p in biomass k:

$$\frac{d\bar{C}_{p,k}}{dt} = \frac{\kappa_p \beta_k}{V_k}(C_p - \bar{C}_{p,k}) + \sum_{ijk=1}^{nmet}\left[\frac{\mu_{max}^{ijk} \rho_k E_p^{ijk}}{Y^{ijk}}\left(\frac{\bar{C}_{i,k}}{K_S^{ijk}\left(1+\sum_{m=1}^{ncs}\frac{\bar{C}_{m,k}}{K_S^{mjk}}\right)+\bar{C}_{i,k}}\right)\cdot\left(\frac{\bar{C}_{j,k}}{K_A^{ijk}+\bar{C}_{j,k}}\right)\left(\frac{\bar{C}_{R,k}}{K_{R,k}+\bar{C}_{R,k}}\right)\prod_{n=1}^{nn}\left(\frac{\bar{C}_{n,k}}{K_{N,n}^{ijk}+\bar{C}_{n,k}}\right)\prod_{ih=1}^{nih}\left(\frac{I_{ih}^{ijk}}{I_{ih}^{ijk}+\bar{C}_{ih,k}}\right)\right] - k_{abio,p}\bar{C}_{p,k}$$

Growth of unattached biomass k:

$$\frac{dX_k}{dt} = \sum_{\substack{i=1\\ i\neq c}}^{ns}\sum_{j=1}^{na}\left\{\mu_{max}^{ijk}X_k\left(\frac{C_i}{K_S^{ijk}\left(1+\sum_{m=1}^{ncs}\frac{C_m}{K_S^{mjk}}\right)+C_i}\right)\left(\frac{C_j}{K_A^{ijk}+C_j}\right)\left(\frac{C_{R,k}}{K_{R,k}+C_{R,k}}\right)\prod_{n=1}^{nn}\left(\frac{C_n}{K_{N,n}^{ijk}+C_n}\right)\prod_{ih=1}^{nih}\left(\frac{I_{ih}^{ijk}}{I_{ih}^{ijk}+C_{ih}}\right)\left(1-\frac{S_X}{0.9S_1}\right)\right\}$$
$$-\sum_{c=1}^{ncom}\sum_{j=1}^{na}\left\{\frac{\mu_{max}^{cjk}X_k}{T_c^{cjk}}\left(\frac{C_c}{K_S^{cjk}\left(1+\sum_{m=1}^{ncs}\frac{C_m}{K_S^{mjk}}\right)+C_c}\right)\left(\frac{C_j}{K_A^{cjk}+C_j}\right)\left(\frac{C_{R,k}}{K_{R,k}+C_{R,k}}\right)\prod_{n=1}^{nn}\left(\frac{C_n}{K_{N,n}^{cjk}+C_n}\right)\prod_{ih=1}^{nih}\left(\frac{I_{ih}^{cjk}}{I_{ih}^{cjk}+C_{ih}}\right)\right\}-b_kX_k$$

Growth of attached biomass k:

$$\frac{d\bar{X}_k}{dt} = \sum_{\substack{i=1\\ i\neq c}}^{ns}\sum_{j=1}^{na}\left\{\mu_{max}^{ijk}\bar{X}_k\left(\frac{\bar{C}_i}{K_S^{ijk}\left(1+\sum_{m=1}^{ncs}\frac{\bar{C}_m}{K_S^{mjk}}\right)+\bar{C}_i}\right)\left(\frac{\bar{C}_j}{K_A^{ijk}+\bar{C}_j}\right)\left(\frac{\bar{C}_{R,k}}{K_{R,k}+\bar{C}_{R,k}}\right)\prod_{n=1}^{nn}\left(\frac{\bar{C}_n}{K_{N,n}^{ijk}+\bar{C}_n}\right)\prod_{ih=1}^{nih}\left(\frac{I_{ih}^{ijk}}{I_{ih}^{ijk}+\bar{C}_{ih}}\right)\left(1-\frac{S_X}{0.9S_1}\right)\right\}$$
$$-\sum_{c=1}^{ncom}\sum_{j=1}^{na}\left\{\frac{\mu_{max}^{cjk}\bar{X}_k}{T_c^{cjk}}\left(\frac{\bar{C}_c}{K_S^{cjk}\left(1+\sum_{m=1}^{ncs}\frac{\bar{C}_m}{K_S^{mjk}}\right)+\bar{C}_c}\right)\left(\frac{\bar{C}_j}{K_A^{cjk}+\bar{C}_j}\right)\left(\frac{\bar{C}_{R,k}}{K_{R,k}+\bar{C}_{R,k}}\right)\prod_{n=1}^{nn}\left(\frac{\bar{C}_n}{K_{N,n}^{cjk}+\bar{C}_n}\right)\prod_{ih=1}^{nih}\left(\frac{I_{ih}^{ijk}}{I_{ih}^{cjk}+\bar{C}_{ih}}\right)\right\}-b_k\bar{X}_k$$

Reducing power (NADH) consumption and production in unattached biomass k (intra-cellular reducing power is limited to a maximum of 0.0029 mmol/mg biomass and a minimum of $0.01R_0$, where R_0 is the initial reducing power concentration in mmol/mg biomass):

$$\frac{dC_{R,k}}{dt} = -\sum_{c=1}^{n}\sum_{j=1}^{na}\left\{\frac{\mu_{max}^{cjk}E_{Rc}^{cjk}X_k}{Y^{cjk}}\left(\frac{C_c}{K_S^{cjk}\left(1+\sum_{m=1}^{ncs}\frac{C_m}{K_S^{mjk}}\right)+C_c}\right)\left(\frac{C_j}{K_A^{cjk}+C_j}\right)\left(\frac{C_{R,k}}{K_{R,k}+C_{R,k}}\right)\prod_{n=1}^{nn}\left(\frac{C_n}{K_{N,n}^{cjk}+C_n}\right)\prod_{ih=1}^{nih}\left(\frac{I_{ih}^{cjk}}{I_{ih}^{cjk}+C_{ih}}\right)\right\}$$
$$+\sum_{g=1}^{ngs}\sum_{j=1}^{na}\left\{\frac{\mu_{max}^{gjk}E_{Rp}^{gjk}X_k}{Y^{gjk}}\left(\frac{C_g}{K_S^{gjk}\left(1+\sum_{m=1}^{ncs}\frac{C_m}{K_S^{mjk}}\right)+C_g}\right)\left(\frac{C_j}{K_A^{gjk}+C_j}\right)\left(\frac{C_{R,k}}{K_{R,k}+C_{R,k}}\right)\prod_{n=1}^{nn}\left(\frac{C_n}{K_{N,n}^{gjk}+C_n}\right)\prod_{ih=1}^{nih}\left(\frac{I_{ih}^{gjk}}{I_{ih}^{gjk}+C_{ih}}\right)\right\}$$

Reducing power (NADH) consumption and production in attached biomass k (intra-cellular reducing power is limited to a maximum of 0.0029 mmol/mg biomass and a minimum of $0.01R_0$, where R_0 is the initial reducing power concentration in mmol/mg biomass):

$$\frac{d\bar{C}_{R,k}}{dt} = -\sum_{c=1}^{n}\sum_{j=1}^{na}\left\{\frac{\mu_{max}^{cjk} E_{Rc}^{cjk} \bar{X}_k}{Y^{cjk}}\left(\frac{\bar{C}_c}{K_S^{cjk}\left(1+\sum_{m=1}^{ncs}\frac{\bar{C}_m}{K_S^{mjk}}\right)+\bar{C}_c}\right)\left(\frac{\bar{C}_j}{K_A^{cjk}+\bar{C}_j}\right)\left(\frac{\bar{C}_{R,k}}{K_{R,k}+\bar{C}_{R,k}}\right)\prod_{n=1}^{nn}\left(\frac{\bar{C}_n}{K_{N,n}^{cjk}+\bar{C}_n}\right)\prod_{ih=1}^{nih}\left(\frac{I_{ih}^{cjk}}{I_{ih}^{cjk}+\bar{C}_{ih}}\right)\right\}$$
$$+\sum_{g=1}^{ngs}\sum_{j=1}^{na}\left\{\frac{\mu_{max}^{gjk} E_{Rp}^{gjk} \bar{X}_k}{Y^{gjk}}\left(\frac{\bar{C}_g}{K_S^{gjk}\left(1+\sum_{m=1}^{ncs}\frac{\bar{C}_m}{K_S^{mjk}}\right)+\bar{C}_g}\right)\left(\frac{\bar{C}_j}{K_A^{gjk}+\bar{C}_j}\right)\left(\frac{\bar{C}_{R,k}}{K_{R,k}+\bar{C}_{R,k}}\right)\prod_{n=1}^{nn}\left(\frac{\bar{C}_n}{K_{N,n}^{gjk}+\bar{C}_n}\right)\prod_{ih=1}^{nih}\left(\frac{I_{ih}^{gjk}}{I_{ih}^{gjk}+\bar{C}_{ih}}\right)\right\}$$

B.2 Nomenclature

- b = Endogenous decay coefficient (T^{-1})
- C_i = concentration of species i in bulk liquid (mass C/volume of aqueous phase)
- $\bar{C}_{i,k}$ = concentration of species i within attached biomass species k (mass C/volume of biomass)
- E_j^{ijk} = consumption coefficient of component j for biodegradation in metabolic combination ijk (mass of j/mass of substrate consumed)
- I_{ih}^{ijk} = inhibition constant for inhibiting component ih for metabolic combination ijk (mass/volume of phase)
- k_{abio} = first-order abiotic reaction coefficient (T^{-1})
- K_A^{ijk} = Monod half-saturation constant for electron acceptor j in metabolic combination ijk (mass electron acceptor/volume of aqueous phase)
- $K_{N,n}^{ijk}$ = Monod half-saturation constant for nutrient n in metabolic combination ijk (mass nutrient/volume of aqueous phase)
- K_R^{ijk} = Monod half-saturation constant for reducing power in metabolic combination ijk (mmol reducing power/mg biomass)
- K_S^{ijk} = Monod half-saturation constant for substrate i in metabolic combination ijk (mass substrate/volume of aqueous phase)
- m_k = mass of a single bacterial colony (mass/colony)
- S_1 = aqueous phase saturation (volume of aqueous phase/unit pore volume)
- S_X = aqueous phase saturation of biomass (volume of total biomass/volume of aqueous phase)
- t = time (T)
- T_c^{ijk} = transformation capacity (mass of biomass deactivated/mass of cometabolite biodegraded)
- V_k = volume of a single bacterial colony (volume/colony)

X_k = concentration of free-floating biological species k (mass/volume of aqueous phase)

$\overline{X}_k$ = concentration of attached biological species k (mass/volume of aqueous phase)

Y^{ijk} = yield coefficient for component i under j-based metabolism by bacterial species k (dimensionless; mass of biomass produced/mass of substrate utilized)

Greek Symbols

β_κ = surface area of a single bacterial colony of biological species k available for mass transfer (L^2/colony)

κ_i = mass transfer coefficient of species i (L/T)

μ_{max}^{ijk} = Maximum specific growth rate for metabolic combination ijk (T^{-1})

ρ_k = biomass density (active biomass/volume of biomass)

Superscripts and Subscripts

c = cometabolite
g = growth substrate
i = substrate
ih = inhibiting compound
j = electron acceptor
k = biological species
m = competing substrate
n = nutrient
na = number of electron acceptors
nb = number of biological species
nc = number of cometabolites
ncs = number of competing substrates
nih = number of inhibiting compounds
nn = number of nutrients
ns = number of substrates
p = product
R = reducing power (NADH)
R_c = reducing power consumption
R_p = reducing power production

Superscripts such as ijk refer to metabolic combinations of substrate, electron acceptor and biological species.

Appendix C
EQBATCH Program Description

C.1 Introduction

EQBATCH is a preprocessor batch program to calculate the equilibrium concentrations for all the flow and solid species based on the chemical reactions considered in UTCHEM simulations. In this program, it is assumed that all the flow species dissolve in a single phase, water. The initial pH of the formation or makeup water can be matched by using EQBATCH with suitable input data. Also, the output of EQBATCH can be used as the input data of UTCHEM for the geochemical options (IREACT = 2-4). In this section, a detailed description for preparation of input data for EQBATCH is presented. To specify the reactions considered in the simulations, elements and chemical species need to be identified. Based on the information of the formation and makeup water analyses and the rock constituents, the key elements and chemical species can be decided. The example shown in this section is based on the water analysis results listed in Table C.1. The elements such as hydrogen, sodium, calcium, magnesium, carbonate, and chlorine, are considered since these chemicals are the primary ions contained in the formation and makeup water. The pseudo-element (oleic acid, A) is taken into account as an element when the mechanism of *in situ* generated surfactant is considered. From these elements, the expected chemical species involved in fluid reactions, clay adsorptions, cation exchange, and solid dissolution/precipitation reactions can be specified (Table C.2). There are 7 elements, 18 fluid species, 4 solid species, 4 clay adsorbed cations, and 3 surfactant cation exchangers considered in this example. To represent the interactions among these chemical species, the reaction equilibrium relations are required (Table C.3). Tables C.4-C.19 give the example input data for different sections of the input file. A sample input file for EQBATCH is given in Table C.20 and the output file for this example is given in Table C.21. The EQBATCH program also writes the output data in a format similar to the geochemistry input data of UTCHEM (Section 3.5 of the UTCHEM user's guide, lines 3.5.4 through 3.5.41) so it can be directly pasted into the UTCHEM input file (Table C.22).

C.2 User's Guide

A detailed user's guide for the EQBATCH program is presented as follows:

1. **TITLE**
   A title line is required.

2. **IREACT, ICHARGE, IMG**
   IREACT - Flag indicating the components to be considered
   Possible values:
   2 - Without acidic crude
   3 - With acidic crude (insitu surfactant generation)
   4- Gel option without acidic crude
   ICHRGE - Flag indicating whether an oxygen mass balance or a charge balance will be used.
   Possible Values:
   0 - Oxygen balance used
   1 - Charge balance in solution used
   Note: If solid SiO_2 is considered, the oxygen balance must be used
   IMG - Flag indicating whether magnesium ions participate in cation exchange reactions or not.
   Possible Values:
   0 - Magnesium ions are considered.
   1 - Magnesium ions are not considered.

3. **NELET, NFLD, NSLD, NSORB, NACAT**
   NELET - Total number of elements less non reacting element.
   NFLD - Total number of fluid species.
   NSLD - Total number of solid species.

NSORB - Total number of sorbed species.
NACAT - Total number of surfactant associated cations.

4. **NIAQ, NEX, NSLEL, NSURF1**
NIAQ - Total number of independent fluid species.
NEX - Total number of insoluble exchangers.
NSLEL - Total number of elements comprising the solid species.
NSURF1 - Position number corresponding to the *in situ* generated surfactant anion in the fluid species array FLDSPS.
Note: NSURF1 is automatically set to 0 by the program if IREACT = 2 or 4.

5. **NH, NNA, NCA, NMG, NCARB**
NH - Position number corresponding to the hydrogen element in the element array ELEMNT.
NNA - Position number corresponding to the sodium element in the element array ELEMNT.
NCA - Position number corresponding to the calcium element in the element array ELEMNT.
NMG - Position number corresponding to the magnesium element in the element array ELEMNT.
NCARB - Position number corresponding to the carbonate pseudo-element in the element array ELEMNT.
Note: If any of these elements is not considered, the position no. must be set equal to 0.

6. **NALU, NSILI, NOXY**
NALU - Position number corresponding to the aluminum element in the element array ELEMNT.
NSILI - Position number corresponding to the silicon element in the element array ELEMNT.
NOXY - Position number corresponding to the oxygen element in the element array ELEMNT.

7. **NACD** (This line is read only if IREACT = 3)
NACD - Position number corresponding to the petroleum acid pseudo-element in the element array ELEMNT.

8a. **NCR, NHFD, NCRFD** (This line is read only if IREACT = 4)
NCR - Position number corresponding to the chromium in the element array ELEMNT.
NHFD - Position number corresponding to the hydrogen ion element in the fluid species array FLDSPS.
NCRFD - Position number corresponding to CR(III) ion in the fluid species array FLDSPS.

8b. **ELEMNT(I), for I = 1, NELET**
ELEMNT(I) - Name of the I^{th} element.
Note: The name of each element may not exceed 32 characters and each name must be on a separate line of the input file.

8c. **ELCRG(I), for I = 1, NELET**
ELCRG(I) - Charge for the Ith element.

9. **FLDSPS(I), for I = 1, NFLD**
FLDSPS(I) - Name of the I^{th} fluid species.
Note: The name of each fluid species may not exceed 32 characters and each name must be on a separate line of the input file. If IREACT=3, the last fluid species must be HA_w (petroleum acid in water).

10. **SLDSPS(I), for I = 1, NSLD** (This line is read only if NSLD > 0)
SLDSPS(I) - Name of the I^{th} solid species.
Note: The name of each solid may not exceed 32 characters and each name must be on a separate line of the input file.

11. **SORBSP(I), for I = 1, NSORB** (This line is read only if NSORB > 0)

SORBSP(I) - Name of the I^{th} adsorbed cation.

Note: The name of each adsorbed cation may not exceed 32 characters and each name must be on a separate line of the input file.

12. **ACATSP(I), for I = 1, NACAT** (This line is read only if NACAT > 0)

ACATSP(I) - Name of the I^{th} surfactant adsorbed cation.

Note: The name of each surfactant adsorbed cation may not exceed 32 characters and each name must be on a separate line of the input file.

13. **NSORBX(I), for I = 1, NEX** (This line is read only if NSORB > 0)

NSORBX(I) - Number of cations for I^{th} exchanger.

14. **AR(I,J), for J = 1, NFLD, for I = 1, NELET** << or >>
AR(I,J), for J = 1, NFLD, for I = 1, NELET-1

AR(I,J) - Stoichiometric coefficient of I^{th} element in J^{th} fluid species.

Note: If ICHRGE = 0, then NFLD × NELET values are required by the program. If ICHRGE = 1, then NFLD × (NELET-1) values are required by the program.

15. **BR(I,J), for J = 1, NSLD, for I = 1, NELET** << or >>
BR(I,J), for J = 1, NSLD, for I = 1, NELET-1 (This line is read only if NSLD > 0)

BR(I,J) - Stoichiometric coefficient of I^{th} element in J^{th} solid species.

Note: If ICHRGE = 0, then NSLD × NELET values are required by the program. If ICHRGE = 1, then NSLD × (NELET-1) values are required by the program.

16. **DR(I,J), for J = 1, NSORB, for I = 1, NELET** << or >>
DR(I,J), for J = 1, NSORB, for I = 1, NELET-1 (This line is read only if NSORB > 1)

DR(I,J) - Stoichiometric coefficient of I^{th} element in J^{th} sorbed species.

Note: If ICHRGE = 0, then NSORB × NELET values are required by the program. If ICHRGE = 1, then NSORB × (NELET-1) values are required by the program.

17. **ER(I,J), for J = 1, NACAT, for I = 1, NELET** << or >>
ER(I,J), for J = 1, NACAT, for I = 1, NELET-1 (This line is read only if NACAT > 1)

ER(I,J) - Stoichiometric coefficient of I^{th} element in J^{th} surfactant associated cation.

Note: If ICHRGE = 0, then NACAT × NELET values are required by the program. If ICHRGE = 1, then NACAT × (NELET-1) values are required by the program.

18. **BB(I,J), for J = 1, NIAQ+NSORB+NACAT, for I = 1, NFLD+NSORB+NACAT**

BB(I,J) - Exponent of the J^{th} independent fluid species concentration when the I^{th} fluid species is expressed in terms of independent species concentrations.

19. **EXSLD(I,J), for J = 1, NIAQ, for I = 1, NSLD** (This line is read only if NSLD > 0)

EXSLD(I,J) - Exponent of the J^{th} independent fluid species concentration in the solubility product definition of the I^{th} solid.

20. **CHARGE(I), for I = 1, NFLD**

CHARGE(I) - Charge of the I^{th} fluid species.

21. **EQK(I), for I = 1, NFLD**

EQK(I) - Equilibrium constant for I^{th} fluid species when expressed in independent species concentrations only.

22. **SCHARG(I,J), for J = 1, NSORBX(I), for I = 1, NEX** (This line is read only if NSORB > 0)

    SCHARG(I,J) - Charge of the J^{th} sorbed species on the I^{th} exchanger.

23. **EXK(I,J), for J = 1, NSORBX(I)-1, for I = 1, NEX** (This line is read only if NEX > 0)

    EXK(I,J) - Exchange equilibrium constant for J^{th} exchange equilibrium of the I^{th} insoluble exchanger.

24. **EXEX(I,J,K), for K = 1, NIAQ+NSORB+NACAT, for J = 1, NSORBX(I)-1, for I = 1, NEX** (This line is read only if and NEX > 0)

    EXEX(I,J,K) - Exponent of K^{th} independent species in J^{th} equilibrium relation of the I^{th} exchanger

25. **REDUC(I,J), for J = 1, NSORBX(I)-1, for I = 1, NEX** (This line is read only if NEX > 0)

    REDUC(I,J) - Valence difference of the two cations involved in the exchange reaction J on exchanger I.

    Note: This value is positive if the higher valence cation bulk concentration has a positive exponent in EXEX(I,J) definition and is negative otherwise.

26. **EXCAI(I), for I = 1, NEX** (This line is read only if NEX >0)

    EXCAI(I) - Exchange capacity of I^{th} insoluble exchanger.
    Units: meq/ml pore volume

27. **SPK(I), for I = 1, NSLD** (This line is read only if NSLD > 0)

    SPK(I) - Solubility product of I^{th} solid defined in terms of independent fluid species concentrations only.

28. **CHACAT(I), for I = 1, NACAT** (This line is read only if NACAT > 0)

    CHACAT(I) - Charge of I^{th} surfactant associated cation.

29. **ACATK(I), for I = 1, NACAT-1** (This line is read only if NACAT > 0)

    ACATK(I) - Equilibrium constant for I^{th} exchange equilibrium for cation exchanges on surfactant.

30. **EXACAT(I,J) for J = 1, NIAQ+NSORB+NACAT, for I = 1, NACAT-1** (This line is read only if NACAT > 0)

    EXACAT(I,J) - Exponent of J^{th} independent species in I^{th} equilibrium for cation exchange on surfactant.

31. **C5I, CSURF**

    C5I - Initial concentration of chloride ion.
    Units: meq/ml
    CSURF- Initial concentration of surfactant.
    Units: vol. fraction

32. **CELAQI(J), for J = 1, NELET-1**

    CELAQI(J) - Initial concentrations of NELET-1 elements.
    Units: mole/liter

33. **CSLDI(I), for I = 1, NSLD** (This line is read only if NSLD > 0)
    CSLDI(I) - Initial concentration of I^{th} solid.
    Units: moles/liter pore volume

34. **CSORBI(I), for I = 1, NSORB** (This line is read only if NSORB > 0)
    CSORBI(I) - Initial concentration of I^{th} adsorbed cation.
    Units: moles/liter pore volume

35. **CAQI(J), for J = 1, NIND**
    CAQI(J) - Initial guesses for J^{th} independent species concentration, adsorbed species, and surfactant associated species.
    Units: moles/liter water

36. **S**
    S - Initial water saturation in core flooding or reservoir condition.
    Units: fraction

37. **EQWPS** (This line is read only if IREACT= 3)
    EQWPS - Equivalent weight of petroleum acid.

C.3 Tables

Table C.1. Water Analysis for Makeup and Formation Water

Ions	Formation water	Makeup water
Na^+, mg/l	2,398.90	52.9
Mg^{2+}, mg/l	36.46	11.54
Ca^{2+}, mg/l	54.2	67.13
Cl^-, mg/l	2091	39.00
HCO_3^-, mg/l	2623	152.55
CO_3^{2-}, mg/l	240	6.00
SO_4^{2-}, mg/l	—	134.56
pH	8.1	7.95

Table C.2. Example List of Elements and Reactive Species

Elements or pseudo-element:	Hydrogen (reactive), Sodium, Calcium, Magnesium, Carbonate, A (from acid HA), Chlorine,
Independent aqueous or oleic species:	H^+, Na^+,Ca^{2+}, Mg^{2+},CO_3^{2-}, HA_o, H_2O
Dependent aqueous or oleic species:	$Ca(OH)^+$, $Mg(OH)^+$, $Ca(HCO_3)^+$, HA_w, $Mg(HCO_3)^+$, OH^-, HCO_3^-, A^-, H_2CO_3, $CaCO_3^o$, $MgCO_3^o$
Solid species:	$CaCO_3$ (Calcite), $Ca(OH)_2$ (Calcium hydroxide), $MgCO_3$ (Magnesite), $Mg(OH)_2$ (Magnesium hydroxide)
Adsorbed cations:	$\overline{H}^+$, $\overline{Na}^+$, $\overline{Ca}^{2+}$, $\overline{Mg}^{2+}$
Adsorbed cations on micelles:	$\overline{\overline{Na}}^+$, $\overline{\overline{Ca}}^{2+}$, $\overline{\overline{Mg}}^{2+}$

Table C.3. List of Reactions for the Example Run

Partitioning of HA	**Partition Coefficient**
$HA_o \overset{K_D}{\rightleftarrows} HA_w$	$K_D = \dfrac{[HA_w]_{water}}{[HA_o]_{oil}}$
Aqueous Reactions	**Equilibrium Constant**
$H_2O \overset{K_1^{eq}}{\rightleftarrows} H^+ + OH^-$	$K_1^{eq} = [H^+]\ [OH^-]$
$HA_w + OH^- \overset{K_2^{eq}}{\rightleftarrows} A^- + H_2O$	$K_2^{eq} = \dfrac{[A^-]\ [H^+]}{[HA_w]}$
$H^+ + CO_3^{2-} \overset{K_3^{eq}}{\rightleftarrows} HCO_3^-$	$K_3^{eq} = \dfrac{[HCO_3^-]}{[H^+]\ [CO_3^{2-}]}$
$Ca^{2+} + H_2O \overset{K_4^{eq}}{\rightleftarrows} Ca(OH)^+ + H^+$	$K_4^{eq} = \dfrac{[Ca(OH)^+]\ [H^+]}{[Ca^{2+}]}$
$Mg^{2+} + H_2O \overset{K_5^{eq}}{\rightleftarrows} Mg(OH)^+ + H^+$	$K_5^{eq} = \dfrac{[Mg(OH)^+]\ [H^+]}{[Mg^{2+}]}$
$Ca^{2+} + H^+ + CO_3^{2-} \overset{K_6^{eq}}{\rightleftarrows} Ca(HCO_3)^+$	$K_6^{eq} = \dfrac{[Ca(HCO_3)^+]}{[Ca^{2+}]\ [CO_3^{2-}][H^+]}$
$Mg^{2+} + H^+ + CO_3^{2-} \overset{K_7^{eq}}{\rightleftarrows} Mg(HCO_3)^+$	$K_7^{eq} = \dfrac{[Mg(HCO_3)^+]}{[Mg^{2+}]\ [CO_3^{2-}][H^+]}$
$2H^+ + CO_3^{2-} \overset{K_8^{eq}}{\rightleftarrows} H_2CO_3$	$K_8^{eq} = \dfrac{[H_2CO_3]}{[CO_3^{2-}][H^+]^2}$
$Ca^{2+} + CO_3^{2-} \overset{K_9^{eq}}{\rightleftarrows} CaCO_3^o$	$K_9^{eq} = \dfrac{[CaCO_3^o]}{[Ca^{2+}]\ [CO_3^{2-}]}$
$Mg^{2+} + CO_3^{2-} \overset{K_{10}^{eq}}{\rightleftarrows} MgCO_3^o$	$K_{10}^{eq} = \dfrac{[MgCO_3^o]}{[Mg^{2+}]\ [CO_3^{2-}]}$

Table C.3. List of Reactions for the Example Run (cont.)

Dissolution Reactions	**Solubility Product**
$CaCO_3 \overset{K_1^{sp}}{\rightleftarrows} Ca^{2+} + CO_3^{2-}$	$K_1^{sp} = [Ca^{2+}]\left[CO_3^{2-}\right]$
$MgCO_3 \overset{K_2^{sp}}{\rightleftarrows} Mg^{2+} + CO_3^{2-}$	$K_2^{sp} = [Mg^{2+}]\left[CO_3^{2-}\right]$
$Ca(OH)_2 \overset{K_3^{sp}}{\rightleftarrows} Ca^{2+} + 2OH^-$	$K_3^{sp} = [Ca^{2+}]\left[H^+\right]^{-2}$
$Mg(OH)_2 \overset{K_4^{sp}}{\rightleftarrows} Mg^{2+} + 2OH^-$	$K_4^{sp} = [Mg^{2+}]\left[H^+\right]^{-2}$
Exchange Reactions (On Matrix)	**Exchange Equilibrium Constan**
$2\overline{Na}^{+} + Ca^{2+} \overset{K_1^{ex}}{\rightleftarrows} 2Na^{+} + \overline{Ca}^{2+}$	$K_1^{ex} = \dfrac{\left[\overline{Ca}^{2+}\right]\left[Na^{+}\right]^2}{\left[Ca^{2+}\right]\left[\overline{Na}^{+}\right]^2}$
$2\overline{Na}^{+} + Mg^{2+} \overset{K_2^{ex}}{\rightleftarrows} 2Na^{+} + \overline{Mg}^{2+}$	$K_2^{ex} = \dfrac{\left[\overline{Mg}^{2+}\right]\left[Na^{+}\right]^2}{\left[Mg^{2+}\right]\left[\overline{Na}^{+}\right]^2}$
$\overline{H}^{+} + Na^{+} + OH^- \overset{K_3^{ex}}{\rightleftarrows} \overline{Na}^{+} + H_2O$	$K_3^{ex} = \dfrac{\left[Na^{+}\right]\left[\overline{H}^{+}\right]}{\left[\overline{Na}^{+}\right]\left[H^{+}\right]}$
Exchange Reactions (On Micelle)	**Exchange Equilibrium Constan**
$2\overline{\overline{Na}}^{+} + Ca^{2+} \overset{K^{exm}_1}{\rightleftarrows} 2Na^{+} + \overline{\overline{Ca}}^{2+}$	$K_1^{exm} = \dfrac{\left[\overline{\overline{Ca}}^{2+}\right]\left[Na^{+}\right]^2}{\left[\overline{\overline{Na}}^{+}\right]^2\left[Ca^{2+}\right]}$ where $K_1^{exm} = \beta_1^{exm}\{[A^-] + [S^-]\}$
$2\overline{\overline{Na}}^{+} + Mg^{2+} \overset{K^{exm}_2}{\rightleftarrows} 2Na^{+} + \overline{\overline{Mg}}^{2+}$	$K_2^{exm} = \dfrac{\left[\overline{\overline{Mg}}^{2+}\right]\left[Na^{+}\right]^2}{\left[\overline{\overline{Na}}^{+}\right]^2\left[Mg^{2+}\right]}$ where $K_2^{exm} = \beta_2^{exm}\{[A^-] + [S^-]\}$

Table C.4. Stoichiometric Coefficient of I^{th} Element in J^{th} Fluid Species (for the AR Array)

		Ca	Mg	CO_3	Na	H	A
1	H^+	0	0	0	0	1	0
2	Na^+	0	0	0	1	0	0
3	Ca^{2+}	1	0	0	0	0	0
4	Mg^{2+}	0	1	0	0	0	0
5	CO_3^{2-}	0	0	1	0	0	0
6	HA_o	0	0	0	0	1	1
7	H_2O	0	0	0	0	2	0
8	$Ca(OH)^+$	1	0	0	0	1	0
9	$Mg(OH)^+$	0	1	0	0	1	0
10	$Ca(HCO_3)^+$	1	0	1	0	1	0
11	$Mg(HCO_3)^+$	0	1	1	0	1	0
12	A^-	0	0	0	0	0	1
13	OH^-	0	0	0	0	1	0
14	HCO_3^-	0	0	1	0	1	0
15	H_2CO_3	0	0	1	0	2	0
16	$CaCO_3$	1	0	1	0	0	0
17	$MgCO_3$	0	1	1	0	0	0
18	HA_w	0	0	0	0	1	1

Note: The transposition of this table is the form required for EQBATCH Program

Table C.5. Stoichiometric Coefficient of I^{th} Element in J^{th} Solid Species (for the BR Array)

	$CaCO_3$	$MgCO_3$	$Ca(OH)_2$	$Mg(OH)_2$
Ca	1	0	1	0
Mg	0	1	0	1
CO_3	1	1	0	0
Na	0	0	0	0
H	0	0	2	2
A	0	0	0	0

Table C.6. Stoichiometric Coefficient of I^{th} Element in J^{th} Sorbed Species (for the DR Array)

	H^+	Na^+	Ca^{2+}	Mg^{2+}
Ca	0	0	1	0
Mg	0	0	0	1
CO_3	0	0	0	0
Na	0	1	0	0
H	1	0	0	0
A	0	0	0	0

Table. C.7. Stoichiometric Coefficient of I^{th} Element in J^{th} Surfactant Associated Cation (for the ER Array)

	Na^+	Ca^{2+}	Mg^{2+}
Ca	0	1	0
Mg	0	0	1
CO_3	0	0	0
Na	1	0	0
H	0	0	0
A	0	0	0

Table C.8. Exponent of J^{th} Independent Fluid Species (for BB Array)

		H^+	Na^+	Ca^{2+}	Mg^{2+}	CO_3^{2-}	HA_o	H_2O	H^+	Na^+	Ca^{2+}	Mg^{2+}	Na^+	Ca^{2+}	Mg^{2+}
1	H^+	1													
2	Na^+		1												
3	Ca^{2+}			1											
4	Mg^{2+}				1										
5	CO_3^{2-}					1									
6	HA_o						1								
7	H_2O							1							
8	$Ca(OH)^+$	-1		1											
9	$Mg(OH)^+$	-1			1										
10	$Ca(HCO_3)^+$	1		1		1									
11	$Mg(HCO_3)^+$	1			1	1									
12	A^-	-1					1								
13	OH^-	-1													
14	HCO_3^-	1				1									
15	H_2CO_3	2				1									
16	$CaCO_3$			1		1									
17	$MgCO_3$				1	1									
18	HA_w						1								
19	H^+s								1						
20	Na^+s									1					
21	$Ca^{2+}s$										1				
22	$Mg^{2+}s$											1			
23	Na^+												1		
24	Ca^{2+}													1	
25	$Mg^{2+}sa$														1
										Sorbed Species			Surfactant Assoc. Cation		

Note: The blank cells in the above table need to be filled with zero for the input data for EQBATCH program.

Table C.9. Exponent of J^{th} Independent Species in the I^{th} Solid (for EXSLD Array)

	H^+	Na^+	Ca^{2+}	Mg^{2+}	CO_3^{2-}	HA_o	H_2O
$CaCO_3$	0	0	1	0	1	0	0
$MgCO_3$	0	0	0	1	1	0	0
$Ca(OH)_2$	-2	0	1	0	0	0	0
$Mg(OH)_2$	-2	0	0	1	0	0	0

Table C.10. Charge of I^{th} Fluid Species (for CHARGE Array)

	Fluid species	Charge
1	H^+	1
2	Na^+	1
3	Ca^{2+}	2
4	Mg^{2+}	2
5	CO_3^{2-}	-2
6	HA_o	0
7	H_2O	0
8	$Ca(OH)^+$	1
9	$Mg(OH)^+$	1
10	$Ca(HCO_3)^+$	1
11	$Mg(HCO_3)^+$	1
12	A^-	-1
13	OH^-	-1
14	HCO_3^-	-1
15	H_2CO_3	0
16	$CaCO_3$	0
17	$MgCO_3$	0
18	HA_w	0

Table C.11. Equilibrium Constants for I^{th} Fluid Species (for EQK Array)

	Fluid species	Equilibrium Constants
1	H^+	1
2	Na^+	1
3	Ca^{2+}	1
4	Mg^{2+}	1
5	CO_3^{2-}	1
6	HA_o	1
7	H_2O	1
8	$Ca(OH)^+$	0.12050E-12
9	$Mg(OH)^+$	0.38871E-11
10	$Ca(HCO_3)^+$	0.14124E+12
11	$Mg(HCO_3)^+$	0.58345E+12
12	A^-	0.85480E-14
13	OH^-	0.10093E-13
14	HCO_3^-	0.21380E+11
15	H_2CO_3	0.39811E+17
16	$CaCO_3$	0.15849E+04
17	$MgCO_3$	0.47863E+04
18	HA_w	0.85480E-04

Table C.12. Charge of J^{th} Sorbed Species (for SCHARG Array)

Adsorbed species	Charge
H^+(sorbed)	1
Na^+(sorbed)	1
Ca^{2+}(sorbed)	2
Mg^{2+}(sorbed)	2

Table C.13. Exchange Equilibrium Constants for J^{th} Exchange (for EXK Array)

Adsorbed	Equilibrium Constants
K_{ex1}	0.2623E+03
K_{ex2}	0.1509E+03
K_{ex3}	0.1460E+08

TableC.14. Exponent of K^{th} Independent Species in J^{th} Equilibrium Relation (for EXEX Array)

H^+	Na^+	Ca^{2+}	Mg^{2+}	CO_3^{2-}	HA_o	H_2O	H^+	Na^+	Ca^{2+}	Mg^{2+}	Na^+	Ca^{2+}	Mg^{2+}
0	2	-1	0	0	0	0	0	-2	1	0	0	0	0
0	2	0	-1	0	0	0	0	-2	0	1	0	0	0
-1	1	0	0	0	0	0	1	-1	0	0	0	0	0
							Sorbed Species				Surfactant Assoc. Cation		

Table C.15. Valence Difference Between Cation Involved In Exchange (for REDU Array)

	Ca^{2+}	Mg^{2+}	Na^+
Na^+	-1		
Na^+		-1	
H^+			0

Table C.16. Solubility Product of I^{th} Solid (for SPK Array)

$CaCO_3$	$MgCO_3$	$Ca(OH)_2$	Mg(OH)
0.4953E-09	0.00007	4.7315E+22	5.6104E+16

Table C.17. Charge of I^{th} Surfactant Associated Cation (for CHACAT Array)

Na^+	Ca^{2+}	Mg^{2+}
1	2	2

Table C.18. Equilibrium Constant for I^{th} Exchange (for ACATK Array)

Na^+	Ca^{2+}
2.5	2.94

Table C.19. Exponent of J^{th} Independent Species in I^{th} Cation Exchange on Surfactant (for EXACAT Array)

H^+	Na^+	Ca^{2+}	Mg^{2+}	CO_3^{2-}	HA_o	H_2O	H^+	Na^+	Ca^{2+}	Mg^{2+}	Na^+	Ca^{2+}	Mg^{2+}
0	2	-1	0	0	0	0	0	0	0	0	-2	1	0
0	2	0	-1	0	0	0	0	0	0	0	-2	0	1
							Sorbed Species				Surfactant Assoc. Cation		

Table C.20. Sample Input Data for EQBATCH Program

```
R1                                                          (* TITLE *)
3   1   1                                             (* IREACT ICHARGE IMG *)
7  18  4  4  3                                (* NNELET NFLD NSLD NSORB NACAT *)
7  1  4  12                                        (* NIAQ NEX NSLWL NSURF1 *)
5  4  1  2  3                                    (* NH NNA NCA NMG NCARB *)
0   0  0                                            (* NALU NSILI NOXYG *)
6                                                          (* NACD *)
CALCIUM
MAGNESIUM
CARBON (AS CARBOBATES)
SODIUM
HYDROGEN (REACTIVE)
ACID (PETROLEUM)
CHLORINE                                                  (* ELEMNT *)
2 2 -2 1 1 -1 -1                                           (* ELCRG *)
HYDROGEN ION
SODIUM ION
CALCIUM ION
```

Table C.20. Sample Input Data for EQBATCH Program (cont.)

```
MAGENSIUM ION
CARBONATE ION
PETROLEUM ACID IN OIL
WATER
CALCIUM MONOHYDROXIDE ION
MAGNESIUM MONOHYROXIDE ION
CA (HC03) +
MG (HCO3) +
PETRLEUM ACID ANION
HYDROXIDE ION
BICARBONATE ION
DISSOLVED CARBON MONOHYDROXIDE
AQUEOUS CALCIUM CARBONATE
AQUEOUS MAGNESIUM CARBONATE
PETROLEUM ACID IN OIL                                                    (* FLDSPS *)
CALCIUM CARBONATE(SOLID)
MAGNESIUM CARBONATE (SOLID)
CALCIUM HYDROXIDE (SOLID)
MAGNESIUM HYDROXIDE(SOLID)                                               (* SLDSPS *)
SORBED HYDROGEN ION
SORBED SODIUM ION
SORBED CALCIUM ION
SORBED MAGNESIUM ION                                                    (* SORBSPS *)
SURF. ASSOCIATED SODIUM ION
SURF. ASSOCIATED CALCIUM ION
SURF. ASSOCIATED MAGNESIUM ION                                          (* ACATSPC *)
4                                                                        (* NSORBX *)
0.  0.  1.  0.  0.  0.  0.  1.  0.  1.  0.  0.  0.  0. 0. 1. 0. 0.
0.  0.  0.  1.  0.  0.  0.  0.  1.  0.  1.  0.  0.  0. 0. 0. 1. 0.
0.  0.  0.  0.  1.  0.  0.  0.  0.  1.  1.  0.  0.  1. 1. 1. 1. 0.
0.  1.  0.  0.  0.  0.  0.  0.  0.  0.  0.  0.  0.  0. 0. 0. 0. 0.
1.  0.  0.  0.  0.  1.  2.  1.  1.  1.  1.  0.  1.  1. 2. 0. 0. 1.
0.  0.  0.  0.  0.  1.  0.  0.  0.  0.  0.  1.  0.  0. 0. 0. 0. 1.       (* AR *)
1.0  0.0  1.0  0.0
0.0  1.0  0.0  1.0
1.0  1.0  0.0  0.0
0.0  0.0  0.0  0.0
0.0  0.0  2.0  2.0
0.0  0.0  0.0  0.0                                                       (* BR *)
0.0  0.0  1.0  0.0
0.0  0.0  0.0  1.0
0.0  0.0  0.0  0.0
0.0  1.0  0.0  0.0
1.0  0.0  0.0  0.0
0.0  0.0  0.0  0.0                                                       (* DR *)
0.0  1.0  0.0
0.0  0.0  1.0
0.0  0.0  0.0
1.0  0.0  0.0
0.0  0.0  0.0
0.0  0.0  0.0                                                            (* ER *)
1.  0.  0.  0.  0.  0.  0.  0.  0.  0.  0.  0.  0.  0.
0.  1.  0.  0.  0.  0.  0.  0.  0.  0.  0.  0.  0.  0.
0.  0.  1.  0.  0.  0.  0.  0.  0.  0.  0.  0.  0.  0.
0.  0.  0.  1.  0.  0.  0.  0.  0.  0.  0.  0.  0.  0.
0.  0.  0.  0.  1.  0.  0.  0.  0.  0.  0.  0.  0.  0.
0.  0.  0.  0.  0.  1.  0.  0.  0.  0.  0.  0.  0.  0.
0.  0.  0.  0.  0.  0.  1.  0.  0.  0.  0.  0.  0.  0.
-1. 0.  1.  0.  0.  0.  0.  0.  0.  0.  0.  0.  0.  0.
-1. 0.  0.  1.  0.  0.  0.  0.  0.  0.  0.  0.  0.  0.
1.  0.  1.  0.  1.  0.  0.  0.  0.  0.  0.  0.  0.  0.
1.  0.  0.  1.  1.  0.  0.  0.  0.  0.  0.  0.  0.  0.
-1. 0.  0.  0.  0.  1.  0.  0.  0.  0.  0.  0.  0.  0.
-1. 0.  0.  0.  0.  0.  0.  0.  0.  0.  0.  0.  0.  0.
1.  0.  0.  0.  1.  0.  0.  0.  0.  0.  0.  0.  0.  0.
2.  0.  0.  0.  1.  0.  0.  0.  0.  0.  0.  0.  0.  0.
0.  0.  1.  0.  1.  0.  0.  0.  0.  0.  0.  0.  0.  0.
0.  0.  0.  1.  1.  0.  0.  0.  0.  0.  0.  0.  0.  0.
0.  0.  0.  0.  0.  1.  0.  0.  0.  0.  0.  0.  0.  0.
0.  0.  0.  0.  0.  0.  1.  0.  0.  0.  0.  0.  0.  0.
0.  0.  0.  0.  0.  0.  0.  1.  0.  0.  0.  0.  0.  0.
0.  0.  0.  0.  0.  0.  0.  0.  1.  0.  0.  0.  0.  0.
0.  0.  0.  0.  0.  0.  0.  0.  0.  1.  0.  0.  0.  0.
0.  0.  0.  0.  0.  0.  0.  0.  0.  0.  1.  0.  0.  0.
0.  0.  0.  0.  0.  0.  0.  0.  0.  0.  0.  1.  0.  0.
0.  0.  0.  0.  0.  0.  0.  0.  0.  0.  0.  0.  1.  0.
0.  0.  0.  0.  0.  0.  0.  0.  0.  0.  0.  0.  0.  1.                   (* BB *)
0.  0.  1.  0.  1.  0.  0.
0.  0.  0.  1.  1.  0.  0.
-2. 0.  1.  0.  0.  0.  0.
-2. 0.  0.  1.  0.  0.  0.                                               (* EXSLD *)
```

Table C.20. Sample Input Data for EQBATCH Program (cont.)

```
1.  1.  2.  2. -2.  0.  0. 1. 1. 1. 1. -1. -1. -1. 0. 0. 0. 0.                    (* CHAEGE *)
1.  1.  1.  1.  1.  1. 1.  0.1205e-12 0.38871e-11 0.14125e+12
0.58345e+12  0.959e-12 0.10093e-13 0.2138e+11 0.3981e+17
0.15849e+04  0.47863e+04  0.959-04                                                 (* KEQ *)
1.  1.  2.  2.                                                                  (* SCHARGE *)
0.793+01  0.52+01 0.27+07                                                         (* KEX *)
0.  2.  -1.  0.  0.  0.  0.  0.  -2.  1.  0.  0.  0.  0.
0.  2.  0.  -1.  0.  0.  0.  0.  -2.  0.  1.  0.  0.  0.
-1. 1.   0.  0.  0.  0.  0.  1.  -1.  0.  0.  0.  0.  0.                          (* EXEX *)
-1.  -1.  0.                                                                     (* REDUC *)
0.3403                                                                           (* EXCAI *)
0.474851e-09  0.00007 0.47315e+23 0.56045e+17                                     (* KSP *)
1.  2.   2.                                                                     (* CHACAT *)
2.5   2.94                                                                       (* KACAT *)
0.  2.  -1.  0.  0.  0.  0.  0.  0.  0.  0.  -2.  1.  0.0
0.  2.  0.  -1.  0.  0.  0.  0.  0.  0.  0.  -2.  0.  1.                        (* EXACAT *)
0.059   0.0                                                                   (*C50, Csurf*)
0.00135  0.0015  0.047 0.1043  111.043  0.019                          (*CELFLT 1,NELEMENT-1*)
2.00  0.0   0.0000  0.0                                                  (*CSLD(I), I=1,NSLD*)
 0.05 0.25  0.01  0.002                                                        (* CSORBI *)
0.1200077231590e-05 0.01 0.1e-04
0.46164233636603e-05 0.30926845820 95e-08 0.5399766653843e-03
55.49999314650  1.0e-06  1.0e-02   1.0e-03  1.0e-04
1.0e-06   1.0e-08   1.0e-08                                                        (*CIND*)
0.602                                                                            (*S1*)
500                                                                              (*EQW*)
```

Table C.21. Sample Output of EQBATCH Program

```
R1

      REACTIVE SYSTEM DESCRIPTION

      TOTAL NO. OF ELEMENTS LESS ONE  =  7
      TOTAL NO. OF FLUID SPECIES      = 18
      TOTAL NO. OF SOLID SPECIES      =  4
      TOTAL NO. OF ADSORBED SPECIES   =  4
      NO. OF CATIONS ASSOC. WITH SURF.=  3
      TOTAL NO. OF IND. FLUID SPECIES =  7
      TOTAL NO. OF EXCHANGER          =  1

     ELEMENT NO.           NAME                                    CHARGE

          1                CALCIUM                                   2
          2                MAGNESIUM                                 2
          3                CARBON (AS CARBOBATES)                   -2
          4                SODIUM                                    1
          5                HYDROGEN (REACTIVE)                       1
          6                ACID (PETROLEUM)                         -1
          7                CHLORINE                                 -1

      FLUID SPECIES NO.     NAME

      (INDEPENDENT)

          1                HYDROGEN ION
          2                SODIUM ION
          3                CALCIUM ION
          4                MAGENSIUM ION
          5                CARBONATE ION
6                PETROLEUM ACID IN OIL
          7                WATER

      (DEPENDENT)

          8                 CALCIUM MONOHYDROXIDE ION
          9                 MAGNESIUM MONOHYROXIDE ION
         10                CA (HC03) +
         11                MG (HCO3) +
         12                PETRLEUM ACID ANION
         13                HYDROXIDE ION
         14                BICARBONATE ION
         15                 DISSOLVED CARBON MONOHYDROXIDE
         16                AQUEOUS CALCIUM CARBONATE
         17                AQUEOUS MAGNESIUM CARBONATE
         18                PETROLEUM ACID IN OIL

      SOLID SPECIES NO.     NAME
```

Table C.21. Sample Output of EQBATCH Program (cont.)

```
          1                CALCIUM CARBONATE(SOLID)
          2                MAGNESIUM CARBONATE (SOLID)
          3                CALCIUM HYDROXIDE (SOLID)
          4                MAGNESIUM HYDROXIDE(SOLID)

     SORBED SPECIES NO.    NAME

          1                SORBED HYDROGEN ION
          2                SORBED SODIUM ION
          3                SORBED CALCIUM ION
          4                SORBED MAGNESIUM ION

     ASSOC. CATION NO.     NAME

          1                SURF. ASSOCIATED SODIUM ION
          2                SURF. ASSOCIATED CALCIUM ION
          3                SURF. ASSOCIATED MAGNESIUM ION


NO. OF MOLES OF ELEMENT I IN ONE MOLE OF
     FLUID SPECIES J

 J=      1   2   3   4   5   6   7   8   9  10  11  12  13  14  15  16  17  18  19  20  21  22  23
24  25

 I= 1   0.  0.  1.  0.  0.  0.  0.  1.  0.  1.  0.  0.  0.  0.  0.  1.  0.  0.
 I= 2   0.  0.  0.  1.  0.  0.  0.  0.  1.  0.  1.  0.  0.  0.  0.  0.  1.  0.
 I= 3   0.  0.  0.  0.  1.  0.  0.  0.  0.  1.  1.  0.  0.  1.  1.  1.  1.  0.
 I= 4   0.  1.  0.  0.  0.  0.  0.  0.  0.  0.  0.  0.  0.  0.  0.  0.  0.  0.
 I= 5   1.  0.  0.  0.  0.  1.  2.  1.  1.  1.  1.  0.  1.  1.  2.  0.  0.  1.
 I= 6   0.  0.  0.  0.  0.  1.  0.  0.  0.  0.  0.  1.  0.  0.  0.  0.  0.  1.


     NO. OF MOLES OF ELEMENT I IN ONE MOLE OF
     SOLID SPECIES K
 K=      1    2    3    4    5    6    7    8    9   10

 I= 1   1.   0.   1.   0.
 I= 2   0.   1.   0.   1.
 I= 3   1.   1.   0.   0.
 I= 4   0.   0.   0.   0.
 I= 5   0.   0.   2.   2.
 I= 6   0.   0.   0.   0.


     NO. OF MOLES OF ELEMENT I IN ONE MOLE OF
     ADSORBED SPECIES K

 K=      1    2    3    4    5

 I= 1   0.   0.   1.   0.
 I= 2   0.   0.   0.   1.
 I= 3   0.   0.   0.   0.
 I= 4   0.   1.   0.   0.
 I= 5   1.   0.   0.   0.
 I= 6   0.   0.   0.   0.


     NO. OF MOLES OF ELEMENT I IN ONE MOLE OF
     SURF. ASS. SPECIES K
```

Table C.21. Sample Output of EQBATCH Program (cont.)

```
 K=      1    2    3    4    5

 I= 1   0.   1.   0.
 I= 2   0.   0.   1.
 I= 3   0.   0.   0.
 I= 4   1.   0.   0.
 I= 5   0.   0.   0.
 I= 6   0.   0.   0.


     EXPONENT OF THE IND. SPECIES CONC. J
     FOR FLUID SPECIES I

 J=        1    2    3    4    5    6    7    8    9   10
```

Table C.21. Sample Output of EQBATCH Program (cont.)

```
 I= 1     1.   0.   0.   0.   0.   0.   0.
 I= 2     0.   1.   0.   0.   0.   0.   0.
 I= 3     0.   0.   1.   0.   0.   0.   0.
 I= 4     0.   0.   0.   1.   0.   0.   0.
 I= 5     0.   0.   0.   0.   1.   0.   0.
 I= 6     0.   0.   0.   0.   0.   1.   0.
 I= 7     0.   0.   0.   0.   0.   0.   1.
 I= 8    -1.   0.   1.   0.   0.   0.   0.
 I= 9    -1.   0.   0.   1.   0.   0.   0.
 I=10     1.   0.   1.   0.   1.   0.   0.
 I=11     1.   0.   0.   1.   1.   0.   0.
 I=12    -1.   0.   0.   0.   0.   1.   0.
 I=13    -1.   0.   0.   0.   0.   0.   0.
 I=14     1.   0.   0.   0.   1.   0.   0.
I=15     2.   0.   0.   0.   1.   0.   0.
 I=16     0.   0.   1.   0.   1.   0.   0.
 I=17     0.   0.   0.   1.   1.   0.   0.
 I=18     0.   0.   0.   0.   0.   1.   0.


FLUID SPECIES NO.                CHARGE

           1                      1.0
           2                      1.0
           3                      2.0
           4                      2.0
           5                     -2.0
           6                      0.0
           7                      0.0
           8                      0.0
           9                      1.0
          10                      1.0
          11                      1.0
          12                     -1.0
          13                     -1.0
          14                     -1.0
          15                      0.0
          16                      0.0
          17                      0.0
          18                      0.0


     ADSORBED SPECIES NO. CHARGE

           1               1.0
           2               1.0
           3               2.0
           4               2.0


     ASSOC. CATION(SURF)  CHARGE

           1               1.0
           2               2.0
           3               2.0


     EXPONENT OF IND. FLUID SPECIES J IN THE
     SOLUBILITY PRODUCT DEFINITION OF SOLID I

 J=        1    2    3    4    5    6    7    8    9   10   11   12   13   14   15

 I= 1     0.   0.   1.   0.   1.   0.   0.
 I= 2     0.   0.   0.   1.   1.   0.   0.
 I= 3    -2.   0.   1.   0.   0.   0.   0.
I= 4    -2.   0.   0.   1.   0.   0.   0.


     FLUID SPECIES NO.    EQUILM. CONSATNT

           1                0.10000E+01
           2                0.10000E+01
           3                0.10000E+01
           4                0.10000E+01
           5                0.10000E+01
           6                0.10000E+01
           7                0.10000E+01
           8                0.12050E-12
           9                0.38871E-11
          10                0.14125E+12
```

Table C.21. Sample Output of EQBATCH Program (cont.)

```
          11                0.58345E+12
          12                0.95900E-12
          13                0.10093E-13
          14                0.21380E+11
          15                0.39810E+17
16                0.15849E+04
          17                0.47863E+04
          18                0.95900E-04


     EXCHANGE EQUILIBRIUM CONSTANT FOR EQUILM. J
     OF THE EXCHANGER I

 J=           1         2         3         4         5

 I= 1   0.7930E+01   0.5200E+01   0.2700E+07


       EXCHANGER NO.       EXCHANGE CAPACITY

           1                              0.34030E+00

     EXPONENT OF THE IND. SPECIES CONC. K IN
     THE EXCHANGE EQUILIBRIUM J ON EXCHANGER I

     I= 1

 K=      1     2     3     4     5     6     7     8     9    10    11    12    13    14    15     16
17   18

 J=1   0.0   2.0  -1.0   0.0   0.0   0.0   0.0   0.0  -2.0   1.0   0.0   0.0   0.0   0.0
 J=2   0.0   2.0   0.0  -1.0   0.0   0.0   0.0   0.0  -2.0   0.0   1.0   0.0   0.0   0.0
 J=3  -1.0   1.0   0.0   0.0   0.0   0.0   0.0   1.0  -1.0   0.0   0.0   0.0   0.0   0.0

     SOLID NUMBER         SOLUBILITY PRODUCT

           1                0.47485E-09
           2                0.70000E-04
           3                0.47315E+23
           4                0.56045E+17

EXCHANGE EQLM. (I) ON SURF.  BETAS(I)

               1                0.25000E+01
               2                0.29400E+01

     EXPONENT OF THE IND. SPECIES CONC. K IN
     THE EXCHANGE EQUILIBRIUM J ON SURFACTANT

 K=      1     2     3     4     5     6     7     8     9    10    11    12    13    14    15     16
17   18

 J=1   0.0   2.0  -1.0   0.0   0.0   0.0   0.0   0.0   0.0   0.0   0.0  -2.0   1.0   0.0
 J=2   0.0   2.0   0.0  -1.0   0.0   0.0   0.0   0.0   0.0   0.0   0.0  -2.0   0.0   1.0

          INITIAL AQ. ELEMENTAL CONCS.(MOLES/L)

    1           2           3           4           5           6           7           8
9          10

 .13500E-02  .15000E-02  .47000E-01  .10430E+00  .11104E+03  .19000E-01

          INITIAL CHLORIDE CONC.(EQ/LITER)   =    0.5900E-01
          INITIAL SURFACTANT CONC.(EQ/LITER) =    0.0000E+00

INITIAL SOLID CONCS.(MOLES/LITRE PV)

    1           2           3           4           5           6           7           8
9          10

 .20000E+01  .00000E+00  .00000E+00  .00000E+00

          INITIAL ADSORED IONS(MOLES/LITRE PV)

    1           2           3           4           5           6           7           8
9          10
.50000E-01  .25000E+00  .10000E-01  .20000E-02

          INITIAL GUESSES OF INDEPENDENT CONCENTRATIONS
```

Table C.21. Sample Output of EQBATCH Program (cont.)

```
  1.200077231590000E-006  1.000000000000000E-002  1.000000000000000E-005
  4.616423363603000E-006  3.092684582095000E-009  5.399766653843000E-004
   55.4999931465000        1.000000000000000E-006  1.000000000000000E-002
  1.000000000000000E-003  1.000000000000000E-004  1.000000000000000E-006
  1.000000000000000E-008  1.000000000000000E-008

          END OF REACTION MODULE INPUT DATA

          RESIDUALS AT THE END OF 18 ITERATIONS IDAMP =  1

0.000E+00 0.000E+00 -.555E-16 0.142E-13 0.000E+00 0.000E+00 0.000E+00 0.999E-15
0.666E-15 0.000E+00 0.000E+00 -.486E-16 -.245E-12 0.000E+00

FLUID SPECIES CONCENTRATIONS

0.7849769316806E-08 0.7529549105585E-01 0.2274287723632E-05 0.5387616767727E-04
0.2087910843759E-03 0.1899585758862E-01 0.5548234868752E+02 0.3491206679296E-10
0.2667875232078E-07 0.5265052518920E-06 0.5151920872179E-04 0.2320708633881E-05
0.1285770268228E-05 0.3504100430504E-01 0.5121744571970E-03 0.7525913499000E-06
0.5384043523296E-04 0.1821702742749E-05

          SOLID SPECIES CONCENTRATIONS

0.2011131391413E+01 0.0000000000000E+00 0.0000000000000E+00 0.0000000000000E+00

          SORBED SPECIES CONCENTRATIONS

0.7318622640939E-01 0.2600025853849E+00 0.2150482869699E-03 0.3340545815905E-02

          SURF. ASSOCIATED CATION CONCS.

0.1900192355929E-01 0.6880963477427E-08 0.1916937102421E-06

          ELEMENT NO.        OLD TOTAL           NEW TOTAL               ERROR

               1         0.2011350000000E+01   0.2011350000000E+01   0.0000000000000E+00
               2         0.3500000000000E-02   0.3500000000000E-02   0.0000000000000E+00
               3         0.2047000000000E+01   0.2047000000000E+01   0.0000000000000E+00
               4         0.3543000000000E+00   0.3543000000000E+00   0.2220446049250E-15
               5         0.1110930000000E+03   0.1110930000000E+03  -0.1110223024625E-15
               6         0.1900000000000E-01   0.1900000000000E-01   0.0000000000000E+00

          ISOLN=  14

          COMPUTATION TIME=  0.00000E+00

          INITIAL CONDITIONS FOR UTCHEM

 C1I,C2I,C50,C60,C12I,C13I,C14I,C15I
  0.999997928798602        0.985633815850358        5.900000000000000E-002
  7.120600401936443E-006   9.429741461513917E-002    111.019813773591
  3.189083681891565E-004   7.173721717434252E-002
 A- + HA(WATER) =    4.142411376630453E-006  HA(OIL) =    2.915115922082504E-002
 VOLUMES FRACTIONS OF WATER,OIL AND ACID
  0.601998753136758        0.392282258708443        5.718988154799202E-003
 EQUIV. OF ACID/LITRE TOTAL VOL  1.143797630959840E-002
 EQK(          12)  EQK(          18)    6.249160552927827E-013
  6.249160552927826E-005
 CSLDI(I),I=1,NSLD UNIT=MOLES/LITER PV
   1.21069859002472        0.000000000000000E+000  0.000000000000000E+000
  0.000000000000000E+000
 CSORBI(I),I=1,NSORB UNIT=MOLES/LITER PV
  4.405801704523635E-002  0.156521232214020        1.294588006200680E-004
  2.011004415971278E-003
 EXCHANGE CAPACITY(MEQ/ML PV)=    0.204860175692439
```

Table C.22. Sample UTCHEM Input File Generated From EQBATCH Program

```
     FOLLOWING LINES OF DATA FORMATED FOR UTCHEM

 7 18  4  4  3  1
 7  1  4 12
 5  4  1  2  3
 6
 CALCIUM                         2
 MAGNESIUM                       2
 CARBON (AS CARBOBATES)          -2
 SODIUM                          1
 HYDROGEN (REACTIVE)             -1
```

Table C.22. Sample UTCHEM Input File Generated From EQBATCH Program (cont.)

```
 ACID (PETROLEUM)                -1
 CHLORINE
 HYDROGEN ION
 SODIUM ION
 CALCIUM ION
 MAGENSIUM ION
 CARBONATE ION
 PETROLEUM ACID IN OIL
 WATER
 CALCIUM MONOHYDROXIDE ION
 MAGNESIUM MONOHYROXIDE ION
 CA (HC03) +
 MG (HCO3) +
 PETRLEUM ACID ANION
 HYDROXIDE ION
 BICARBONATE ION
 DISSOLVED CARBON MONOHYDROXIDE
 AQUEOUS CALCIUM CARBONATE
 AQUEOUS MAGNESIUM CARBONATE
 PETROLEUM ACID IN OIL
 CALCIUM CARBONATE(SOLID)
 MAGNESIUM CARBONATE (SOLID)
 CALCIUM HYDROXIDE (SOLID)
 MAGNESIUM HYDROXIDE(SOLID)   (*
 SORBED HYDROGEN ION
 SORBED SODIUM ION
 SORBED CALCIUM ION
 SORBED MAGNESIUM ION         (*
 SURF. ASSOCIATED SODIUM ION
 SURF. ASSOCIATED CALCIUM ION
 SURF. ASSOCIATED MAGNESIUM ION
 4
 0.  0.  1.  0.  0.  0.  0.  1.  0.  1.  0.  0.  0.  0.  0.
 1.  0.  0.
 0.  0.  0.  1.  0.  0.  0.  0.  1.  0.  1.  0.  0.  0.  0.
 0.  1.  0.
 0.  0.  0.  0.  1.  0.  0.  0.  0.  1.  1.  0.  0.  1.  1.
 1.  1.  0.
0.  1.  0.  0.  0.  0.  0.  0.  0.  0.  0.  0.  0.  0.  0.
 0.  0.  0.
 1.  0.  0.  0.  0.  1.  2.  1.  1.  1.  1.  0.  1.  1.  2.
 0.  0.  1.
 0.  0.  0.  0.  0.  1.  0.  0.  0.  0.  0.  1.  0.  0.  0.
 0.  0.  1.
 1.  0.  1.  0.
 0.  1.  0.  1.
 1.  1.  0.  0.
 0.  0.  0.  0.
 0.  0.  2.  2.
 0.  0.  0.  0.
 0.  0.  1.  0.
 0.  0.  0.  1.
 0.  0.  0.  0.
 0.  1.  0.  0.
 1.  0.  0.  0.
 0.  0.  0.  0.
 0.  1.  0.
 0.  0.  1.
 0.  0.  0.
1.  0.  0.
 0.  0.  0.
 0.  0.  0.
 1.0  0.0  0.0  0.0  0.0  0.0  0.0  0.0  0.0  0.0  0.0  0.0
 0.0  0.0
 0.0  1.0  0.0  0.0  0.0  0.0  0.0  0.0  0.0  0.0  0.0  0.0
 0.0  0.0
 0.0  0.0  1.0  0.0  0.0  0.0  0.0  0.0  0.0  0.0  0.0  0.0
 0.0  0.0
 0.0  0.0  0.0  1.0  0.0  0.0  0.0  0.0  0.0  0.0  0.0  0.0
0.0  0.0
 0.0  0.0  0.0  0.0  1.0  0.0  0.0  0.0  0.0  0.0  0.0  0.0
 0.0  0.0
 0.0  0.0  0.0  0.0  0.0  1.0  0.0  0.0  0.0  0.0  0.0  0.0
 0.0  0.0
 0.0  0.0  0.0  0.0  0.0  0.0  1.0  0.0  0.0  0.0  0.0  0.0
 0.0  0.0
-1.0  0.0  1.0  0.0  0.0  0.0  0.0  0.0  0.0  0.0  0.0  0.0
 0.0  0.0
-1.0  0.0  0.0  1.0  0.0  0.0  0.0  0.0  0.0  0.0  0.0  0.0
 0.0  0.0
```

Table C.22. Sample UTCHEM Input File Generated From EQBATCH Program (cont.)

```
 1.0  0.0  1.0  0.0  1.0  0.0  0.0  0.0  0.0  0.0  0.0  0.0
 0.0  0.0
 1.0  0.0  0.0  1.0  1.0  0.0  0.0  0.0  0.0  0.0  0.0  0.0
 0.0  0.0
-1.0  0.0  0.0  0.0  0.0  1.0  0.0  0.0  0.0  0.0  0.0  0.0
 0.0  0.0
-1.0  0.0  0.0  0.0  0.0  0.0  0.0  0.0  0.0  0.0  0.0  0.0
0.0  0.0
1.0  0.0  0.0  0.0  1.0  0.0  0.0  0.0  0.0  0.0  0.0  0.0
 0.0  0.0
 2.0  0.0  0.0  0.0  1.0  0.0  0.0  0.0  0.0  0.0  0.0  0.0
 0.0  0.0
 0.0  0.0  1.0  0.0  1.0  0.0  0.0  0.0  0.0  0.0  0.0  0.0
 0.0  0.0
 0.0  0.0  0.0  1.0  1.0  0.0  0.0  0.0  0.0  0.0  0.0  0.0
 0.0  0.0
 0.0  0.0  0.0  0.0  0.0  1.0  0.0  0.0  0.0  0.0  0.0  0.0
 0.0  0.0
 0.0  0.0  0.0  0.0  0.0  0.0  0.0  1.0  0.0  0.0  0.0  0.0
 0.0  0.0
 0.0  0.0  0.0  0.0  0.0  0.0  0.0  0.0  1.0  0.0  0.0  0.0
 0.0  0.0
 0.0  0.0  0.0  0.0  0.0  0.0  0.0  0.0  0.0  1.0  0.0  0.0
 0.0  0.0
 0.0  0.0  0.0  0.0  0.0  0.0  0.0  0.0  0.0  0.0  1.0  0.0
 0.0  0.0
 0.0  0.0  0.0  0.0  0.0  0.0  0.0  0.0  0.0  0.0  0.0  1.0
 0.0  0.0
 0.0  0.0  0.0  0.0  0.0  0.0  0.0  0.0  0.0  0.0  0.0  0.0
 1.0  0.0
 0.0  0.0  0.0  0.0  0.0  0.0  0.0  0.0  0.0  0.0  0.0  0.0
 0.0  1.0
 0.0  0.0  1.0  0.0  1.0  0.0  0.0
 0.0  0.0  0.0  1.0  1.0  0.0  0.0
-2.0  0.0  1.0  0.0  0.0  0.0  0.0
-2.0  0.0  0.0  1.0  0.0  0.0  0.0
 1.0  1.0  2.0  2.0 -2.0  0.0  0.0  1.0  1.0  1.0  1.0 -1.0
-1.0 -1.0  0.0  0.0  0.0  0.0
 1.0  1.0  2.0  2.0
0.1000000000000E+01  0.1000000000000E+01  0.1000000000000E+01
0.1000000000000E+01  0.1000000000000E+01  0.1000000000000E+01
0.1000000000000E+01  0.1205000000000E-12  0.3887100000000E-11
0.1412500000000E+12  0.5834500000000E+12  0.6249160552928E-12
0.1009300000000E-13  0.2138000000000E+11  0.3981000000000E+17
0.1584900000000E+04  0.4786300000000E+04  0.6249160552928E-04
0.7930000000000E+01  0.5200000000000E+01  0.2700000000000E+07
 0.0  2.0 -1.0  0.0  0.0  0.0  0.0  0.0 -2.0  1.0  0.0  0.0
 0.0  0.0
 0.0  2.0  0.0 -1.0  0.0  0.0  0.0  0.0 -2.0  0.0  1.0  0.0
 0.0  0.0
-1.0  1.0  0.0  0.0  0.0  0.0  0.0  1.0 -1.0  0.0  0.0  0.0
 0.0  0.0
-1.0 -1.0  0.0
0.2048601756924E+00
0.4748510000000E-09  0.7000000000000E-04  0.4731500000000E+23
0.56045000000000E+17
1.0  2.0  2.0
0.2500000000000E+01  0.2940000000000E+01
 0.0  2.0 -1.0  0.0  0.0  0.0  0.0  0.0  0.0  0.0  0.0 -2.0
 1.0  0.0
 0.0  2.0  0.0 -1.0  0.0  0.0  0.0  0.0  0.0  0.0  0.0 -2.0
 0.0  1.0
0.1900192355929E-01  0.6880963477427E-08  0.1916937102421E-06
0.59000000000000E-01  0.71206000401936E-05
0.9429741461514E-01  0.1110198137736E+03  0.3189083681892E-03
0.7173721717434E-01  0.4142411376630E-05
0.2915115922083E-01
0.7849769316806E-08  0.7529549105585E-01  0.2274287723632E-05
0.5387616767727E-04  0.2087910843759E-03  0.1899585758862E-01
0.5548234868752E+02
0.1210698590025E+01  0.0000000000000E+00  0.0000000000000E+00
0.00000000000000E+00
0.4405801704524E-01  0.1565212322140E+00  0.1294588006201E-03
0.2011004415971E-02
0.9999979287986E+00  0.9856338158504E+00
0.1000000000000E-07  0.5000000000000E+03
```

References

Abbaszadeh-Dehghani, M. and W. E. Brigham. **1984**. "Analysis of Well to Well Tracer to Determine Reservoir Layering," *J. Pet. Tech.*, **36**(11), 1753-1762.

Abriola, L. M. and G. F. Pinder. **1985a**. "A Multiphase Approach to the Modeling of Porous Media Contamination by Organic Compounds: 2. Numerical Simulation," *Water Resources Res.*, **21** (1), 19.

Abriola, L. M. and G. F. Pinder. **1985b**. "Two-Dimensional Numerical Simulation of Subsurface Contamination by Organic Compounds - A Multiphase Approach," *Proceedings of Specialty Conference on Computer Applications in Water Resources,* ASCE.

Abriola, L. M., G. A. Pope and W. H. Wade. **1992**. "Surfactant Enhanced Remediation of Aquifers Contaminated by Dense Non-Aqueous Phase Liquids," Quarterly progress report for Dec. 1991-Feb. 1992 to R. S. Kerr Laboratories, U.S. EPA, Ada, OK.

Abriola, L. M., T. J. Dekker and K. D. Pennell. **1993**. "Surfactant Enhanced Solubilization of Residual Dodecane in Soil Columns: 2. Mathematical Modeling," *Environmental Science and Technology*, **27**(12), 2341-2351.

Abriola, L. M., K. D. Pennell, G. A. Pope, T. J. Dekker and D. J. Luning. **1994**. "Impact of Surfactant Flushing on the Solubilization and Mobilization of Dense Nonaqueous Phase Liquids," Paper presented before the division of Environmental Chemistry at the *207th National Meeting of American Chemical Society*, San Diego, CA, March 13-18.

Abriola, L. M., G. A. Pope, W. H. Wade and K. D. Pennell. **1995**. "Surfactant Enhanced Remediation of Aquifers Contaminated by Dense Non-Aqueous Phase Liquids," Final report to R. S. Kerr Laboratories, U.S. EPA, Ada, OK.

Adeel, Z. and R. G. Luthy. **1994**. "Concentration-Dependent Regimes in Sorption and Transport of a Nonionic Surfactant in Sand-Aqueous Systems," Paper presented before the division of Environmental Chemistry at the *207th National Meeting of American Chemical Society*, San Diego, CA, March 13-17.

Allison, S. B., G. A. Pope and K. Sepehrnoori. **1991**. "Analysis of Field Tracers for Reservoir Description," *J. Pet. Sci. Eng.*, **5**(2), 173.

Annable, M. D., J. W. Jawitz, P. S. C. Rao, D. P. Dai, H. Kim, H. and A. L. Wood. **1998**. "Field Evaluation of Interfacial and Partitioning Tracers for Characterization of Effective NAPL-Water Contact Areas," *Ground Water*, **36**, 495-502.

Arbogast, T. and M. F. Wheeler. **1995**. "A Characteristics-Mixed Finite Element Method for Advection Dominated Transport Problems," *SIAM Journal on Numerical analysis*, **32**, 404-424.

Babu, D. K. and A. S. Odeh. **1989**. "Productivity of a Horizontal Well," *Soc. Pet. Eng. Reservoir Eng.*, **4**, 417-421, Nov.

Babu, D. K., A. S. Odeh, A. J. Al-Khalifa and R. C. McCann. **1991**. "The Relation Between Wellblock and Wellbore Pressures in Numerical Simulation of Horizontal Wells," *Soc. Pet. Eng. Reservoir Eng.*, **6**, 324-328, Aug.

Baehr, A. L. and M. Y. Corapcioglu. **1987**. "Groundwater Contamination by Petroleum Products: 2. Numerical Solution," *Water Resour. Res.*, **23**(10), 201.

Bailey, J. E. and D. F. Ollis. **1986**. Biochemical Engineering Fundamentals, 2nd ed., McGraw Hill, New York, NY.

Ball, W. P. and P. V. Roberts. **1991**. "Long-Term Sorption of Halogenated Organic Chemicals by Aquifer Material: 1. Equilibrium," *Environmental Science and Technology*, **25**(7), 1223-1236.

Baran, J. R., Jr., G. A. Pope, W. H. Wade and V. Weerasooriya. **1994a**. "Phase Behavior of Water/Perchloroethylene/Anionic Surfactant Systems," *Langmuir*, **10**, 1146-1150.

References

Baran, J. R., Jr., G. A. Pope, W. H. Wade, V. Weerasooriya and A. Yapa. **1994b**. "Microemulsion Formation With Chlorinated Hydrocarbons of Differing Polarity," *Environmental Science and Technology*, **28**(7), 1361-1366.

Baran, J. R., Jr., G. A. Pope, W. H. Wade, V. Weerasooriya and A. Yapa. **1994c**. "Microemulsion Formation With Mixed Chlorinated Hydrocarbon Liquids," *J. Colloid and Interface Science*, **168**, 67-72.

Bear, J. **1979**. Hydraulics of Ground Water, McGraw Hill, New York.

Bell, J. B., P. Colella and J. A. Trangenstein. **1989**. "Higher-Order Godunov Methods for General Systems of Hyperbolic Conservation Laws," *J. Comp. Phys.*, **8**, 362-397.

Bennett, K. E., J. L. Fitzjohn, R. A. Harmon and P. C. Yates. **1988**. "Colloidal Silica-Based Fluid Diversions," U.S. Patent 4,732,213, March 22.

Bhuyan, D. **1989**. "Development of an Alkaline/Surfactant/Polymer Flood Compositional Reservoir Simulator," Ph.D. dissertation, The University of Texas at Austin.

Bhuyan, D., G. A. Pope and L. W. Lake. **1990**. "Mathematical Modeling of High-pH Chemical Flooding," *Soc. Pet. Eng. Reservoir Eng.*, May.

Bhuyan, D., G. A. Pope and L. W. Lake. **1991**. "Simulation of High-pH Coreflood Experiments Using a Compositional Chemical Flood Simulator," *Proceedings of the SPE International Symposium on Oilfield Chemistry*, Anaheim, CA, Feb. 20-22.

Blunt, M. and B. Rubin. 1992. "Implicit Flux Limiting Schemes for Petroleum Reservoir Simulation," *J. of Computational Physics*, **102**(1), 194-209.

Borden, R. C. and P. B. Bedient. **1986**. "Transport of Dissolved Hydrocarbons Influenced by Oxygen-Limited Biodegradation; 1. Theoretical Development," *Water Resour. Res.*, **22**(13), 1973-1982, Dec.

Bourrel, M. and R. S. Schechter. **1988**. Microemulsions and Related Systems, Marcel Dekker, Inc., New York.

Brock, Thomas D., D. W. Smith and M. T. Madigan. **1984**. Biology of Microorganisms, 4th Ed., Prentice-Hall, Englewood Cliffs, NJ.

Brooks, R. H. and A. T. Corey. **1966**. "Properties of Porous Media Affecting Fluid Flow," *J. Irrig. Drain. Div.*, **6**, 61.

Brown, C. L. **1993**. "Simulation of Surfactant Enhanced Remediation of Aquifers Contaminated with Dense Non-Aqueous Phase Liquids," M.S. thesis, The University of Texas at Austin.

Brown, C. L., G. A. Pope, L. M. Abriola and K. Sepehrnoori. **1994**. "Simulation of Surfactant Enhanced Aquifer Remediation," *Water Res. Res.*, **30**(11), 2959-2977.

Brown, C. L., M. Delshad, V. Dwarakanath, D.C. McKinney and G. A. Pope. **1996**. "Design of a Field-Scale Surfactant Enhanced Remediation of a DNAPL Contaminated Aquifer," presented at the *I&EC Special Symposium, American Chemical Society*, Birmingham, AL, Sept. 9-12.

Brownell, L. E and D. L. Katz. **1949**. "Flow of Fluids Through Porous Media, Part II," *Chemical Engineering Process*, **43**, 601-612.

Brusseau, M. L. and P. S. C. Rao. **1989**. "Sorption Nonideality During Organic Contaminant Transport in Porous Media," *CRC Crit. Rev. Enviorn. Control*, **19**(1), 33-93.

Bryant, S. L., R. S. Schechter and L. W. Lake. **1986**. "Interaction of Precipitation/Dissolution Waves and Ion-Exchange in Flow Through Porous Media," *AIChE J.*, 751-764, May.

Buckley, S. E. and M. C. Leverett. **1942**. "Mechanism of Fluid Displacements in Sands," *Trans. AIME*, **146**, 107-116.

Burdine, N. T. **1953**. "Relative Permeability Calculations from Pore-Size Distribution Data," *Petr. Trans., Am. Inst. Mining Metall. Eng.*, **198**, 71-77.

References

Butler, G and M. Jin. **1996**. "Application of the UTCHEM Simulator to DNAPL Characterization and Remediation Problems," *report prepared for the Center for Petroleum and Geosystems Engineering*, Sept.

Camilleri, D., A. Fil, G. A. Pope, B. A. Rouse and K. Sepehrnoori. **1987a**. "Comparison of an Improved Compositional Micellar/Polymer Simulator With Laboratory Core Floods," *Soc. Pet. Eng. Reservoir Eng.*, Nov.

Camilleri, D., A. Fil, G. A. Pope and K. Sepehrnoori. **1987b**. "Improvements in Physical-Property Models Used in Micellar/Polymer Flooding," *Soc. Pet. Eng. Reservoir Eng.*, Nov.

Camilleri, D., E. Lin, T. Ohno, S. Engelsen, G. A. Pope and K. Sepehrnoori. **1987c**. "Description of an Improved Compositional Micellar/Polymer Simulator," *Soc. Pet. Eng. Reservoir Eng.*, Nov.

Cayais, J. L., R. S. Schechter and W. H. Wade. **1975**. "The Measurement of Low Interfacial Tension Via the Spinning Drop Technique," in Adsorption at Interfaces, ACS Symposium series, 8, J. R. Gould (ed), American Chemical Society, Washington DC, 234.

Chang, H. and L. Alvarez-Cohen. **1995**. "Model for the Cometabolic Biodegradation of Chlorinated Organics," *Environmental Science and Technology*, **29**(9), 2357-2367.

Chatzis, I. and N. R. Morrow. **1981**. "Correlation of Capillary Number Relationships for Sandstones," SPE 10114, *Proceedings of the 56th Annual Conference of the SPE*, San Antonio, TX, Oct. 5-7.

Chen, J. **1993**. "New Approaches to Dual Porosity Modeling of Waterflooding in Naturally Fractured Reservoirs," Ph.D. dissertation, The University of Texas at Austin.

Chen, J., M. A. Miller and K. Sepehrnoori. **1994**. "An Approach for Implementing Dual Porosity Models in Existing Simulators," SPE 28001, presented at the *University of Tulsa/SPE Centennial Petroleum Engineering Symposium*, Tulsa, OK, Aug. 29-31.

Chen, M. M. **1993**. "Deriving the Shape Factor of a Fractured Rock Matrix," *U.S. Dept. of Energy Topical Report*, NIPER-696, Sept.

Chen, Y., L. M. Abriola, P. J. J. Alvarez, P. J. Anid and T. M. Vogel. **1992**. "Modeling Transport and Biodegradation of Benzene and Toluene in Sandy Aquifer Material: Comparisons With Experimental Measurements," *Water Resour. Res.*, **28**(7): 1833-1847, July.

Cherry, J. A., S. Feenstra, B.H. Kueper and D. W. McWhorter. **1990**. "Status of In Situ Technologies for Cleanup of Aquifers Contaminated by DNAPLs Below Water Table," *Int'l Specialty Conf. on How Clean is Clean?, Cleanup Criteria for Contaminated Soil and Groundwater, Air and Waste Management Association*, Nov.

Chiou, C. T., P. E. Porter and D. W. Schmedding. **1983**. "Partition Equilibria of Nonionic Organic Compounds Between Soil Organic Matter and Water," *Environmental Science and Technology* **17**, 227-231.

Corey, A. T., C. H. Rathjens, J. H. Henderson and M. R. Wyllie. **1956**. "Three-Phase Relative Permeability," *Trans. AIME*, 349-351.

DE&S. **1999a**. "DNAPL Site Characterization Using a Partitioning Interwell Tracer Test at Site 88, Marine Corps Base, Camp Lejeune, North Carolina," *report prepared for Naval Facilities Engineering Service Center, Port Hueneme, California*.

DE&S. **1999b**. "Work Plan for Surfactant-Enhanced Aquifer Remediation Demonstration, Site 88 Marine Corps Base, Camp Lejeune, North Carolina," *report prepared for Naval Facilities Engineering Service Center, Port Hueneme, California*.

Dakhlia, H., W. Wu, M. T. Lim, M. Delshad, G. A. Pope and K. Sepehrnoori. **1995**. "Simulation of Surfactant Flooding Using Horizontal Wells," SPE/CIM 95-82, *SPE/CIM Annual Technical Meeting*, Banff, Alberta, Canada, May 14-17.

References

Datta Gupta, A., G. A. Pope, K. Sepehrnoori and R. L. Thrasher. **1986**. "A Symmetric, Positive Definite Formulation of a Three-Dimensional Micellar/Polymer Simulator," *Soc. Pet. Eng. Reservoir Eng.*, **1**(6), 622-632, Nov.

Datta Gupta, A., L. W. Lake, G. A. Pope, K. Sepehrnoori and M. J. King. **1991**. "High Resolution Monotonic Schemes for Reservoir Fluid Flow Simulation," *In Situ*, **15**(3), 289-317.

Dawson, C. N. **1993**. "Godunov-Mixed Methods for Advection-Diffusion Equations in Multidimensions," *SIAM Journal on Numerical Analysis*, **3**(5), 1315-1332.

de Blanc, P. C. **1998**. "Development and Demonstration of a Biodegradation Model for Non-Aqueous Phase Liquids in Groundwater," Ph.D. dissertation, The University of Texas at Austin.

de Blanc, P. C., D. C. McKinney and G. E. Speitel, Jr. **1995**. "Modeling Subsurface Biodegradation of Non-Aqueous Phase Liquids: A Literature Review," Technical Report CMWR 257, The University of Texas at Austin.

de Blanc, P. C., D. C. McKinney, G. E. Speitel, Jr., K. Sepehrnoori and M. Delshad. **1996a**. "A 3-D NAPL Flow and Biodegradation Model," *Non-aqueous Phase Liquids (NAPLs), Subsurface Environment: Assessment and Remediation* (Proceedings of the specialty conference held in conjunction with the ASCE National convention, Washington D.C.), L. N. Reddi, (ed.), ASCE, New York, NY, Nov. 12-14.

de Blanc, P. C., K. Sepehrnoori, G. E. Speitel, Jr. and D. C. McKinney. **1996b**. "Investigation of Numerical Solution Techniques for Biodegradation Equations in a Groundwater Flow Model," *Proceedings of the XI International Conference on Computational Methods in Water Resources*, Cancun, Mexico, July 22-26.

Deimbacher, F. X. and Z. E. Heinemann. **1993**. "Time Dependent Incorporation of Locally Irregular Grids in Large Reservoir Simulation Models," paper SPE 25260, Proc., *Twelfth SPE Reservoir Simulation Symposium*, New Orleans, LA, 301 - 320, Feb. 28 - Mar. 3.

Delshad, Mohammad. **1990**. "Trapping of Micellar Fluids in Berea Sandstone," Ph.D. dissertation, The University of Texas at Austin.

Delshad, Mojdeh, Mohammad Delshad, D. Bhuyan, G. A. Pope and L. Lake. **1986**. "Effect of Capillary Number on the Residual Saturation of a Three-Phase Micellar Solution," SPE 14911, *Proceedings of the SPE/DOE Fifth Symposium on Enhanced Oil Recovery*, Tulsa, OK, April 20-23.

Delshad, Mojdeh, Mohammad Delshad, G. A. Pope and L.W. Lake. **1987**. "Two- and Three-Phase Relative Permeabilities of Micellar Fluids," *SPE Formation Evaluation.*, Sept.

Delshad, Mojdeh and G. A. Pope. **1989**. "Comparison of the Three-Phase Oil Relative Permeability Models," *J. Transport in Porous Media*, **4**, 59-83.

Delshad, Mojdeh, G. A. Freeze, R. E. Jackson, D. C. McKinney, G. A. Pope, K. Sepehrnoori, M. M. Sharma and G. E. Speitel, Jr. **1994**. "Three-Dimensional NAPL Fate and Transport Model," poster presented at *RSKERL Ground Water Research Seminar*, Oklahoma City, OK, June 1-3.

Delshad, Mojdeh, G. A. Pope and K. Sepehrnoori. **1996**. "A Compositional Simulator for Modeling Surfactant Enhanced Aquifer Remediation," *Journal of Contaminant Hydrology*, **23**, 303-327.

Descant, F. J., III. **1989**. "Simulation of single–well tracer flow," M.S. thesis, The University of Texas at Austin.

Dwarakanath, V. **1997**. "Characterization and Remediation of Aquifers Contaminated by Nonaqueous Phase Liquids Using Partitioning Tracers and Surfactants," Ph.D. dissertation, The University of Texas at Austin.

Dwarakanath, V., B. A. Rouse, G. A. Pope, D. Kostarelos, D. Shotts and K. Sepehrnoori. **1998**. "Surfactant Remediation of Soil Columns Contaminated by Nonaqueous Phase Liquids," accepted by *Journal of Contaminant Hydrology*.

References

Dwarakanath, V., K. Kostarelos, D. Shotts, G. A. Pope and W. H. Wade. **1999**. "Anionic Surfactant Remediation of Soil Columns Contaminated by Nonaqueous Phase Liquids," *J. Contaminant Hydrology*, **38**(4), 465-488.

Dwarakanath, V. and G. A. Pope. **2000**. "Surfactant Phase Behavior with Field Degreasing Solvent," submitted to *ES&T*, Jan.

Edwards, M. G. **1992a**. "A Dynamically Adaptive Godunov Scheme for Reservoir Simulation on Large Aspect Ratio Grids," *Proc., Numerical Methods For Fluid Dynamics*, K. W. Morton and M. J. Baines (eds.), Reading University, UK, April 7-10.

Edwards, M. G. **1992b**. "A Dynamically Adaptive Higher Order Godunov Scheme for Reservoir Simulation in Two Dimensions," *Proc., 3rd European Conference on the Mathematics of Oil Recovery*, M. A. Christie, F.V. Da Silva, C. L. Farmer, O. Guillon, and Z. E. Heinmann (eds.), Delft University Press, The Netherlands, 239-249, June 17-19.

Edwards M. G. and M. A. Christie. **1993**. "Dynamically Adaptive Godunov Schemes With Renormalization for Reservoir Simulation," SPE 25268, *Proc., Twelfth SPE Reservoir Simulation Symposium*, New Orleans, LA, 413-422, Feb. 28 - Mar. 3.

Espedal, M. S., R. E. Ewing and T. F. Russell. **1990**. "Mixed Methods, Operator Splitting, and Local Refinement Techniques for Simulation on Irregular Grids," *Proc., 2nd European Conference on the Mathematics of Oil Recovery*, Arles, France, Sept. 11-14.

Faust, J. C., J. H. Guswa and J. W. Mercer. **1989**. "Simulation of Three-Dimensional Flow of Immiscible Fluids Within and Below the Saturated Zone," *Water Resour. Res.*, **25**(12), 2449.

Fayers, F. J. and J. P. Matthews. **1982**. "Evaluation of Normalized Stone's Methods for Estimating Three-Phase Relative Permeabilities," *Soc. Pet. Eng. J.*, **24**, 224-232.

Ferreira, L. E. A., F. J. Descant, M. Delshad, G. A. Pope and K. Sepehrnoori. **1992**. "A Single–Well Tracer Test to Estimate Wettability," SPE 24136, presented at the *SPE/DOE Eighth Symposium on Enhanced Oil Recovery*, Tulsa, Oklahoma, April 22–24.

Fetter, C. W. **1993**. Contaminant Hydrology, Macmillan Publishing Company, New York.

Flory, P. J. **1953**. Principles of Polymer Chemistry, Ithaca, New York. Cornell University Press.

Fountain, J. C. **1992**. "Field Test of Surfactant Flooding: Mobility Control of Dense Nonaqueous Phase Liquids," Chapter 15 in Transport and Remediation of Subsurface Contaminants, D. A. Sabatini and R. C. Knox (eds.), American Chemical Society Symposium Series 491, ACS, Washington, DC.

Fountain, J. C. and D. S. Hodge. **1992**. "Extraction of Organic Pollutants Using Enhanced Surfactant Flushing: Initial Field Test (Part 1)," *Project Summary, New York Center for Hazardous Waste Management*, State University of New York at Buffalo, Buffalo, NY, Feb.

Fountain, J. C., R. C. Starr, T. Middleton, M. Beikirch, C. Taylor and D. Hodge. **1996**. "A Controlled Field Test of Surfactant-Enhanced Aquifer Remediation," *Ground Water*, **34**, 910-916.

Freeze, G. A., J. C. Fountain and G. A. Pope. **1985**. "Modeling the Surfactant-Enhanced Remediation of PCE at the Borden Test Site Using the UTCHEM Compositional Simulator," *Toxic Subsurface and the Hydrologic Sciences*, American Institute of Hydrology, 339-345.

Fulcher, R. A., T. Ertekin and C. D. Stahl. **1985**. "Effect of Capillary Number and its Constituents on Two-Phase Relative Permeability Curves," *Journal of Petroleum Technology*, 249-260, Feb.

Garver, F. J., M. M. Sharma and G. A. Pope. **1989**. "The Competition for Chromium Between Xanthan Biopolymer and Resident Clays in Sandstone," SPE 19632, *Proceedings of the 64th Annual Conference*, San Antonio, TX, Oct. 8-11.

Gear, C. W. **1971**. Numerical Initial Value Problems in Ordinary Differential Equations, Prentice-Hall, Englewood Cliffs, NJ.

References

Glover, C. J., M. C. Puerto, J. M. Maerker and E. I. Sandvik. 1979. "Surfactant Phase Behavior and Retention in Porous Media," *Soc. Pet. Eng. J.*, **19**, 183-193.

Guarnaccia, J. F., P. T. Imhoff, B. C. Missildine, M. Oostrom, M. A. Celia, J. H. Dane, P. R. Jaffe and G. F. Pinder. **1992**. "Multiphase Chemical Transport in porous media," *EPA Environmental Research Brief*, EPA/600/S-92/002, March.

Hand, D. B. **1939**. "Dineric Distribution: I. The Distribution of a Consolute Liquid Between Two Immiscible Liquids," *J. of Physics and Chem.*, **34**, 1961-2000.

Harten, A. **1983**. "High Resolution Schemes for Hyperbolic Conservation Laws," *SIAM Rev.*, **25**(1), 35-67.

Harvey, R. H., R. L. Smith and L. H. George. **1984**. "Effect of Organic Contamination Upon Microorganism Distributions and Heterotrophic Uptake in a Cape Cod, Mass., Aquifer," *Applied and Environmental Microbiology*, **48**(6), 1197-1202, Dec.

Healy, R. N. and R. L. Reed. **1974**. "Physicochemical Aspects of Microemulsion Flooding," *Soc. Pet. Eng. J.*, **14**, 491-501.

Hirasaki, G. J. **1981**. "Application of the Theory of Multicomponent, Multiphase Displacement to Three-Component, Two-Phase Surfactant Flooding," *Soc. Pet. Eng. J.*, 191-204.

Hirasaki, G. J. **1982**. "Interpretation of the Change in Optimal Salinity With Overall Surfactant Concentration," *Soc. Pet. Eng. J.*, 971-982, Dec.

Hirasaki, G. J. and G. A. Pope. **1974**. "Analysis of Factors Influencing Mobility and Adsorption in the Flow of Polymer Solution Through Porous Media," *Soc. Pet. Eng. J.*, 337-346, Aug.

Hirasaki, G. J., C. A. Miller, R. Szafranski, D. Tanzil, J. B. Lawson, H. Meinardus, M. Jin, R. E. Jackson, G. A. Pope and W. H. Wade. **1997**. Presented at the *1997 SPE Annual Technical Conference and Exhibition*, San Antonio, TX, October 5-8.

Holzmer, F. J., G. A. Pope and L. Yeh. **2000**. "Surfactant-Enhanced Aquifer Remediation of PCE-DNAPL in Low-Permeability Sand," presented at *The Second International Conference on Remediation of Chlorinated and Recalcitrant Compounds*, May 22-25, Monterey, CA.

Huh, C. **1979**. "Interfacial Tension and Solubilizing Ability of a Microemulsion Phase That Coexists With Oil and Brine," *J. Colloid Interface Sci.*, **71**, 408-428.

Hunt, J. A. **1987**. "An Experimental Study of the Kinetics of the Crosslinking Reaction Between Chromium(III) and Polyacrylamide," Ph.D. dissertation, U. of Kansas, Lawrence.

Iler, R. K. **1979**. The Chemistry of Silica: Solubility, Polymerization, Colloid and Surface Properties, and Biochemistry, John Wiley & Sons, New York.

Imhoff, P. T., S. N. Gleyzer, J. F. McBride, L. A. Vancho, I. Okuda and C. T. Miller. **1995**. "Cosolvent-Enhanced Remediation of Residual Dense Nonaqueous Phase Liquids: Experimental Investigation," *Environmental Science and Technology*, **29**, 1966-1976.

Intera. **1996**. "Phase I Work Plan," Hill Air Force Base, 00-ALC/EMR.

Intera. **1997**. "AATDF Surfactant/Foam Process for *Contaminant Hydrology* **34** 383-397, Aquifer Remediation," prepared for the Advanced Applied Technology Demonstration Facility, Rice University, Houston, TX, Nov.

Intera. **1998**. "Demonstration of Surfactant Enhanced Aquifer Remediation of Chlorinated Solvent DNAPL at Operable Unit 2, Hill AFB, Utah," Final Report prepared by INTERA for the Air Force Center for Environmental Excellence, Technology Transfer Division, January.

Jin, M. **1995**. "A Study of Nonaqueous Phase Liquid Characterization and Surfactant Remediation," Ph.D. dissertation, The University of Texas at Austin.

References

Jin, M, M. Delshad, V. Dwarakanath, D. C. McKinney, G. A. Pope, K. Sepehrnoori, C. E. Tilburg and R. E. Jackson. **1995**. "Partitioning Tracer Test for Detection, Estimation, and Remediation Performance Assessment of Subsurface Nonaqueous Phase Liquids," *Water Resour. Res.*, **31**(5), 1201-1211.

Jurinak, J. J., L. E. Summers and K. E. Bennett. **1989**. "Oilfield Application of Colloidal Silica Gel," SPE 18505, presented at the *SPE International Symposium on Oilfield Chemistry*, Houston, Texas, Feb. 8-10.

Kahaner, D., C. Moler and S. Nash. **1989**. Numerical Methods and Software, Prentice Hall, Englewood Cliffs, NJ.

Kalurachchi, J. J. and J. C. Parker. **1990**. "Modeling Multicomponent Organic Chemical Transport in Three-Phase Porous Media," *J. of Contaminant Transport*, **5**, 349.

Kalurachchi, J. J. and J. C. Parker. **1992**. "Multiphase Flow With a Simplified Model for Oil Entrapment," *Journal of Transport in Porous Media*, **7**, 1-14.

Karickhoff, S. W. **1984**. "Organic Pollutant Sorption in Aquatic Systems," *J. Hydraulic Eng.*, **110**(6), 707-735.

Kazemi, H., L. S. Merrill, Jr., K. L. Porterfield and P. R. Zeman. **1976**. "Numerical Simulation of Water-Oil Imbibition in Naturally Fractured Reservoirs," *Soc. Pet. Eng. J.*, 317-326, Dec.

Kim, H. **1995**. "A Simulation Study of Gel Conformance Treatments," Ph.D. dissertation, The University of Texas, Austin.

Kinniburgh, J. G. **1986**. "General Purpose Adsorption Isotherms," *Environmental Science and Technology*, **20**, 895-904.

Kostarelos, K. **1998**. "Surfactant Enhanced Aquifer Remediation at Neutral Buoyancy," Ph.D dissertation, The University of Texas at Austin.

Knox, R. C., D. A. Sabatini and A. Thal, A. **1996**. In Proceedings of the *I&EC Special Symposium*, Tedder, D. W., Ed., American Chemical Society, Birmingham, AL, 116.

Kostarelos, K., G. A. Pope, B. A. Rouse and G. M. Shook. **1998**. "A New Concept: The Use of Neutrally-Buoyant Microemulsions for DNAPL Remediation," *J. Contaminant Hydrology*, **34** 383-397.

Kristensen, R., T. Lund, V. I. Titov and N. I. Akimov. **1993**. "Laboratory Evaluation and Field Tests of a Silicate Gel System Aimed to be Under North Sea Conditions," paper presented at the *Seventh European IOR Symposium*, Moscow, Russia, Oct. 26-29.

Kueper, B. H. **1989**. "The Behavior of Dense, Non-Aqueous Phase Liquid Contaminants in Heterogeneous Porous Media," Ph.D. dissertation, The University of Waterloo, Ontario.

Kueper, B. H. and E. O. Frind. **1991**. "Two-Phase Flow in Heterogeneous Porous Media 1. Model Development," *Water Resour. Res.*, **27**(6), 1049-1057.

Kueper, B. H., D. Redman, R. C. Starr, S. Reitsma and M. Mah. **1993**. "A Field Experiment to Study the Behavior of Tetrachloroethylene Below the Water Table: Spatial Distribution of Residual and Pooled DNAPL," *Groundwater*, **31**(5).

Lake, L. W. **1989**. Enhanced Oil Recovery, Prentice-Hall, Inc., Englewood Cliff, NJ.

Lake, L. W., G. A. Pope, G. F. Carey and K. Sepehrnoori. **1984**. "Isothermal, Multiphase, Multicomponent Fluid-Flow in Permeable Media, Part I: Description and Mathematical Formulation," *In Situ*, **8**(1).

Land, C. S. **1968**. "Calculation of Imbibition Relative Permeability for Two- And Three-Phase Flow From Rock Properties," *Soc. Pet. Eng. J.*, **8**, 149-156.

Le Veque, R. J. **1990**. "Numerical Methods for Conservation Laws," *Lectures in Mathematics*, Birkhauser Verlag, Basel.

References

Lenhard, R .J. **1996**. "Improved Predictions of Multiphase Flow in Petroleum Reservoirs," Monthly Report to Pacific Northwest National Laboratory, Feb.

Lenhard, R .J. **1997**. "Improved Predictions of Multiphase Flow in Petroleum Reservoirs," Monthly Report to Pacific Northwest National Laboratory, Feb.

Leonard, B. P. **1979**. "A Stable and Accurate Convective Modeling Procedure Based on Quadratic Upstream Interpolation," *Computer Methods in Applied Mechanics and Engineering*, **19**, pp. 59-98.

Letniowski, F. W. and P. A. Forsyth. **1990**. "A Control Volume Finite Element Approach for Three-Dimensional NAPL Groundwater Contamination," University of Waterloo, Ontario, Canada, Dept. of Computer Science, Report No. CS90-21, May.

Leverett, M. C. **1941**. "Capillary Behavior in Porous Solids," *Trans. AIME*, **142,** 152.

Liang, Z. **1997**. "Development of a Dual Porosity Thermal Simulator," Ph.D. dissertation, The University of Texas at Austin.

Lin, E. **1981**. "A Study of Micellar/Polymer Flooding Using a Compositional Simulator," Ph.D. dissertation, The University of Texas at Austin.

Liu, J. **1993**. "High-Resolution Methods for Enhanced Oil Recovery Simulation," Ph.D. dissertation, The University of Texas at Austin.

Liu, J., M. Delshad, G. A. Pope and K. Sepehrnoori. **1994**. "Application of Higher Order Flux-Limited Methods in Compositional Simulations," *Journal of Transport in Porous Media*, **16**, 1-29.

Lockhart, T.P. **1992**. "A New Gelation Technology for In-Depth Placement of Cr^{3+}/Polymer Gels in High Temperature Reservoirs," SPE/DOE 24194, presented at the *SPE/DOE Eighth Symposium on Enhanced Oil Recovery*, Tulsa, OK, April 22-24.

Lyman, W. J., W. F. Reehl and D. H. Rosenblatt. **1982**. Handbook of Chemical Property Estimation Methods, American Chemical Society, McGraw Hill, Inc., Washington, DC.

Mackay, D. M., P. V. Roberts and J. A. Cherry. **1985**. "Transport of Organic Contaminants in Ground Water," *Environmental Science & Technology*, **19**(5), 384-392.

Mackay, D. M. and J. A. Cherry. **1989**. "Groundwater Contamination: Pump-and-Treat Remediation," *Environ. Sci. Technol.*, **23**, 630-636.

Mayer, A. S. and C. T. Miller. **1990**. "A Compositional Model for Simulating Multiphase Flow, Transport and Mass Transfer in Groundwater Systems," paper presented at the *Eighth International Conference on Computational Methods in Water Resources*, Venice, Italy, June 11-15.

McCarty, P. L. and L. Semprini. **1993**. "Ground-Water Treatment for Chlorinated Solvents," *Handbook of Bioremediation*, (J. E. Mathews project officer), Lewis Publishers, Boca Raton, FL, 87-116.

Means, J. C., S. G. Wood, J. J. Hassett and W.L. Banwart. **1980**. "Sorption of Polynuclear Hydrocarbons by Sediments and Soils," *Environmental Science and Technology*, **14**(12), 1524-1528.

Mercer, J. W. and R. M. Cohen. **1990**. "A Review of Immiscible Fluids in the Subsurface: Properties, Models, Characterization and Remediation," *J. Contaminant Hydrology*, **6**, 107-163.

Meter, D. M. and R. B. Bird. **1964**. "Tube Flow of Non-Newtonian Polymer Solutions, Parts I and II-Laminar Flow and Rheological Models," *AIChE J.*, 878-881, 1143-1150, Nov.

Miller, C. T and W. J. Weber, Jr. **1984**. "Modeling Organic Contaminant Partitioning in Groundwater Systems," *Ground Water*, **22**, 584-592.

Molz, F. J., M. A. Widdowson and L. D. Benefield. 1986. "Simulation of Microbial Growth Dynamics Coupled to Nutrient and Oxygen Transport in Porous Media," *Water Resour. Res.*, **22**(8): 1207-1216.

References

Morrow, N. R. and I. Chatzis. **1981**. "Measurement and Correlation of Conditions for Entrapment and Mobilization of Residual Oil," *final report to the U.S. Department of Energy,* Report no. DOE/BETC/3251-12, Oct.

Morrow, N. R. and B. Songkran. **1982**. Surface Phenomena in Enhanced Oil Recovery, D. O. Shah (ed.), Plenum Press, New York City, 387-411.

Morrow, N. R., I. Chatzis and H. Lim. **1985**. "Relative Permeabilities at Reduced Residual Saturation," *J. Can. Pet. Techol.*, 62-69, July-Aug.

Nelson, N. T. and M. L. Brusseau. **1996**. "Field Study of the Partitioning Tracer Methods for Detection of Dense Non-Aqueous Phase Liquids in a Trichloroethene-Contaminated Aquifer," *Environ. Sci. Technol.*, **30**, 2859-2863.

Nelson, R. C. **1982**. "The Salinity-Requirement Diagram - A Useful Tool in Chemical Flooding," *Soc. Pet. Eng. J.*, 259-270, April.

Nelson, R. C. and G. A. Pope. **1978**. "Phase Relationships in Chemical Flooding," *Soc. Pet. Eng. J.*, **18**, 325-338, Trans. AIME, 265, Oct.

Nolen, J. S. and D. W. Berry. **1972**. "Tests of the Stability and Time-Step Sensitivity of Semi-Implicit Reservoir Simulation Techniques," *Soc. Pet. Eng. J.*, **12** (3), 253-266.

Oak, M. J. **1990**. "Three-Phase Relative Permeability of Water-Wet Berea," SPE/DOE 20183, *Proceedings of the SPE/DOE Symposium on Enhanced Oil Recovery*, Tulsa, OK, April 22-25.

Oak, M. J., L. E. Baker and D. R. Thomas. **1990**. "Three-Phase Relative Permeability of Berea Sandstone," *J. Pet. Tech.*, 1054-1061, Aug.

Ooi, K. C. **1998**. "Laboratory Evaluation of Surfactant Remediation of Nonaqueous Phase Liquids," M.S. thesis, The University of Texas at Austin.

Oolman, T., S. T. Godard, G. A. Pope, M. Jin and K. Kirchner. **1995**. "DNAPL Flow Behavior in a Contaminated Aquifer: Evaluation of Field Data," *GMWR*, 125-137.

Parker, J. C., R. J. Lenhard and T. Kuppusamy. **1987**. "A Parametric Model for Constitutive Properties Governing Multiphase Flow in Porous Media," *Water Resour. Res.*, **23**(4), 618-624.

Peaceman, D. W. **1983**. "Interpretation of Well-Block Pressures in Numerical Reservoir Simulation With Nonsquare Gridblocks and Anisotropic Permeability," *Soc. Pet. Eng. J.*, **23**(3), 531-543.

Pennell, K. D., L. M. Abriola and W. J. Weber, Jr. **1993**. "Surfactant Enhanced Solubilization of Residual Dodecane in Soil Columns: 1. Experimental Investigation," *Environmental Science and Technology*, **27**(12), 2332-2340.

Pennell, K. D., M. Jin, L. M. Abriola and G. A. Pope. **1994**. "Surfactant Enhanced Remediation of Soil Columns Contaminated by Residual Tetrachloroethylene," *J. Contaminant Hydrology*, **16**, 35-53.

Pennell, K. D., G. A. Pope and L. M. Abriola. **1996**. "Influence of Viscous and Buoyancy Forces on the Mobilization of Residual Tetrachloroethylene During Surfactant Flushing," *Environmental Science and Technology*, **30** (4), 1328-1335.

Pickens, J. F., R. E. Jackson, W. H. Statham, C. L. Brown and G. A. Pope. **1993**. "Simulation of DNAPL Migration and Surfactant Enhanced Aquifer Remediation," presented at *Hazmat Southwest Conference*, Dallas, TX, Sept. 28-30.

Pope, G. A., L. W. Lake and F. G. Helfferich. **1978**. "Cation Exchange in Chemical Flooding: Part 1 - Basic Theory Without Dispersion," *Soc. Pet. Eng. J.*, **18**, 418-434, Dec.

Pope, G. A. and R. C. Nelson. **1978**. "A Chemical Flooding Compositional Simulator," *Soc. Pet. Eng. J.*, **18**, 339-354.

References

Pope, G. A. and M. Baviere. **1991**. "Basic Concepts in Enhanced Oil Recovery Processes," in *Critical Reports on Applied Chemistry*, 33, M. Baviere (ed.), Elsevier Science Publishing, London.

Pope, G. A., M. Jin, V. Dwarakanath, B. A. Rouse and K. Sepehrnoori, K. **1994**. "Partitioning Tracer Tests to Characterization Organic Contaminants," in proceedings of the *Second Tracer Workshop*, Bjørnstad, T. and G. A. Pope, Eds., Austin, TX.

Pope, G. A., K. Sepehrnoori, M. Delshad, B. A. Rouse, V. Dwarakanath and M. Jin. **1994**. "NAPL Partitioning Interwell Tracer Test in OU1 Test Cell at Hill Air Force Base, Utah," Final Report, ManTech Environmental Research Services Corp., P.O. number 94RC0251, GL number 2000-602-4600.

Powers, S. E., C. O. Loureiro, L. M. Abriola and W. J. Weber, Jr. **1991**. "Theoretical Study of the Significance of Nonequilibrium Dissolution of Nonaqueous Phase Liquids in Subsurface Systems," *Water Resour. Res.*, **27**(4), 463-477.

Powers, S. E., L. M. Abriola and W. J. Weber, Jr. **1992**. "An Experimental Investigation of Nonaqueous Phase Liquid Dissolution in Saturated Subsurface System: Steady-State Mass Transfer Rates," *Water Resour. Res.*, **28**(10), 2691-2705.

Prouvost, L., G. A. Pope and B. A. Rouse. **1985**. "Microemulsion Phase Behavior: A Thermodynamic Modeling of the Phase Partitioning of Amphiphilic Species," *Soc. Pet. Eng. J.*, 693-703, Oct.

Prouvost, L., G. A. Pope and K. Sepehrnoori. **1986**. "Modeling of Phase Behavior of Micellar Systems Used for EOR," *Surfactants in Solution*, **4**, K. L. Mittal and P. Bothorel (eds.), Plenum Press.

Prouvost, L., T. Satoh and G. A. Pope. **1984a**. "The Application of a Micellar Phase Behavior Model to Reservoir Modeling of Oil Displacement," presented at the *5th Symposium on Surfactants in Solution*, Bordeaux-Talence, France, July 9-13.

Prouvost, L., T. Satoh, G. A. Pope and K. Sepehrnoori. **1984b**. "A New Micellar Phase-Behavior Model for Simulating Systems With Up to Three Amphiphilic Species," SPE 13031, *Proceedings of the 59th Annual Meeting of the Society of Petroleum Engineers*, Houston, TX, Sept.

Radian. **1992**. "Final Remedial Investigation for Operable Unit 2-Sites WP07 and SS21," Prepared for Hill Air Force Base, UT.

Radian. **1994**. "Aquifer Data Evaluation Report, Operable Unit 2," Hill Air Force Base, UT, RCN 279-100-26-41.

Rao, P. S. C and R. E. Jassup. **1982**. "Development and Verification of Simulation Models for Describing Pesticide Dynamics in Soils," *Ecological Modeling*, **16**, 67-75.

Reed, R. L. and R. N. Healy. **1977**. "Some Physico-Chemical Aspects of Microemulsion Flooding: A Review," *Improved Oil recovery by Surfactant and Polymer Flooding*, D. O. Shah and R. S. Schechter (eds.), Academic Press, New York.

Reeves, M, D. S. Ward, P. A. Davis and E. J. Bonano. **1986**. "SWIFT II Self-Teaching Curriculum–Illustrative Problems for the Sandia Waste-Isolation Flow and Transport Model for Fractured Media," SAND84-1586, Sandia National Laboratories, Albuquerque, NM, Aug.

Reinhard, M. **1993**. "In-Situ Bioremediation Technologies for Petroleum-Derived Hydrocarbons Based on Alternate Electron Acceptors (Other Than Molecular Oxygen)," *Handbook of Bioremediation*, (J. E. Mathews project officer), Lewis Publishers, Boca Raton, FL, 131-147.

Rouse, J. D., D. A. Sabatini and J. H. Harwell. **1993**. "Minimizing Surfactant Losses Using Twin-Head Anionic Surfactants in Subsurface Remediation," *Environmental Science and Technology*, **27**(10), 2072-2078.

Saad, N. **1989**. "Field Scale Studies With a 3-D Chemical Flooding Simulator," Ph.D. dissertation, The University of Texas at Austin.

References

Saad, N., G. A. Pope and K. Sepehrnoori. **1989**. "Simulation of Big Muddy Surfactant Pilot," *Soc. Pet. Eng. Reservoir Eng.*, Feb.

Sabljic, A. **1987**. "On the Prediction of Soil Sorption Coefficients of Organic Pollutants from Molecular Structure: Application of Molecular Topology Model," *Environmental Science and Technology*, **21**(4), 358-366.

Salager, J. L., E. Vasquez, J. C. Morgan, R. S. Schechter and W. H. Wade. **1979**. "Optimum Formulation of Surfactant-Oil-Water Systems for Minimum Interfacial Tension or Phase Behavior," *Soc. Pet. Eng. J.*, **23**, 107.

Saraf, D. N. and I. Fatt. **1967**. "Three-Phase Relative Permeability Measurements Using a Nuclear Magnetic Resonance Technique for Estimating Fluid Saturation," *Trans. AIME*, **240**, 235-242.

Saraf, D. N., J. P. Batycky, C. H. Jackson and D. B. Fisher. **1982**. "An Experimental Investigation of Three-Phase Flow of Water-Oil-Gas Mixture Through Water-Wet Sandstone," SPE 10761, presented at the *California Regional Meeting of SPE*, San Francisco, CA, March 24-26.

Satoh, T. **1984**. "Treatment of Phase Behavior and Associated Properties Used in a Micellar-Polymer Flood Simulator," M.S. thesis, The University of Texas at Austin.

Scamehorn, J. F., R. S. Schechter and W. H. Wade. **1982**. "Adsorption of Surfactants on Mineral Oxide Surface from Aqueous Solutions, I: Isometrically Pure Anionic Surfactants," *J. of Colloid and interface science*, **85**(2), 463-477, Feb.

Schiesser, W. E. **1991**. The Numerical Method of Lines, Academic Press, Inc., New York.

Schneider, F. N. and W. W. Owens. **1970**. "Sandstone and Carbonate Two and Three-Phase Relative Permeability Characteristics," *Trans. AIME*, **249**, 75-84.

Schwarzenbach, R. P. and J. Westall. **1981**. "Transport of Nonpolar Organic Compounds from Surface Water to Groundwater," *Environmental Science and Technology*, **15**(11), 1360-1367.

Seright, R. S. and F. D. Martin. **1991**. "Impact of Gelation pH, Rock Permeability and Lithology on the Performance of a Monomer-Based Gel," SPE 20999, presented at the *SPE International Symposium on Oilfield Chemistry*, Anaheim, CA, Feb 20-22.

Shaiu, B. J., D. A. Sabatini and J. H. Harwell. **1995**. "Properties of Food Grade (Edible) Surfactants Affecting Subsurface Remediation of Chlorinated Solvents," *Environ. Sci. Technol.*, **29** 2929-2935.

Shook, G. M., G. A. Pope and K. Kostarelos. **1998**. "Prediction and Minimization of Vertical Migration of DNAPLs Using Surfactant Enhanced Aquifer Remediation at Neutral Buoyancy," *J. Contaminant Hydrology*, **34** 363-382.

Sleep, B. E. and J. F. Sykes. **1990**. "Numerical Simulation of Three-Phase Multi-Dimensional Flow in Porous Media," *Computational Methods in Subsurface Hydrology*, G. Gambolati *et al.* (eds.), Springer-Verlag, Berlin.

Sleep, B. E. and J. F. Sykes. **1993**. "Compositional Simulation of Groundwater Contamination by Organic Compounds: 1. Model Development and Verification," *Water Resour. Res.*, **29**(6), 1697-1708, June.

Smith, J. C., M. Delshad, G. A. Pope, W. G. Anderson and D. Marcel. **1988**. "Analysis of Unsteady-State Displacements Using a Capacitance-Dispersion Model," *In Situ*, **12**(1 & 2).

Soerens, T. S., D. A. Sabatini and J. H. Harwell. **1992**. "Surfactant Enhanced Solubilization of Residual DNAPL: Column Studies," in proceedings of the *Subsurface Restoration Conference, Third International Conference on Ground Water Quality Research*, EPA - R.S. Kerr Environmental Research Lab, Dallas, TX, 269-270.

Somasundaran, P. and H. S. Hanna. **1977**. "Physico-Chemical Aspects of Adsorption at Solid/Liquid Interfaces," *Improved Oil Recovery by Surfactant and Polymer Flooding*, D. O. Shah and R. S. Schechter (eds.), Academic Press, New York, 205-274.

References

Sorbie, K. S. **1991**. Polymer-Improved Oil Recovery, CRC Press, Inc., Boca Raton, Florida.

Stegemeier, G. L. **1977**. Mechanisms of Entrapment and Mobilization of Oil in Porous Media, *Improved Oil Recovery by Surfactant and Polymer Flooding*, D. O. Shah and R. S. Schechter (eds.), Academic Press, New York, 205-274.

Studer, J. E., P. Mariner, M. Jin, G. A. Pope, D. C. McKinney and R. Fate. **1996**. "Application of a NAPL Partitioning Interwell Tracer Test (PITT) to Support DNAPL Remediation at the Sandia National Laboratories/New Mexico Chemical Waste Landfill," in proceedings of the *Superfund/Hazwaste West Conference*, Las Vegas, NV.

Sweby, P. K. **1984**. "High Resolution Schemes Using Flux Limiters for Hyperbolic Conservation Laws," *SIAM Journal on Numerical Analysis*, **21**(5), 995-1011.

Taggart, I. J. and W. V. Pinczewski. **1987**. "The Use of Higher-Order Differencing Techniques in Reservoir Simulation," *Soc. Pet. Eng. J.*, **2**(3)**,** 360-372.

Tang, D. H, E. O. Frind and E. A. Sudicky. **1981**. "Contaminant Transport in Fractured Porous Media: Analytical Solution for Single Fracture," *Water Resour. Res.*, **17**(3), 555-564, June.

Thurston, G. B., P. M. Ozon and G. A. Pope. **1987**. "The Viscoelasticity and Gelation of Some Polyacrylamide and Xanthan Gum Solutions," Presented at *AICHE meeting*, March.

Todd, M. R., P. M. O'Dell and G. J. Hirasaki. **1972**. "Methods for Increased Accuracy in Numerical Reservoir Simulators," *Soc. Pet. Eng. J.* **12**, 515-529.

Travis, C. C. and E. L. Etnier. **1981**. "A Survey of Sorption Relationships for Reactive Solutes in Soil," *J. Environ. Qual.*, **10**(1), 8-17.

Tuck, D. M., P. R. Jaffe, D. A. Crerar and R. T. Mueller. **1988**. "Enhancing the Recovery of Immobile Residual Non-Wetting Hydrocarbons from Unsaturated Zone Using Surfactant Solutions," *Proceedings of the Conference on Petroleum Hydrocarbons and Organic Chemicals in Groundwater: Prevention, Detection and Restoration, National Water Well Association*, Dublin, OH.

Valocchi, A. J. and M. Malmstead. **1992**. "Accuracy of Operator Splitting for Advection-Dispersion-Reaction Problems," *Water Resour. Res.*, **28**(5), 1471-1476, May.

van Genuchten, M. T. **1980**. "A Closed-Form Equation for Predicting the Hydraulic Conductivity of Unsaturated Soils," *Soil Science Society of America Journal*, **44,** 892-989.

van Genuchten, M. T. and W. J. Alves. **1982**. "Analytical Solution of the One-Dimensional Convection-Dispersion Solute Transport Equation," *U. S. Department of Agriculture Technical Bulletin 1161.*

Vinsome, P. K. and J. Westerveld. **1980**. "A Simple Method for Predicting Cap and Base Rock Heat Losses in Thermal Reservoir Simulators," *J. Can. Pet. Technol.*, 87-90, July-Sept..

Walsh, M. P. **1983**. "Geochemical Flow Modeling," Ph.D. dissertation, The University of Texas at Austin.

Walter, A. L., E. O. Frind, D. W. Blowes, C. J. Ptacek and J. W. Molson. **1994**. "Modeling of Multicomponent Reactive Transport in Groundwater, 2: Metal Mobility in Aquifers Impacted by Acidic Mine Tailing Discharge," *Water Resour. Res.*, **30**(11), 3137-3158.

Weerasooriya, V., S. L. Yeh and G. A. Pope. **1999**. "Integrated Demonstration of Surfactant-Enhanced Aquifer Remediation (SEAR) with surfactant Regeneration and Reuse," in *Surfactant-Based Separations*: *Recent Advances*, Scamehorn. J. F. and Harwell J. H. (eds), ACS Symposium Series 740.

Weerasooriya, V., S. L. Yeh and G. A. Pope. **2000**. "Integrated Demonstration of Surfactant-Enhanced Aquifer Remediation (SEAR) with Surfactant Regeneration and Reuse," *Surfactant-Based Separations: Science and Technology*, J.F. Scamehorn and J.H. Harwell (eds.), ACS Symposium Series 740, American Chemical Society, Washington, DC.

West, C. C. and J. H. Harwell. **1992**. "Surfactant and Subsurface Remediation," *Environmental Science & Technology*, **26**(12), 2324-2330.

References

Widdowson, M. A., F. J. Molz and L. D. Benefield. **1988**. "A Numerical Transport Model for Oxygen- and Nitrate-Based Respiration Linked to Substrate and Nutrient Availability in Porous Media," *Water Resour. Res.*, **24**(9), 1553-1565, Sept.

Wilkins, M. D., L. M. Abriola and K. D Pennell. **1995**. "An Experimental Investigation of Rate-Limited Nonaqueous Phase Liquid Volatilization in Unsaturated Porous Media: Steady State Mass Transfer," *Water Resour. Res.*, **21**(9), 2159-2172, Sept.

Wilson, D. J. **1989**. "Soil Clean Up by In-Situ Surfactant Flushing: I. Mathematical Modeling," *Separation Science and Technology*, **24**, 863-892.

Wilson, D. J. and A. N. Clarke. **1991**. "Soil Clean Up by In-Situ Surfactant Flushing: IV. A Two-Component Mathematical Model," *Separation Science and Technology*, **26**(9), 1177-1194.

Wilson, J. T. and D. J. Geankoplis. **1966**. "Liquid Mass Transfer at Very Low Reynolds Numbers in Packed Beds," *Industrial Engineering Chemistry Fundamentals*, **5**, 9-14.

Winsor, P. A. **1954**. Solvent Properties of Amphiphilic Compounds, Butterworths, London.

Wolery, T. J. **1979**. "Calculation of Chemical Equilibria Between Aqueous Solutions and Minerals: The EQ3/EQ6 Software Package," Lawrence Livermore Lab. Report UCRL-52658.

Wreath, D. G. **1989**. "A Study of Polymerflooding and Residual Oil Saturation," M.S. thesis, The University of Texas at Austin.

Wreath, D., G. A. Pope and K. S. Sepehrnoori. **1990**. "Dependence of Polymer Apparent Viscosity on the Permeable Media and Flow Conditions," *In Situ*, **14**(3), 263-284.

Wunderlich, R. W., J. C. Fountain and R. E. Jackson. **1992**. "In-Situ Remediation of Aquifers Contaminated With Dense Nonaqueous Phase Liquids by Chemically Enhanced Solubilization," presented at the *Third Annual West Coast Conference on Hydrocarbon Contaminated Soils and Groundwater*, Long Beach, CA, March 9-12 and to be published in Hydrocarbon Contaminated Soils and Groundwater: Volume Three, Lewis Publishers, Inc., Chelsea, MI.